ACOUSTIC SCATTERING BY CYLINDRICAL SCATTERERS COMPRISING ISOTROPIC FLUID AND ORTHOTROPIC ELASTIC LAYERS

by

Chunyan Bao

M.S., Chongqing University of Technology, China, 2009

AN ABSTRACT OF A DISSERTATION

submitted in partial fulfillment of the
requirements for the degree

DOCTOR OF PHILOSOPHY

Department of Mechanical and Nuclear Engineering
College of Engineering

KANSAS STATE UNIVERSITY
Manhattan, Kansas

2016

Abstract

Acoustic scattering by a cylindrical scatterer comprising isotropic acoustic and orthotropic elastic layers is theoretically solved. The orthotropic material is used for the scattering problem because the sound speeds along radial and tangential axes can be different; which is an important property for acoustic cloaking design. A computational system is built for verifying the solutions and conducting simulations.

Scattering solutions are obtained based on two theoretical developments. The first one is exact solutions for elastic waves in cylindrically orthotropic elastic media, which are solved using Frobenius method. The second theoretical development is a set of two canonical problems for acoustic-orthotropic-acoustic media.

Based on the two theoretical developments, scattering by three specially selected simple multilayer scatterers are analyzed via multiple-scattering approach. Solutions for the three scatterers are then used for solving a "general" multilayer scatterer through a recursive solution procedure. The word "general" means the scatterer can have an arbitrary number of layers and each layer can be either isotropic acoustic or orthotropic elastic. No approximations have been used in the process. The resulting analytically-exact solutions are implemented and verified.

As an application example, acoustic scattering by a scatterer with a single orthotropic layer is presented. The effects on the scattering due to changing parameters of the orthotropic layer are studied. Acoustic scattering by a specially designed multilayer scatterer is also numerically simulated. Ratios of the sound speeds of the orthotropic layers along r and θ directions are defined to satisfy the requirement of the Cummer-Schurig cloaking design. The simulations demonstrate that both the formalism and the computational implementation of the scattering solutions are correct.

ACOUSTIC SCATTERING BY CYLINDRICAL SCATTERERS COMPRISING ISOTROPIC FLUID AND ORTHOTROPIC ELASTIC LAYERS

by

Chunyan Bao

M.S., Chongqing University of Technology, China, 2009

A DISSERTATION

submitted in partial fulfillment of the
requirements for the degree

DOCTOR OF PHILOSOPHY

Department of Mechanical and Nuclear Engineering
College of Engineering

KANSAS STATE UNIVERSITY
Manhattan, Kansas

2016

Approved by:

Major Professor
Liang-Wu Cai

Abstract

Acoustic scattering by a cylindrical scatterer comprising isotropic acoustic and orthotropic elastic layers is theoretically solved. The orthotropic material is used for the scattering problem because the sound speeds along radial and tangential axes can be different; which is an important property for acoustic cloaking design. A computational system is built for verifying the solutions and conducting simulations.

Scattering solutions are obtained based on two theoretical developments. The first one is exact solutions for elastic waves in cylindrically orthotropic elastic media, which are solved using Frobenius method. The second theoretical development is a set of two canonical problems for acoustic-orthotropic-acoustic media.

Based on the two theoretical developments, scattering by three specially selected simple multilayer scatterers are analyzed via multiple-scattering approach. Solutions for the three scatterers are then used for solving a "general" multilayer scatterer through a recursive solution procedure. The word "general" means the scatterer can have an arbitrary number of layers and each layer can be either isotropic acoustic or orthotropic elastic. No approximations have been used in the process. The resulting analytically-exact solutions are implemented and verified.

As an application example, acoustic scattering by a scatterer with a single orthotropic layer is presented. The effects on the scattering due to changing parameters of the orthotropic layer are studied. Acoustic scattering by a specially designed multilayer scatterer is also numerically simulated. Ratios of the sound speeds of the orthotropic layers along r and θ directions are defined to satisfy the requirement of the Cummer-Schurig cloaking design. The simulations demonstrate that both the formalism and the computational implementation of the scattering solutions are correct.

Table of Contents

Table of Contents v

List of Figures ix

List of Tables xvii

Acknowledgements xviii

1 Introduction 1

1.1 Background 1

1.1.1 Acoustic Cloaks Based on Cummer-Schurig Design 6

1.1.2 Experimentally Realized Acoustic Cloaks Based on Cummer-Schurig Design 14

1.1.3 Carpet Cloaks 20

1.1.4 Cloaks with Solid Pentamode Materials 25

1.1.5 Our Previous Work: Acoustic Cloaks with Mixture of Conventional Isotropic Fluid and Isotropic Solid Layers 31

1.2 Motivation for the Thesis 36

1.3 Research Objectives and Methods 37

1.4 Organization of Thesis 38

2 Waves in Cylindrically Orthotropic Elastic Media 39

2.1 Introduction 39

2.2 Equations of Motion for Orthotropic Medium 39

2.3 General Solutions for the Equations of Motion Using Frobenius Method . . . 41
2.3.1 Frobenius Series 43
2.3.2 The Index and the Indicial Equations 44
2.3.3 The Recurrence Relations 46
2.3.4 The General Solutions 48
2.3.5 Special Cases in the General Solutions 48
2.4 Special Case 1: Two α's Differ by an Integer 50
2.4.1 When $N = 1$ 53
2.4.2 When $N = 2$ 55
2.4.3 When $N > 2$ 59
2.4.4 Verifying the Solutions for Special Case 62
2.5 Special Case 2: When α is a Repeated Root 66
2.5.1 Solutions When α is a Repeated Root 67
2.5.2 Verifying the Solutions When α is a Repeat Root 70
2.6 Special Case 3: Mode $n = 0$ 72
2.6.1 Solution for U_0 72
2.6.2 Verifying Solution for U_0 76
2.6.3 Solution for V_0 79
2.6.4 Verifying Solution for V_0 82

3 Acoustic Wave Scattering by Cylindrical Scatterer Comprising Isotropic Acoustic and Orthotropic Elastic Layers 85

3.1 Introduction 85
3.2 Basis Equations and Field Expressions 86
3.2.1 Acoustic Field 86
3.2.2 Orthotropic Medium 88

3.3 Canonical Problems 89

3.3.1 First Canonical Problem 90

3.3.2 Second Canonical Problem 95

3.4 Acoustic Scattering by Multilayer Scatterers 97

3.4.1 Special Multilayer Scatterers 97

3.4.2 Solutions for a General Multilayer Scatterer 112

4 Solution Verification Through Two Approaches 119

4.1 Verification Via Exact Analytical Solution 120

4.1.1 Problem Statement 120

4.1.2 Obtaining the Exact Analytical Solution Using Single Scattering Method 120

4.1.3 Comparison of the Solutions Obtained with Two Methods 124

4.2 Verification Via Solutions for Scatterer which Comprises Both Isotropic Acoustic and Elastic Media 126

4.2.1 Single Layer Scatterer 127

4.2.2 Multiple Layer Scatterer 131

5 Scattering Numerical Simulations 135

5.1 Simulations of Acoustic Scattering by an Orthotropic Pipe 135

5.2 Scattering Simulation Study Through Parametric Changing of Orthotropic Medium 138

5.2.1 Young's Modulus Along Radial Direction (E_r) Greater Than That Along Tangential Direction (E_θ) 139

5.2.2 Young's Modulus Along Radial Direction (E_r) Smaller Than That Along Tangential Direction (E_θ) 148

5.2.3 Remarks 154

5.3 Simulation of Acoustic Scattering by a Specially Designed Multilayered Scatterer . . . 154

6 Conclusion **161**

6.1 Summary . . . 161

6.2 Future Work . . . 162

Bibliography **163**

List of Figures

1.1 A cloaking device near a point charge (from Pendry et al. (2006)). Orange core: cloaked region. Blue shell: cloaking shell. 2
1.2 Pendry *et al*'s illustration of transformation optics: a field line in electric field (A) before the transformation and (B) after the transformation (Pendry et al., 2006). 3
1.3 A view of transformation process. A: a point located in a free space (the orange disk) before transformation. B: transmitted space. White circle: cloaked region. Orange annulus: cloaking shell. 3
1.4 Cummer and Schurig's illustration of the acoustic pressure field (Cummer and Schurig, 2007). Left: without a scatterer. Middle: with an uncloaked scatterer. Right: with a cloaked scatterer. 5
1.5 Pressure field with planar incident wave (Cai and Sanchez-Dehesa, 2007). Left: Cummer-Schurig's design; Right: Cai and Sánchez-Dehesa's analysis . . 5
1.6 Pressure field with scatterer surrounded by 3D cloaking shell designed by Chen and Chan (2007) 6
1.7 Plane wave diffraction by square cloak filled with 256 sectors obtained by Farhat et al. (2008b). 7
1.8 Structure of cloak illustrated by Cheng et al. (2008). (a) Structure of acoustic layered system. (b) Structure of cloak. (c) Design procedure for multilayered cloak. 8
1.9 Schematic view of cloaking shell built by Torrent and Sánchez-Dehesa (2008) 9

1.10 Pressure field for planar incident wave impinging on a rigid scatterer surrounded by cloaking shells designed by Torrent and Sánchez-Dehesa (2008). Left: cloaking shell with 50 layers; Right: cloaking shell with 200 layers. Note that R_1 is the radius of the core. 9
1.11 Normalized total scattering cross section of a rigid cylinder cloaked by cloaks comprising 5 pairs of isotropic layers by Cai and Sánchez-Dehesa (2012). Solid curve: anisotropic cloak. Dot dashed curve: the heavier layer of each pair was placed closer to the object. Dashed curve: the softer layer of each pair was placed closer to the object. 11
1.12 The simulation results of the scattering by the coated scatterer obtained by Chen et al. (2008). f: the scattering amplitude. σ: total scattering cross section. 12
1.13 The normalized total scattering cross section of the cloak with 10 isotropic layers designed by Cai (2012). Blue dashed line: initial design. Red solid line: optimized design. 14
1.14 The three dimensional unidirection acoustic cloak presented by Urzhumov et al. (2012). (a) Acoustic pressure distribution on the cross-section of the cloak; (b) The picture of the three dimensional cloak. 15
1.15 Numerical results obtained by Farhat et al. (2008a) for a rigid cylinder covered by two cloaks under concentric surface wave. Left: cloak with 256 curved sectors; Right: cloak with 100 curved sectors. 15
1.16 The measured diffraction of surface waves obtained by Farhat et al. (2008a). Left: diffraction by a rigid cylinder surrounded by the structured cloak. Right: diffraction by the rigid cylinder on its own. 16

1.17 Structure of the 2D cloak fabricated by Zhang et al. (2011) with a network of serial inductors and shunt capacitors. The cavities with large volume work as shunt capacitors. The narrow channels which connect the cavities act as serial inductors. 16
1.18 The averaged visibility $\bar{\gamma}$ plotted by Zhang et al. (2011) for three cases: 1. with the object which is a steel cylinder and covered by the cloak (magenta circles); 2. with only the steel cylinder (green squares); no object (blue triangles). 17
1.19 Distribution of the cylinders designed by García-Chocano et al. (2011) to cloak a rigid body displaced at the center. The positions of the cylinders are represented by blue solid circles. 18
1.20 Total pressure fields for two cases simulated by García-Chocano et al. (2011) at 3 kHz: (a) with only the rigid object; (b) with the object covered the cloak. The impinging sound has a plane wavefront. 19
1.21 The averaged visibility obtained by García-Chocano et al. (2011). Black: free space. Blue: with only the object (an aluminum cylinder). Red: with the object covered by the cloak. The symbols represent the measured results. The continuous lines represent the calculated results by using finite element method. 20
1.22 (a) Schematic representation of the designed cloak and the central spherical object. (b) Photograph of the fabricated cloak. (Presented by Sanchis et al. (2015)) 21
1.23 Real part of the total pressure measured at 5.55kHz on the horizontal (left) and vertical (right) planes by Sanchis et al. (2015). (a) Free space, (b) bare sphere rigid object, (c) the object covered by the cloak. 22
1.24 The simulated acoustic fields plotted by Popa and Cummer (2011). 23

1.25 The simulated acoustic fields plotted by Popa et al. (2011). Top: with a triangular object. Bottom: with the same object but covered by the cloak. The pressure field in the region within the dashed rectangle were measured experimentally. 23

1.26 The measured acoustic fields plotted by Popa et al. (2011). Left: with only the ground plane. Middle: with the object placed on the ground plane. Right: with the object which covered by the cloak placed on the ground plane. . . 24

1.27 The simulated acoustic fields plotted by Ren et al. (2011). (a) without the cloak; (b) with the cloak 24

1.28 Snapshots of the fabricated cloak and cloaked object by Zigoneanu et al. (2014). (a), The fabricated cloak and the unit cell. (b), Photograph of the cloaked object, placed on the ground. 25

1.29 (a) The experimental set-up of carpet cloak by Zigoneanu et al. (2014). (b) The measured and mirrored pressure fields for three cases. From top to bottom: with nothing on the ground; with the object on the ground; with the object covered by the cloak on the ground. 26

1.30 Kadic *et al*'s illustration which shows the structures of the pentamode metamaterial designed by (a) Milton and Cherkaev and (b) Kadic et al. (2012). . 28

1.31 Kadic *et al*'s experimentally achievevable pentamode material structures (Kadic et al., 2012). 29

1.32 The scattering coefficients from a rigid object which covered with continuous and three-layer cloaks obtained by Scandrett et al. (2010). Blue solid line: PMIC cloak. Red dashed line: PM cloak. Green dot dashed line: IC cloak. Black dotted line: continuous cloak. 30

1.33 The scattering coefficients from a rigid object which covered with continuous and layered cloaks obtained by Scandrett et al. (2010). 31

1.34 Latticed pentamode acoustic design by Chen et al. (2015). (a) Profiles of continuously varying material properties of the cloak (solid lines), and their layered approximation by the pentamode lattice (dashed lines). (b) The schematic illustration of the recursive implantation of lattice cells into cyindrical layers. (c) The layout of the latticed cloak. 32
1.35 Simulated acoustic pressure fields by Chen et al. (2015). (a) Uncloaked case at $ka = 1.57$. (b) Cloaked case at $ka = 1.57$. (c) Uncloaked case at $ka = 2.51$. (d) Cloaked case at $ka = 2.51$. 33
1.36 Normalized total scattering cross section of the cloak with 10 isotropic fluid-solid mixture of layers designed by Bao and Cai (2012). Dot dashed curve: initial design. Dashed curve: optimized design at $ka = 3$. Solid curve: optimized design at $k_i a = 1, 2, 3$. 34
1.37 Total acoustic pressure distribution due to impinging of a planar incident wave onto a rigid cylinder cloaked by the design of Bao and Cai (2012). . . . 35

2.1 Solutions of $V_n^{(3)}(r)$ at $n = 0$ with $\alpha_0^{(3)} = 1$ 83
2.2 Solutions of $V_n^{(4)}(r)$ at $n = 0$ with $\alpha_0^{(4)} = -1$ 83

3.1 Canonical problems defined by Cai (2004): (a) first canonical problem; (b) second canonical problem 89
3.2 First Canonical Problem 90
3.3 Second Canonical Problem 91
3.4 Acoustic-Acoustic-Orthotropic-Acoustic 98
3.5 Scattering process in scatterer with acoustic-orthotropic-acoustic layers . . . 99
3.6 Acoustic-Orthotropic-Acoustic-Orthotropic-Acoustic 106
3.7 Acoustic-Orthotropic-Acoustic-Acoustic 111
3.8 Layer structure of the multilayer scatterer (Cai, 2008) 113

4.1 Modulus of $[\boldsymbol{T}]_0$ for the orthotropic-acousitc case at different E_r 129
4.2 Total acoustic pressure field. Left: orthotropic scatterer; Right: elastic scatterer. 130
4.3 Total acoustic pressure field. (a1)-(a2): scattering by the scatterer having orthotropic elastic layers at frequency $ka = 1, 3$, respectively; (b1)-(b2): scattering by the scatterer having isotropic elastic layers at frequency $ka = 1, 3$, respectively. 132
4.4 Modulus of acoustic pressure along radial direction ($0.98 < x/a < 1.2$, $y/a = 0$) for both cases at frequency $ka = 1$. 133
4.5 Modulus of acoustic pressure along radial direction ($0.98 < x/a < 1.2$, $y/a = 0$) for both cases at frequency $ka = 3$. 134

5.1 Total acoustic pressure field due to impinging of a planar incident wave onto a orthotropic pipe. [(a1)-(a3)]: the case which has the host defined as water and the pipe is filled with water at frequency $ka = 2, 4, 6$, respectively. [(b1)-(b3)]: the case which has the host defined as air and the pipe is filled with air at frequency $ka = 2, 4, 6$, respectively. 137
5.2 Total acoustic pressure field for the $E_r/E_\theta \approx 1$ case, at frequency $ka = 2$ (left), 4 (middle), and 6 (right). 140
5.3 Enlarged view of pressure field around scatterer for the $E_r/E_\theta \approx 1$ case, at frequency $ka = 2$ (left), 4 (middle), and 6 (right). 141
5.4 Total acoustic pressure field for the $E_r/E_\theta \approx 10$ case, at frequency $ka = 2$ (left), 4 (middle), and 6 (right). 142
5.5 Enlarged view of pressure field around scatterer for the $E_r/E_\theta \approx 10$ case, at frequency $ka = 2$ (left), 4 (middle), and 6 (right). 143

5.6 Same pressure with shown in Fig. 5.5 (right), while increasing maximum value of the pressure for the color bar increased to 3.5. 144
5.7 Total acoustic pressure field for the $E_r/E_\theta \approx 100$ case, at frequency $ka = 2$ (left), 4 (middle), and 6 (right). 145
5.8 Total acoustic pressure field for the $E_r/E_\theta \approx 1 \times 10^7$ case, at frequency $ka =$ 2 (left), 4 (middle), and 6 (right). 147
5.9 Total acoustic pressure field for the $E_r/E_\theta \approx 1 \times 10^7$ case, at frequency $ka =$ 2 (left), 4 (middle), and 6 (right). 147
5.10 Total acoustic pressure field for the $E_r/E_\theta \approx 10^{-1}$ case, at frequency $ka = 1$ (left), 3 (middle), and 5 (right). 150
5.11 Enlarged view of total acoustic pressure field for the $E_r/E_\theta \approx 10^{-1}$ case, at frequency $ka = 1$ (left), 3 (middle), and 5 (right). 150
5.12 Total acoustic pressure field for the $E_r/E_\theta \approx 10^{-2}$ case, at frequency $ka = 1$ (left), 3 (middle), and 5 (right). 151
5.13 Enlarged view of pressure field around the scatterer in Fig. 5.12. 152
5.14 Total acoustic pressure field for the $E_r/E_\theta \approx 10^{-5}$ case, at frequency $ka = 1$ (left), 3 (middle), and 5 (right). 153
5.15 Enlarged view of the pressure distribution of Fig. 5.14 153
5.16 Enlarged view of the pressure distribution of Fig. 5.14 and Fig. 5.15. 154
5.17 Total acoustic pressure field distribution due to impinging of a planar incident wave onto the multi-layer scatterer at frequency $ka = 2$ (left), 4 (middle), and 6 (right). 157
5.18 Enlarged view of total acoustic pressure field distribution around the scatterer of Fig. 5.17 at frequency $ka = 4$. 158
5.19 Enlarged view of total acoustic pressure field distribution around the scatterer of Fig. 5.18 at frequency $ka = 4$. 158

5.20 Modulus of acoustic pressure $|p|$ along radial direction ($-1.2 < x/a < -0.98, y/a = 0$) at frequency $ka = 4$. 159
5.21 Modulus of acoustic pressure $|p|$ along radial direction ($0.98 < x/a < 1.2, y/a = 0$) at frequency $ka = 4$. 159

List of Tables

2.1 Material properties of the orthotropic medium 62

2.2 The numerical results of F_1, F_2, F_3, and F_4 under different radii r 63

2.3 The numerical results of $W_U(r)$ and $W_V(r)$ under different radii r 63

2.4 Material properties of the orthotropic medium 64

2.5 The numerical results of H_1, H_2, H_3, and H_4 under different radii r 64

2.6 The numerical results of $W_U(r)$ and $W_V(r)$ under different radii r 65

2.7 Material properties of the orthotropic medium 65

2.8 The numerical results of F_1, F_2, F_3, and F_4 under different radii r 66

2.9 The numerical results of $W_U(r)$ and $W_V(r)$ under different radii r 66

2.10 Material properties of the orthotropic medium 70

2.11 The numerical results of G_1, G_2, G_3, and G_4 under different radii r 71

2.12 The numerical results of $W_U(r)$ and $W_V(r)$ under different radii r 71

2.13 Material properties of the orthotropic medium 77

2.14 The numerical results of E_1, E_2 under different radii r 78

2.15 The numerical results of $W_U(r)$ under different radii r 78

2.16 Material properties of the orthotropic medium 78

2.17 The numerical results of E_1 and E_2 under different radii r 79

2.18 The numerical results of $W_U(r)$ under different radii r 79

2.19 Material properties of the orthotropic medium 79

2.20 The numerical results of E_1 and E_2 under different radii r 80

2.21 The numerical results of $W_U(r)$ under different radii r 80

2.22 Numerical results of E_3 and E_4 under different radii r 82

2.23 The numerical results of $W_V(r)$ under different radii r 82

4.1 Material properties for acoustic media 1, 2, and 4 125

4.2 Material properties of the orthotropic medium 3 125

4.3 The results and comparison for each pair of matrices at $n = 0$ 125

4.4 The results and comparison for each pair of matrices at $n = 7$ 126

4.5 Material properties for the media of the host and the core. 127

4.6 Material properties of the orthotropic medium 128

4.7 Modulus of $[\boldsymbol{T}]_0$ for the orthotropic scatterer, when the value of Young's modulus along axis r is changing. 129

4.8 Modulus of acoustic pressure along radial direction ($0.98 < x/a < 1.2$, $y/a = 0$) for both cases 134

5.1 The entries of coefficient matrix $\{\boldsymbol{R}\}$ at different terms (shown in modulus) for the $E_r/E_\theta \approx 1$ case 140

5.2 The entries of coefficient matrix $\{\boldsymbol{R}\}$ at different terms (shown in modulus) for the $E_r/E_\theta \approx 10$ case 142

5.3 The entries of coefficient matrix $\{\boldsymbol{R}\}$ at different terms (shown in modulus) for the $E_r/E_\theta \approx 10^7$ case 146

5.4 The values of b_0, U_n, and V_n for the orthotropic medium when index $\alpha = \alpha_1$ at term $n = 30$ (shown in modulus). 148

5.5 The entries of coefficient matrix $\{\boldsymbol{R}\}$ at different terms (shown in modulus) for the $E_r/E_\theta \approx 10^{-1}$ case 149

5.6 The entries of coefficient matrix $\{\boldsymbol{R}\}$ at different terms (shown in modulus) for the $E_r/E_\theta \approx 10^{-2}$ case 151

5.7 Material properties of the orthotropic medium 156

Acknowledgments

First of all, I am very grateful to my academic advisor Professor Liang-Wu Cai for his guidance and support during my years in Kansas State University. I am also very grateful to Profs. Youqi Wang, Jack Xin, Sameer I. Madanshetty, Caterina Scoglio, and Glenn Horton-Smith for their willingness to serve as my supervisory committee and outside chairperson.

Chapter 1

Introduction

In this chapter, the background, motivation, research objectives and methods, and organization of the thesis are presented.

1.1 Background

The topic of cloaking has attracted significant attention in recent years. Cloaking devices are designed to cause an object to become invisible under certain conditions. Figure 1.1 (Pendry et al., 2006) illustrates a cloaking device in an electrostatic displacement field. The core is the cloaked object, and the shell is the cloaking device. A point charge is located nearby. The cloaking shell smoothly bends the field lines around the cloaked object. Observing from outside of the cloaking shell, it is as if nothing were there.

The theory of transformation optics was the basis for the design of electromagnetic cloaking, pioneered by Pendry et al. (2006) and Leonhardt (2006). In transformation optics, through a coordinate transformation, the original space is transformed to a new space. Based on the form-invariance of Maxwell's equations in both the original and the transformed spaces, the material properties in the new space can be obtained through the coordinate transformation. Figure 1.2 (Pendry et al., 2006) (A) shows a field line in the electric field

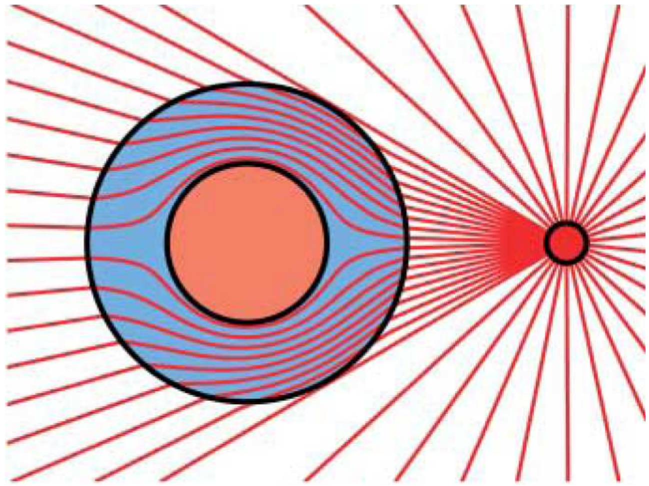

Figure 1.1: *A cloaking device near a point charge (from Pendry et al. (2006)). Orange core: cloaked region. Blue shell: cloaking shell.*

against a background of the Cartesian mesh. Figure 1.2 (B) shows the distorted field line, as well as the distorted mesh in the new space. Based on the transformation optics for the cloaking design, if a point in the original space can be transformed into a region in the new space, then anything in the region is cloaked. This is illustrated in Figure 1.3, where (A) shows a point located in the original space; and (B) shows that after transformation, the disk in Figure 1.3 (A) is transformed into an annulus, called the cloaking shell. The point at the center in the original space is transformed into the circle in the new space, which is the cloaked region.

In Pendry et al. (2006)'s study, the permittivity (ε) and permeability (μ) tensor components in the new coordinate system vary as the following

$$\frac{\varepsilon_r}{\varepsilon_0} = \frac{\mu_r}{\mu_0} = \frac{r-a}{r}, \qquad \frac{\varepsilon_\theta}{\varepsilon_0} = \frac{\mu_\theta}{\mu_0} = \frac{r}{r-a}, \qquad \frac{\varepsilon_z}{\varepsilon_0} = \frac{\mu_z}{\mu_0} = \left(\frac{b}{b-a}\right)^2 \frac{r-a}{r} \tag{1.1}$$

where ε_r, ε_θ, and ε_z are the permittivity in the radial, tangential and axial directions, respectively; μ_r, μ_θ and μ_z are the permeability in the radial, tangential and axial directions, respectively; ε_0 is the vacuum permittivity, and μ_0 is the vacuum permeability; a and b are the radii of the cloaked region and of the exterior of the cloaking shell, respectively; r is the radius. Eqn. 1.1 shows that anisotropic properties are required for the cloaking design.

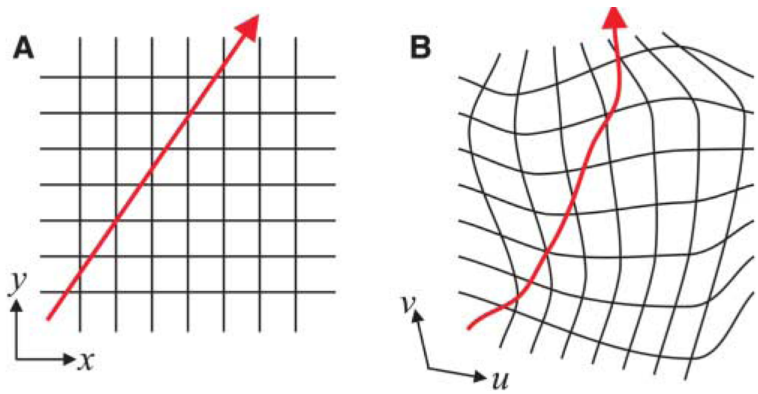

Figure 1.2: *Pendry* et al*'s illustration of transformation optics: a field line in electric field (A) before the transformation and (B) after the transformation (Pendry et al., 2006).*

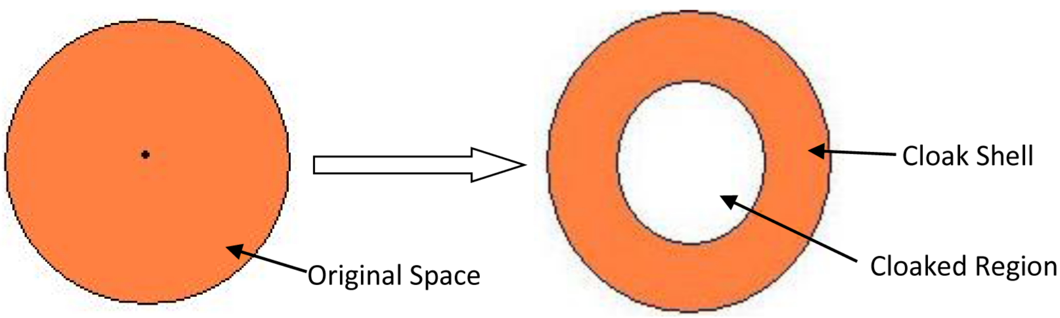

Figure 1.3: *A view of transformation process. A: a point located in a free space (the orange disk) before transformation. B: transmitted space. White circle: cloaked region. Orange annulus: cloaking shell.*

Since then, many cloaking designs for electromagnetic fields have been reported, such as Schurig et al. (2006a,b); Cummer et al. (2006); Miller (2006); Ruan et al. (2007); Chen et al. (2007); Chen and Chan (2008); Li and Pendry (2008); Kwon and Werner (2008); Rahm et al. (2008); Jiang et al. (2008); Liu et al. (2008); Hu et al. (2009). Cummer and Schurig (2007) found that the transformation optics can also be used for acoustic cloaking. They showed that via a variable exchange, the acoustic equations in a fluid are identical in form to the single polarization Maxwell equations in two-dimensions (2D). The variable exchange between electromagnetics and acoustic fields in two dimensions is given by

$$\left[p, v_r, v_\theta, \rho_r, \rho_\theta, K^{-1}\right] \leftrightarrow \left[-E_z, H_\theta, -H_r, \mu_\theta, \mu_r, \epsilon_z\right] \tag{1.2}$$

where the left group is for the acoustic case and the right group is for the electromagnetic case, respectively; p is the acoustic pressure, v_r, v_θ, ρ_r and ρ_θ are the velocities and mass densities in the radial and tangential directions, K is the bulk modulus; E_z is the electric field intensity in the axial direction, H_θ, and H_r are the magnetic field intensities in the tangential and radial directions, respectively. The relations between H and μ are shown as the following

$$i\omega\mu_r(-H_r) = -\frac{1}{r}\frac{\partial(-E_z)}{\partial\phi}, \tag{1.3}$$

$$i\omega\mu_\phi H_\phi = -\frac{\partial(-E_z)}{\partial r}, \tag{1.4}$$

$$i\omega\epsilon_z(-E_z) = -\frac{1}{r}\frac{\partial(rH_\phi)}{\partial r} - \frac{1}{r}\frac{\partial(-H_r)}{\partial\phi} \tag{1.5}$$

where ω is angular frequency and $i = \sqrt{-1}$.

The Cummer-Schurig acoustic cloak consists of a cylindrical shell with radially varying acoustical properties. The mass density and bulk modulus of the cloak have to satisfy the following relationships

$$\frac{\rho_r}{\rho_0} = \frac{r}{r-a}, \qquad \frac{\rho_\theta}{\rho_0} = \frac{r-a}{r}, \qquad \frac{K}{K_0} = \left(\frac{b-a}{b}\right)^2 \frac{r}{r-a} \tag{1.6}$$

properties with a subscript 0 are those of the host material. Figure 1.4 (Cummer and Schurig, 2007) shows three acoustic pressure fields obtained through numerical simulations. The left image shows the pressure field without a scatterer. The center image shows the pressure field with the uncloaked rigid scatterer. The right image shows the pressure field with the cloaked rigid scatterer. Figure 1.4 shows the good performance of the Cummer-Schurig cloak. The acoustic wave scattered by the rigid scatterer was significantly reduced by using the acoustic cloak.

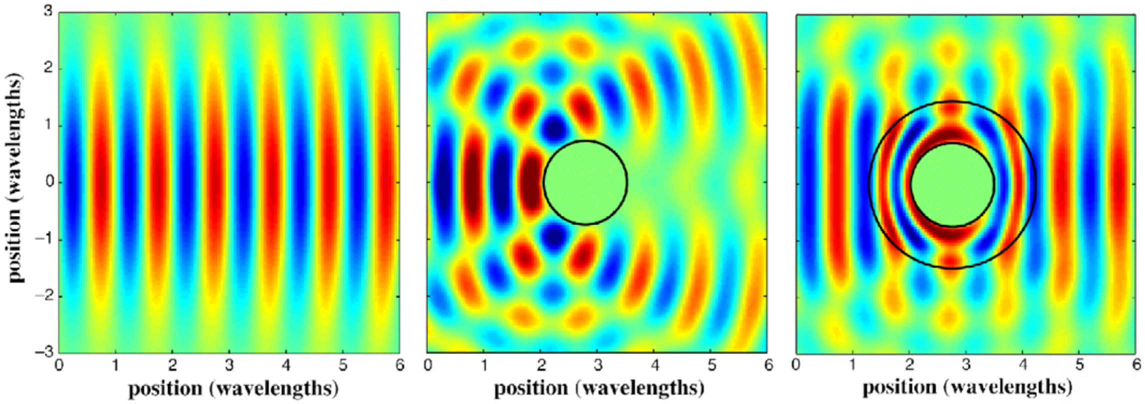

Figure 1.4: *Cummer and Schurig's illustration of the acoustic pressure field (Cummer and Schurig, 2007). Left: without a scatterer. Middle: with an uncloaked scatterer. Right: with a cloaked scatterer.*

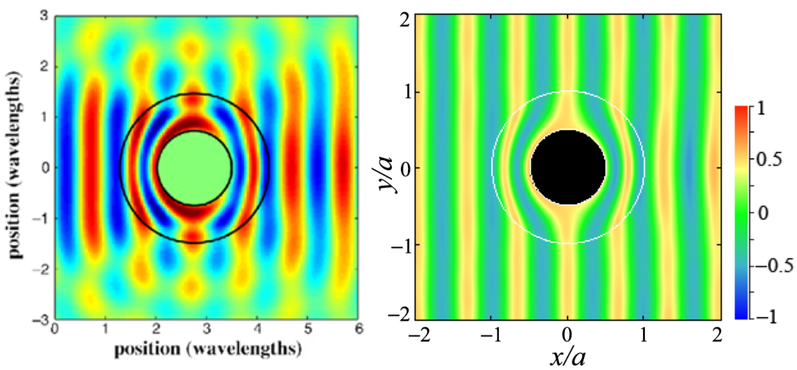

Figure 1.5: *Pressure field with planar incident wave (Cai and Sanchez-Dehesa, 2007). Left: Cummer-Schurig's design; Right: Cai and Sánchez-Dehesa's analysis*

Cai and Sanchez-Dehesa (2007) further analyzed the Cummer-Schurig acoustic cloak design. In their study, the Cummer-Schurig cloaking shell is approximated by a series of uniform anisotropic fluid layers. Figure 1.5 shows a comparison of the results of the Cummer-Schurig simulation (Cummer and Schurig, 2007) (left image) and Cai and Sánchez-Dehesa's analysis (right image). The left image has the planar acoustic Gaussian beam as the incident wave, while the right image has the planar incident wave.

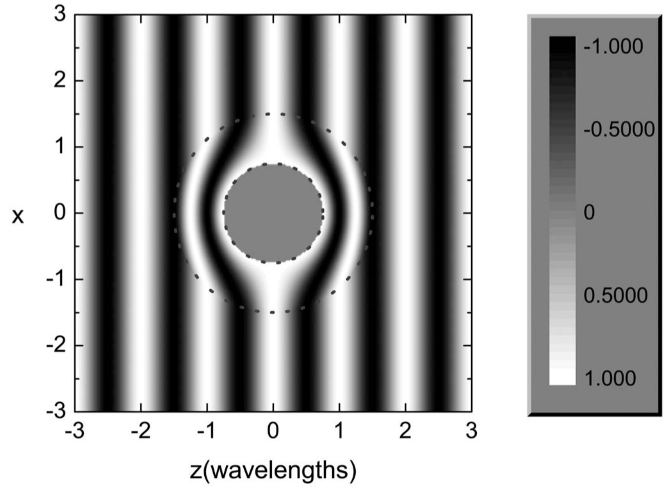

Figure 1.6: *Pressure field with scatterer surrounded by 3D cloaking shell designed by Chen and Chan (2007)*

1.1.1 Acoustic Cloaks Based on Cummer-Schurig Design

Based on Pendry et al. (2006)'s study, Chen and Chan (2007) obtained the three dimensional acoustic cloaking by mapping the acoustic equations to the conductivity equation, and confirmed the perfect cloaking. The material properties needed for three dimensional acoustic cloaking are as follows

$$\rho_r = \frac{b-a}{b}\frac{r^2}{(r-a)^2}, \qquad \rho_\theta = \frac{b-a}{b}, \qquad K = \left(\frac{b-a}{b}\right)^3 \frac{r^3}{(r-a)^3} \tag{1.7}$$

According to Eqn. 1.7, the materials required for the three dimensional acoustic cloaking design have radially varying properties. Figure 1.6 shows the pressure field in the x-z plane ($y = 0$) with the scatterer surrounded by the three dimensional cloaking shell designed by Chen and Chan (2007). Good performance of this three dimensional cloak can be observed in Figure 1.6.

Cummer et al. (2008) derived the three dimensional acoustic cloaking shell in a different way, but arrived at the same set of properties as shown in Eq. (1.7). In their study, acoustic scattering by an arbitrary object covered by a spherical shell is investigated. The mass

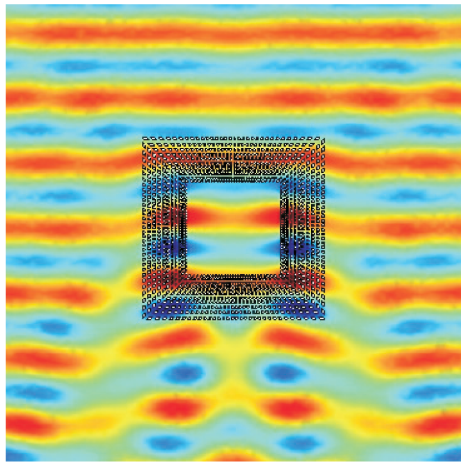

Figure 1.7: *Plane wave diffraction by square cloak filled with 256 sectors obtained by Farhat et al. (2008b).*

density and bulk modulus of the spherical shell which is the cloaking shell are derived to cancel the scattering from the arbitrary object. There is no scattered wave in any direction.

Farhat et al. (2008b) designed a square acoustic cloak through a geometric transform. Figure 1.7 shows the simulation result of a plane wave diffraction by a square cloak which is filled with 256 sectors.

There are two significant difficulties in realizing Cummer-Schurig cloaks. The first is that the design requires mass-anisotropic materials which do not exist in the natural world. Cheng et al. (2008) and Torrent and Sánchez-Dehesa (2008) designed acoustic cloaking shell by approximating Cummer-Schurig's anisotropic cloaking shell with multiple isotropic fluid layers. In Cheng et al. (2008)'s study, to approximate Cummer-Schurig's inhomogeneous anisotropic cloaking shell with homogeneous fluid materials, a two-step procedure is applied. First, the ideal acoustic cloaking shell is approximated by N homogeneous anisotropic layers. Next, each anisotropic layer is replaced by a pair of isotropic layers, denoted as layers A and B. Figure 1.8 shows the structure of the ideal acoustic cloak and the procedure for the approximation. The isotropic-anisotropic equivalence relations are expressed as

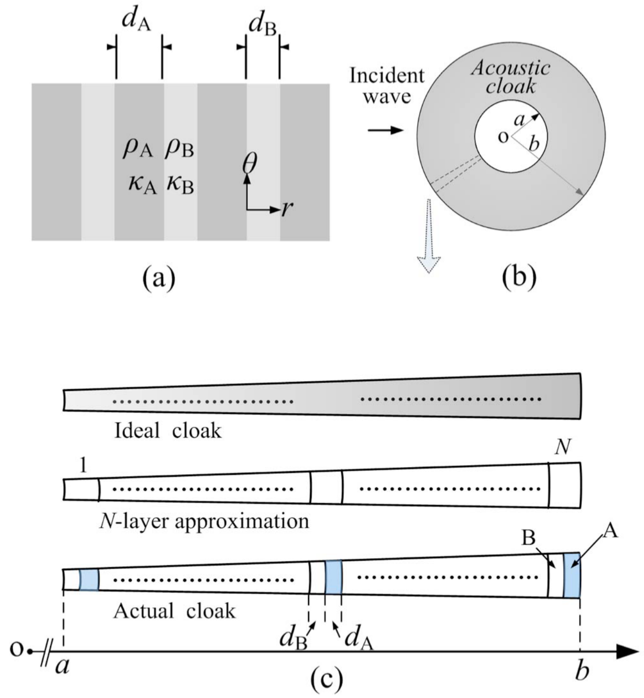

Figure 1.8: *Structure of cloak illustrated by Cheng et al. (2008). (a) Structure of acoustic layered system. (b) Structure of cloak. (c) Design procedure for multilayered cloak.*

$$\rho_r = \frac{1}{1+\eta}\left(\rho_A + \eta\rho_B\right) \tag{1.8}$$

$$\frac{1}{\rho_\theta} = \frac{1}{1+\eta}\left(\frac{1}{\rho_A} + \frac{\eta}{\rho_B}\right) \tag{1.9}$$

$$\frac{1}{K} = \frac{1}{1+\eta}\left(\frac{1}{K_A} + \frac{\eta}{K_B}\right) \tag{1.10}$$

where η is the thickness ratio of layer B to A. Acoustic scattering by a scatterer coated with the designed cloaking shell is simulated using the finite element method. The simulation results showed good performance of the cloak when $d_A \ll \lambda$ and $d_B \ll \lambda$, such as $\lambda = 40d_A$. Here d_A and d_B are the thicknesses of layers A and B, and λ is the wavelength. When the frequency increases, the thickness of each layer needs to be reduced to maintain favorable of the cloak.

In Torrent and Sánchez-Dehesa (2008)'s study, numerical experiments were applied to demonstrate the performance of the cloaking shell. It was shown that good performance

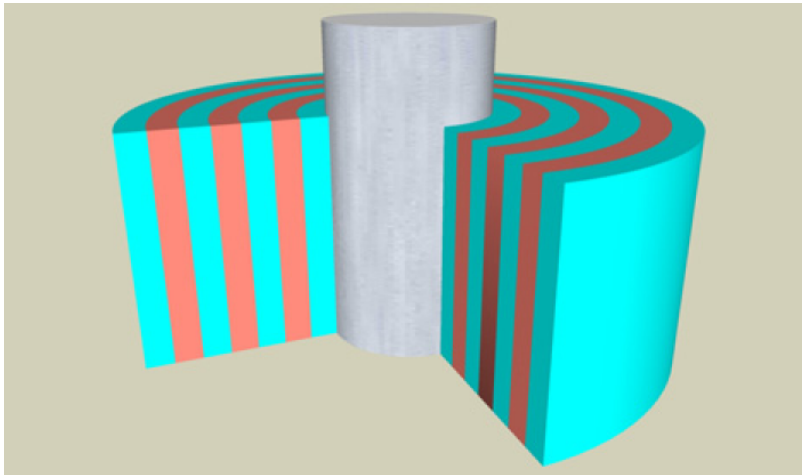

Figure 1.9: *Schematic view of cloaking shell built by Torrent and Sánchez-Dehesa (2008)*

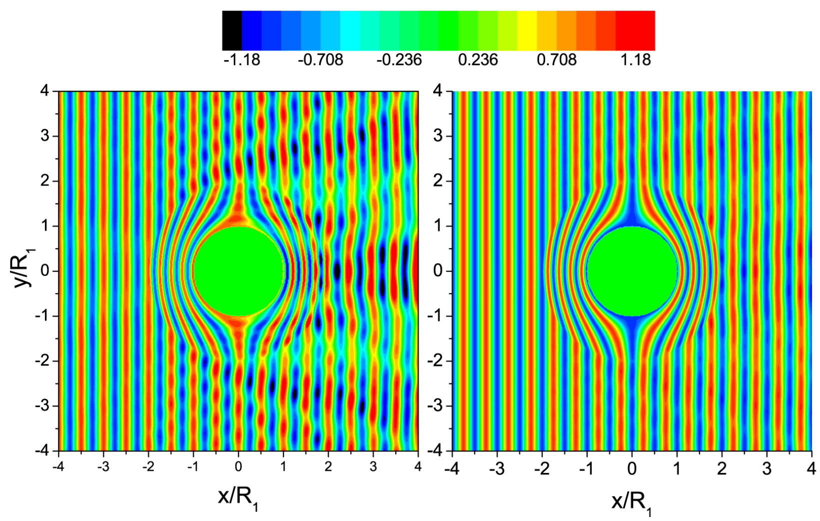

Figure 1.10: *Pressure field for planar incident wave impinging on a rigid scatterer surrounded by cloaking shells designed by Torrent and Sánchez-Dehesa (2008). Left: cloaking shell with 50 layers; Right: cloaking shell with 200 layers. Note that R_1 is the radius of the core.*

of the cloaking shell can be achieved by using a large number of layers, for example 200 layers. Figure 1.10 shows the pressure field for an incident planar wave impinging on rigid scatterer surrounded by cloaking shell of Torrent and Sánchez-Dehesa (2008). The cloaking shell shown in Figure 1.10 (left) has 50 layers, while the cloaking shell shown in Figure 1.10 (right) has 200 layers. Figure 1.10 shows that the cloaking shell with a larger number of layers is more effective than those with a smaller number of layers. The limitation of this cloak is that it only works at low frequency range and needs a large number of layers.

In-depth analyses of Cheng et al. (2008)'s acoustic cloak which is comprised of multiple isotropic layers are presented by Cheng and Liu (2008a,b) and Cheng et al. (2009). Cheng and Liu (2008a) theoretically analyzed the frequency response of the multilayered acoustic cloak. When cloaking a penetrable object, the performance of the cloak is strongly influenced by the resonances excited by different order penetrated waves around the resonant frequencies. The theoretical results were verified through numerical simulations using finite element method. Cheng and Liu (2008b) further demonstrated the performance of the acoustic cloak when the cloaked objects have a wide range of material parameters. Cheng et al. (2009) analyzed and obtained the details of pressure field distribution in each cloak layer. Their results show that the cloak's macroscopic scattering characteristics are determined by the microscopic material distribution and structural details in the multilayered structure.

Cai and Sánchez-Dehesa (2012) studied the equivalence between a single mass-anisotropic layer and two isotropic layers. Mass densities of two isotropic layers ρ_A and ρ_B can be easily found using Eqns. (1.8) and (1.9). To determine the bulk modulus of the two isotropic layers (K_A and K_B), having only one equation (Eqn. (1.10)) is not sufficient. Cai and Sánchez-Dehesa (2012) explored a few popular choices for the additional condition for K's, such as two layers having the same bulk modulus or the bulk modulus of the two layers are proportional to their respective mass densities. They concluded that the particular choices are not as important as the proper placement of layers. Also, according to Cai and Sánchez-Dehesa (2012), the *proper layer placement* requires the heavier layer to be placed closer to the cloaked region to maintain better cloak performance. Figure 1.11 shows the simulated normalized total scattering cross section of a rigid cylinder cloaked by cloaks comprising 5 pairs of isotropic layers. Each pair has the same sound speed and wave number. The total scattering cross section is defined as the total scattered energy transmitted through a closed

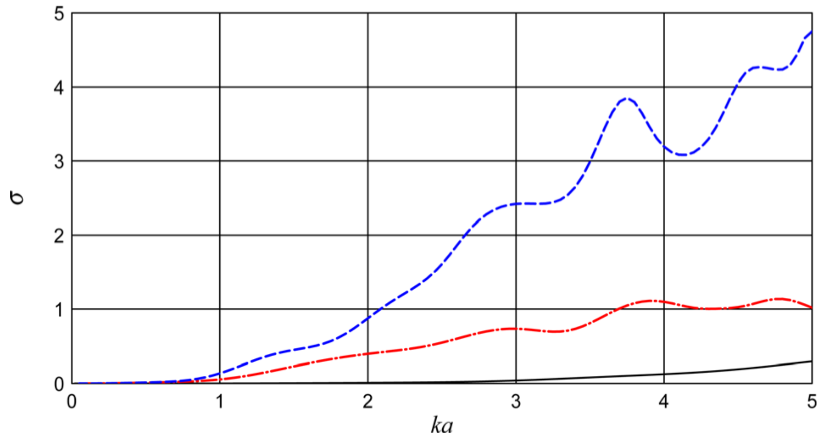

Figure 1.11: *Normalized total scattering cross section of a rigid cylinder cloaked by cloaks comprising 5 pairs of isotropic layers by Cai and Sánchez-Dehesa (2012). Solid curve: anisotropic cloak. Dot dashed curve: the heavier layer of each pair was placed closer to the object. Dashed curve: the softer layer of each pair was placed closer to the object.*

surface enclosing the scatterer. The normalized total scattering cross section is obtained by normalizing the total scattering cross section by the diameter of the cloaked region. It is a scalar quantity that represents the scattering strength of a scatterer. It vanishes when the scatterer is completely hidden. In Figure 1.11, two cloaks which have properly placed layers and improperly placed layers are compared with the anisotropic cloak. The cloak with the heavier layer of each pair placed closer to the object has better performance compared to the cloak with the soft layer of each pair placed closer to the object.

The second significant difficulty of the Cummer-Schurig design is material singularity. Eqn. (1.6) shows that at the interface between the cloaking shell and the cloaked region, ρ_r and K approach to infinity while ρ_θ approaches to zero. Chen et al. (2008) proposed a reduced acoustic cloak comprising of isotropic layers. The reduced acoustic cloak is obtained by loosening the requirement of the properties for the Cummer-Schurig design. In this way, the required mass is in a realizable range. The expressions for the parameters in this study are given as

$$\frac{\rho_r}{\rho_0} = \frac{b}{b-a} \qquad \frac{\rho_\theta}{\rho_0} = \frac{b}{b-a}\left(\frac{r-a}{r}\right)^2 \qquad \frac{K}{K_0} = \frac{b-a}{b} \tag{1.11}$$

According to Eqn. (1.11), ρ_r and K are constants, while only ρ_θ varies along radial direction.

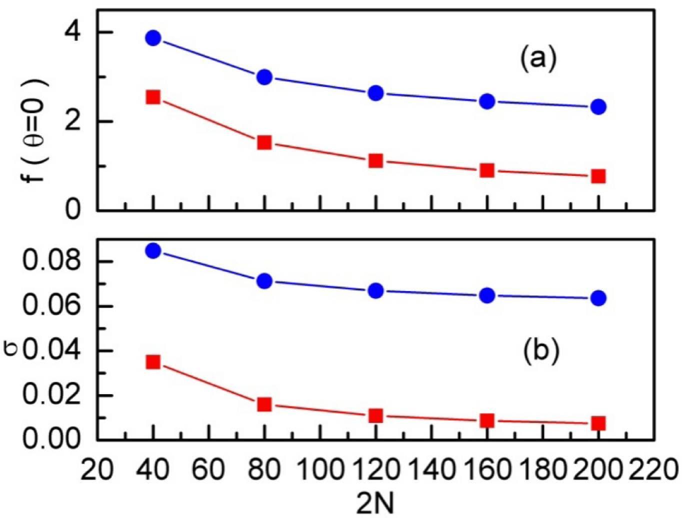

Figure 1.12: *The simulation results of the scattering by the coated scatterer obtained by Chen et al. (2008). f: the scattering amplitude. σ: total scattering cross section.*

Based on the expression for the parameters given in Eqn. (1.11), the cloak is designed by alternating multiple isotropic layers using the procedure presented by Cheng et al. (2008). Figure 1.12 (a) and (b) show the simulation results of scattering amplitude $f(\theta)$ and the total scattering cross section σ when the cloaks have different numbers of layers ($2N$). Scattering amplitude can be defined as the amplitude of the outgoing wave normalized by the amplitude of the incoming wave, since the incoming wave is assumed to have unit amplitude. It is defined as the following (Cai and Sanchez-Dehesa, 2007) when the incoming plane wave has unit amplitude:

$$f(\theta) = \lim_{r \to \infty} |p^{scr}| \sqrt{\pi k r / 2} \tag{1.12}$$

where p^{scr} is the pressure due to the scattered wave.

The circles in Figure 1.12 denote the reduced case while the squares denote the ideal case. For the ideal case, when the number of layers $2N$ is large enough, the scattering amplitude $f(\theta)$ and the total scattering cross section σ approach to zero. It can be observed from Figure 1.12 that by reducing the requirement of the properties, the performance of the cloak is also reduced. Also the cloak has better performance if the number of the layers is large, for example when $2N = 200$.

Cai (2012) explored the question of whether the material singularity is a requirement for perfect cloaking, and concluded that a perfect cloaking without material singularity can be achieved by fine-tuning material properties using various optimization schemes. The initial design is based on the Cummer-Schurig design, with each anisotropic layer replaced by a pair of isotropic layers using the isotropic-anisotropic equivalence relations. Then the material properties of each isotropic layer are fine-tuned through optimization schemes. Figure 1.13 shows the normalized total scattering cross section of both the initial design (blue dashed line) and optimized design (red solid line). These designs have 10 isotropic layers. For the optimized design, the optimization is run at frequency $ka = 3$. It can be observed from Figure 1.13 that the cloaking effect is perfect at the optimized frequency. Figure 1.13 also shows that both the initial and optimized designs have strong frequency dependency. The initial design effect deteriorates when frequency increases, which starts at frequency $ka = 1$. The optimized design effect is perfect at the optimized frequency $ka = 3$, but deteriorates at other frequencies, for example, at frequency $ka = 1$.

Urzhumov et al. (2012) presented a three dimensional unidirectional acoustic cloak comprising isotropic acoustic materials. It was shown in their study that the unidirectional acoustic cloak with isotropic materials can be achieved when the positions of the source and detector were given. The simulated pressure distribution inside the cloak of Figure 1.14, shows nearly ideal cloaking. Unlike the omnidirectional cloaks, the unidirectional cloak can only reduce visibility of the object for a very limited range of observation angles.

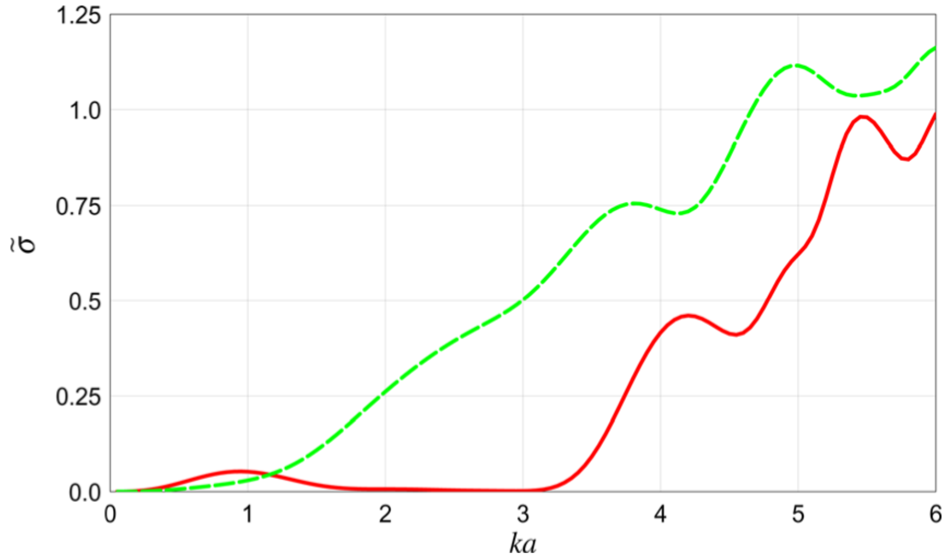

Figure 1.13: *The normalized total scattering cross section of the cloak with 10 isotropic layers designed by Cai (2012). Blue dashed line: initial design. Red solid line: optimized design.*

1.1.2 Experimentally Realized Acoustic Cloaks Based on Cummer-Schurig Design

Acoustic cloaks for linear liquid surface waves were presented by Farhat et al. (2008a). In Farhat et al. (2008a)'s study, a cylindrical acoustic cloak was constructed with curved rigid sectors. The performance of the cloak was demonstrated theoretically and numerically. Figure 1.15 shows the numerical results. A concentric surface wave was used as the incident wave. The cloaked object is a rigid cylinder. The cloak in Figure 1.15 (left) has 256 curved sectors; while the cloak in Figure 1.15 (right) has 100 curved sectors. Both cloaks have good performance. Figure 1.16 shows the measured diffraction of surface waves by a rigid cylinder surrounded by the structured cloak (left) and the rigid cylinder on its own (right). The structured cloak is comprised of 100 curved sectors. The experimental results showed that the wave backscattered by the rigid cylinder covered by the cloaking shell is greatly reduced. However, the reduction of the wave scattered by the cloak in all directions was not experimentally provided in this paper.

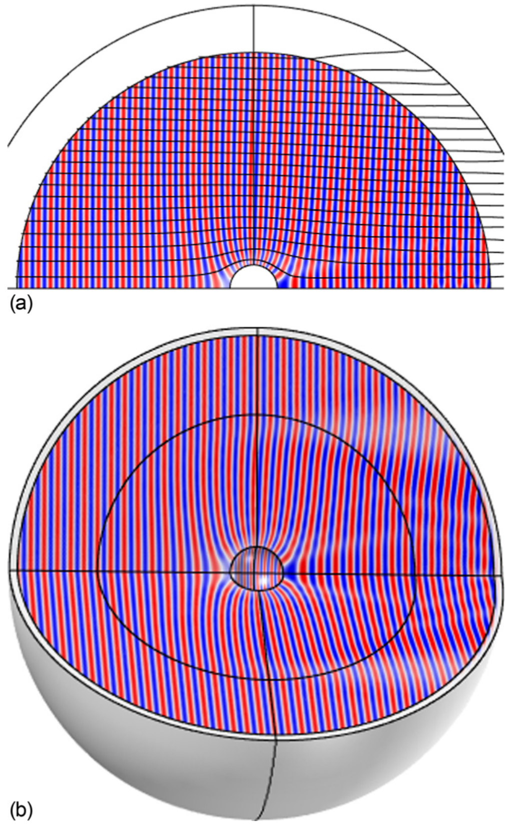

Figure 1.14: *The three dimensional unidirection acoustic cloak presented by Urzhumov et al. (2012). (a) Acoustic pressure distribution on the cross-section of the cloak; (b) The picture of the three dimensional cloak.*

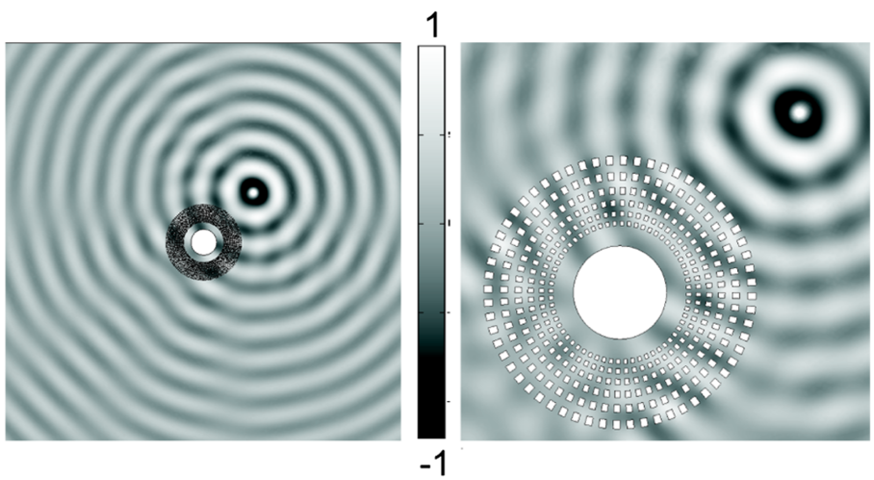

Figure 1.15: *Numerical results obtained by Farhat et al. (2008a) for a rigid cylinder covered by two cloaks under concentric surface wave. Left: cloak with 256 curved sectors; Right: cloak with 100 curved sectors.*

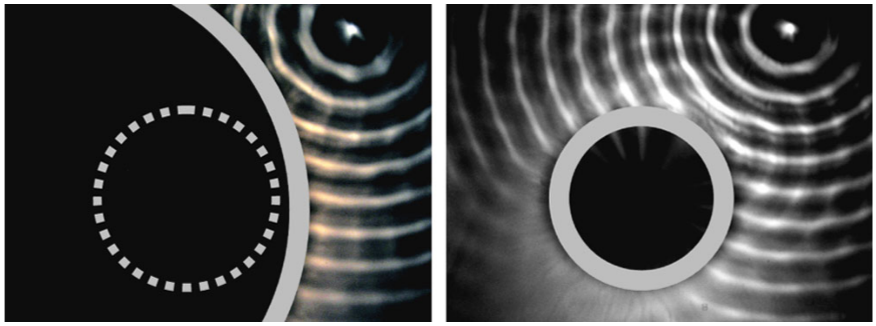

Figure 1.16: *The measured diffraction of surface waves obtained by Farhat et al. (2008a). Left: diffraction by a rigid cylinder surrounded by the structured cloak. Right: diffraction by the rigid cylinder on its own.*

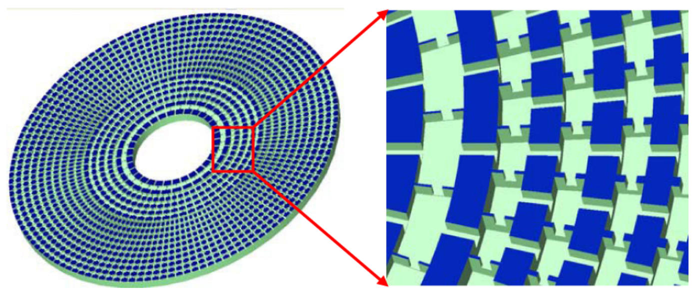

Figure 1.17: *Structure of the 2D cloak fabricated by Zhang et al. (2011) with a network of serial inductors and shunt capacitors. The cavities with large volume work as shunt capacitors. The narrow channels which connect the cavities act as serial inductors.*

Zhang et al. (2011) was the first to realize an acoustic cloak for underwater ultrasonic waves. This cloak is fabricated with a network of acoustic circuit elements which are serial inductors and shunt capacitors. The structure of the cloak is shown in Figure 1.17. The two dimensional acoustic cloak comprises 16 homogenous concentric cylinders. Figure 1.18 shows the measured averaged visibility ($\bar{\gamma}$) over the frequency range from 52 kHz to 64 kHz. $\bar{\gamma}$ is a parameter used for characterizing the performance of the cloak. It is defined as (Zhang et al., 2011)

$$\bar{\gamma} = \frac{1}{n}\sum_{j=1}^{n}\frac{P_{\max,j} - P_{\min,j}}{P_{\max,j} + P_{\min,j}} \tag{1.13}$$

where $P_{\max,j}$ and $P_{\min,j}$ are the maximum and minimum peak values of the pressure along the wave front numbered by j. According to Eqn. 1.13, when $P_{\max,j} = P_{\min,j}$, the minimum

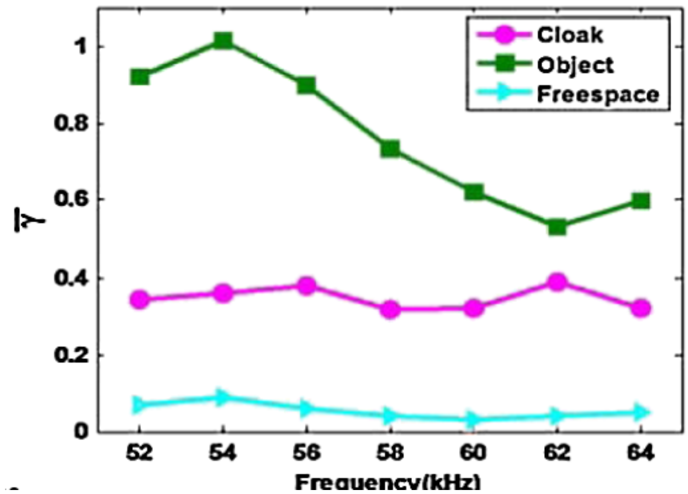

Figure 1.18: *The averaged visibility $\bar{\gamma}$ plotted by Zhang et al. (2011) for three cases: 1. with the object which is a steel cylinder and covered by the cloak (magenta circles); 2. with only the steel cylinder (green squares); no object (blue triangles).*

value of $\bar{\gamma}$ can be obtained, which is $\bar{\gamma}_{\min} = 0$. When $P_{\min,j} = 0$, the maximum value of $\bar{\gamma}$ can be obtained, which is $\bar{\gamma}_{\max} = 1$. When the averaged visibility vanishes, the cloaked object is totally invisible. This means that the cloak is perfect. A wave front is a surface representing corresponding points of a wave that have the same phase. It is usually perpendicular to the direction of propagation. The comparison of the three cases in Figure 1.18 shows that the cloak is effective in a broad frequency range.

García-Chocano et al. (2011) realized a two dimensional directional acoustic cloak in air. The cloak is comprised of 120 aluminum cylinders of 1.5 cm diameter. The positions of the cylinders were determined through optimization approaches at the frequency of 3061 Hz. Figure 1.19 shows the distribution of the cylinders designed to cloak a rigid cylinder of 22.5 cm diameter. Figure 1.20 shows the simulated total pressure fields for two cases: (a) with only the rigid object and (b) with the object covered by the cloak. The simulation results show that the strong scattering produced by the rigid object is significantly reduced by using the cloak. An experiment was also conducted to verify the performance of the constructed cloak. An aluminum cylinder was employed as the object to be cloaked in the experimental setup. A series of measurements around the selected operating frequency (3 kHz) of the

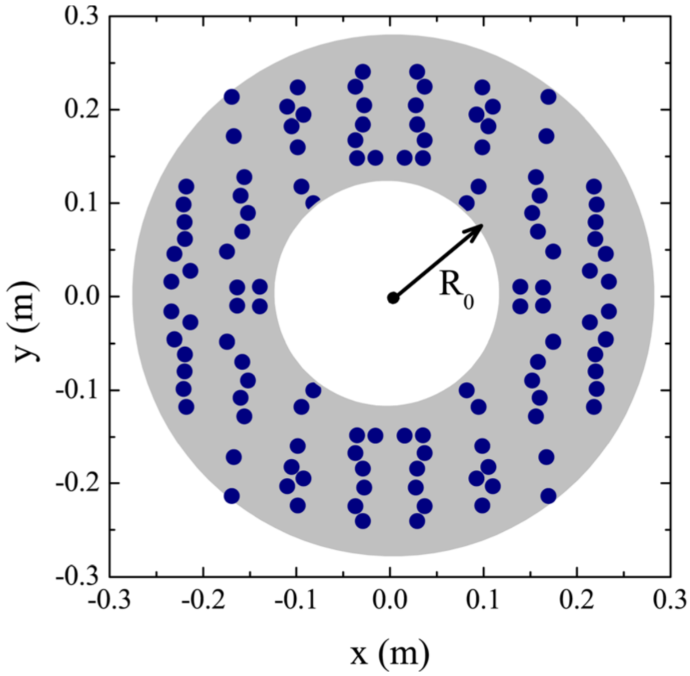

Figure 1.19: *Distribution of the cylinders designed by García-Chocano et al. (2011) to cloak a rigid body displaced at the center. The positions of the cylinders are represented by blue solid circles.*

cloak were conducted to quantify the reduction of scattering by using the cloak. Figure 1.21 shows the measured averaged visibility around the selected operating frequency (3 kHz) for three cases: 1. with no object (black circles), 2. with only the object; an aluminum cylinder (blue squares), and 3. with the object covered by a cloak (red triangles). The experimental results show that the averaged visibility ($\bar{\gamma}$) of the object is very close to that measured for the empty space (no object) near the operation frequency (3 kHz). However, it also has a strong frequency dependence.

Sanchis et al. (2015) designed and fabricated a directional three dimensional acoustic cloak in air, which is shown in Figure 1.22. Figure 1.22 (a) shows the schematic of the designed cloak and the central spherical object. Figure 1.22 (b) shows a photograph of the fabricated cloak. The cloak is comprised of 60 rigid tori which are positioned concentrically around the 4 cm radius cloaked sphere. Experimental measurements show that the averaged visibility ($\bar{\gamma}$) of the bare sphere was reduced from 0.25 to 0.10 by using the cloak at the

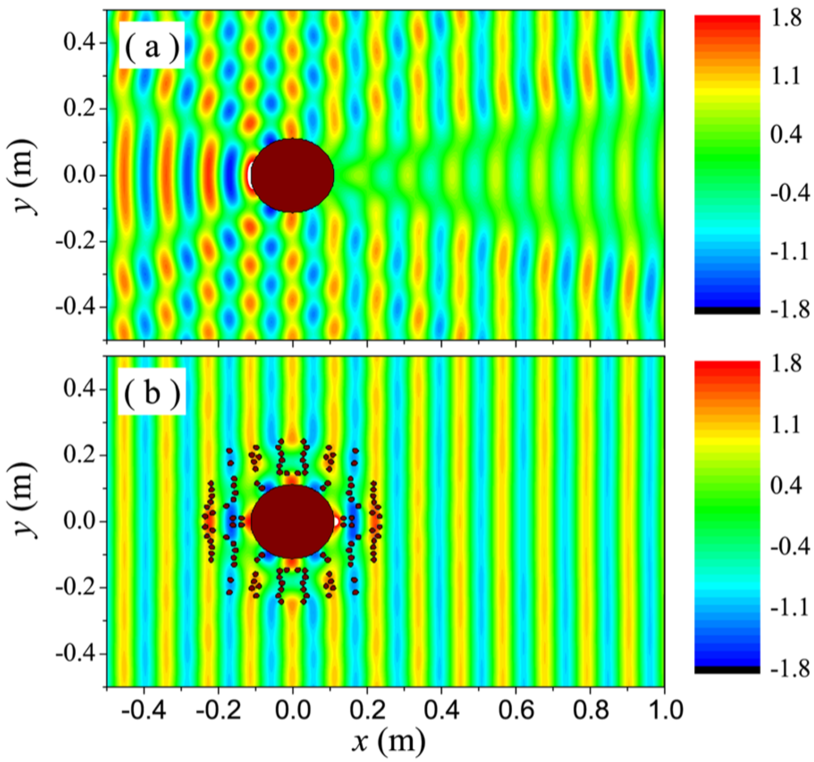

Figure 1.20: *Total pressure fields for two cases simulated by García-Chocano et al. (2011) at 3 kHz: (a) with only the rigid object; (b) with the object covered the cloak. The impinging sound has a plane wavefront.*

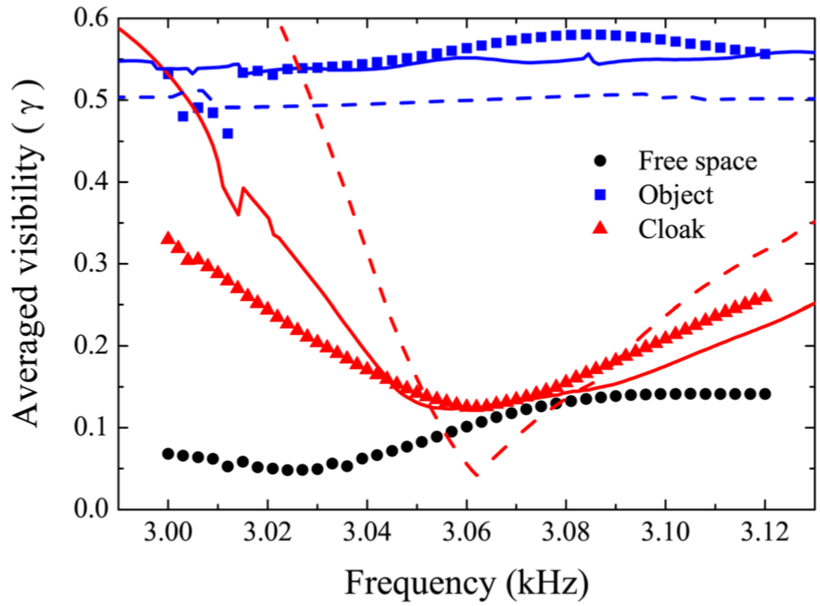

Figure 1.21: *The averaged visibility obtained by García-Chocano et al. (2011). Black: free space. Blue: with only the object (an aluminum cylinder). Red: with the object covered by the cloak. The symbols represent the measured results. The continuous lines represent the calculated results by using finite element method.*

frequency of 8.55 kHz. Figure 1.23 shows the real part of the total pressure measured on the horizontal XZ plane (left-hand panels) and vertical YZ plane (right-hand panels) for three cases: (a) free space, (b) bare rigid sphere object, and (c) sphere object covered by the cloak. It can be observed from Figure 1.23 that the wave reflections due to the object are significantly reduced by using the fabricated cloak.

1.1.3 Carpet Cloaks

"Carpet" or "ground" cloaks are devices that are used to hide objects positioned on reflecting surfaces. An acoustic ground cloak comprised of easily-found materials was designed by Popa and Cummer (2011). In their study, a two dimensional triangular shaped object is hidden under a triangular shaped "carpet". Figure 1.24 shows the simulation results of the acoustic fields. Figure 1.24 (a) and (b) show the acoustic fields after the incident beam impinges at 45° on both the ground and the rigid object not coated by the cloak. Figure

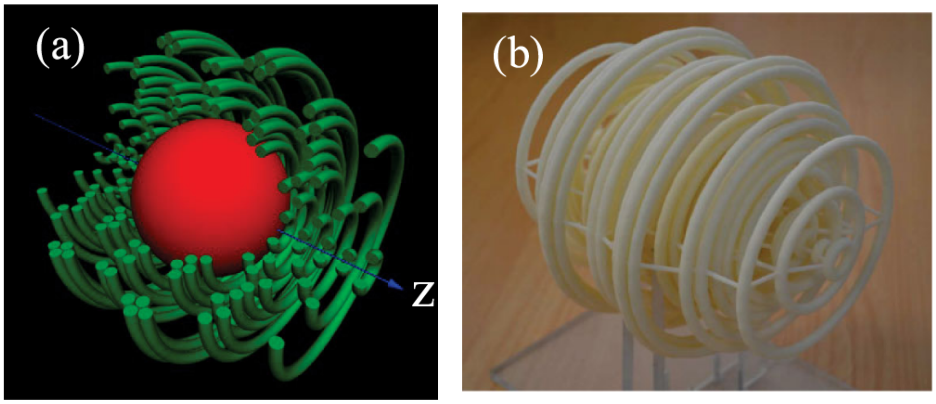

Figure 1.22: *(a) Schematic representation of the designed cloak and the central spherical object. (b) Photograph of the fabricated cloak. (Presented by Sanchis et al. (2015))*

1.24 (c) and (d) show the acoustic fields when the same incident beam encountered the same object which is coated with the theoretical cloak and the physically realized cloak, respectively. Figure 1.24 (e) is similar with (d); the only difference is that the incident beam impinges on the object at different directions. Figure 1.24 (f) is also similar with (d), but the incident beam has different frequency. Through comparison of the acoustic fields provided in Figure 1.24, the effectiveness of the ground acoustic cloaks is demonstrated.

A broadband acoustic ground cloak in air was experimentally realized by Popa et al. (2011). Figure 1.25 shows the two simulated acoustic pressure fields: with a triangular object (top) and with the object covered by the cloak (bottom). Figure 1.25 shows that the strong scattering from the object was significantly reduced by using the cloak. The acoustic pressure fields in the dashed square region were experimentally measured. Figure 1.26 shows the measured scattered fields of three cases with only the ground plane (left), with an object placed on the top of the ground plane (middle), and with an object covered by the fabricated cloak placed on the top of the ground plane (right). The good performance of this cloak was experimentally demonstrated through measurement of the acoustic pressure fields around the cloak.

Ren et al. (2011) designed a petal-shaped acoustic carpet cloak. This cloak has two open windows, through which the communication between the inner and outer side of the

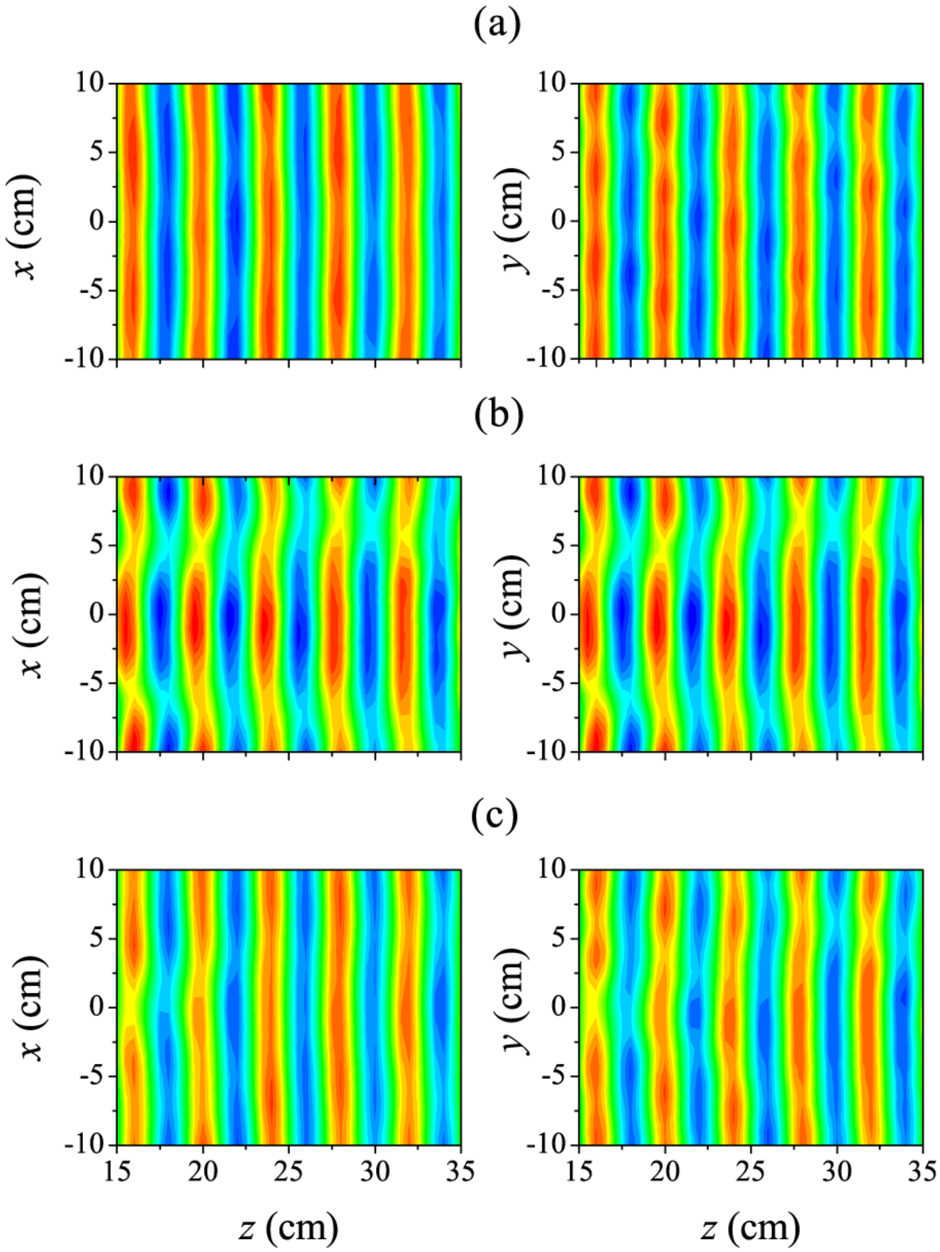

Figure 1.23: *Real part of the total pressure measured at 5.55kHz on the horizontal (left) and vertical (right) planes by Sanchis et al. (2015). (a) Free space, (b) bare sphere rigid object, (c) the object covered by the cloak.*

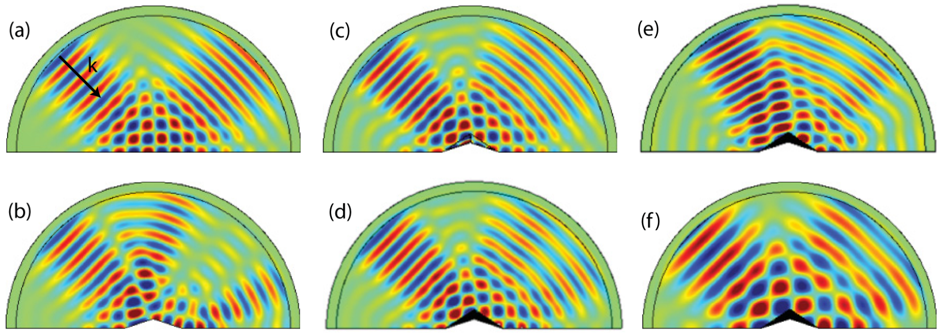

Figure 1.24: *The simulated acoustic fields plotted by Popa and Cummer (2011).*

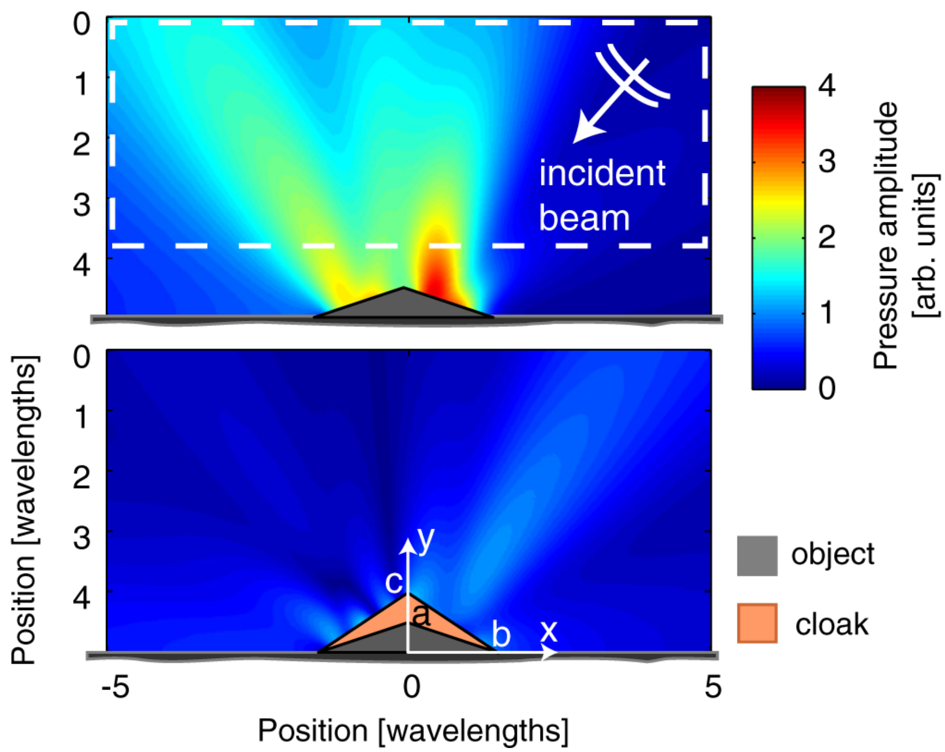

Figure 1.25: *The simulated acoustic fields plotted by Popa et al. (2011). Top: with a triangular object. Bottom: with the same object but covered by the cloak. The pressure field in the region within the dashed rectangle were measured experimentally.*

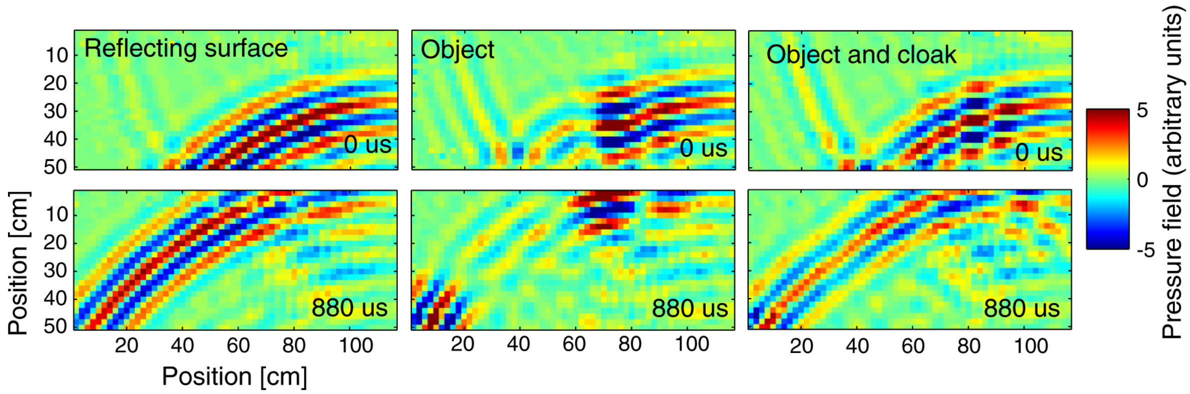

Figure 1.26: *The measured acoustic fields plotted by Popa et al. (2011). Left: with only the ground plane. Middle: with the object placed on the ground plane. Right: with the object which covered by the cloak placed on the ground plane.*

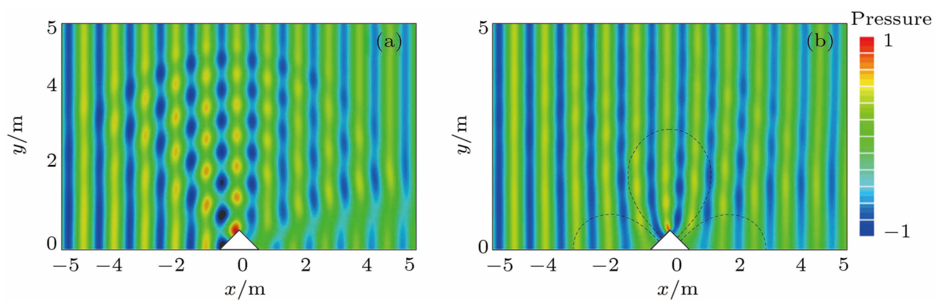

Figure 1.27: *The simulated acoustic fields plotted by Ren et al. (2011). (a) without the cloak; (b) with the cloak*

cloak can be carried out. Favorable performance of the cloak was demonstrated through simulations. Figure 1.27 shows the simulated acoustic fields by Ren et al. (2011). A strong scattering from the object can be observed from Figure 1.27 (a) when the object was not covered by the cloak. Figure 1.27 (b) shows that the scattering was significantly reduced by using the designed petal-shaped acoustic carpet cloak. These designs avoid the material singularity, but do rely on the availability of a "ground".

A three-dimensional omnidirectional acoustic ground cloak was designed and experimentally realized by Zigoneanu et al. (2014). Figure 1.28 (a) shows a snapshot of the fabricated cloak and the unit cell. One quater of the cloak is not shown, so that the cross-section of the cloak could be displayed. Figure 1.28 (b) shows a photograph of the cloaked object.

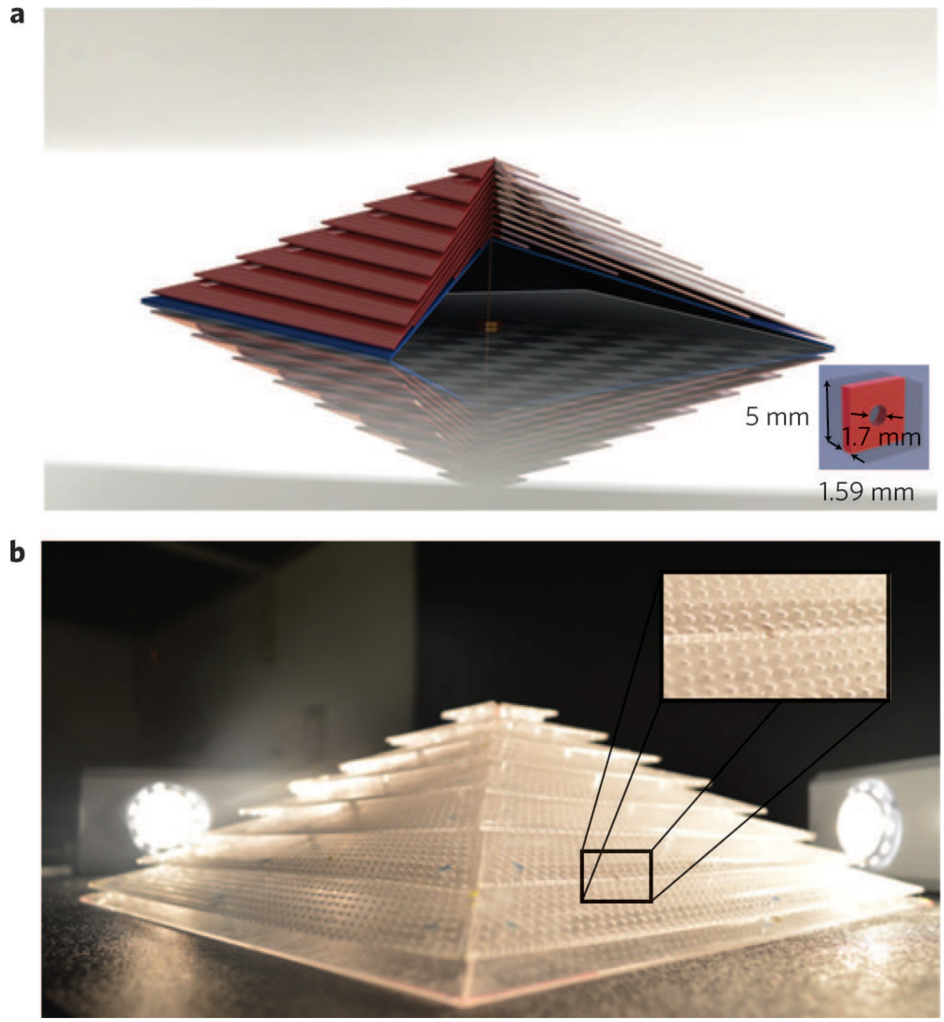

Figure 1.28: *Snapshots of the fabricated cloak and cloaked object by Zigoneanu et al. (2014). (a), The fabricated cloak and the unit cell. (b), Photograph of the cloaked object, placed on the ground.*

Figure 1.29 shows the experimental set-up (a) and the measured and mirrored results (b). The cloak shows a good performance under the incident sound, a short Gaussian pulse of 600 μs half-amplitude duration modulated with a 3 kHz sinusoidal.

1.1.4 Cloaks with Solid Pentamode Materials

Materials with anisotropic mass densities do not physically exist in the natural world. Approximations of these materials are challenging and cause imperfect cloaking perfor-

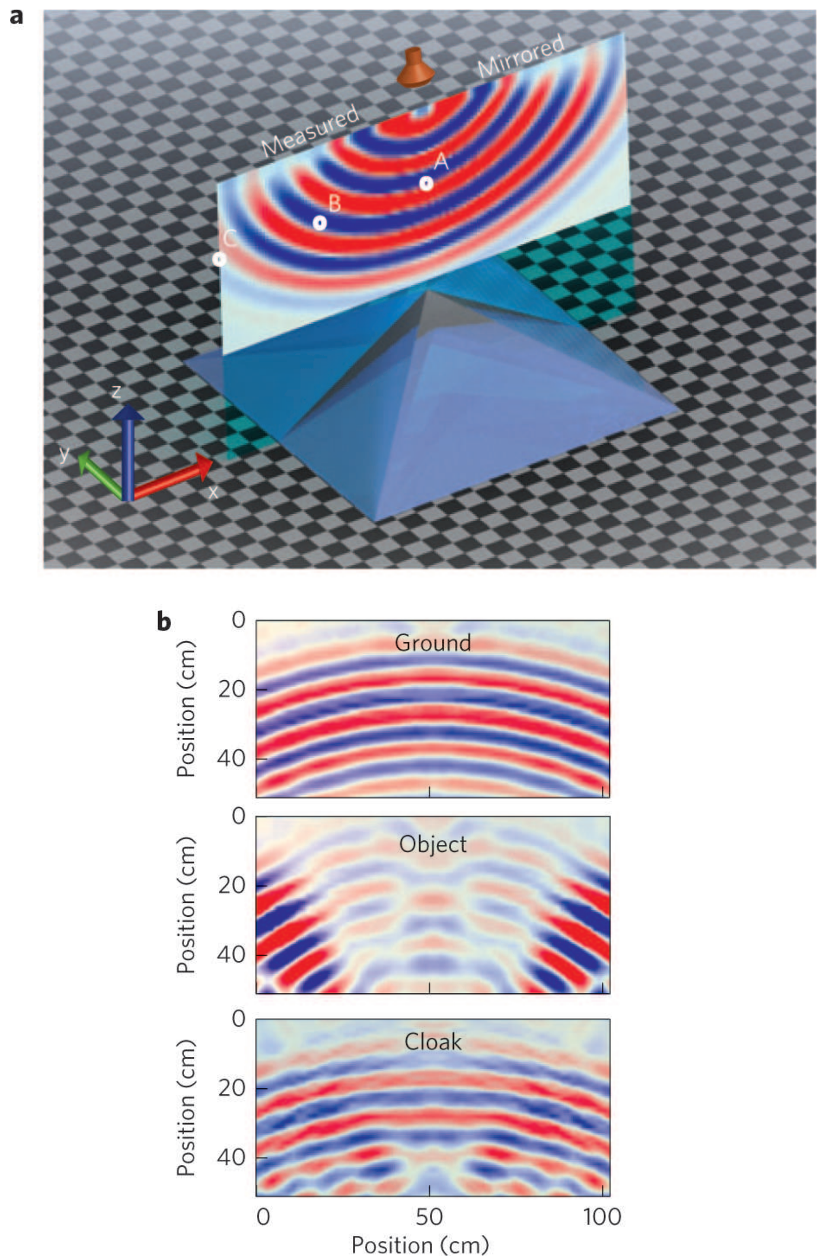

Figure 1.29: *(a) The experimental set-up of carpet cloak by Zigoneanu et al. (2014). (b) The measured and mirrored pressure fields for three cases. From top to bottom: with nothing on the ground; with the object on the ground; with the object covered by the cloak on the ground.*

mance. Additionally, cloaks designed with materials which have anisotropic mass densities may only be effective at a limited frequency range, due to their discrete nature (Scandrett et al., 2011). More recent, Norris (2008a,b, 2009) showed that the transformation optics used by Pendry et al. (2006) and Cummer and Schurig (2007) is in fact a special case of a general class of transformations for acoustic cloaking design. Norris (2008a)'s study shows that in both two and three dimensions, the effective cloaking which has finite mass can be realized by appropriately choosing material properties of the cloaking shell. Norris (2008b) formulated the acoustic cloaking which can be achieved using either anisotropic densities and isotropic bulk moduli or isotropic densities and anisotropic bulk moduli. The general class of the elastic anisotropic materials is called pentamode materials. Norris (2009) also presented the possibility for designing broadband cloaking using pentamode materials.

Pentamode metamaterials are artificial structures that have anisotropic elastic properties. Pentamode metamaterials have finite bulk modulus but vanishing shear modulus, which is one of the important properties for acoustic cloaking design. The effect of shear modulus for the Cummer-Schurig acoustic cloak design is investigated by Smith and Verrier (2011). It is shown that the shear modulus limits the effectiveness of acoustic cloaks to a small frequency range. The frequency range can be widened while reducing the shear modulus. Shear modulus can also cause the coupling of compression and shear waves which can cause imperfect cloaking. The pentamode materials are first structured theoretically from specific microstructures by Milton and Cherkaev (1995).

In building pentamode materials, the bulk modulus B should be much larger than the shear modulus G (Milton and Cherkaev, 1995; Kadic et al., 2012). Pentamode materials are first experimentally realized by Kadic et al. (2012). In this study, the bulk modulus is 1000 times larger than the shear modulus. Figure 1.30 (a) illustrates the pentamode metamaterial structure suggested by Milton and Cherkaev (1995). As shown in Figure 1.30 (a), deal pentamode materials require truncated cones to meet at their strictly point-like tips. In order to obtain realizable and stable pentamode materials, the point-like tip at the

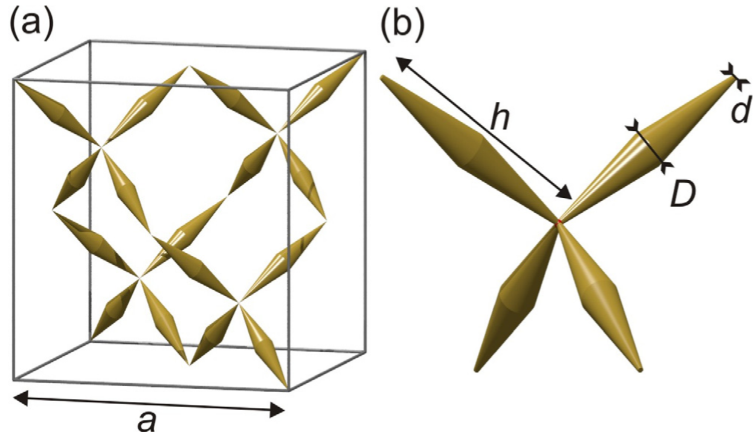

Figure 1.30: *Kadic* et al*'s illustration which shows the structures of the pentamode metamaterial designed by (a) Milton and Cherkaev and (b) Kadic et al. (2012).*

connection is changed to a connection region having a finite diameter d (shown in Figure 1.30 (b)). Figure 1.31 shows the structures of the pentamode which can be experimentally achieved.

Scandrett et al. (2010) proposed an acoustic cloaking design using layered pentamode materials. In their study, three cloaks that are designed with different materials are analyzed and compared with the continuous cloak. They are cloaks comprised of anisotropic density and isotropic bulk modulus materials which is so-called inertial cloak (IC), isotropic density and anisotropic bulk modulus materials which are pentamode materials (PM), and anisotropic density and anisotropic bulk modulus materials, which is the combination of IC and PM cloaks (PMIC). The continuously cloak was designed based on the coordinate transformation with continuous varying anisotropic materials. An optimization approach is adopted to improve the performance of the cloaks at a certain frequency, for example, $ka = 4.34$. The scattering coefficient which is also called the total scattering cross section, σ_c, is defined as objective function, and the material properties are defined as optimization parameters. Scattering coefficient presents the ratio of the total scattered energy to the total energy due to the impinging of the waves on an object. In this study, the covered object is a rigid sphere. Figure 1.32 shows the scattering coefficients for the optimized discrete three-layer cloaks. The optimization was run at frequency $ka = 4.34$. The scattering coeffi-

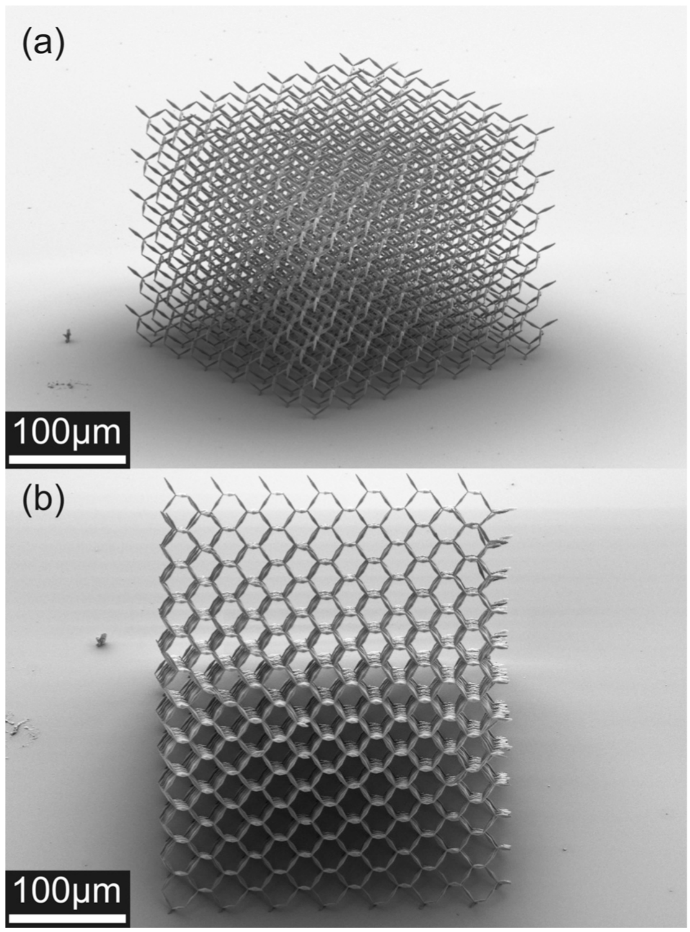

Figure 1.31: *Kadic* et al*'s experimentally achievevable pentamode material structures (Kadic et al., 2012).*

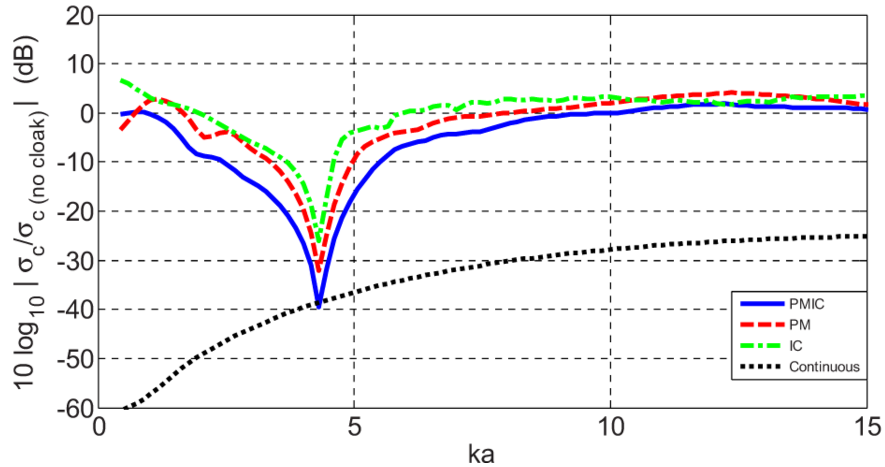

Figure 1.32: *The scattering coefficients from a rigid object which covered with continuous and three-layer cloaks obtained by Scandrett et al. (2010). Blue solid line: PMIC cloak. Red dashed line: PM cloak. Green dot dashed line: IC cloak. Black dotted line: continuous cloak.*

cient for a continuous cloak is also provided for reference. Figure 1.32 shows that the three discrete cloaks all have good preformance at the optimized frequency. The three-layer PMIC cloak has almost the same performance as the continuous cloak, while the performance of IC and PM cloaks are also close to that of the continuous cloak.

In their later study, Scandrett et al. (2011) focused on designing cloaks comprised of pentamode materials which have anisotropic bulk moduli and isotropic densities. The reason is that materials with anisotropic densities do not physically exist in the natural world and are much more challenging for engineering realization. Figure 1.33 shows the scattering coefficients for the layered cloaks over a wide frequency range, from $ka = 1$ to 10. Figure 1.33 shows that the cloaks with more layers have better performance.

Chen et al. (2015) designed an acoustic cloak with a latticed pentamode material, shown in Figure 1.34. Figure 1.34 (a) shows the continuous material properties of the cloaking shell (solid lines) and their layered approximation (dashed lines). Figure 1.34 (b) shows a schematic of the recursive implantation of lattices into cylindrical layers. The layout of the cloak is shown in Figure 1.34 (c). The performance of the cloak which shields a rigid object under plane acoustic wave was numerically verified. Figure 1.35 shows the simulated

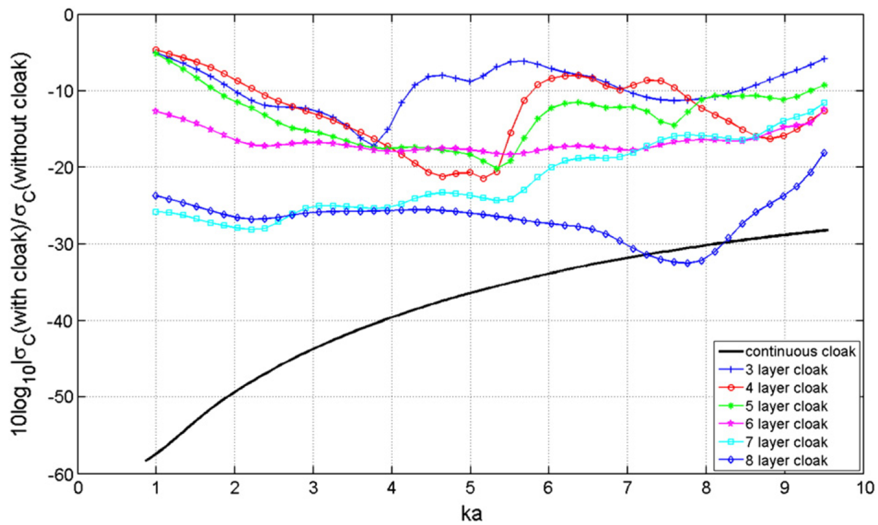

Figure 1.33: *The scattering coefficients from a rigid object which covered with continuous and layered cloaks obtained by Scandrett et al. (2010).*

scattering pressure fields at two frequencies: $ka = 1.57$ (top panel) and $ka = 2.51$ (bottom panel). At both frequencies, compared with the uncloaked cases (left panel), a significant reduction of scattering can be found from the cloaked cases (right panel).

1.1.5 Our Previous Work: Acoustic Cloaks with Mixture of Conventional Isotropic Fluid and Isotropic Solid Layers

Cai (2012) introduced optimization to acoustic cloaking design, and concluded that a perfect cloaking without material singularity can be achieved by fine-tuning material properties using various optimization schemes. The initial design to be optimized in his study is based on the Cummer-Schurig prescription. The optimization is run at a frequency selected *a priori*. Perfect cloaking with all fluid layers can be achieved through the optimization at a given frequency. However, it is also observed that, sometimes, the cloaking effect may deteriorate at other frequencies.

Bao and Cai (2012) attempt to minimize such deterioration by using multi-objective optimization methods such that the cloaking performance will be maintained over a wide

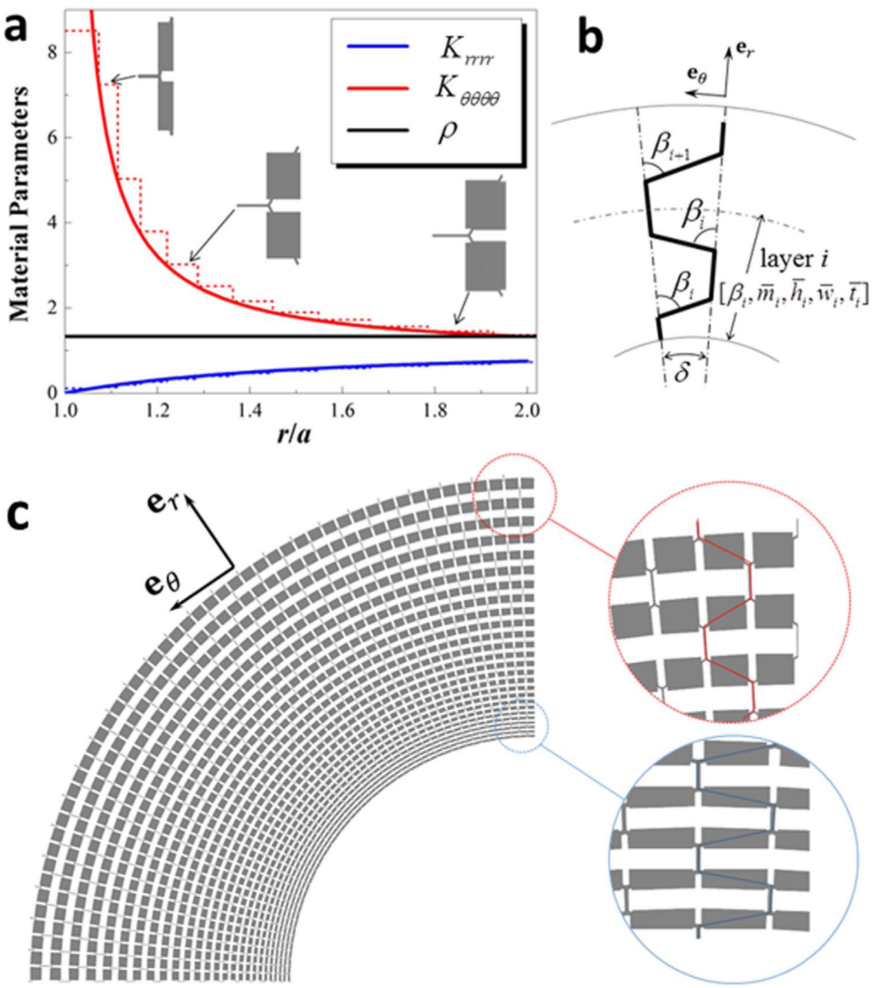

Figure 1.34: *Latticed pentamode acoustic design by Chen et al. (2015). (a) Profiles of continuously varying material properties of the cloak (solid lines), and their layered approximation by the pentamode lattice (dashed lines). (b) The schematic illustration of the recursive implantation of lattice cells into cyindrical layers. (c) The layout of the latticed cloak.*

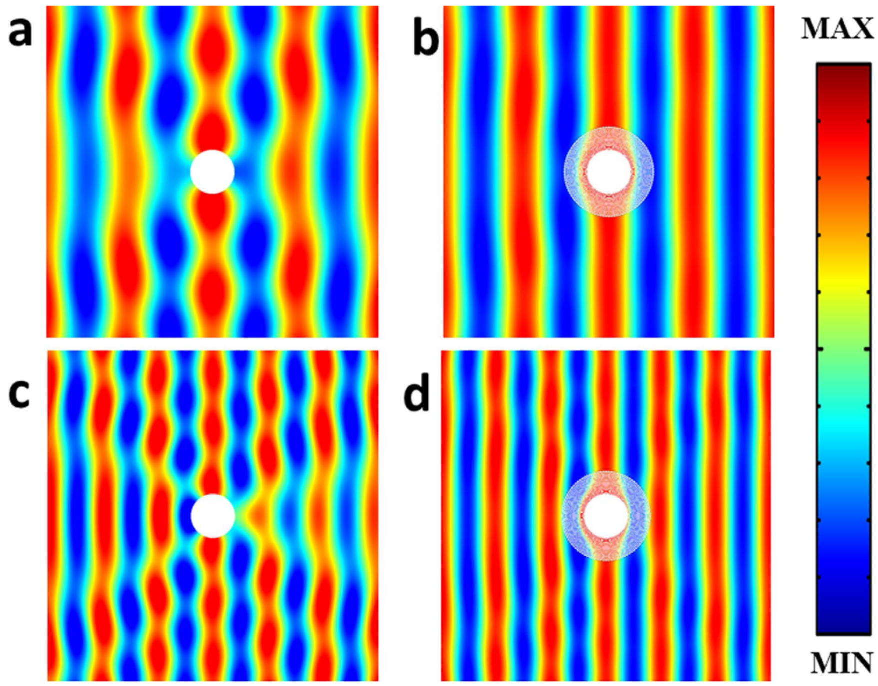

Figure 1.35: *Simulated acoustic pressure fields by Chen et al. (2015). (a) Uncloaked case at $ka = 1.57$. (b) Cloaked case at $ka = 1.57$. (c) Uncloaked case at $ka = 2.51$. (d) Cloaked case at $ka = 2.51$.*

range of frequencies. In their study, two examples are presented. The first cloak comprises all conventional acoustic layers, and the second comprises a mixture of conventional acoustic and elastic layers.

The initial design is based on Cummer-Schurig prescription, discretized into 5 anisotropic layers. Each anisotropic layer is then replaced by a pair of isotropic layers, denoted as layers A and B. The isotropic-anisotropic equivalence relations (Cheng et al., 2008; Torrent and Sánchez-Dehesa, 2008) are given in equations 1.8 through 1.10. In this study, $\eta = 1$ because all ten isotropic layers have equal thickness. The following relation is used in their study, $K_A/K_B = \rho_A/\rho_B$, when combined with Eqn. (1.10) this gives (Cai, 2012)

$$K_A = \frac{1}{2}K\left(\frac{\rho_A + \rho_B}{\rho_B}\right) \tag{1.14}$$

$$K_B = \frac{1}{2}K\left(\frac{\rho_A + \rho_B}{\rho_A}\right) \tag{1.15}$$

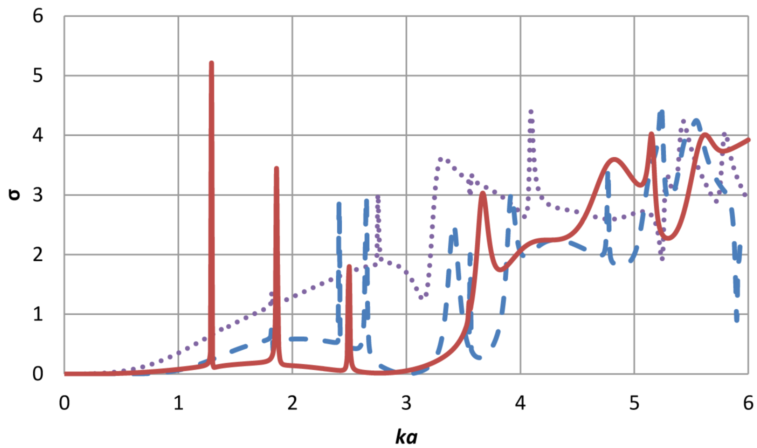

Figure 1.36: *Normalized total scattering cross section of the cloak with 10 isotropic fluid-solid mixture of layers designed by Bao and Cai (2012). Dot dashed curve: initial design. Dashed curve: optimized design at $ka = 3$. Solid curve: optimized design at $k_i a = 1, 2, 3$.*

The odd-numbered isotropic layer A uses the lighter density and the even-numbered isotropic layer B uses the heavier density. To obtain the initial design with fluid-solid mixture of layers, the odd-numbered layers remain the same while the even-numbered layers are converted to elastic layers. The material properties of the elastic layers are based on the original acoustical properties, with the addition of an assumed Poissons ratio of 0.33. The optimization is ran at three discrete frequencies, $k_i a = 1, 2$, and 3, where $i = 1, 2, 3$. The mass density ρ of all layers, Lamé constants λ and μ of the elastic layers, and the sound speed c of the acoustic layers are defined as the optimization variables.

Figure 1.36 shows the normalized total scattering cross section of three designs over the frequency range from $ka = 0$ to 6: the initial design based on Cummer-Schurig prescription (dot dashed curve); the single-objective optimized design at $ka = 3$ (dashed curve); and the multi-objective optimized design at $k_i a = 1, 2, 3$ (solid curve). The dashed curve shows that the value of the normalized total scattering cross section at $ka = 3$ is very small, as this is the frequency at which the optimization is run. But the normalized total scattering cross section over the frequency range between $ka = 1$ and 3 is much higher. The solid line shows that the normalized total scattering cross section is much flatter from $ka = 0$ to

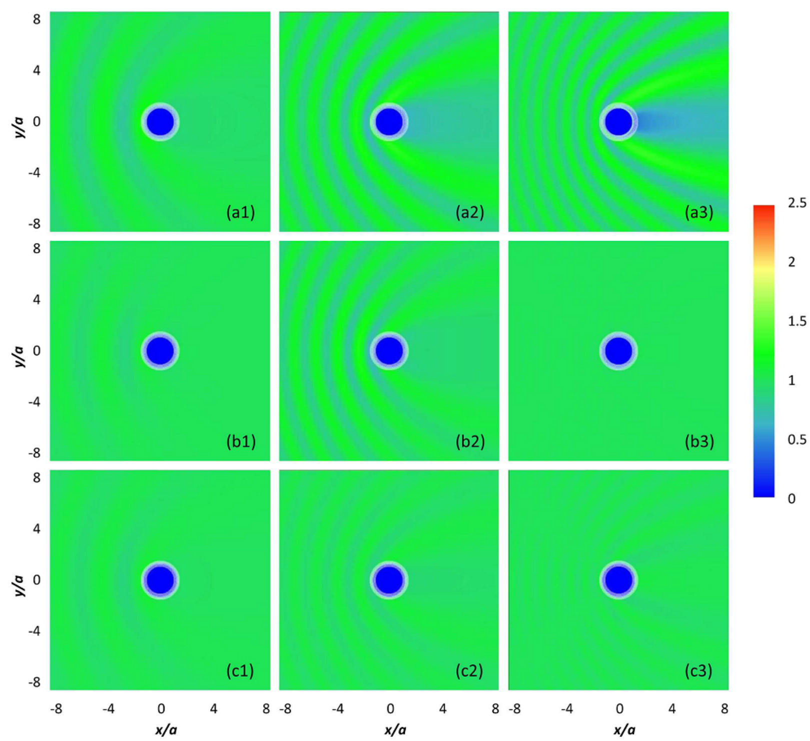

Figure 1.37: *Total acoustic pressure distribution due to impinging of a planar incident wave onto a rigid cylinder cloaked by the design of Bao and Cai (2012).*

3. Figure 1.37 shows the amplitude of the acoustic pressure when a planar wave impinges onto the initial design ((a1)-(a3)), the single-objective optimized cloak ((b1)-(b3)), and the multi-objective optimized cloak ((c1)-(c3)) at $k_i a = 1, 2, 3$.

From Bao and Cai (2012)'s study, we find that the cloaks have strong frequency dependency because the equivalence relation between a single anisotropic layer and a pair of isotropic layers is valid only at low frequency range. Through multi-objective optimization, the performance of the cloak could be maintained at a wider frequency range. The limitation of this study is that the frequency dependency cannot be avoided, even though the multi-objective method was applied. The performance of the cloaks could be maintained at a lower frequency range. If the wider and higher frequency range is chosen to be optimized, then it is harder to get good results. In addition, the optimization process takes a huge amount of computation. The advantage of this study is that it proved the conventional isotropic elastic materials could be used for a perfect acoustic cloaking design.

1.2 Motivation for the Thesis

Through the introduction of the cloaks in Section 1.1, it is apparent that there are limitations for practical realization of cloaking materials. Fluid materials with anisotropic mass densities are not real world materials. The approximation of anisotropic mass densities reduces the effectiveness of the cloaks. In addition, it is difficult to mix two fluids while requiring each to maintain a shape of a thin shell for the layered acoustic cloaking designs (Cai and Sanchez-Dehesa, 2007; Cheng et al., 2008; Chen et al., 2008; Torrent and Sánchez-Dehesa, 2008; Cai, 2012). There are also challenges for physically realizing pentamode elastic materials. Perfect pentamode materials are not stable, because the vanishing shear modulus implies that they are hard to compress yet easy to deform. The deformation would change the structure of the material, which would lead to destruction of the material. So the ideal pentamode materials only exist conceptually. They can only be realized approximately. Kadic et al. (2012) approximately realized the pentamode material which was suggested by Milton and Cherkaev (1995) with a three-dimensional microstructure. Their pentamode material is built to have a finite shear modulus for stability. The ratio of bulk modulus to shear modulus is made to be 1000. Smith and Verrier (2011) investigated the effect of shear modulus for cloaking design. Their study showed that the non-vanishing shear modulus will couple the compression and shear waves which could cause imperfect acoustic cloaking. Thus, the approximately realized pentamode materials which have non-vanishing shear modulus would inevitably lower the effectiveness of the cloaks.

This current work is to investigate conventional orthotropic materials for acoustic scattering problems, which will be helpful for the study of practical realization of acoustic cloaking. According to Norris (2008b)'s study, materials required for cloaking design need to have either anisotropic mass densities and isotropic bulk moduli or isotropic mass densities and anisotropic bulk moduli. The conventional elastic orthotropic materials investigated in this study have isotropic mass density and anisotropic bulk modulus which satisfy the requirement for cloaking design. In addition, compared with the materials that have been used for acoustic cloaking design, the conventional elastic orthotropic materials have some advantages for practical realization. First, compared with fluid cloaking materials with anisotropic mass densities, the conventional elastic orthotropic materials which have isotropic mass densities are easier to construct. In addition, by using conventional elastic orthotropic materials, the difficulty of holding layered fluid materials together is solved. Second, conventional elastic orthotropic materials have non-vanishing shear moduli, which overcomes the limitation of pentamode materials. Even though pentamode materials also have isotropic mass densities and anisotropic bulk moduli, it is difficult to practically realize pentamode materials because of their vanishing shear moduli properties.

1.3 Research Objectives and Methods

In the author's previous study (Bao and Cai, 2012), acoustic cloaks with a mixture of conventional isotropic fluid and isotropic elastic layers are numerically designed through optimization approaches. It is shown that the perfect acoustic cloaking can be successfully designed by using a mixture of fluid and solid layers. The objective of this research is to study acoustic scattering by cylindrical scatterers with a mixture of conventional isotropic fluid and elastic orthotropic layers. A computational system will also be built to verify and conduct the numerical simulations of the scattering problem solutions.

There are two main tasks in this research. The first task is to obtain the general solution for waves in cylindrical, linear elastic orthotropic media. Frobenius method is applied to accomplish this task. Frobenius method is a powerful technique for finding solutions of second-order ordinary differential equations in the form of power series. It gives exact analytical solution. The second task is to solve the problem of acoustic scattering by multi-layer cylindrical scatterer which comprises both isotropic fluid and linearly ealstic orthotropic materials. To accomplish this task, a set of two canonical problems is first defined. Each canonical problem involves two isotropic acoustic media and one linearly elastic orthotropic medium which are separated by two interfaces. The linearly elastic orthotropic medium is in the middle. Canonical problems describe the interactions of the waves at the interfaces for scattering in the multilayered scatterer. Scattering by three multilayered scatterers is analyzed based on the canonical problems. The three scatterers comprise: acoustic-orthotropic-acoustic layers, orthotropic-acoustic-orthotropic-acoustic layers, and orthotropic-acoustic-acoustic layers, respectively. Then the solution for a multilayer scatterer with an arbitrary number of layers, each layer being either linearly elastic orthotropic or isotropic acoustic, is obtained by recursively using the solution for the three basic multilayer scatterers.

1.4 Organization of Thesis

The organization of the thesis is as follows:

Chapter 1 gives an introduction to the background and objectives of this research. The approaches to achieve the objectives are also briefly introduced.

In Chapter 2, Frobenius method is used for solving elastic waves in cylindrically linearly elastic orthotropic media.

Chapter 3 explores the procedure to solve acoustic scattering by cylindrical scatterers which have both conventional isotropic acoustic and elastic orthotropic layers.

Chapter 4 provides the verification of the solutions through two approaches.

In Chapter 5, acoustic scattering by various scatterers are studied through numerical simulations. A computational system is built for conducting simulations of scattering by the multilayer scatterers which were solved in the earlier chapters.

The conclusions of this thesis are presented in Chapter 6.

Chapter 2

Waves in Cylindrically Orthotropic Elastic Media

2.1 Introduction

The general solutions for elastic wave propagation in a cylindrically orthotropic elastic media are explored in this chapter. Using the Frobenius method, exact analytical solutions of elastic waves in cylindrical elastic orthotropic media are obtained. Possibilities when orthotropic media have special properties are also considered to ensure the completeness of the solutions. Only the two dimensional problem known as the plane-strain problem is considered.

2.2 Equations of Motion for Orthotropic Medium

In this section, the equations of motion for cylindrically orthotropic elastic medium in terms of displacements for two dimensional problems are obtained.

For a plane-strain problems, the strain along the azimuthal direction is zero. This means that $\varepsilon_{zz} = \varepsilon_{rz} = \varepsilon_{\theta z} = 0$. As a result, $\sigma_{rz} = \sigma_{\theta} z = 0$. The stress-strain relations of orthotropic materials in stiffness form are

$$\begin{bmatrix} \sigma_{rr} \\ \sigma_{\theta\theta} \\ \sigma_{r\theta} \end{bmatrix} = \begin{bmatrix} C_{11} & C_{12} & 0 \\ C_{12} & C_{22} & 0 \\ 0 & 0 & C_{44} \end{bmatrix} \begin{bmatrix} \varepsilon_{rr} \\ \varepsilon_{\theta\theta} \\ 2\varepsilon_{r\theta} \end{bmatrix} \tag{2.1}$$

where C_{ij} are four independent elastic constants, r is the radius, θ is the angle, σ_{rr} and $\sigma_{\theta\theta}$ are the normal stresses along the radial (r) and tangential (θ) directions, respectively; ε_{rr}, and $\varepsilon_{\theta\theta}$ are the normal strains along the radial (r) and tangential (θ) directions, respectively; $\sigma_{r\theta}$ and $\varepsilon_{r\theta}$ are the shear stress and shear strain in direction θ on the plane whose normal is in direction r, respectively. For a plane-strain problem, the equations of motion in terms of stresses are

$$\frac{\partial \sigma_{rr}}{\partial r} + \frac{1}{r}\frac{\partial \sigma_{r\theta}}{\partial \theta} + \frac{1}{r}(\sigma_{rr} - \sigma_{\theta\theta}) = \rho \ddot{u}_r \tag{2.2}$$

$$\frac{\partial \sigma_{r\theta}}{\partial r} + \frac{1}{r}\frac{\sigma_{\theta\theta}}{\partial \theta} + \frac{2}{r}\sigma_{r\theta} = \rho \ddot{u}_\theta \tag{2.3}$$

where $u_r = u_r(r, \theta)$ and $u_\theta = u_\theta(r, \theta)$ are the displacements along r and θ directions, respectively; $\ddot{u}_r$ and $\ddot{u}_\theta$ are the accelerations along r and θ directions, respectively; $(\ddot{\bullet})$ represents the second derivative with respect to time. Recalling the strain-displacement relations

$$\varepsilon_{rr} = \frac{\partial u_r}{\partial r} \tag{2.4}$$

$$\varepsilon_{\theta\theta} = \frac{1}{r}\left(u_r + \frac{\partial u_\theta}{\partial \theta}\right) \tag{2.5}$$

$$\varepsilon_{r\theta} = \frac{1}{2}\left(\frac{1}{r}\frac{\partial u_r}{\partial \theta} + \frac{\partial u_\theta}{\partial r} - \frac{u_\theta}{r}\right) \tag{2.6}$$

stresses in terms of displacements are, by substituting Eqns. (2.4) through (2.6) into Eqn.

(2.1),

$$\begin{aligned}
\sigma_{rr} &= C_{11}\varepsilon_{rr} + C_{12}\varepsilon_{\theta\theta} \\
&= C_{11}\frac{\partial u_r}{\partial r} + C_{12}\left(\frac{u_r}{r} + \frac{1}{r}\frac{\partial u_\theta}{\partial \theta}\right) \qquad (2.7) \\
\sigma_{\theta\theta} &= C_{12}\varepsilon_{rr} + C_{22}\varepsilon_{\theta\theta} \\
&= C_{12}\frac{\partial u_r}{\partial r} + C_{22}\left(\frac{u_r}{r} + \frac{1}{r}\frac{\partial u_\theta}{\partial \theta}\right) \qquad (2.8) \\
\sigma_{r\theta} &= C_{44}(2\varepsilon_{r\theta}) \\
&= C_{44}\left(\frac{1}{r}\frac{\partial u_r}{\partial \theta} + \frac{\partial u_\theta}{\partial r} - \frac{u_\theta}{r}\right) \qquad (2.9)
\end{aligned}$$

By substituting the Eqns. (2.7) through (2.9) into Eqns. (2.2) and (2.3), the equations of motion in terms of displacements for the orthotropic medium are obtained,

$$\begin{aligned}
C_{11}\frac{\partial^2 u_r}{\partial r^2} + C_{11}\frac{1}{r}\frac{\partial u_r}{r} + C_{44}\frac{1}{r^2}\frac{\partial^2 u_r}{\partial \theta^2} - C_{22}\frac{u_r}{r^2} & \\
+(C_{12}+C_{44})\frac{1}{r}\frac{\partial^2 u_\theta}{\partial r \partial \theta} - (C_{22}+C_{44})\frac{1}{r^2}\frac{\partial u_\theta}{\partial \theta} &= \rho \ddot{u}_r \qquad (2.10) \\
(C_{12}+C_{44})\frac{1}{r}\frac{\partial^2 u_r}{\partial r \partial \theta} + (C_{22}+C_{44})\frac{1}{r^2}\frac{\partial u_r}{\partial \theta} & \\
+C_{22}\frac{1}{r^2}\frac{\partial^2 u_\theta}{\partial \theta^2} + C_{44}\left(\frac{\partial^2 u_\theta}{\partial r^2} + \frac{1}{r}\frac{\partial u_\theta}{\partial r} - \frac{u_\theta}{r^2}\right) &= \rho \ddot{u}_\theta \qquad (2.11)
\end{aligned}$$

2.3 General Solutions for the Equations of Motion Using Frobenius Method

In this section, Frobenius method is used to solve the equations of motion in terms of displacements (Eqns. (2.10) and (2.11)) for the orthotropic media.

The displacements u_r and u_θ in Eqns. (2.10) and (2.11) are assumed to be expressible in the variable-separated form (Misky, 1965; Markus and Mead, 1995; Martin and Berger, 2001; Shuvalov, 2002)

$$u_r = \sum_{n=-\infty}^{\infty} U_n(r) e^{in\theta} e^{i\omega t} \tag{2.12}$$

$$u_\theta = \sum_{n=-\infty}^{\infty} V_n(r) e^{in\theta} e^{i\omega t} \tag{2.13}$$

where $i = \sqrt{-1}$ is the unit of imaginary numbers, ω is the angular frequency, n runs from $-\infty$ to ∞. Substituting Eqns. (2.12) and (2.13) into Eqns. (2.10) and (2.11), gives

$$\sum_{n=-\infty}^{\infty} \left[C_{11} U_n'' + C_{11} \frac{1}{r} U_n' + \left(\rho\omega^2 - \frac{n^2 C_{44} + C_{22}}{r^2} \right) U_n + in(C_{12} + C_{44}) \frac{1}{r} V_n' - in(C_{22} + C_{44}) \frac{1}{r^2} V_n \right] e^{in\theta} e^{i\omega t} = 0 \tag{2.14}$$

$$\sum_{n=-\infty}^{\infty} \left[in(C_{12} + C_{44}) \frac{1}{r} U_n' + in(C_{22} + C_{44}) \frac{1}{r^2} U_n + C_{44} V_n'' + C_{44} \frac{1}{r} V_n' + \left(\rho\omega^2 - \frac{n^2 C_{22} + C_{44}}{r^2} \right) V_n \right] e^{in\theta} e^{i\omega t} = 0 \tag{2.15}$$

Since $e^{in\theta}$ are orthogonal functions, each bracketed term within the summations of Eqns (2.14) and (2.15) has to be equal to zero, which gives

$$C_{11} U_n'' + C_{11} \frac{1}{r} U_n' + \left(\rho\omega^2 - \frac{n^2 C_{44} + C_{22}}{r^2} \right) U_n + in(C_{12} + C_{44}) \frac{1}{r} V_n' - in(C_{22} + C_{44}) \frac{1}{r^2} V_n = 0 \tag{2.16}$$

$$in(C_{12} + C_{44}) \frac{1}{r} U_n' + in(C_{22} + C_{44}) \frac{1}{r^2} U_n + C_{44} V_n'' + C_{44} \frac{1}{r} V_n' + \left(\rho\omega^2 - \frac{n^2 C_{22} + C_{44}}{r^2} \right) V_n = 0 \tag{2.17}$$

Following Martin and Berger (Martin and Berger, 2001), for simplicity in notation, the following dimensionless stiffness ratios are introduced as

$$c_{11} = \frac{C_{11}}{C_{44}}, \quad c_{12} = \frac{C_{12}}{C_{44}}, \quad c_{22} = \frac{C_{22}}{C_{44}} \tag{2.18}$$

Then, the set of ordinary differential equations in Eqns. (2.16) and (2.17) for $U_n(r)$ and $V_n(r)$ becomes

$$c_{11}\left(r^2U_n'' + rU_n'\right) + \left(k^2r^2 - n^2 - c_{22}\right)U_n + in(c_{12}+1)rV_n' - in(c_{22}+1)V_n = 0 \tag{2.19}$$

$$r^2V_n'' + rV_n' + in(c_{12}+1)rU_n' + (k^2r^2 - n^2c_{22} - 1)V_n + in(c_{22}+1)U_n = 0 \tag{2.20}$$

where k is the wave number and $k^2 = \rho\omega^2/C_{44}$.

2.3.1 Frobenius Series

Assuming that $U_n(r)$ and $V_n(r)$ have solutions in the following Frobenius series form,

$$U_n(r) = \sum_{m=0}^{\infty} a_{mn}r^{m+\alpha_n}, \qquad V_n(r) = \sum_{m=0}^{\infty} b_{mn}r^{m+\alpha_n} \tag{2.21}$$

where index α_n and the coefficients a_{nm}, b_{nm} are as yet undetermined. Substituting expressions Eqn. (2.21) into Eqns. (2.19) and (2.20) gives

$$\begin{aligned}\sum_{m=0}^{\infty}\left\{c_{11}\left[(m+\alpha)(m+\alpha-1)+(m+\alpha)\right]+(k^2r^2-n^2-c_{22})\right\}a_{mn}r^{m+\alpha_n}& \\ +\sum_{m=0}^{\infty}\left\{in(c_{12}+1)(m+\alpha)-in(c_{22}+1)\right\}b_{mn}r^{m+\alpha_n} &= 0 \quad (2.22)\\ \sum_{m=0}^{\infty}\left\{in(c_{12}+1)(m+\alpha)+in(c_{22}+1)\right\}a_{mn}r^{m+\alpha_n}& \\ +\sum_{m=0}^{\infty}\left\{(m+\alpha)(m+\alpha-1)+(m+\alpha)+(k^2r^2-n^2c_{22}-1)\right\}b_{mn}r^{m+\alpha_n} &= 0 \quad (2.23)\end{aligned}$$

2.3.2 The Index and the Indicial Equations

Eqns. (2.22) and (2.23) need to be satisfied for all powers of r. Dividing the common factor r^{α_n}, for the 0-th power, they become the following set of indicial equations

$$a_{0n}[c_{11}\alpha_n^2 - (n^2 + c_{22})] + b_{0n}(in)[(c_{12}+1)\alpha_n - (c_{22}+1)] = 0 \tag{2.24}$$

$$a_{0n}(in)[(c_{12}+1)\alpha_n + (c_{22}+1)] + b_{0n}[\alpha_n^2 - (n^2 c_{22}+1)] = 0 \tag{2.25}$$

which can be written in the matrix form as

$$\begin{bmatrix} c_{11}\alpha_n^2 - (n^2 + c_{22}) & (in)[(c_{12}+1)\alpha_n - (c_{22}+1)] \\ (in)[(c_{12}+1)\alpha_n + (c_{22}+1)] & \alpha_n^2 - (n^2 c_{22}+1) \end{bmatrix} \begin{bmatrix} a_{0n} \\ b_{0n} \end{bmatrix} = \begin{bmatrix} 0 \\ 0 \end{bmatrix} \tag{2.26}$$

To have non-vanishing a_{n0} and b_{n0}, the determinant of the system matrix should vanish, that is

$$\begin{aligned} D &= [c_{11}\alpha_n^2 - (n^2 + c_{22})][\alpha_n^2 - (n^2 c_{22}+1)] \\ &- (in)[(c_{12}+1)\alpha_n - (c_{22}+1)](in)[(c_{12}+1)\alpha_n + (c_{22}+1)] = 0 \end{aligned} \tag{2.27}$$

For simplicity, Eqn. (2.27) is written as (Markus and Mead, 1995)

$$D = A_0\alpha_n^4 - A_1\alpha_n^2 + A_2 = 0 \tag{2.28}$$

with

$$A_0 = c_{11}, \quad A_1 = c_{11} + c_{22} + n^2(c_{11}c_{22} - c_{12}^2 - 2c_{12}), \quad A_2 = c_{22}(n^2-1)^2 \tag{2.29}$$

So the solutions for Eqn. (2.28) are

$$\alpha_n^2 = \frac{A_1 \pm \sqrt{A_1^2 - 4A_0A_2}}{2A_0} \tag{2.30}$$

The sign of the discriminant $\mathscr{D}$ determines whether the solution will be real or complex, which can be expressed as

$$\begin{aligned}\mathscr{D} =& A_1^2 - 4A_0A_2 \\ =& (c_{11} - c_{12})^2 + n^4\Delta[\Delta - 4(1 + c_{12})] \\ &+ 2n^2[\Delta(c_{11} + c_{22}) + 4\Delta + 2c_{12}(2c_{12} - c_{11} - c_{22})]\end{aligned}$$

where

$$\Delta = c_{11}c_{22} - c_{12}^2 \tag{2.31}$$

Martin and Berger (2001) concluded that $\mathscr{D}$ will be positive when the following relation is satisfied

$$\Delta \geq 4(1 + c_{12}) \tag{2.32}$$

So α can have real solutions if the stiffness constants can satisfy the following relation

$$c_{11}c_{22} - c_{12}^2 \geq 4(1 + c_{12}) \tag{2.33}$$

When $\mathscr{D} \geq 0$, Eqn. (2.30) gives four real solutions of α, which can be written as

$$\alpha_n^{(1,2)} = \pm\sqrt{\frac{A_1 + \sqrt{\mathscr{D}}}{2A_0}}, \quad \alpha_n^{(3,4)} = \pm\sqrt{\frac{A_1 - \sqrt{\mathscr{D}}}{2A_0}} \tag{2.34}$$

There are two special cases that will need to be considered when using Frobenius method: 1) when α_n has repeated roots and 2) when α_n has two roots differ by an integer. Details of these two special cases are discussed in Sections 2.4, 2.5, and 2.6.

2.3.3 The Recurrence Relations

Eqns. (2.22) and (2.23) can also be written as

$$\sum_{m=0}^{\infty}\left\{c_{11}\left[(m+\alpha_n)(m+\alpha_n-1)+(m+\alpha_n)\right]-(n^2+c_{22})\right\}a_{mn}r^{m+\alpha_n}$$
$$+\sum_{m=2}^{\infty}k^2a_{(m-2)n}r^{m+\alpha_n}+\sum_{m=0}^{\infty}\{in(c_{12}+1)(m+\alpha_n)-in(c_{22}+1)\}\,b_{mn}r^{m+\alpha_n}=0 \quad (2.35)$$

$$\sum_{m=0}^{\infty}\{in(c_{12}+1)(m+\alpha_n)+in(c_{22}+1)\}\,a_{mn}r^{m+\alpha_n}+\sum_{m=2}^{\infty}k^2b_{(m-2)n}r^{m+\alpha_n}$$
$$+\sum_{m=0}^{\infty}\left\{(m+\alpha_n)(m+\alpha_n-1)+(m+\alpha_n)-(n^2c_{22}+1)\right\}b_{mn}r^{m+\alpha_n}=0 \quad (2.36)$$

Eqns. (2.35) and (2.36) need to be satisfied for all powers of r. Dividing the common factor r^{α_n}, for the 0-th power, they become the set of indicial equations Eqns. (3.28) and (2.25). For the 1-st power, they become

$$a_{1n}[c_{11}(\alpha_n+1)^2-(n^2+c_{22})]+b_{1n}(in)[(c_{12}+1)(\alpha_n+1)-(c_{22}+1)] = 0 \quad (2.37)$$
$$a_{1n}(in)[(c_{12}+1)(\alpha_n+1)+(c_{22}+1)]+b_{1n}[(\alpha_n+1)^2-(n^2c_{22}+1)] = 0 \quad (2.38)$$

which can be written in the matrix form as

$$\begin{bmatrix} c_{11}(\alpha_n+1)^2-(n^2+c_{22}) & (in)[(c_{12}+1)(\alpha_n+1)-(c_{22}+1)] \\ (in)[(c_{12}+1)(\alpha_n+1)+(c_{22}+1)] & (\alpha_n+1)^2-(n^2c_{22}+1) \end{bmatrix}\begin{bmatrix} a_{1n} \\ b_{1n} \end{bmatrix} = \begin{bmatrix} 0 \\ 0 \end{bmatrix} \quad (2.39)$$

Since the determinant D of the system matrix in Eqn. (2.26) vanishes, the determinant of the system matrix in Eqn. (2.39) does not vanish. Thus, a_{1n} and b_{1n} have to be zero. For the m-th power, where m goes from 2 to ∞, they become

$$\begin{aligned}
\{c_{11}[(m+\alpha_n)(m+\alpha_n-1)+(m+\alpha_n)]-(n^2+c_{22})\}a_{mn}+k^2a_{(m-2)n}& \\
+\{in(c_{12}+1)(m+\alpha_n)-in(c_{22}+1)\}b_{mn} &= 0 \quad (2.40) \\
\{in(c_{12}+1)(m+\alpha_n)+in(c_{22}+1)\}a_{mn}& \\
+[(m+\alpha_n)(m+\alpha_n-1)+(m+\alpha_n)-(n^2c_{22}+1)]b_{mn}+k^2b_{(m-2)n} &= 0 \quad (2.41)
\end{aligned}$$

Eqns. (2.40) and (2.41) can be written in matrix form as

$$\begin{bmatrix} c_{11}(m+\alpha_n)^2-(n^2+c_{22}) & in[(c_{12}+1)(m+\alpha_n)-(c_{22}+1)] \\ in[(c_{12}+1)(m+\alpha_n)+(c_{22}+1)] & (m+\alpha_n)^2-(n^2c_{22}+1) \end{bmatrix} \begin{bmatrix} a_{mn} \\ b_{mn} \end{bmatrix} = -k^2 \begin{bmatrix} a_{(m-2)n} \\ b_{(m-2)n} \end{bmatrix} \quad (2.42)$$

The recursive relationship shown in Eqn. (2.42) is a two step recursion which starts with a_{0n} and b_{0n}. Following the Frobenius method, the initial value of a_{0n} can be assumed as an arbitrary non-zero value. By setting $a_{0n}=1$, Eq. (2.25) gives

$$b_{0n} = -\frac{in[(c_{12}+1)\alpha_n+(c_{22}+1)]}{\alpha_n^2-(n^2c_{22}+1)} \quad (2.43)$$

Through Eqn. (2.42), even numbered real coefficients a_{mn} and b_{mn} can be obtained with the defined initial values of a_{0n} and b_{0n}, while odd numbered coefficients are set to zero.

2.3.4 The General Solutions

For each real $\alpha_n^{(\sigma)}$ $(\sigma = 1, 2, 3, 4)$ from Eqn. (2.34), coefficients $a_{mn}^{(\sigma)}$ and $b_{mn}^{(\sigma)}$ can be calculated from Eqn. (2.42). The resulting displacement U_n and V_n can be written as

$$U_n^{(\sigma)}(r) = \sum_{m=0}^{\infty} a_{mn}^{(\sigma)} r^{m+\alpha_n^{(\sigma)}}, \quad V_n^{(\sigma)}(r) = \sum_{m=0}^{\infty} b_{mn}^{(\sigma)} r^{m+\alpha_n^{(\sigma)}}, \tag{2.44}$$

Thus, the general solution of displacement for the waves in a cylindrically orthotropic medium can be written as

$$u_r = \sum_{n=-\infty}^{\infty} \left[\mathsf{a}_n U_n^{(1)}(r) + \mathsf{b}_n U_n^{(2)}(r) + \mathsf{c}_n U_n^{(3)}(r) + \mathsf{d}_n U_n^{(4)}(r)\right] e^{in\theta} e^{i\omega t} \tag{2.45}$$

$$u_\theta = \sum_{n=-\infty}^{\infty} \left[\mathsf{a}_n V_n^{(1)}(r) + \mathsf{b}_n V_n^{(2)}(r) + \mathsf{c}_n V_n^{(3)}(r) + \mathsf{d}_n V_n^{(4)}(r)\right] e^{in\theta} e^{i\omega t} \tag{2.46}$$

Or the general solution can be written in a compact form as

$$\begin{Bmatrix} u_r \\ u_\theta \end{Bmatrix} = \sum_{n=-\infty}^{\infty} \left[\mathsf{a}_n \begin{Bmatrix} U_n^{(1)} \\ V_n^{(1)} \end{Bmatrix} + \mathsf{b}_n \begin{Bmatrix} U_n^{(2)} \\ V_n^{(2)} \end{Bmatrix} + \mathsf{c}_n \begin{Bmatrix} U_n^{(3)} \\ V_n^{(3)} \end{Bmatrix} + \mathsf{d}_n \begin{Bmatrix} U_n^{(4)} \\ V_n^{(4)} \end{Bmatrix}\right] e^{in\theta} e^{i\omega t} \tag{2.47}$$

where a_n, b_n, c_n and d_n are constants to be determined.

2.3.5 Special Cases in the General Solutions

According to Eqns. (2.29) and (2.30), we have $\alpha_n = \alpha_{-n}$. Since $a_{0n} = 1$, the relation in Eqn. (2.42) gives $a_{mn} = a_{m(-n)}$. According to Eqn. (2.43), we have $b_{0n} = -b_{0(-n)}$. Then, Eqn. (2.42), gives $b_{mn} = -b_{m(-n)}$. Therefore, Eqn. (3.43) gives $U_n = U_{-n}$ and $V_n = -V_{-n}$. So without any loss in generality, only when $n >= 0$ is discussed. There are three special cases that need to be further considered.

The first special case is when α_n has two roots which differ by an integer at mode $n > 0$. If α_n has two roots that differ by an integer, to obtain the second linearly independent solution, if the first solution corresponding to α_1 is $y_1(r)$, the second solution has the form (Edwards and Penney, 1996; Campbell and Haberman, 1996; Riley et al., 2006; Farlow, 2006; Patnaik, 2009)

$$y_2(r) = cy_1(r)\ln r + \sum_{m=0}^{\infty} B_m r^{m+\alpha_2} \tag{2.48}$$

where c is a constant. Constant c and coefficients B_m can be obtained by substituting the Eqn. (2.48) into the original ordinary differential equation.

The second special case that will be discussed is when α has repeated roots. If α has repeated roots, it will lead to two identical solutions. So the second solution needs to be considered specially. According to Campbell and Haberman (1996); Farlow (2006), if the first solution corresponding to α_1 is $y_1(r)$, the second solution has the form

$$y_2(r) = y_1(r)\ln r + \sum_{m=0}^{\infty} B_m r^{m+\alpha_1} \tag{2.49}$$

where B_m can be obtained by substituting the second solution into the original ordinary differential equations.

The third special case is when $n = 0$, in which case, Eqns. (2.19) and (2.20) are decoupled. The process of obtaining the general solutions for the decoupled case is different from that of the coupled case. So this case is discussed as a special case.

The first two special cases are due to Frobenius method for solving ordinary differential equations. The third special case is due to the specific situation for the problem at hand. In the following sections, each of three special cases for solving the equations of motion (2.19) and (2.20) is discussed.

2.4 Special Case 1: Two α's Differ by an Integer

In this section, the special case when $n > 0$ and $\alpha_n^{(1)}$ and $\alpha_n^{(2)}$ differ by an integer is solved. One numerical example is used for verifying the solutions. Other possibilities follow the same solution approach. Some examples are when $\alpha_n^{(1)}$ and $\alpha_n^{(3)}$ differ by an integer or $\alpha_n^{(1)}$ and $\alpha_n^{(4)}$ differ by an integer. Therefore, only the situation when $\alpha_n^{(1)}$ and $\alpha_n^{(2)}$ differ by an integer is considered in this section.

Let $\alpha_n^{(1)} - \alpha_n^{(2)} = N$, where N is an integer. The first solution is given as (Edwards and Penney, 1996; Campbell and Haberman, 1996; Riley et al., 2006; Farlow, 2006; Patnaik, 2009),

$$U_n^{(1)} = \sum_{m=0}^{\infty} a_{mn}^{(1)} r^{m+\alpha_n^{(1)}} \tag{2.50}$$

The second solution can be given as

$$U_n^{(2)} = cU_n^{(1)} \ln r + \sum_{m=0}^{\infty} a_{mn}^{(2)} r^{m+\alpha_n^{(2)}} \tag{2.51}$$

Similarly we have

$$V_n^{(1)} = \sum_{m=0}^{\infty} b_{mn}^{(1)} r^{m+\alpha_n^{(1)}} \tag{2.52}$$

and

$$V_n^{(2)} = cV_n^{(1)} \ln r + \sum_{m=0}^{\infty} b_{mn}^{(2)} r^{m+\alpha_n^{(2)}} \tag{2.53}$$

where the constant c and coefficients $a_{mn}^{(2)}$ and $b_{mn}^{(2)}$ can be obtained by substituting the assumed solutions (2.50) through (2.53) into the original pair of ODEs. For easier reference, the pair of ODEs, is repeated here

$$\begin{aligned} c_{11}\left(r^2U_n'' + rU_n'\right) + \left(k^2r^2 - n^2 - c_{22}\right)U_n + in(c_{12}+1)rV_n' & \\ -in(c_{22}+1)V_n &= 0 \qquad (2.54) \\ r^2V_n'' + rV_n' + in(c_{12}+1)rU_n' + (k^2r^2 - n^2c_{22} - 1)V_n & \\ +in(c_{22}+1)U_n &= 0 \qquad (2.55) \end{aligned}$$

Substituting the assumed solutions (2.50) through (2.53) into Eqns. (2.54) and (2.55) gives

$$\begin{aligned} \sum_{m=0}^{\infty} 2c_{11}c\left(m+\alpha_n^{(1)}\right)a_{mn}^{(1)}r^{m+N} + \sum_{m=0}^{\infty} in(c_{12}+1)cb_{mn}^{(1)}r^{m+N} & \\ +\sum_{m=0}^{\infty}\left[c_{11}\left(m+\alpha_n^{(2)}\right)^2 - (n^2+c_{22})\right]a_{mn}^{(2)}r^m + \sum_{m=0}^{\infty} k^2a_{mn}^{(2)}r^{m+2} & \\ +\sum_{m=0}^{\infty} in\left[(c_{12}+1)\left(m+\alpha_n^{(2)}\right) - (c_{22}+1)\right]b_{mn}^{(2)}r^m &= 0 \qquad (2.56) \\ \sum_{m=0}^{\infty} 2c\left(m+\alpha_n^{(1)}\right)b_{mn}^{(1)}r^{m+N} + \sum_{m=0}^{\infty} in(c_{12}+1)ca_{mn}^{(1)}r^{m+N} & \\ +\sum_{m=0}^{\infty}\left[\left(m+\alpha_n^{(2)}\right)^2 - (n^2c_{22}+1)\right]b_{mn}^{(2)}r^m + \sum_{m=0}^{\infty} k^2b_{mn}^{(2)}r^{m+2} & \\ +\sum_{m=0}^{\infty}\left[in(c_{12}+1)\left(m+\alpha_n^{(2)}\right) + in(c_{22}+1)\right]a_{mn}^{(2)}r^m &= 0 \qquad (2.57) \end{aligned}$$

Setting $r = 0$, the only non-vanishing terms are those with $m = 0$, giving the following set of indicial equations

$$\begin{aligned} \left[c_{11}\left(\alpha_n^{(2)}\right)^2 - (n^2+c_{22})\right]a_{0n}^{(2)} + in[(c_{12}+1)\alpha_n^{(2)} - (c_{22}+1)b_{0n}^{(2)} &= 0 \qquad (2.58) \\ in\left[(c_{12}+1)\alpha_n^{(2)} + (c_{22}+1)\right]a_{0n}^{(2)} + \left[\left(\alpha_n^{(2)}\right)^2 - (n^2c_{22}+1)\right]b_{0n}^{(2)} &= 0 \qquad (2.59) \end{aligned}$$

which can be written in the matrix form as

$$\begin{bmatrix} c_{11}\left(\alpha_n^{(2)}\right)^2 - (n^2 + c_{22}) & (in)[(c_{12}+1)\alpha_n^{(2)} - (c_{22}+1)] \\ (in)[(c_{12}+1)\alpha_n^{(2)} + (c_{22}+1)] & \left(\alpha_n^{(2)}\right)^2 - (n^2 c_{22} + 1) \end{bmatrix} \begin{bmatrix} a_{0n}^{(2)} \\ b_{0n}^{(2)} \end{bmatrix} = \begin{bmatrix} 0 \\ 0 \end{bmatrix} \tag{2.60}$$

According to Eqn. (2.27), the determinant of the system matrix in Eqn. (2.60) must vanish. Thus, $a_{0n}^{(2)}$ and $b_{0n}^{(2)}$ are non-zero. Choose $a_{0n}^{(2)} = 1$, then $b_{0n}^{(2)}$ can be obtained through above relations (2.58) and (2.59).

$$b_{0n}^{(2)} = -\frac{in\left[(c_{12}+1)\alpha_n^{(2)} + (c_{22}+1)\right] a_{0n}^{(2)}}{\left(\alpha_n^{(2)}\right)^2 - (n^2 c_{22} + 1)} \tag{2.61}$$

Since the terms for 0-th power of r equal to zero, Eqns. (2.56) and (2.57) can be written as

$$\begin{aligned} &\sum_{m=0}^{\infty} 2c_{11}c\left(m + \alpha_n^{(1)}\right) a_{mn}^{(1)} r^{m+N} + \sum_{m=0}^{\infty} in(c_{12}+1)c b_{mn}^{(1)} r^{m+N} \\ &+ \sum_{m=0}^{\infty}\left[c_{11}\left(m+1+\alpha_n^{(2)}\right)^2 - (n^2 + c_{22})\right] a_{(m+1)n}^{(2)} r^{m+1} + \sum_{m=0}^{\infty} k^2 a_{mn}^{(2)} r^{m+2} \\ &+ \sum_{m=0}^{\infty} in\left[(c_{12}+1)\left(m+1+\alpha_n^{(2)}\right) - (c_{22}+1)\right] b_{(m+1)n}^{(2)} r^{m+1} = 0 \end{aligned} \tag{2.62}$$

$$\begin{aligned} &\sum_{m=0}^{\infty} 2c\left(m + \alpha_n^{(1)}\right) b_{mn}^{(1)} r^{m+N} + \sum_{m=0}^{\infty} in(c_{12}+1)c a_{mn}^{(1)} r^{m+N} \\ &+ \sum_{m=0}^{\infty}\left[\left(m+1+\alpha_n^{(2)}\right)^2 - (n^2 c_{22} + 1)\right] b_{(m+1)n}^{(2)} r^{m+1} + \sum_{m=0}^{\infty} k^2 b_{mn}^{(2)} r^{m+2} \\ &+ \sum_{m=0}^{\infty}\left[in(c_{12}+1)\left(m+1+\alpha_n^{(2)}\right) + in(c_{22}+1)\right] a_{(m+1)n}^{(2)} r^{m+1} = 0 \end{aligned} \tag{2.63}$$

In Eqns. (2.62) and (2.63), the exponents of r for the third and fifth series start from $m+1$, and the fourth series starts from $m+2$. Since integer $N \geq 1$, three situations of the exponents of r for the first and second series need to be considered: 1: when $m+N=m+1$, 2: when $m+N=m+2$, and 3: when $m+N>m+2$. Therefore, the following three situations will be discussed in details: 1: when $N=1$, 2: when $N=2$, and 3: when $N>2$.

2.4.1 When $N=1$

Eqns. (2.62) and (2.63) can be written as

$$\begin{aligned}
&\sum_{m=0}^{\infty} 2c_{11}c\left(m+\alpha_n^{(1)}\right)a_{mn}^{(1)}r^{m+1}+\sum_{m=0}^{\infty} in(c_{12}+1)cb_{mn}^{(1)}r^{m+1} \\
&+\sum_{m=0}^{\infty}\left[c_{11}\left(m+1+\alpha_n^{(2)}\right)^2-(n^2+c_{22})\right]a_{(m+1)n}^{(2)}r^{m+1}+\sum_{m=0}^{\infty}k^2a_{mn}^{(2)}r^{m+2} \\
&+\sum_{m=0}^{\infty} in\left[(c_{12}+1)\left(m+1+\alpha_n^{(2)}\right)-(c_{22}+1)\right]b_{(m+1)n}^{(2)}r^{m+1} = 0 \quad (2.64)
\end{aligned}$$

$$\begin{aligned}
&\sum_{m=0}^{\infty} 2c\left(m+\alpha_n^{(1)}\right)b_{mn}^{(1)}r^{m+1}+\sum_{m=0}^{\infty} in(c_{12}+1)ca_{mn}^{(1)}r^{m+1} \\
&+\sum_{m=0}^{\infty}\left[\left(m+1+\alpha_n^{(2)}\right)^2-(n^2c_{22}+1)\right]b_{(m+1)n}^{(2)}r^{m+1}+\sum_{m=0}^{\infty}k^2b_{mn}^{(2)}r^{m+2} \\
&+\sum_{m=0}^{\infty}\left[in(c_{12}+1)\left(m+1+\alpha_n^{(2)}\right)+in(c_{22}+1)\right]a_{(m+1)n}^{(2)}r^{m+1} = 0 \quad (2.65)
\end{aligned}$$

Eqns. (2.64) and (2.65) should be satisfied for all powers of r. Dividing the factor r, for $m=0$, they become

$$\begin{aligned}
&2c_{11}c\alpha_n^{(1)}a_{0n}^{(1)}+in(c_{12}+1)cb_{0n}^{(1)}+\left[c_{11}\left(1+\alpha_n^{(2)}\right)^2-(n^2+c_{22})\right]a_{1n}^{(2)} \\
&+in\left[(c_{12}+1)\left(1+\alpha_n^{(2)}\right)-(c_{22}+1)\right]b_{1n}^{(2)} = 0 \quad (2.66)
\end{aligned}$$

$$\begin{aligned}
&2c\alpha_n^{(1)}b_{0n}^{(1)}+in(c_{12}+1)ca_{0n}^{(1)}+\left[\left(1+\alpha_n^{(2)}\right)^2-(n^2c_{22}+1)\right]b_{1n}^{(2)} \\
&+\left[in(c_{12}+1)\left(1+\alpha_n^{(2)}\right)+in(c_{22}+1)\right]a_{1n}^{(2)} = 0 \quad (2.67)
\end{aligned}$$

Since $N=1$, $1+\alpha_n^{(2)}=\alpha_n^{(1)}$, Eqns. (2.66) and (2.67) can be written in matrix form

$$\begin{bmatrix} c_{11}\left(\alpha_n^{(1)}\right)^2-(n^2+c_{22}) & (in)[(c_{12}+1)\alpha_n^{(1)}-(c_{22}+1)] \\ (in)[(c_{12}+1)\alpha_n^{(1)}+(c_{22}+1)] & \left(\alpha_n^{(1)}\right)^2-(n^2c_{22}+1) \end{bmatrix}\begin{bmatrix} a_{1n}^{(2)} \\ b_{1n}^{(2)} \end{bmatrix} = -c\begin{bmatrix} 2c_{11}\alpha_n^{(1)}a_{0n}^{(1)}+in(c_{12}+1)b_{0n}^{(1)} \\ 2\alpha_1 b_{0n}^{(1)}+in(c_{12}+1)a_{0n}^{(1)} \end{bmatrix} \tag{2.68}$$

According to Eqn. (2.27), the determinant of the system matrix in Eqn. (2.68) must vanish, which gives $c=0$. $a_{1n}^{(2)}$ and $b_{1n}^{(2)}$ can be chosen as arbitrary values. After setting $a_{1n}^{(2)}=b_{1n}^{(2)}=0$, Eqns. (2.64) and (2.65) can be written as

$$\begin{aligned} \sum_{m=0}^{\infty}\left[c_{11}\left(m+2+\alpha_n^{(2)}\right)^2-(n^2+c_{22})\right]a_{(m+2)n}^{(2)}r^m+\sum_{m=0}^{\infty}k^2a_{mn}^{(2)}r^m & \\ +\sum_{m=0}^{\infty}in\left[(c_{12}+1)\left(m+2+\alpha_n^{(2)}\right)-(c_{22}+1)\right]b_{(m+2)n}^{(2)}r^m &= 0 \qquad (2.69) \\ \sum_{m=0}^{\infty}\left[\left(m+2+\alpha_n^{(2)}\right)^2-(n^2c_{22}+1)\right]b_{(m+2)n}^{(2)}r^m+\sum_{m=0}^{\infty}k^2b_{mn}^{(2)}r^m & \\ +\sum_{m=0}^{\infty}\left[in(c_{12}+1)\left(m+2+\alpha_n^{(2)}\right)+in(c_{22}+1)\right]a_{(m+2)n}^{(2)}r^m &= 0 \qquad (2.70) \end{aligned}$$

Eqns. (2.69) and (2.70) need to be satisfied for all different power of r. For the m-th power, they become

$$\begin{aligned} \left[c_{11}\left(m+\alpha_n^{(2)}\right)^2-(n^2+c_{22})\right]a_{mn}^{(2)}+k^2a_{(m-2)n}^{(2)} & \\ +in\left[(c_{12}+1)\left(m+\alpha_n^{(2)}\right)-(c_{22}+1)\right]b_{mn}^{(2)} &= 0 \qquad (2.71) \\ \left[\left(m+\alpha_n^{(2)}\right)^2-(n^2c_{22}+1)\right]b_{mn}^{(2)}+k^2b_{(m-2)n}^{(2)} & \\ +\left[in(c_{12}+1)\left(m+\alpha_n^{(2)}\right)+in(c_{22}+1)\right]a_{mn}^{(2)} &= 0 \qquad (2.72) \end{aligned}$$

where $2 < m < \infty$. The coefficients $a_{mn}^{(2)}$ and $b_{mn}^{(2)}$ can be obtained through the above recurrence relations. The relations can be written in matrix form as

$$\begin{bmatrix} c_{11}\left(m+\alpha_n^{(2)}\right)^2-(n^2+c_{22}) & in[(c_{12}+1)\left(m+\alpha_n^{(2)}\right)-(c_{22}+1)] \\ in[(c_{12}+1)\left(m+\alpha_n^{(2)}\right)+(c_{22}+1)] & \left(m+\alpha_n^{(2)}\right)^2-(n^2c_{22}+1) \end{bmatrix}\begin{bmatrix} a_{mn}^{(2)} \\ b_{mn}^{(2)} \end{bmatrix} = -k^2\begin{bmatrix} a_{(m-2)n}^{(2)} \\ b_{(m-2)n}^{(2)} \end{bmatrix} \tag{2.73}$$

2.4.2 When $N = 2$

Eqns. (2.62) and (2.63) can be written as

$$\begin{aligned} &\sum_{m=0}^{\infty} 2c_{11}c\left(m+\alpha_n^{(1)}\right)a_{mn}^{(1)}r^{m+2}+\sum_{m=0}^{\infty} in(c_{12}+1)cb_{mn}^{(1)}r^{m+2} \\ &+\sum_{m=0}^{\infty}\left[c_{11}\left(m+1+\alpha_n^{(2)}\right)^2-(n^2+c_{22})\right]a_{(m+1)n}^{(2)}r^{m+1}+\sum_{m=0}^{\infty}k^2a_{mn}^{(2)}r^{m+2} \\ &+\sum_{m=0}^{\infty} in\left[(c_{12}+1)\left(m+1+\alpha_n^{(2)}\right)-(c_{22}+1)\right]b_{(m+1)n}^{(2)}r^{(m+1)n} = 0 \end{aligned} \tag{2.74}$$

$$\begin{aligned} &\sum_{m=0}^{\infty} 2c\left(m+\alpha_n^{(1)}\right)b_{mn}^{(1)}r^{m+2}+\sum_{m=0}^{\infty} in(c_{12}+1)ca_{mn}^{(1)}r^{m+2} \\ &+\sum_{m=0}^{\infty}\left[\left(m+1+\alpha_n^{(2)}\right)^2-(n^2c_{22}+1)\right]b_{(m+1)n}^{(2)}r^{m+1}+\sum_{m=0}^{\infty}k^2b_{mn}^{(2)}r^{m+2} \\ &+\sum_{m=0}^{\infty}\left[in(c_{12}+1)\left(m+1+\alpha_n^{(2)}\right)+in(c_{22}+1)\right]a_{(m+1)n}^{(2)}r^{m+1} = 0 \end{aligned} \tag{2.75}$$

Dividing by the common factor r^{m+1}, for the 0-th power, the equations become

$$\left[c_{11}\left(1+\alpha_n^{(2)}\right)^2-(n^2+c_{22})\right]a_{1n}^{(2)}+in\left[(c_{12}+1)\left(1+\alpha_n^{(2)}\right)-(c_{22}+1)\right]b_{1n}^{(2)}=0 \tag{2.76}$$

$$\left[\left(1+\alpha_n^{(2)}\right)^2-(n^2c_{22}+1)\right]b_{1n}^{(2)}+in\left[(c_{12}+1)\left(1+\alpha_n^{(2)}\right)+(c_{22}+1)\right]a_{1n}^{(2)}=0 \tag{2.77}$$

which can be written in matrix form as

$$\begin{bmatrix} c_{11}\left(1+\alpha_n^{(2)}\right)^2-(n^2+c_{22}) & (in)[(c_{12}+1)\left(1+\alpha_n^{(2)}\right)-(c_{22}+1)] \\ (in)[(c_{12}+1)\left(1+\alpha_n^{(2)}\right)+(c_{22}+1)] & \left(1+\alpha_n^{(2)}\right)^2-(n^2c_{22}+1) \end{bmatrix}\begin{bmatrix} a_{1n}^{(2)} \\ b_{1n}^{(2)} \end{bmatrix} = \begin{bmatrix} 0 \\ 0 \end{bmatrix} \tag{2.78}$$

Since $1+\alpha_n^{(2)} \neq \alpha_n^{(1)}$, the determinant of the system matrix in Eqn. (2.68) is non-zero. Therefore, this gives $a_{1n}^{(2)} = b_{1n}^{(2)} = 0$. Then Eqns. (2.74) and (2.75) can be written as

$$\begin{aligned} &\sum_{m=0}^{\infty} 2c_{11}c\left(m+\alpha_n^{(1)}\right)a_{mn}^{(1)}r^{m+2} + \sum_{m=0}^{\infty} in(c_{12}+1)cb_{mn}^{(1)}r^{m+2} \\ &+\sum_{m=0}^{\infty}\left[c_{11}\left(m+2+\alpha_n^{(2)}\right)^2-(n^2+c_{22})\right]a_{(m+2)n}^{(2)}r^{m+2} + \sum_{m=0}^{\infty} k^2 a_{mn}^{(2)}r^{m+2} \\ &+\sum_{m=0}^{\infty} in\left[(c_{12}+1)\left(m+2+\alpha_n^{(2)}\right)-(c_{22}+1)\right]b_{(m+2)n}^{(2)}r^{m+2} = 0 \end{aligned} \tag{2.79}$$

$$\begin{aligned} &\sum_{m=0}^{\infty} 2c\left(m+\alpha_n^{(1)}\right)b_{mn}^{(1)}r^{m+2} + \sum_{m=0}^{\infty} in(c_{12}+1)ca_{mn}^{(1)}r^{m+2} \\ &+\sum_{m=0}^{\infty}\left[\left(m+2+\alpha_n^{(2)}\right)^2-(n^2c_{22}+1)\right]b_{(m+2)n}^{(2)}r^{m+2} + \sum_{m=0}^{\infty} k^2 b_{mn}^{(2)}r^{m+2} \\ &+\sum_{m=0}^{\infty}\left[in(c_{12}+1)\left(m+2+\alpha_n^{(2)}\right)+in(c_{22}+1)\right]a_{(m+2)n}^{(2)}r^{m+2} = 0 \end{aligned} \tag{2.80}$$

Dividing by the common factor r^{m+2}, for the 0-th power of r, the equations are

$$
\begin{aligned}
2c_{11}c\alpha_n^{(1)}a_{0n}^{(1)} + in(c_{12}+1)cb_{0n}^{(1)} + \\
\left[c_{11}\left(2+\alpha_n^{(2)}\right)^2 - (n^2+c_{22})\right]a_{2n}^{(2)} + k^2a_{0n}^{(2)} \\
+in\left[(c_{12}+1)\left(2+\alpha_n^{(2)}\right) - (c_{22}+1)\right]b_{2n}^{(2)} &= 0 \qquad (2.81)\\
2c\alpha_n^{(1)}b_{0n}^{(1)} + in(c_{12}+1)ca_{0n}^{(1)} + \\
\left[\left(2+\alpha_n^{(2)}\right)^2 - (n^2c_{22}+1)\right]b_{2n}^{(2)} + k^2b_{0n}^{(2)} \\
+\left[in(c_{12}+1)\left(2+\alpha_n^{(2)}\right) + in(c_{22}+1)\right]a_{2n}^{(2)} &= 0 \qquad (2.82)
\end{aligned}
$$

Since $2+\alpha_n^{(2)} = \alpha_n^{(1)}$, the above Eqns. (2.79) and (2.80) can be written in matrix form

$$
\begin{bmatrix} c_{11}\left(\alpha_n^{(1)}\right)^2 - (n^2+c_{22}) & (in)[(c_{12}+1)\alpha_n^{(1)} - (c_{22}+1)] \\ (in)[(c_{12}+1)\alpha_n^{(1)} + (c_{22}+1)] & \left(\alpha_n^{(1)}\right)^2 - (n^2c_{22}+1) \end{bmatrix} \begin{bmatrix} a_{2n}^{(2)} \\ b_{2n}^{(2)} \end{bmatrix}
= -\begin{bmatrix} 2c_{11}c\alpha_1a_{0n}^{(1)} + inc(c_{12}+1)b_{0n}^{(1)} + k^2a_{0n}^{(2)} \\ 2c\alpha_1b_{0n}^{(1)} + inc(c_{12}+1)a_{0n}^{(1)} + k^2b_{0n}^{(2)} \end{bmatrix} \qquad (2.83)
$$

Since the determinant of the system matrix in Eqn. (2.83) vanishes, $a_{2n}^{(2)}$ can be chosen as arbitrary value. Now let $a_{2n}^{(2)} = 1$. Then c and $b_{2n}^{(2)}$ can be obtained through the following relation

$$
\begin{bmatrix} 2c_{11}\alpha_n^{(1)}a_{0n}^{(1)} + in(c_{12}+1)b_{0n}^{(1)} & in[(c_{12}+1)\alpha_n^{(1)} - (c_{22}+1)] \\ 2\alpha_n^{(1)}b_{0n}^{(1)} + in(c_{12}+1)a_{0n}^{(1)} & \left(\alpha_n^{(1)}\right)^2 - (n^2c_{22}+1) \end{bmatrix} \begin{bmatrix} c \\ b_{2n}^{(2)} \end{bmatrix}
= \begin{bmatrix} -[c_{11}\left(\alpha_n^{(1)}\right)^2 - (n^2+c_{22})]a_{2n}^{(2)} - k^2a_{0n}^{(2)} \\ in[(c_{12}+1)\alpha_n^{(1)} + (c_{22}+1)]a_{2n}^{(2)} - k^2b_{0n}^{(2)} \end{bmatrix} \qquad (2.84)
$$

After obtaining the value of constant c and coefficients $a_{0n}^{(2)}$, $b_{0n}^{(2)}$, $a_{2n}^{(2)}$, and $b_{2n}^{(2)}$, the coefficients

$a^{(2)}_{(m+2)n}$ and $b^{(2)}_{(m+2)n}$ can be obtained through the following recurrence relations

$$\begin{aligned}
&\left[c_{11}(m+\alpha_n^{(1)})^2-(n^2+c_{22})\right]a^{(2)}_{(m+2)n}\\
&+in\left[(c_{12}+1)(m+\alpha_n^{(1)})-(c_{22}+1)\right]b^{(2)}_{(m+2)n}=\\
&-c\left[2c_{11}(m+\alpha_n^{(1)})a^{(1)}_{mn}+in(c_{12}+1)b^{(1)}_{mn}\right]-k^2a^{(2)}_{mn}
\end{aligned}\tag{2.85}$$

$$\begin{aligned}
&\left[in(c_{12}+1)(m+\alpha_n^{(1)})+in(c_{22}+1)\right]a^{(2)}_{(m+2)n}\\
&+\left[(m+\alpha_n^{(1)})^2-(n^2c_{22}+1)\right]b^{(2)}_{(m+2)n}=\\
&-c\left[2(m+\alpha_n^{(1)})b^{(1)}_{mn}+in(c_{12}+1)a^{(1)}_{mn}\right]-k^2b^{(2)}_{mm}
\end{aligned}\tag{2.86}$$

where $2\leqslant m<\infty$. The above two equations can be written in matrix form as

$$\begin{bmatrix} c_{11}(m+\alpha_n^{(1)})^2-(n^2+c_{22}) & in\left[(c_{12}+1)(m+\alpha_n^{(1)})-(c_{22}+1)\right] \\ in(c_{12}+1)(m+\alpha_n^{(1)})+in(c_{22}+1) & (m+\alpha_n^{(1)})^2-(n^2c_{22}+1)\end{bmatrix}\begin{bmatrix} a^{(2)}_{(m+2)n} \\ b^{(2)}_{(m+2)n}\end{bmatrix}$$
$$=\begin{bmatrix} -c\left[2c_{11}(m+\alpha_n^{(1)})a^{(1)}_{mn}+in(c_{12}+1)b^{(1)}_{mn}\right]-k^2a^{(2)}_{mn} \\ -c\left[2(m+\alpha_n^{(1)})b^{(1)}_{mn}+in(c_{12}+1)a^{(1)}_{mn}\right]-k^2b^{(2)}_{mn}\end{bmatrix}\tag{2.87}$$

2.4.3 When $N > 2$

Eqns. (2.79) and (2.80) can be written as

$$\begin{aligned}
&\sum_{m=0}^{\infty} 2c_{11}c(m+\alpha_n^{(1)})a_{mn}^{(1)}r^{m+N-2} + \sum_{m=0}^{\infty} in(c_{12}+1)cb_{mn}^{(1)}r^{m+N-2} \\
&+\sum_{m=0}^{\infty}\left[c_{11}(m+2+\alpha_n^{(2)})^2-(n^2+c_{22})\right]a_{(m+2)n}^{(2)}r^m + \sum_{m=0}^{\infty} k^2 a_{mn}^{(2)}r^m \\
&+\sum_{m=0}^{\infty} in\left[(c_{12}+1)(m+2+\alpha_n^{(2)})-(c_{22}+1)\right]b_{(m+2)n}^{(2)}r^m = 0 \qquad (2.88)\\
&\sum_{m=0}^{\infty} 2c(m+\alpha_n^{(1)})b_{mn}^{(1)}r^{m+N-2} + \sum_{m=0}^{\infty} in(c_{12}+1)ca_{mn}^{(1)}r^{m+N-2} \\
&+\sum_{m=0}^{\infty}\left[(m+2+\alpha_n^{(2)})^2-(n^2c_{22}+1)\right]b_{(m+2)n}^{(2)}r^m + \sum_{m=0}^{\infty} k^2 b_{mn}^{(2)}r^m \\
&+\sum_{m=0}^{\infty}\left[in(c_{12}+1)(m+2+\alpha_n^{(2)})+in(c_{22}+1)\right]a_{(m+2)n}^{(2)}r^m = 0 \qquad (2.89)
\end{aligned}$$

For $0 \leqslant m < N-2$, coefficients $a_{mn}^{(2)}$ and $b_{mn}^{(2)}$ can be obtained through the following relations,

$$\begin{aligned}
&[c_{11}(m+2+\alpha_n^{(2)})^2-(n^2+c_{22})]a_{(m+2)n}^{(2)} + k^2a_{mn}^{(2)} \\
&+in[(c_{12}+1)(m+2+\alpha_n^{(2)})-(c_{22}+1)]b_{(m+2)n}^{(2)} = 0 \qquad (2.90)\\
&\left[(m+2+\alpha_n^{(2)})^2-(n^2c_{22}+1)\right]b_{(m+2)n}^{(2)} + k^2b_{mn}^{(2)} \\
&+in[(c_{12}+1)(m+2+\alpha_n^{(2)})+(c_{22}+1)]a_{(m+2)n}^{(2)} = 0 \qquad (2.91)
\end{aligned}$$

which can also be written as

$$\begin{aligned}
&[c_{11}(m+\alpha_n^{(2)})^2-(n^2+c_{22})]a_{mn}^{(2)} + k^2a_{(m-2)n}^{(2)} \\
&+in[(c_{12}+1)(m+\alpha_n^{(2)})-(c_{22}+1)]b_{mn}^{(2)} = 0 \qquad (2.92)\\
&\left[(m+\alpha_n^{(2)})^2-(n^2c_{22}+1)\right]b_{mn}^{(2)} + k^2b_{(m-2)n}^{(2)} \\
&+in[(c_{12}+1)(m+\alpha_n^{(2)})+(c_{22}+1)]a_{mn}^{(2)} = 0 \qquad (2.93)
\end{aligned}$$

where $2 \leqslant m < N$. Then Eqns. (2.88) and (2.89) can be written as

$$\begin{aligned}
&\sum_{m=0}^{\infty} 2c_{11}c(m+\alpha_n^{(1)})a_{mn}^{(1)}r^{m+N-2} + \sum_{m=0}^{\infty} in(c_{12}+1)cb_{mn}^{(1)}r^{m+N-2} \\
&+\sum_{m=0}^{\infty}\left[c_{11}(m+N+\alpha_n^{(2)})^2-(n^2+c_{22})\right]a_{(m+N)n}^{(2)}r^{m+N-2}+\sum_{m=0}^{\infty}k^2a_{(m+N-2)n}^{(2)}r^{m+N-2} \\
&+\sum_{m=0}^{\infty} in\left[(c_{12}+1)(m+N+\alpha_n^{(2)})-(c_{22}+1)\right]b_{(m+N)n}^{(2)}r^{m+N-2}=0
\end{aligned} \tag{2.94}$$

$$\begin{aligned}
&\sum_{m=0}^{\infty} 2c(m+\alpha_n^{(1)})b_{mn}^{(1)}r^{m+N-2} + \sum_{m=0}^{\infty} in(c_{12}+1)ca_{mn}^{(1)}r^{m+N-2} \\
&+\sum_{m=0}^{\infty}\left[(m+N+\alpha_n^{(2)})^2-(n^2c_{22}+1)\right]b_{(m+N)n}^{(2)}r^{m+N-2}+\sum_{m=0}^{\infty}k^2b_{(m+N-2)n}^{(2)}r^{m+N-2} \\
&+\sum_{m=0}^{\infty}\left[in(c_{12}+1)(m+N+\alpha_n^{(2)})+in(c_{22}+1)\right]a_{(m+N)}^{(2)}r^{m+N-2}=0
\end{aligned} \tag{2.95}$$

Dividing by the common factor r^{N-2}, for the 0-th power of r, gives

$$\begin{aligned}
&2c_{11}c\alpha_n^{(1)}a_{0n}^{(1)}+in(c_{12}+1)cb_{0n}^{(1)}+\left[c_{11}(N+\alpha_n^{(2)})^2-(n^2+c_{22})\right]a_{Nn}^{(2)}+k^2a_{(N-2)n}^{(2)} \\
&\qquad +in\left[(c_{12}+1)(N+\alpha_n^{(2)})-(c_{22}+1)\right]b_{Nn}^{(2)}=0
\end{aligned} \tag{2.96}$$

$$\begin{aligned}
&2c\alpha_n^{(1)}b_{0n}^{(1)}+in(c_{12}+1)ca_{0n}^{(1)}+\left[(N+\alpha_n^{(2)})^2-(n^2c_{22}+1)\right]b_{Nn}^{(2)}+k^2b_{(N-2)n}^{(2)} \\
&\qquad +\left[in(c_{12}+1)(N+\alpha_n^{(2)})+in(c_{22}+1)\right]a_{Nn}^{(2)}=0
\end{aligned} \tag{2.97}$$

Since $N+\alpha_n^{(2)}=\alpha_n^{(1)}$, the above relations can be written in matrix form

$$\begin{aligned}
&\begin{bmatrix} c_{11}(\alpha_n^{(1)})^2-(n^2+c_{22}) & in\left[(c_{12}+1)\alpha_n^{(1)}-(c_{22}+1)\right] \\ in(c_{12}+1)\alpha_n^{(1)}+in(c_{22}+1) & (\alpha_n^{(1)})^2-(n^2c_{22}+1) \end{bmatrix}\begin{bmatrix} a_{Nn}^{(2)} \\ b_{Nn}^{(2)} \end{bmatrix} \\
&=\begin{bmatrix} -c\left[2c_{11}\alpha_n^{(1)}a_{0n}^{(1)}+in(c_{12}+1)b_{0n}^{(1)}\right]-k^2a_{(N-2)n}^{(2)} \\ -c\left[2\alpha_n^{(1)}b_{0n}^{(1)}+in(c_{12}+1)a_{0n}^{(1)}\right]-k^2b_{(N-2)n}^{(2)} \end{bmatrix}
\end{aligned} \tag{2.98}$$

Since the determinant of the system matrix in Eqn. (2.98) vanishes, $a_{Nn}^{(2)}$ can be an arbitrary value. By setting $a_{Nn}^{(2)} = 1$, c and $b_{Nn}^{(2)}$ can be obtained through the following relation,

$$\begin{bmatrix} 2c_{11}\alpha_n^{(1)}a_{0n}^{(1)} + in(c_{12}+1)b_{0n}^{(1)} & in[(c_{12}+1)\alpha_n^{(1)} - (c_{22}+1)] \\ 2\alpha_n^{(1)}b_{0n}^{(1)} + in(c_{12}+1)a_{0n}^{(1)} & (\alpha_n^{(1)})^2 - (n^2c_{22}+1) \end{bmatrix} \begin{bmatrix} c \\ b_{Nn}^{(2)} \end{bmatrix} = \begin{bmatrix} -[c_{11}(\alpha_n^{(1)})^2 - (n^2+c_{22})]a_{Nn}^{(2)} - k^2a_{(N-2)n}^{(2)} \\ in[(c_{12}+1)\alpha_n^{(1)} + (c_{22}+1)]a_{Nn}^{(2)} - k^2b_{(N-2)n}^{(2)} \end{bmatrix} \tag{2.99}$$

When $N < m < \infty$, $a_{mn}^{(2)}$ and $b_{mn}^{(2)}$ can be obtained through the following recurrence relations

$$\begin{aligned} \left[c_{11}(m+\alpha_n^{(1)})^2 - (n^2+c_{22})\right] a_{(m+N)n}^{(2)} + \\ in\left[(c_{12}+1)(m+\alpha_n^{(1)}) - (c_{22}+1)\right] b_{(m+N)n}^{(2)} &= \\ -c\left[2c_{11}(m+\alpha_n^{(1)})a_{mn}^{(1)} + in(c_{12}+1)b_{mn}^{(1)}\right] - k^2a_{(m+N-2)n}^{(2)} \end{aligned} \tag{2.100}$$

$$\begin{aligned} \left[in(c_{12}+1)(m+\alpha_n^{(1)}) + in(c_{22}+1)\right] a_{(m+N)n}^{(2)} + \\ \left[(m+\alpha_n^{(1)})^2 - (n^2c_{22}+1)\right] b_{(m+N)n}^{(2)} &= \\ -c\left[2(m+\alpha_n^{(1)})b_{mn}^{(1)} + in(c_{12}+1)a_{mn}^{(1)}\right] - k^2b_{(m+N-2)n}^{(2)} \end{aligned} \tag{2.101}$$

The above two Eqns. (2.100) and (2.101) can be written in matrix form as

$$\begin{bmatrix} c_{11}(m+\alpha_n^{(1)})^2 - (n^2+c_{22}) & in\left[(c_{12}+1)(m+\alpha_n^{(1)}) - (c_{22}+1)\right] \\ in(c_{12}+1)(m+\alpha_n^{(1)}) + in(c_{22}+1) & (m+\alpha_n^{(1)})^2 - (n^2c_{22}+1) \end{bmatrix} \begin{bmatrix} a_{(m+N)n}^{(2)} \\ b_{(m+N)n}^{(2)} \end{bmatrix} = \begin{bmatrix} -c\left[2c_{11}(m+\alpha_n^{(1)})a_{mn}^{(1)} + in(c_{12}+1)b_{mn}^{(1)}\right] - k^2a_{(m+N-2)n}^{(2)} \\ -c\left[2(m+\alpha_n^{(1)})b_{mn}^{(1)} + in(c_{12}+1)a_{mn}^{(1)}\right] - k^2b_{(m+N-2)n}^{(2)} \end{bmatrix} \tag{2.102}$$

Table 2.1: *Material properties of the orthotropic medium*

ρ (kg/m^3)	E_r(GPa)	E_θ(GPa)	$G_{r\theta}$(GPa)	$\nu_{r\theta}$	c_{11}	c_{12}	c_{22}
1303.44	1.11114	0.740763	4.85	1.17705	3.0	2.35410	2.0

2.4.4 Verifying the Solutions for Special Case

In this section, three numerical examples are used to verify the solutions for three situations when the indicies differ by an integer: $N = 1$, $N = 2$, and $N > 2$.

For the first example, $n = 1$, the indicies differ by an integer; $N = 1$. The material properties are listed in in Table 2.1. The wave number $k = \omega\sqrt{\rho/C_{44}} = \omega\sqrt{\rho/G_{xy}} = 0.699856$, where $\omega = 1350$. For this case we have $\alpha_n^{(1,2)} = \pm\frac{1}{2}$. Back substitute the numerical solutions of $U_n^{(1)}(r)$, $V_n^{(1)}(r)$, $U_n^{(2)}(r)$, and $V_n^{(2)}(r)$ into the original pair of ODEs in Eqns. (2.54) and (2.55). Then define the numerical values of the left side the Eqns. (2.54) and (2.55) as

$$\begin{aligned}
F_1 &= c_{11}\left(r^2 U_n^{(1)''} + rU_n^{(1)'}\right) + \left(k^2r^2 - 1 - c_{22}\right)U_n^{(1)} + i(c_{12}+1)rV_n^{(1)'} - i(c_{22}+1)V_n^{(1)} \\
F_2 &= r^2V_n^{(1)''} + rV_n^{(1)'} + i(c_{12}+1)rU_n^{(1)'} + (k^2r^2 - c_{22} - 1)V_n^{(1)} + i(c_{22}+1)U_n^{(1)} \\
F_3 &= c_{11}\left(r^2 U_n^{(2)''} + rU_n^{(2)'}\right) + \left(k^2r^2 - 1 - c_{22}\right)U_n^{(2)} + i(c_{12}+1)rV_n^{(2)'} - i(c_{22}+1)V_n^{(2)} \\
F_4 &= r^2V_n^{(2)''} + rV_n^{(2)'} + i(c_{12}+1)rU_n^{(2)'} + (k^2r^2 - c_{22} - 1)V_n^{(2)} + i(c_{22}+1)U_n^{(2)}
\end{aligned} \tag{2.103}$$

Table 2.2 shows that the numerical results of F_1, F_2, F_3, and F_4 are very close to zero under different radii r. The errors are considered as computing errors. Note that in Eqns. (2.50) through (2.53), the solutions are expressed as infinite series. To implement a numerical computation, the infinite series needs to be truncated to a finite number of terms to approximate the exact value. The largest term is denoted as $\mathbb{M}$, which is called the truncation term. In Eqns. (2.50) through (2.53), the values of $a_{mn}^{(1)}r^{m+\alpha_n^{(1)}}$, $a_{mn}^{(2)}r^{m+\alpha_n^{(2)}}$, $b_{mn}^{(1)}r^{m+\alpha_n^{(1)}}$, and $b_{mn}^{(2)}r^{m+\alpha_n^{(2)}}$ get smaller when m gets larger. When $m > \mathbb{M}$, the values are too small to be added to the summation. Thus they can be truncated. Table 2.8 also provides the truncation numbers under different radius. Table 2.2 shows that $U_n^{(1)}(r)$, $V_n^{(1)}(r)$, $U_n^{(2)}(r)$,

Table 2.2: *The numerical results of F_1, F_2, F_3, and F_4 under different radii r*

r	$\mathbb{M}$	F_1	F_2	F_3	F_4
0.2	11	$-8.88178 \times 10^{-16} + 0i$	$0 + 2.22045 \times 10^{-16}i$	$-4.44089 \times 10^{-15} + 0i$	$0 + 8.88178 \times 10^{-16}i$
1.2	20	$0 + 0i$	$0 + 4.44089 \times 10^{-16}i$	$0 + 0i$	$0 - 8.88178 \times 10^{-16}i$
2.1	24	$-4.44089 \times 10^{-15} + 0i$	$0 + 1.77636 \times 10^{-15}i$	$-1.33227 \times 10^{-15} + 0i$	$0 - 8.88178 \times 10^{-16}i$
10.2	44	$2.01617 \times 10^{-13} + 0i$	$0 + 6.91003 \times 10^{-13}i$	$3.88698 \times 10^{-13} + 0i$	$0 - 4.18776 \times 10^{-13}i$

and $V_n^{(2)}(r)$ are solutions of Eqns. (2.54) and (2.55).

To prove that two functions are linearly independent, the Wronskian of two functions can be calculated. If the Wronskian of two functions is non-zero, the two functions are linearly independent. The Wronskians of $U_n^{(1)}(r)$, $U_n^{(2)}(r)$ and $V_n^{(1)}(r)$, $V_n^{(2)}(r)$ are defined as $W_U(r)$ and $W_V(r)$, respectively, which are given as (McQuarrie, 2003)

$$W_U(r) = U_n^{(2)'}(r) \times U_n^{(1)}(r) - U_n^{(1)'}(r) \times U_n^{(2)}(r) \tag{2.104}$$

$$W_V(r) = V_n^{(2)'}(r) \times V_n^{(1)}(r) - V_n^{(1)'}(r) \times V_n^{(2)}(r) \tag{2.105}$$

The numerical solutions of $U_n^{(1)}(r)$, $U_n^{(1)'}(r)$, $V_n^{(1)}(r)$, $V_n^{(1)'}(r)$, $U_n^{(2)}(r)$, $U_n^{(2)'}(r)$, $V_n^{(2)}(r)$, and $V_n^{(2)'}(r)$ can be obtained by using the material properties listed in in Table 2.1. Table 2.3 shows the numerical results of $W_U(r)$ and $W_V(r)$ under different radii r. Since $W_U(r)$ and

Table 2.3: *The numerical results of $W_U(r)$ and $W_V(r)$ under different radii r*

r	0.2	1.2	2.1	10.2
$W_U(r)$	$-4.96931 + 0i$	$-0.665689 + 0i$	$-0.235756 + 0i$	$0.0496441 + 0i$
$W_V(r)$	$3.99496 + 0i$	$0.156908 + 0i$	$-0.362892 + 0i$	$0.0204908 + 0i$

$W_V(r)$ are non-zero, $U_n^{(1)}(r)$, $U_n^{(2)}(r)$ and $V_n^{(1)}(r)$, $V_n^{(2)}(r)$ are linearly independent solutions.

For the second example, $n = 2$, the indicies differ by an integer; $N = 2$. The material properties are listed in Table 2.4. The wave number $k = \omega\sqrt{\rho/C_{44}} = \omega\sqrt{\rho/G_{xy}} = 0.699856$, where $\omega = 1350$. For this case we have $\alpha_n^{(3,4)} = \pm 1$. Back substitute the numerical solutions

Table 2.4: *Material properties of the orthotropic medium*

ρ (kg/m^3)	E_r(GPa)	E_θ(GPa)	$G_{r\theta}$(GPa)	$\nu_{r\theta}$	c_{11}	c_{12}	c_{22}
1303.44	13.2504	8.83363	4.85	0.366	3.0	0.732051	2.0

of $U_n^{(3)}(r)$, $V_n^{(3)}(r)$, $U_n^{(4)}(r)$, and $V_n^{(4)}(r)$ into the original pair of ODEs in Eqns. (2.54) and (2.55). Then define the numerical values of the left side the Eqns. (2.54) and (2.55) as

$$\begin{aligned}
H_1 &= c_{11}\left(r^2 U_n^{(3)''} + rU_n^{(3)'}\right) + \left(k^2r^2 - 1 - c_{22}\right) U_n^{(3)} + i(c_{12}+1)rV_n^{(3)'} - i(c_{22}+1)V_n^{(3)} \\
H_2 &= r^2 V_n^{(3)''} + rV_n^{(3)'} + i(c_{12}+1)rU_n^{(3)'} + (k^2r^2 - c_{22} - 1)V_n^{(3)} + i(c_{22}+1)U_n^{(3)} \\
H_3 &= c_{11}\left(r^2 U_n^{(4)''} + rU_n^{(4)'}\right) + \left(k^2r^2 - 1 - c_{22}\right) U_n^{(4)} + i(c_{12}+1)rV_n^{(4)'} - i(c_{22}+1)V_n^{(4)} \\
H_4 &= r^2 V_n^{(4)''} + rV_n^{(4)'} + i(c_{12}+1)rU_n^{(4)'} + (k^2r^2 - c_{22} - 1)V_n^{(4)} + i(c_{22}+1)U_n^{(4)}
\end{aligned} \tag{2.106}$$

Table 2.5 shows that the numerical results of H_1, H_2, H_3, and H_4 are very close to zero under different radii r. The errors are considered as computing errors. Table 2.5 shows that

Table 2.5: *The numerical results of H_1, H_2, H_3, and H_4 under different radii r*

r	$\mathbb{M}$	H_1	H_2	H_3	H_4
0.2	11	$-2.22045\times10^{-16}+0i$	$0+0i$	$-1.38794\times10^{-10}+0i$	$0-3.42347\times10^{-10}i$
1.2	20	$-2.66454\times10^{-15}+0i$	$0+8.88178\times10^{-16}i$	$-7.39721\times10^{-10}+0i$	$0-2.48433\times10^{-9}i$
2.1	24	$-1.77636\times10^{-15}+0i$	$0+5.32907\times10^{-15}i$	$-2.02540\times10^{-10}+0i$	$0-3.67832\times10^{-9}i$
10.2	44	$9.13047\times10^{-13}+0i$	$0-7.01661\times10^{-13}i$	$9.00742\times10^{-9}+0i$	$0+2.81449\times10^{-9}i$

$U_n^{(3)}(r)$, $V_n^{(3)}(r)$, $U_n^{(4)}(r)$, and $V_n^{(4)}(r)$ are solutions of Eqns. (2.54) and (2.55).

The Wronskians of $U_n^{(3)}(r)$, $U_n^{(4)}(r)$ and $V_n^{(3)}(r)$, $V_n^{(4)}(r)$ are defined as $W_U(r)$ and $W_V(r)$, respectively.

$$W_U(r) = U_n^{(4)'}(r)\times U_n^{(3)}(r) - U_n^{(3)'}(r)\times U_n^{(4)}(r) \tag{2.107}$$

$$W_V(r) = V_n^{(4)'}(r)\times V_n^{(3)}(r) - V_n^{(3)'}(r)\times V_n^{(4)}(r) \tag{2.108}$$

Numerical solutions of $U_n^{(3)}(r)$, $U_n^{(3)'}(r)$, $V_n^{(3)}(r)$, $V_n^{(3)'}(r)$, $U_n^{(4)}(r)$, $U_n^{(4)'}(r)$, $V_n^{(4)}(r)$, and

$V_n^{(4)'}(r)$ can be obtained by using the material properties listed in in Table 2.4. Table 2.6 shows the numerical results of $W_U(r)$ and $W_V(r)$ under different radii r. Since $W_U(r)$ and

Table 2.6: *The numerical results of $W_U(r)$ and $W_V(r)$ under different radii r*

r	0.2	1.2	2.1	10.2
$W_U(r)$	$-10.0004 + 0i$	$-1.66235 + 0i$	$-0.924726 + 0i$	$-0.0686259 + 0i$
$W_V(r)$	$3.77546 + 0i$	$0.739945 + 0i$	$0.441632 + 0i$	$0.197156 + 0i$

$W_V(r)$ do not vanish, $U_n^{(3)}(r)$, $U_n^{(4)}(r)$ and $V_n^{(3)}(r)$, $V_n^{(4)}(r)$ are linearly independent solutions.

For the third example, $n = 1$, the indicies differ by an integer; $N = 4$. The material properties are listed in in Table 2.7. The wave number $k = \omega\sqrt{\rho/C_{44}} = \omega\sqrt{\rho/G_{xy}} = 0.699856$, where $\omega = 1350$. For this case we have $\alpha_n^{(1,2)} = \pm 2$. Back substitute the numerical solutions of $U_n^{(1)}(r)$, $V_n^{(1)}(r)$, $U_n^{(2)}(r)$, and $V_n^{(2)}(r)$ into the original pair of ODEs in Eqns. (2.54) and (2.55). Then define the numerical values of the left side of Eqns. (2.54) and (2.55) as

$$
\begin{aligned}
F_1 &= c_{11}\left(r^2U_n^{(1)''} + rU_n^{(1)'}\right) + \left(k^2r^2 - 1 - c_{22}\right)U_n^{(1)} + i(c_{12}+1)rV_n^{(1)'} - i(c_{22}+1)V_n^{(1)} \\
F_2 &= r^2V_n^{(1)''} + rV_n^{(1)'} + i(c_{12}+1)rU_n^{(1)'} + (k^2r^2 - c_{22} - 1)V_n^{(1)} + i(c_{22}+1)U_n^{(1)} \\
F_3 &= c_{11}\left(r^2U_n^{(2)''} + rU_n^{(2)'}\right) + \left(k^2r^2 - 1 - c_{22}\right)U_n^{(2)} + i(c_{12}+1)rV_n^{(2)'} - i(c_{22}+1)V_n^{(2)} \\
F_4 &= r^2V_n^{(2)''} + rV_n^{(2)'} + i(c_{12}+1)rU_n^{(2)'} + (k^2r^2 - c_{22} - 1)V_n^{(2)} + i(c_{22}+1)U_n^{(2)}
\end{aligned}
\tag{2.109}
$$

Table 2.8 shows that the numerical results of F_1, F_2, F_3, and F_4 are very close to zero under different radii r. The errors are considered as computing errors. Table 2.8 shows that $U_n^{(1)}(r)$, $V_n^{(1)}(r)$, $U_n^{(2)}(r)$, and $V_n^{(2)}(r)$ are solutions of Eqns. (2.54) and (2.55).

The Wronskian of $U_n^{(1)}(r)$, $U_n^{(2)}(r)$ and $V_n^{(1)}(r)$, $V_n^{(2)}(r)$ are defined as $W_U(r)$ and $W_V(r)$,

Table 2.7: *Material properties of the orthotropic medium*

ρ (kg/m^3)	E_r(GPa)	E_θ(GPa)	$G_{r\theta}$(GPa)	$\nu_{r\theta}$	c_{11}	c_{12}	c_{22}
1303.44	13.21	13.21	4.85	0.3618	3.13402	1.13402	3.13402

Table 2.8: *The numerical results of F_1, F_2, F_3, and F_4 under different radii r*

r	$\mathbb{M}$	F_1	F_2	F_3	F_4
0.2	14	$-3.55271 \times 10^{-15} + 0i$	$0 + 6.52256 \times 10^{-15}i$	$-2.27373 \times 10^{-13} + 0i$	$0 + 7.10543 \times 10^{-14}i$
1.2	22	$5.68434 \times 10^{-14} + 0i$	$0 - 8.88178 \times 10^{-16}i$	$1.30740 \times 10^{-12} + 0i$	$0 - 2.57749 \times 10^{-12}i$
2.1	26	$2.27374 \times 10^{-13} + 0i$	$0 + 2.44693 \times 10^{-13}i$	$4.54747 \times 10^{-12} + 0i$	$0 - 6.65423 \times 10^{-12}i$
10.2	48	$-3.51292 \times 10^{-11} + 0i$	$0 + 9.12678 \times 10^{-10}i$	$1.27557 \times 10^{-10} + 0i$	$0 + 1.87515 \times 10^{-9}i$

respectively.

$$W_U(r) = U_n^{(2)'}(r) \times U_n^{(1)}(r) - U_n^{(1)'}(r) \times U_n^{(2)}(r) \tag{2.110}$$

$$W_V(r) = V_n^{(2)'}(r) \times V_n^{(1)}(r) - V_n^{(1)'}(r) \times V_n^{(2)}(r) \tag{2.111}$$

The numerical solutions of $U_n^{(1)}(r)$, $U_n^{(1)'}(r)$, $V_n^{(1)}(r)$, $V_n^{(1)'}(r)$, $U_n^{(2)}(r)$, $U_n^{(2)'}(r)$, $V_n^{(2)}(r)$, and $V_n^{(2)'}(r)$ can be obtained by using the material properties listed in in Table 2.7. Table 2.9 shows the numerical results of $W_U(r)$ and $W_V(r)$ under different radii r. Since $W_U(r)$

Table 2.9: *The numerical results of $W_U(r)$ and $W_V(r)$ under different radii r*

r	0.2	1.2	2.1	10.2
$W_U(r)$	$-20.1116 + 0i$	$-2.59316 + 0i$	$3.48920 + 0i$	$-8.04834 + 0i$
$W_V(r)$	$-1229.01 + 0i$	$-74.6142 + 0i$	$67.9769 + 0i$	$-26.4469 + 0i$

and $W_V(r)$ are non-vanishing, therefore, $U_n^{(1)}(r)$, $U_n^{(2)}(r)$ and $V_n^{(1)}(r)$, $V_n^{(2)}(r)$ are linearly independent solutions.

2.5 Special Case 2: When α is a Repeated Root

In this study, the only situation when α has repeated roots is when $n = 1$. Following Martin and Berger (2001), $\mathscr{D}$ is expected to be positive-definite. Recalling Eqn. (2.30), if α_n has repeated roots, the only possibility is $\alpha_n^2 = 0$. This requires

$$A_1 \pm \sqrt{A_1^2 - 4A_0A_2} = 0 \tag{2.112}$$

Recalling Eqn. (2.29), Eqn. (2.112) can be written as

$$A_0 A_2 = c_{11} c_{22} (n^2 - 1)^2 = 0 \tag{2.113}$$

Since c_{11} and c_{22} cannot vanish, $n^2 = 1$. Only $n \geq 0$ is considered in this study, so only $n = 1$ will be discussed.

2.5.1 Solutions When α is a Repeated Root

At $n = 1$, Eqns. (2.19) and (2.20) can be written as

$$\begin{aligned} c_{11}\left(r^2 U_1'' + r U_1'\right) + \left(k^2 r^2 - 1 - c_{22}\right) U_1 + i(c_{12}+1) r V_1' - i(c_{22}+1) V_1 &= 0 \quad (2.114) \\ r^2 V_1'' + r V_1' + i(c_{12}+1) r U_1' + (k^2 r^2 - c_{22} - 1) V_1 + i(c_{22}+1) U_1 &= 0 \quad (2.115) \end{aligned}$$

where $k^2 = \rho\omega^2 / C_{44}$. Recalling Eqns. (2.29) and (2.30)

$$\alpha_1^2 = \frac{A_1 \pm \sqrt{A_1^2 - 4A_0 A_2}}{2A_0} \tag{2.116}$$

where

$$A_0 = c_{11}, \quad A_1 = c_{11} + c_{22} + n^2(c_{11}c_{22} - c_{12}^2 - 2c_{12}), \quad A_2 = c_{22}(n^2 - 1)^2 \tag{2.117}$$

When $n = 1$, Eqn. (2.117) gives

$$A_0 = c_{11}, \quad A_1 = c_{11} + c_{22} + c_{11}c_{22} - c_{12}^2 - 2c_{12}, \quad A_2 = c_{22}(1-1)^2 = 0 \tag{2.118}$$

Eqn. (2.118) shows that $A_2 = 0$, therefore Eqn. (2.116) can be written as

$$\alpha_1^2 = \frac{A_1 \pm \sqrt{A_1^2}}{2A_0} \tag{2.119}$$

which gives the roots of α

$$\alpha_1^{(1,2)} = \pm\sqrt{\frac{A_1}{A_0}}, \quad \alpha_1^{(3,4)} = 0 \tag{2.120}$$

Recalling Eqn. (2.33), A_1 can be expressed as

$$A_1 = c_{11} + c_{22} + c_{11}c_{22} - c_{12}^2 - 2c_{12} \geq c_{11} + c_{22} - 2c_{12} + 4(1 + c_{12}) > 0 \tag{2.121}$$

So $\alpha_1^{(1,2)} \neq 0$ and α_1 only has repeated roots: $\alpha_1^{(3)} = \alpha_1^{(4)} = 0$. Thus, the solutions corresponding to $\alpha_1^{(3,4)}$ will be solved. The first solution corresponding to root $\alpha_1^{(3)}$ is written as

$$U_1^{(3)}(r) = \sum_{m=0}^{\infty} a_{m1}^{(3)} r^{m+\alpha_1^{(3)}} = \sum_{m=0}^{\infty} a_{m1}^{(3)} r^m \tag{2.122}$$

According to Campbell and Haberman (1996) and Farlow (2006), the second solution corresponding to $\alpha_1^{(4)}$ can be written in the form

$$U_1^{(4)}(r) = U_1^{(3)} \ln r + \sum_{m=0}^{\infty} a_{m1}^{(4)} r^{m+\alpha_1^{(3)}} \tag{2.123}$$

Similarly we have

$$V_1^{(3)}(r) = \sum_{m=0}^{\infty} b_{m1}^{(3)} r^{m+\alpha_1^{(3)}} = \sum_{m=0}^{\infty} b_{m1}^{(3)} r^m \tag{2.124}$$

and

$$V_1^{(4)}(r) = V_1^{(3)} \ln r + \sum_{m=0}^{\infty} b_{m1}^{(4)} r^{m+\alpha_1^{(3)}} \tag{2.125}$$

where $a_{m1}^{(4)}$ and $b_{m1}^{(4)}$ are coefficients to be determined. Substituting the assumed solutions (2.122) through (2.125) into the pair of ODEs (2.114) and (2.115) gives

$$\begin{aligned}\sum_{m=0}^{\infty} 2c_{11} m a_{m1}^{(3)} r^m + \sum_{m=0}^{\infty} i(c_{12}+1) b_{m1}^{(3)} r^m + \sum_{m=0}^{\infty} [c_{11}m^2 - (1+c_{22})] a_{m1}^{(4)} r^m & \\ + \sum_{m=0}^{\infty} k^2 a_{m1}^{(4)} r^{m+2} + \sum_{m=0}^{\infty} i[m(c_{12}+1) - (c_{22}+1)] b_{m1}^{(4)} r^m &= 0 \quad (2.126)\\ \sum_{m=0}^{\infty} 2m b_{m1}^{(3)} r^m + i(c_{12}+1)\sum_{m=0}^{\infty} a_{m1}^{(3)} r^m + \sum_{m=0}^{\infty} [m^2 - (c_{22}+1)] b_{m1}^{(4)} r^m & \\ + \sum_{m=0}^{\infty} k^2 b_{m1}^{(4)} r^{m+2} + \sum_{m=0}^{\infty} i[m(c_{12}+1) + (c_{22}+1)] a_{m1}^{(4)} r^m &= 0 \quad (2.127)\end{aligned}$$

Dividing by the common factor r^m and setting $r = 0$, the only non-vanishing terms are those with $m = 0$. This gives the following set of indicial equations

$$i(c_{12}+1) b_{01}^{(3)} - (1+c_{22}) a_{01}^{(4)} - i(c_{22}+1) b_{01}^{(4)} = 0 \quad (2.128)$$

$$i(c_{12}+1) a_{01}^{(3)} + i(c_{22}+1) a_{01}^{(4)} - (c_{22}+1) b_{01}^{(4)} = 0 \quad (2.129)$$

Recalling Eqn. (2.43) with $n = 1$

$$b_{01}^{(3)} = -\frac{i[(c_{12}+1)\alpha_1^{(3)} + (c_{22}+1)] a_{01}^{(3)}}{(\alpha_1^{(3)})^2 - (2c_{22}+1)} = i a_{01}^{(3)} \quad (2.130)$$

Substituting Eqn. (2.130) into (2.128) gives

$$-(c_{12}+1) a_{01}^{(3)} - (1+c_{22}) a_{01}^{(4)} - i(c_{22}+1) b_{01}^{(4)} = 0 \quad (2.131)$$

It can be found that Eqns. (2.131) and (2.129) are identical. Setting $a_{01}^{(4)} = 1$ gives

$$b_{01}^{(4)} = i\frac{(c_{12}+1) a_{01}^{(3)} + (c_{22}+1)}{(1+c_{22})} \quad (2.132)$$

Table 2.10: *Material properties of the orthotropic medium*

ρ (kg/m^3)	E_r(GPa)	E_θ(GPa)	$G_{r\theta}$(GPa)	$\nu_{r\theta}$	c_{11}	c_{12}	c_{22}
1303.44	11.32	5.81	0.66	0.705	23.0303	8.3333	11.8182

By requiring that the coefficients of r^m vanish in Eqns. (2.126) and (2.127), we can obtain the following recurrence relations

$$\begin{aligned}\left[2c_{11}ma_{m1}^{(3)} + i(c_{12}+1)b_{m1}^{(3)}\right] + [c_{11}m^2 - (1+c_{22})]a_{m1}^{(4)} + k^2a_{(m-2)1}^{(4)}& \\ +i[m(c_{12}+1)-(c_{22}+1)]b_{m1}^{(4)} &= 0 \qquad (2.133)\\ \left[2mb_{m1}^{(3)} + i(c_{12}+1)a_{m1}^{(3)}\right] + i[m(c_{12}+1)+(c_{22}+1)]a_{m1}^{(4)}& \\ +[m^2-(c_{22}+1)]b_{m1}^{(4)} + k^2b_{(m-2)1}^{(4)} &= 0 \qquad (2.134)\end{aligned}$$

Written in matrix form

$$\begin{bmatrix} c_{11}m^2-(1+c_{22}) & i[m(c_{12}+1)-(c_{22}+1)] \\ i[m(c_{12}+1)+(c_{22}+1)] & m^2-(c_{22}+1) \end{bmatrix} \begin{bmatrix} a_{m1}^{(4)} \\ b_{m1}^{(4)} \end{bmatrix} = \begin{bmatrix} -k^2a_{(m-2)1}^{(4)} - \left[2c_{11}ma_{m1}^{(3)} + i(c_{12}+1)b_{m1}^{(3)}\right] \\ -k^2b_{(m-2)1}^{(4)} - \left[2mb_{m1}^{(3)} + i(c_{12}+1)a_{m1}^{(3)}\right] \end{bmatrix} \qquad (2.135)$$

According to Eqn. (2.135), even numbered real coefficients $a_{m1}^{(4)}$ and $b_{m1}^{(4)}$ can be obtained with the defined initial values of $a_{01}^{(4)}$ and $b_{01}^{(4)}$. Odd numbered coefficients are set to zero.

2.5.2 Verifying the Solutions When α is a Repeat Root

An numerical method is applied to verify the solutions obtained above. The orthotropic material properties applied for this verification are listed in Table 2.10. The wave number $k = \omega\sqrt{\rho/C_{44}} = \omega\sqrt{\rho/G_{xy}} = 1.89717$, where $\omega = 1350$. Under this case $\alpha_1^{(3,4)} = 0$. Substitute the numerical values of $U_1^{(3)}(r)$, $U_1^{(4)}(r)$, $V_1^{(3)}(r)$, and $V_1^{(4)}(r)$ into Eqns. (2.114) and (2.115), and define the numerical values of the left sides of the two equations as

$$
\begin{aligned}
G_1 &= c_{11}\left(r^2 U_1^{(3)''} + rU_1^{(3)'}\right) + \left(k^2r^2 - 1 - c_{22}\right)U_1^{(3)} + i(c_{12}+1)rV_1^{(3)'} - i(c_{22}+1)V_1^{(3)} \\
G_2 &= r^2V_1^{(3)''} + rV_n^{(3)'} + i(c_{12}+1)rU_1^{(3)'} + (k^2r^2 - c_{22} - 1)V_1^{(3)} + i(c_{22}+1)U_1^{(3)} \\
G_3 &= c_{11}\left(r^2 U_1^{(4)''} + rU_1^{(4)'}\right) + \left(k^2r^2 - 1 - c_{22}\right)U_1^{(4)} + i(c_{12}+1)rV_1^{(4)'} - i(c_{22}+1)V_1^{(4)} \\
G_4 &= r^2V_1^{(4)''} + rV_1^{(4)'} + i(c_{12}+1)rU_1^{(4)'} + (k^2r^2 - c_{22} - 1)V_1^{(4)} + i(c_{22}+1)U_1^{(4)}
\end{aligned}
\tag{2.136}
$$

Table 2.11 shows numerical results of G_1, G_2, G_3, and G_4 under different radii r and values of $\mathbb{M}$. The values of G_1, G_2, G_3, and G_4 in Table 2.11 under different radii r are all close

Table 2.11: *The numerical results of G_1, G_2, G_3, and G_4 under different radii r*

r	$\mathbb{M}$	G_1	G_2	G_3	G_4
0.2	15	$1.77636 \times 10^{-15} + 0i$	$0 - 1.77636 \times 10^{-15}i$	$-1.04361 \times 10^{-14} + 0i$	$0 + 8.88178 \times 10^{-16}i$
1.2	35	$-5.32907 \times 10^{-15} + 0i$	$0 + 1.77636 \times 10^{-15}i$	$7.10543 \times 10^{-15} + 0i$	$0 - 3.55271 \times 10^{-15}i$
2.1	33	$6.21725 \times 10^{-15} + 0i$	$0 - 1.95399 \times 10^{-14}i$	$3.90799 \times 10^{-14} + 0i$	$0 - 1.42109 \times 10^{-14}i$
10.2	80	$5.29076 \times 10^{-7} + 0i$	$0 - 1.43608 \times 10^{-6}i$	$1.12914 \times 10^{-6} + 0i$	$0 - 4.79253 \times 10^{-6}i$

to zero. Thus, $U_1^{(3)}(r)$, $U_1^{(4)}(r)$, $V_1^{(3)}(r)$, and $V_1^{(4)}(r)$ are proved to be the solutions for Eqns. (2.114) and (2.115).

The Wronskian $W_U(r)$ of $U_1^{(3)}(r)$ and $U_1^{(4)}(r)$ is given as $W_U(r) = U_1^{(4)'}(r) \times U_1^{(3)}(r) - U_1^{(3)'}(r) \times U_1^{(4)}(r)$. The Wronskian $W_V(r)$ of $V_1^{(3)}(r)$ and $V_1^{(4)}(r)$ is given as $W_V(r) = V_1^{(4)'}(r) \times V_1^{(3)}(r) - V_1^{(3)'}(r) \times V_1^{(4)}(r)$. Table 2.12 shows the numerical results of $W_U(r)$ and $W_V(r)$ under different radii r. Since $W_U(r)$ and $W_V(r)$ are non-zero, $U_n^{(3)}(r)$, $U_n^{(4)}(r)$ and $V_n^{(3)}(r)$,

Table 2.12: *The numerical results of $W_U(r)$ and $W_V(r)$ under different radii r*

r	0.2	1.2	2.1	10.2
$W_U(r)$	$5.04251 + 0i$	$0.965482 + 0i$	$-0.476737 + 0i$	$0.0558213 + 0i$
$W_V(r)$	$-5.38539 + 0i$	$-2.20883 + 0i$	$-1.26622 + 0i$	$-0.536510 + 0i$

$V_n^{(4)}(r)$ are linearly independent solutions.

2.6 Special Case 3: Mode $n = 0$

When $n = 0$, Eqns. (2.19) and (2.20) can be written as

$$c_{11}\left(r^2U_0'' + rU_0'\right) + \left(k^2r^2 - c_{22}\right)U_0 = 0 \tag{2.137}$$

$$r^2V_0'' + rV_0' + (k^2r^2 - 1)V_0 = 0 \tag{2.138}$$

For this special case, the two equations are decoupled. So the two equations can be solved individually with the Frobenius method.

2.6.1 Solution for U_0

Assume that $U_0(r)$ has a solution in the following Frobenius series form,

$$U_0(r) = \sum_{m=0}^{\infty} a_{m0}r^{m+\alpha_0} \tag{2.139}$$

substituting Eqn. (2.139) into Eqn. (2.137) gives

$$\sum_{m=0}^{\infty}\left\{c_{11}(m+\alpha_0)^2 + (k^2r^2 - c_{22})\right\}a_{m0}r^{m+\alpha_0} = 0 \tag{2.140}$$

Dividing by the common factor r^{α_0}, then setting $r = 0$, the only non-vanishing terms are those with $m = 0$, giving the following indicial equation

$$\left(c_{11}\alpha_0^2 - c_{22}\right)a_{00} = 0 \tag{2.141}$$

Then α_0's can be obtained as

$$\alpha_0^{(1,2)} = \pm\sqrt{c_{22}/c_{11}} \tag{2.142}$$

Eqn. (2.140) needs to be satisfied for all powers of r. When $m = 1$, it becomes

$$[c_{11}(1+\alpha_0)^2 - c_{22}]a_{10} = 0 \tag{2.143}$$

If $c_{11}(1+\alpha_0)^2 - c_{22} \neq 0$, a_{10} has to equal to zero. If $c_{11}(1+\alpha_0)^2 - c_{22} = 0$, a_{10} can be an arbitrary value. Therefore, let $a_{10} = 0$. For the m-th power, where m goes from 2 to ∞, the equation becomes

$$\left[c_{11}(m+\alpha_0)^2 - c_{22}\right] a_{m0} + k^2 a_{(m-2)0} \;\; = \;\; 0 \tag{2.144}$$

According to Eqn. (2.142), $\alpha_0^{(1)}$ and $\alpha_0^{(2)}$ may or may not differ by an integer. Both cases need to be considered.

1. When $\alpha_0^{(1)}$ and $\alpha_0^{(2)}$ do not differ by an integer

If $\alpha_0^{(1)}$ and $\alpha_0^{(2)}$ do not differ by an integer, through Eqn. (2.144), the even numbered real coefficients a_{m0} can be obtained by arbitrarily selecting real values of a_{00}. Let $a_{00} = 1$. The odd numbered coefficients are set to zero. Then, the resulting special functions for displacement U_0 can be written as, for $\sigma = 1$ and, 2,

$$U_0^{(\sigma)}(r) = \sum_{m=0}^{\infty} a_{m0}^{(\sigma)} r^{m+\alpha_0^{(\sigma)}}, \tag{2.145}$$

Thus, the general solution of displacement u_r can be given as

$$u_r = \sum_{n=0}^{\infty} \left[\mathsf{a}_n U_0^{(1)}(r) + \mathsf{b}_n U_0^{(2)}(r)\right] e^{in\theta} e^{i\omega t} \tag{2.146}$$

2. When $\alpha_0^{(1)}$ and $\alpha_0^{(2)}$ differ by an integer

If $\alpha_0^{(1)}$ and $\alpha_0^{(2)}$ differ by an integer, which is denoted as $N = \alpha_0^{(1)} - \alpha_0^{(2)} = 2\sqrt{c_{22}/c_{11}}$, the first solution is assumed as

$$U_0^{(1)} = \sum_{m=0}^{\infty} a_{m0}^{(1)} r^{m+\alpha_0^{(1)}} \tag{2.147}$$

where $a_{m0}^{(1)}$ can be obtained through the recurrence relation (2.144) by setting $a_{00}^{(1)} = 1$. The second solution is assumed as the following

$$U_0^{(2)} = cU_0^{(1)} \ln r + \sum_{m=0}^{\infty} a_{m0}^{(2)} r^{m+\alpha_0^{(2)}} \tag{2.148}$$

where c is constant and $a_{m0}^{(2)}$ are coefficients. Substituting the solution (2.148) into the ODE (2.137), gives

$$\sum_{m=0}^{\infty} 2cc_{11}(m+\alpha_0^{(1)})a_{m0}^{(1)} r^{m+N} + \sum_{m=0}^{\infty} \left[c_{11}(m+\alpha_0^{(2)})^2 - c_{22}\right] a_{m0}^{(2)} r^m + \sum_{m=0}^{\infty} k^2 a_{m0}^{(2)} r^{m+2} = 0 \tag{2.149}$$

By setting $r = 0$, the only non-vanishing terms are those with $m = 0$. This yields the following equation

$$\left[c_{11}(\alpha_0^{(2)})^2 - c_{22}\right] a_{00}^{(2)} = 0 \tag{2.150}$$

Recalling Eqn. (2.141), gives $c_{11}\left(\alpha_0^{(2)}\right)^2 - c_{22} = 0$. So in Eqn. (2.150), $a_{00}^{(2)}$ can be chosen as an arbitrary value. Now let $a_{00}^{(2)} = 1$. Since the terms for 0-th power of r equal zero, Eqn. (2.149) can be written as

$$\begin{aligned}\sum_{m=0}^{\infty} 2cc_{11}(m+\alpha_0^{(1)})a_{m0}^{(1)} r^{m+N} + \sum_{m=0}^{\infty} \left[c_{11}(m+1+\alpha_0^{(2)})^2 - c_{22}\right] a_{(m+1)0}^{(2)} r^{m+1} \\ + \sum_{m=0}^{\infty} k^2 a_{m0}^{(2)} r^{m+2} = 0\end{aligned} \tag{2.151}$$

Three situations need to be considered: 1) when $N = 1$, 2) when $N = 2$, and 3) when $N > 2$. Since the solution process is similar to the special case when $n > 0$, some details will be skipped.

- When $N = 1$, $c = 0$, and the coefficients $a_{m0}^{(2)}$ can be obtained through the following recurrence relation

$$\left[c_{11}(m+\alpha_0^{(2)})^2 - c_{22}\right] a_{m0}^{(2)} + k^2 a_{(m-2)0}^{(2)} = 0 \tag{2.152}$$

where m goes from 2 to ∞. Then, the resulting special functions for displacement U_0 can be written as

$$U_0^{(1)}(r) = \sum_{m=0}^{\infty} a_{m0}^{(1)} r^{m+\alpha_0^{(1)}}, \quad U_0^{(2)}(r) = \sum_{m=0}^{\infty} a_{m0}^{(2)} r^{m+\alpha_0^{(2)}} \tag{2.153}$$

Eqn. (2.153) shows that the second solution can also be written in Frobenius series form. The general solution of displacement u_r can be written as

$$u_r = \sum_{n=0}^{\infty} \left[\mathfrak{a}_n U_0^{(1)}(r) + \mathfrak{b}_n U_0^{(2)}(r)\right] e^{in\theta} e^{i\omega t} \tag{2.154}$$

- When $N = 2$, the constant c and coefficient $a_{20}^{(2)}$ have the following relation:

$$2cc_{11}\alpha_0^{(1)} a_{00}^{(1)} + \left[c_{11}\left(\alpha_0^{(1)}\right)^2 - c_{22}\right] a_{20}^{(2)} + k^2 a_{00}^{(2)} = 0 \tag{2.155}$$

Since we have

$$c_{11}\left(2+\alpha_0^{(2)}\right)^2 - c_{22} = c_{11}\left(\alpha_0^{(1)}\right)^2 - c_{22} = 0 \tag{2.156}$$

$a_{20}^{(2)}$ in Eqn. (2.155) can be chosen as any value. Now let $a_{20}^{(2)} = 1$. Constant c can be obtained through Eqn. (2.155),

$$c = -\frac{k^2 a_{00}^{(2)}}{2c_{11}\alpha_0^{(1)} a_{00}^{(1)}} \tag{2.157}$$

The coefficient $a_{m0}^{(2)}$ can be obtained through the following relation

$$2c_{11}c\left(m-2+\alpha_0^{(1)}\right) a_{(m-2)0}^{(1)} + \left[c_{11}\left(m-2+\alpha_0^{(1)}\right)^2 - c_{22}\right] a_{m0}^{(2)} + k^2 a_{(m-2)0}^{(2)} = 0 \tag{2.158}$$

where m goes from 2 to ∞. Since the constant c and coefficients $a_{m0}^{(2)}$ were obtained in Eqns. (2.157) and (2.158), the second solution $U_0^{(2)}$ is solved.

- When $N > 2$, for $0 \leqslant m < N-2$, $a_{00}^{(2)}$ through $a_{(N-2)0}^{(2)}$ can be obtained through the following equation:

$$\left[c_{11}\left(m+2+\alpha_0^{(2)}\right)^2 - c_{22}\right] a_{(m+2)0}^{(2)} + k^2 a_{m0}^{(2)} = 0 \tag{2.159}$$

The above equation Eqn. (2.159) can also be written as

$$\left[c_{11}\left(m+\alpha_0^{(2)}\right)^2 - c_{22}\right] a_{m0}^{(2)} + k^2 a_{(m-2)0}^{(2)} = 0 \tag{2.160}$$

where $2 \leqslant m < N$. When $m = N$, the constant c and coefficient $a_{N0}^{(2)}$ have the following relation

$$2cc_{11}\alpha_0^{(1)} a_{00}^{(1)} + \left[c_{11}\left(\alpha_0^{(1)}\right)^2 - c_{22}\right] a_{N0}^{(2)} + k^2 a_{(N-2)0}^{(2)} = 0 \tag{2.161}$$

Since $c_{11}\left(\alpha_0^{(1)}\right)^2 - c_{22} = 0$, $a_{N0}^{(2)}$ can be an arbitrary value. Setting $a_{N0}^{(2)} = 1$, constant c can be obtained by the following relation

$$c = -\frac{k^2 a_{(N-2)0}^{(2)}}{2c_{11}\alpha_0^{(1)} a_{00}^{(1)}} \tag{2.162}$$

Finally, the problem can be solved through the following recurrence relation

$$2cc_{11}(m+\alpha_0^{(1)})a_{m0}^{(1)} + \left[c_{11}\left(m+\alpha_0^{(1)}\right)^2 - c_{22}\right] a_{(m+N)0}^{(2)} + k^2 a_{(m+N-2)0}^{(2)} = 0 \tag{2.163}$$

where $2 \leqslant m < \infty$.

2.6.2 Verifying Solution for U_0

In this section, three numerical examples are used to verify the solutions of $U_0^{(1)}(r)$ and $U_0^{(2)}(r)$. The solutions for three situations when the indicies differ by an integer ($N = 1$,

Table 2.13: *Material properties of the orthotropic medium*

ρ (kg/m^3)	E_r(GPa)	E_θ(GPa)	$G_{r\theta}$(GPa)	$\nu_{r\theta}$	c_{11}	c_{12}	c_{22}
1303.44	59.994	14.9985	0.66	0.2303	92.1212	5.30303	23.0303

$N = 2$, and $N > 2$) are all verified.

For the first example, the indicies differ by an integer $N = 1$. The orthotropic material properties considered in this example are listed in Table 2.13. The circular frequency ω is 1350. The wave number k can be obtained through the following equation,

$$k = \omega\sqrt{\rho/C_{44}} = \omega\sqrt{\rho/G_{xy}} = 1.89717 \tag{2.164}$$

For this example, the indicies $\alpha_0^{(1)} = \sqrt{c_{22}/c_{11}} = \frac{1}{2}$ and $\alpha_0^{(2)} = -\sqrt{c_{22}/c_{11}} = -\frac{1}{2}$. The numerical solutions $U_0^{(1)}(r)$ and $U_0^{(2)}(r)$ can be obtained by substituting the properties of the orthotropic medium into Eqn. (2.153). Note that in Eqn. (2.153), the solutions are expressed as infinite series. To implement a numerical computation, the infinite series needs to be truncated to a finite number of terms to approximate the exact value. The largest term is denoted as $\mathbb{M}$, which is called the truncation term. In Eqn. (2.153), the value of $a_{m0}r^{m+\alpha_0}$ gets smaller when m gets larger. When $m > \mathbb{M}$, the values of $a_{m0}r^{m+\alpha_0}$ are too small to be added to the summation. Thus they can be truncated.

Now the numerical solutions $U_0^{(1)}(r)$ and $U_0^{(2)}(r)$ are back-substituted into Eqn. (2.137). Define the numerical values of the left side of Eqn. (2.137) as

$$E_1 = c_{11}\left(r^2 U_0^{(1)''} + rU_0^{(1)'}\right) + \left(k^2r^2 - c_{22}\right)U_0^{(1)} \tag{2.165}$$

$$E_2 = c_{11}\left(r^2 U_0^{(2)''} + rU_0^{(2)'}\right) + \left(k^2r^2 - c_{22}\right)U_0^{(2)} \tag{2.166}$$

Theoretically, the left side of of Eqn. (2.137) should vanish. For numerical computation, E_1 and E_2 can get close to zero but are not exactly due to computing error. Table 2.14 provides the values of E_1, E_2, and the truncation numbers $\mathbb{M}$ under different radii r. Table

Table 2.14: *The numerical results of E_1, E_2 under different radii r*

r	$\mathbb{M}$	E_1	E_2
0.2	9	$0 + 0i$	$2.84217 \times 10^{-14} + 0i$
1.2	13	$-3.55271 \times 10^{-15} + 0i$	$-8.88178 \times 10^{-15} + 0i$
2.1	15	$-2.4869 \times 10^{-14} + 0i$	$-7.10543 \times 10^{-15} + 0i$
10.2	25	$-1.13687 \times 10^{-13} + 0i$	$-2.13163 \times 10^{-14} + 0i$

2.14 shows that E_1 and E_2 are very close to or equal to zero. The errors are small which are considered as computing errors. Thus, it is verified that both $U_0^{(1)}(r)$ and $U_0^{(2)}(r)$ are solutions for Eqn. (2.137). The Wronskian $W_U(r)$ of $U_0^{(1)}(r)$ and $U_0^{(2)}(r)$ is given as $W_U(r) = U_0^{(2)'}(r) \times U_0^{(1)}(r) - U_0^{(1)'}(r) \times U_0^{(2)}(r)$. Table 2.15 shows the numerical results of $W_U(r)$ and $W_V(r)$ under different radii r. Since $W_U(r)$ does not vanish, $U_0^{(1)}(r)$ and $U_0^{(2)}(r)$ are linearly

Table 2.15: *The numerical results of $W_U(r)$ under different radii r*

r	0.2	1.2	2.1	10.2
$W_U(r)$	$-5.00000 + 0i$	$-0.833333 + 0i$	$-0.476190 + 0i$	$-0.0980392 + 0i$

independent solutions.

For the second example, the indicies differ by an integer; $N = 2$. The orthotropic material properties applied for this example are listed in Table 2.16. The wave number $k = \omega\sqrt{\rho/C_{44}} = \omega\sqrt{\rho/G_{xy}} = 1.89717$, where $\omega = 1350$. For this case, we have $\alpha_0^{(1,2)} = \pm 1$. The numerical solutions $U_0^{(1)}(r)$ and $U_0^{(2)}(r)$ are back-substituted into Eqn. (2.137). The numerical values of the left side of Eqn. (2.137), E_1 and E_2, are defined in Eqns. (2.165) and (2.166). Table 2.17 shows numerical values of E_1 and E_2 under different radii r. Table 2.17 shows that E_1 and E_2 are very close or equal to zero. The small errors are considered as computing errors. Thus, it is verified that both $U_0^{(1)}(r)$ and $U_0^{(2)}(r)$ are solutions for Eqn. (2.137). Table 2.18 shows the numerical results of $W_U(r)$ under different radii r. Since $W_U(r)$ is not vanishing, therefore, $U_0^{(1)}(r)$ and $U_0^{(2)}(r)$ are linearly independent solutions.

Table 2.16: *Material properties of the orthotropic medium*

ρ (kg/m^3)	E_r(GPa)	E_θ(GPa)	$G_{r\theta}$(GPa)	$\nu_{r\theta}$	c_{11}	c_{12}	c_{22}
1303.44	13.20987	13.20987	0.66	0.3618	23.0303	8.33333	23.0303

Table 2.17: *The numerical results of E_1 and E_2 under different radii r*

r	$\mathbb{M}$	E_1	E_2
0.2	11	$0 + 0i$	$0 + 0i$
1.2	18	$3.55271 \times 10^{-15} + 0i$	$0 + 0i$
10.2	35	$-1.25056 \times 10^{-12} + 0i$	$-1.10845 \times 10^{-12} + 0i$

Table 2.18: *The numerical results of $W_U(r)$ under different radii r*

r	0.2	1.2	10.2
$W_U(r)$	$-10.0000 + 0i$	$-1.66667 + 0i$	$-0.196078 + 0i$

For the third example, the indicies differ by an integer; $N = 4$. The orthotropic material properties applied for this example are listed in Table 2.19. For this example, we have $\alpha_0^{(1,2)} = \pm 2$. The circular frequency ω is the same as in the last two examples. The numerical values of $U_0^{(1)}(r)$ and $U_0^{(2)}(r)$ are back substituted into Eqn. (2.137). The values on the left side of Eqn. (2.137), E_1 and E_2, are defined in Eqns. (2.165) and (2.166). Table 2.20 shows numerical results of E_1, E_2, and truncation numbers $\mathbb{M}$ under different radii r. The results of E_1 and E_2 shown in Table 2.20 are very close to zero. The errors are considered as computing errors.

Table 2.21 shows the numerical results of $W_U(r)$ under different radii r. Since $W_U(r)$ does not vanish, $U_0^{(1)}(r)$ and $U_0^{(2)}(r)$ are linearly independent solutions.

2.6.3 Solution for V_0

The general solutions for the second ODE (2.138) will be solved in this section. Assume that $V_0(r)$ has a solution in the following Frobenius series form

$$V_0(r) = \sum_{m=0}^{\infty} b_{m0} r^{m+\alpha_0} \tag{2.167}$$

Table 2.19: *Material properties of the orthotropic medium*

ρ (kg/m^3)	E_r(GPa)	E_θ(GPa)	$G_{r\theta}$(GPa)	$\nu_{r\theta}$	c_{11}	c_{12}	c_{22}
1303.44	14.702467	58.80987	0.66	0.0905	23.0303	8.3333	92.1212

Table 2.20: *The numerical results of E_1 and E_2 under different radii r*

r	$\mathbb{M}$	E_1	E_2
0.2	11	$-4.44089 \times 10^{-16} + 0i$	$1.33241 \times 10^{-10} + 0i$
1.2	20	$0 + 0i$	$4.57078 \times 10^{-9} + 0i$
10.2	35	$-1.81899 \times 10^{-11} + 0i$	$-8.72069 \times 10^{-8} + 0i$

Table 2.21: *The numerical results of $W_U(r)$ under different radii r*

r	0.2	1.2	10.2
$W_U(r)$	$-20.0000 + 0i$	$-3.33333 + 0i$	$-0.392159 + 0i$

Substituting Eqn. (2.167) into Eqn. (2.138), gives

$$\sum_{m=0}^{\infty} \left\{(m+\alpha_0)^2 + (k^2r^2 - 1)\right\} b_{m0} r^{m+\alpha_0} = 0 \tag{2.168}$$

After dividing by the common factor r^{α_0}, and then setting $r = 0$, the only non-vanishing terms are those with $m = 0$. This gives the following indicial equation

$$\left(\alpha_0^2 - 1\right) b_{00} = 0 \tag{2.169}$$

Then α's can be obtained as

$$\alpha_0^{(3,4)} = \pm 1 \tag{2.170}$$

Eqn. (2.168) need to be satisfied for all different powers of r. For the m-th power, it becomes

$$\left[(m+\alpha_0)^2 - 1\right] b_{m0} + k^2 b_{(m-2)0} = 0 \tag{2.171}$$

where m goes from 2 to ∞. According to Eqn. (2.170), α_0 has two roots that differ by integer; $N = \alpha_0^{(3)} - \alpha_0^{(4)} = 2$. When $\alpha_0^{(3)} = 1$, the first solution can be given as

$$V_0^{(3)} = \sum_{m=0}^{\infty} b_{m0}^{(3)} r^{m+\alpha_0^{(3)}} = \sum_{m=0}^{\infty} b_{m0}^{(3)} r^{m+1} \tag{2.172}$$

Coefficients $b_{m0}^{(3)}$ can be obtained through Eqn. (2.171). The even numbered real coefficients $b_{m0}^{(3)}$ can be obtained by setting $b_{00}^{(3)} = 1$; the odd numbered coefficients are set to zero. When $\alpha_0^{(3)} = -1$, the second solution can be given as

$$V_0^{(4)} = cV_0^{(3)} \ln r + \sum_{m=0}^{\infty} b_{m0}^{(4)} r^{m+\alpha_0^{(4)}} = cV_0^{(3)} \ln r + \sum_{m=0}^{\infty} b_{m0}^{(4)} r^{m-1} \tag{2.173}$$

where c is a constant, and $b_{m0}^{(4)}$ are the coefficients that need to be determined. The solving procedure is the same as when solving the first ODE. So most details of the solving process will be skipped.

By substituting Eqn. (2.173) into Eqn. (2.138), the recurrence relation is given as

$$2c(m+1)b_{m0}^{(3)} + k^2 b_{m0}^{(4)} + \left[(m+1)^2 - 1\right] b_{(m+2)0}^{(4)} = 0 \tag{2.174}$$

where m goes from 0 to ∞. When $m = 0$, the above Eqn. (2.174) can be written as

$$2c(0+1)b_{00}^{(3)} + k^2 b_{00}^{(4)} + \left[(0+1)^2 - 1\right]\, b_{(0+2)0}^{(4)} = 2c(0+1)b_{00}^{(3)} + k^2 b_{00}^{(4)} + 0b_{20}^{(4)} = 0 \tag{2.175}$$

which gives

$$c = -\frac{k^2 b_{00}^{(4)}}{2b_{00}^{(3)}} = -\frac{k^2}{2b_{00}^{(3)}} \tag{2.176}$$

Here $b_{00}^{(4)} = 1$. Eqn. (2.175) also shows that $b_{20}^{(4)}$ can be chosen as an arbitrary value. Let $b_{20}^{(4)} = 1$. Then for $m \geq 2$, $b_{m0}^{(4)}$ can be obtained through the relation

$$\left[(m+1)^2 - 1\right] b_{(m+2)0}^{(4)} = -\left[2c(m+1)b_{m0}^{(3)} + k^2 b_{m0}^{(4)}\right] \tag{2.177}$$

The odd numbered coefficients are set to zero. Thus, the general solution for Eqn. (2.138), can be given as

$$v_r = \sum_{n=0}^{\infty} \left[\mathsf{c}_n V_0^{(3)}(r) + \mathsf{d}_n V_0^{(4)}(r)\right] e^{in\theta} e^{i\omega t} \tag{2.178}$$

2.6.4 Verifying Solution for V_0

The solutions are verified by back substituting $V_0^{(3)}(r)$ and $V_0^{(4)}(r)$ into the second ODE (2.138) using numerical methods. The orthotropic material properties applied for this example are listed in Table 2.13. Under this case, we have $\alpha_0^{(3,4)} = \pm 1$. The wave number k and frequency ω are the same with those in the last example. The numerical results of the left side of Eqn. (2.138) are defined as

$$E_3 = r^2 V_0^{(3)''} + r V_0^{(3)'} + \left(k^2 r^2 - 1\right) V_0^{(3)} \tag{2.179}$$

$$E_4 = r^2 V_0^{(4)''} + r V_0^{(4)'} + \left(k^2 r^2 - 1\right) V_0^{(4)} \tag{2.180}$$

The results of E_3 and E_4 shown in Table 2.22 verified the solutions $V_0^{(3)}(r)$ and $V_0^{(4)}(r)$. The numerical values of E_3 and E_4 are both close to zero under different radius r. The errors are very small which is considered as computing errors. Table 2.22 also shows the truncation numbers $\mathbb{M}$ that are taken under different radii r.

Table 2.22: *Numerical results of E_3 and E_4 under different radii r*

r	$\mathbb{M}$	E_3	E_4
0.2	15	$2.77556 \times 10^{-17} + 0i$	$0 + 0i$
1.2	29	$-8.88178 \times 10^{-16} + 0i$	$8.88178 \times 10^{-16} + 0i$
2.1	34	$-3.9968 \times 10^{-15} + 0i$	$3.55271 \times 10^{-15} + 0i$
10.2	79	$-1.14778 \times 10^{-7} + 0i$	$1.18119 \times 10^{-6} + 0i$

The Wronskian $W_V(r)$ of $V_0^{(3)}(r)$ and $V_0^{(4)}(r)$ is given as $W_V(r) = V_0^{(4)'}(r) \times V_0^{(3)}(r) - V_0^{(3)'}(r) \times V_0^{(4)}(r)$. Table 2.23 shows the numerical results of $W_V(r)$ under different radii r. Since $W_V(r)$ is not vanishing, $V_0^{(3)}(r)$ and $V_0^{(4)}(r)$ are linearly independent solutions. Figure

Table 2.23: *The numerical results of $W_V(r)$ under different radii r*

r	0.2	1.2	2.1	10.2
$W_V(r)$	$-10.0000 + 0i$	$-1.66667 + 0i$	$-0.952381 + 0i$	$-0.196078 + 0i$

2.1 and 2.2 show the numerical values of $V_0^{(3)}(r)$ and $V_0^{(4)}(r)$ at $\alpha_0^{(3,4)} = \pm 1$, respectively.

The second ODE (2.138) is actually a Bessel's differential equation. So the solutions of

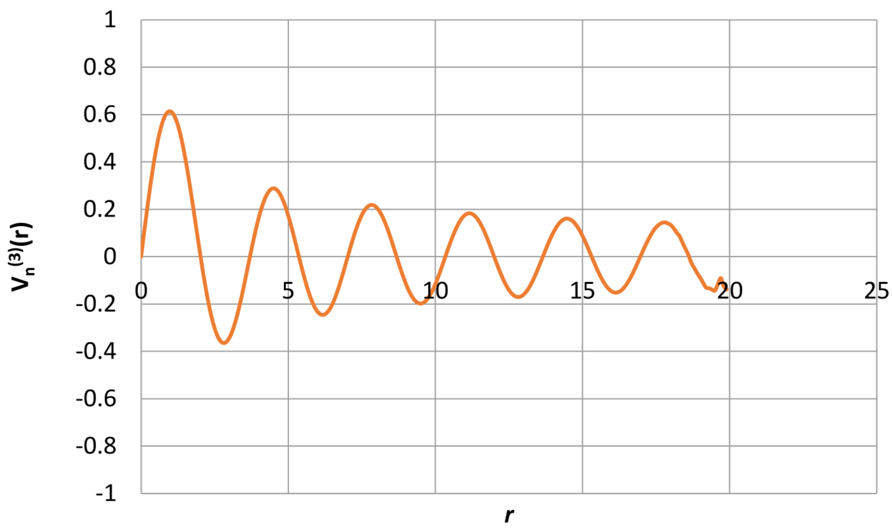

Figure 2.1: *Solutions of* $V_n^{(3)}(r)$ *at* $n = 0$ *with* $\alpha_0^{(3)} = 1$

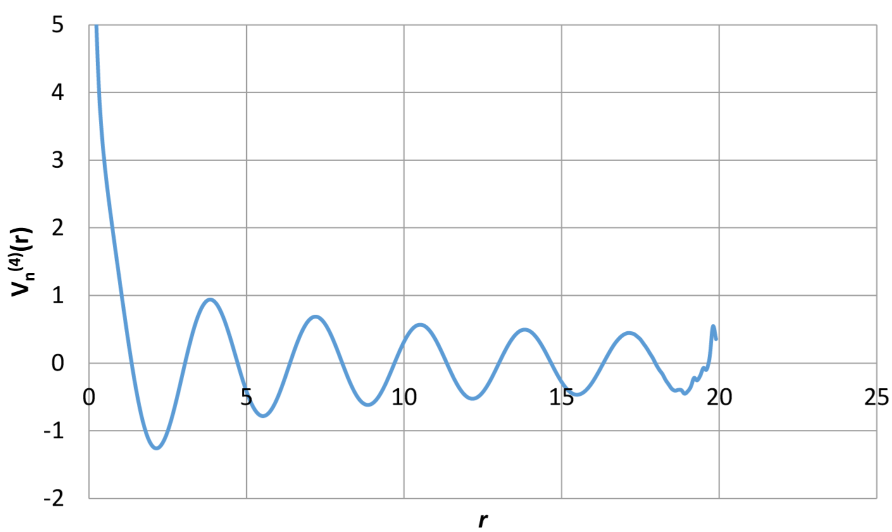

Figure 2.2: *Solutions of* $V_n^{(4)}(r)$ *at* $n = 0$ *with* $\alpha_0^{(4)} = -1$

Eqn. (2.138) are Bessel functions. Figure 2.1 and 2.2 show that the solutions of $V_0^{(3)}(r)$ and $V_0^{(4)}(r)$ are Bessel functions of the first and second kind, respectively. From 2.2 we can find that when radius r gets close to 20, the curve has some oscillation. This is because when r increases, the errors also increase, as shown in Table 2.22.

Chapter 3

Acoustic Wave Scattering by Cylindrical Scatterer Comprising Isotropic Acoustic and Orthotropic Elastic Layers

3.1 Introduction

In this chapter the general solutions for elastic waves in cylindrically orthotropic elastic media, which were obtained in Chapter 2, are used for defining a set of two canonical problems. Then, based on the canonical problems, acoustic scattering by a “general” multilayer cylindrical scatterer is solved. The word “general” means that the number of layers is arbitrary and the medium of each layer can be either orthotropic elastic or isotropic acoustic.

3.2 Basis Equations and Field Expressions

3.2.1 Acoustic Field

Following the standard methods of theoretical acoustics, the basic equations for linear acoustics include (Pierce, 1991)

$$\mathbf{v} = -\bigtriangledown \phi, \qquad p = -i\omega\rho\phi \tag{3.1}$$

where ρ is density, p is acoustic pressure, $\mathbf{v}$ is the fluid particle velocity vector, and ϕ is the amplitude of acoustic pressure. Noting that in the steady state, all waves in the field have a same temporal factor $e^{i\omega t}$. In polar coordinates, $\phi = \phi(r, \theta)$. The amplitude of acoustic pressure can be obtained by solving the Helmholtz equation,

$$\bigtriangledown^2 \phi + k^2\phi = 0 \tag{3.2}$$

where $k = \omega/c$ is the wavenumber, c is the sound speed. The general solutions to the Helmholtz equation are called cylindrical wave functions $J_n(kr)e^{in\theta}$ and $Y_n(kr)e^{in\theta}$ (Pao and Mow, 1971). $J_n(kr)$ and $Y_n(kr)$ are the Bessel functions of the first and the second kinds, respectively. Since the Bessel function of the first kind is non-singular throughout the plane, $J_n(kr)e^{in\theta}$ can be used in any problem domain. The Bessel function of the second kind is singular at the origin, therefore $Y_n(kr)e^{in\theta}$ is only suitable for describing waves in regions which do not include the origin. Hankel functions which are combinations of Bessel functions are alternatively used for describing waves. Waves represented by $H_n^{(1)}(r,\theta)e^{in\theta}$ and $H_n^{(2)}(r,\theta)e^{in\theta}$ are called incoming waves and outgoing waves, respectively. $H_n^{(1)}(r,\theta)e^{in\theta}$ and $H_n^{(2)}(r,\theta)e^{in\theta}$ are Hankel functions of the first and second kinds, respectively.

A general expression for a wave can be written as the inner product of wave expansion basis with the wave expansion coefficient matrices. The wave expansion basis includes: the regular wave expansion basis $\{\boldsymbol{J}(k,\boldsymbol{r})\}$ and the singular wave expansion basis $\{\boldsymbol{H}(k,\boldsymbol{r})\}$, which are column matrices. Their entries at the n-th row can be expressed as

$$J(r,\theta)_n = J_n(kr)e^{in\theta}, \qquad H(r,\theta)_n = H_n^{(1)}(kr)e^{in\theta} \tag{3.3}$$

where n runs from $-\infty$ to ∞.

For all the cases to be discussed, which are acoustic scattering by multilayer scatterers having isotropic acoustic and orhotropic elastic solid layers, the incident wave is assumed to be regular throughout the entire plane. Incident wave is an incoming wave that impinges onto a scatterer. The expansion of the incident plane wave propagating in the fluid medium has the form

$$\phi^{inc} = \sum_{n=-\infty}^{\infty} A_n J_n(kr)e^{in\theta} = \{\boldsymbol{A}\}^T\{\boldsymbol{J}(k,\boldsymbol{r})\} \tag{3.4}$$

where $\{\boldsymbol{A}\}$ is the incident wave expansion coefficient column matrix whose row index runs from $-\infty$ to ∞. When the incident wave impinges onto the scatterer, a scattered wave will be generated. The scattered wave is an outgoing wave, so the expansion of the scattered plane wave propagating in the fluid medium has the form

$$\phi^{scr} = \sum_{n=-\infty}^{\infty} B_n H_n^{(1)}(kr)e^{in\theta} = \{\boldsymbol{B}\}^T\{\boldsymbol{H}(k,\boldsymbol{r})\} \tag{3.5}$$

where $\{\boldsymbol{B}\}$ is the scattered wave expansion coefficient column matrix whose row index runs from $-\infty$ to ∞.

3.2.2 Orthotropic Medium

The general expression for the wave in the orthotropic medium in cylindrical coordinates was obtained in the last chapter, which is

$$u_r = \sum_{n=-\infty}^{\infty} \left[\mathsf{a}_n U_n^{(1)}(r) + \mathsf{b}_n U_n^{(2)}(r) + \mathsf{c}_n U_n^{(3)}(r) + \mathsf{d}_n U_n^{(4)}(r)\right] e^{in\theta} \quad (3.6)$$

$$u_\theta = \sum_{n=-\infty}^{\infty} \left[\mathsf{a}_n V_n^{(1)}(r) + \mathsf{b}_n V_n^{(2)}(r) + \mathsf{c}_n V_n^{(3)}(r) + \mathsf{d}_n V_n^{(4)}(r)\right] e^{in\theta} \quad (3.7)$$

where a_n, b_n, c_n and d_n are constants to be determined by the physical problems. Using the obtained general solutions in Eqns. (3.6) and (3.7), the displacement and stress in medium q can be obtained through a unified expression as

$$\begin{aligned} \aleph_{iq}(\boldsymbol{r}) &= \sum_{n=-\infty}^{\infty} \left[\mathsf{a}_{nq}\mathfrak{X}_{iq}^1(n,r) + \mathsf{b}_{nq}\mathfrak{X}_{iq}^2(n,r) + \mathsf{c}_{nq}\mathfrak{X}_{iq}^3(n,r) + \mathsf{d}_{nq}\mathfrak{X}_{iq}^4(n,r)\right] e^{in\theta} && (3.8) \\ &= \{\boldsymbol{a}\}_q^T\{\boldsymbol{\mathfrak{X}}_{iq}^1(\boldsymbol{r})\} + \{\boldsymbol{b}\}_q^T\{\boldsymbol{\mathfrak{X}}_{iq}^2(\boldsymbol{r})\} + \{\boldsymbol{c}\}_q^T\{\boldsymbol{\mathfrak{X}}_{iq}^3(\boldsymbol{r})\} + \{\boldsymbol{d}\}_q^T\{\boldsymbol{\mathfrak{X}}_{iq}^4(\boldsymbol{r})\} && (3.9) \end{aligned}$$

where $\{\boldsymbol{a}\}$, $\{\boldsymbol{b}\}$, $\{\boldsymbol{c}\}$ and $\{\boldsymbol{d}\}$ are the constants column matrices whose row index runs from $-\infty$ to ∞, $\aleph_i$ is a displacement, strain or stress component defined in the following order

$$\{\boldsymbol{\aleph}\} = \left\{\varepsilon_{rr}, r\varepsilon_{\theta\theta}, \sigma_{zz}, \sigma_{rr}, \sigma_{\theta\theta}, \frac{r}{C_{44}}\sigma_{r\theta} \text{ or } 2r\varepsilon_{r\theta}, u_r, u_\theta\right\} \quad (3.10)$$

and $\mathfrak{X}_{iq}^\sigma(n,r)$ $(\sigma = 1,2,3,4)$ is a series of functions defined in this study. $\{\boldsymbol{\aleph}\}$ is a vector. In this series of functions, i denotes the component, and q denotes the medium in which the

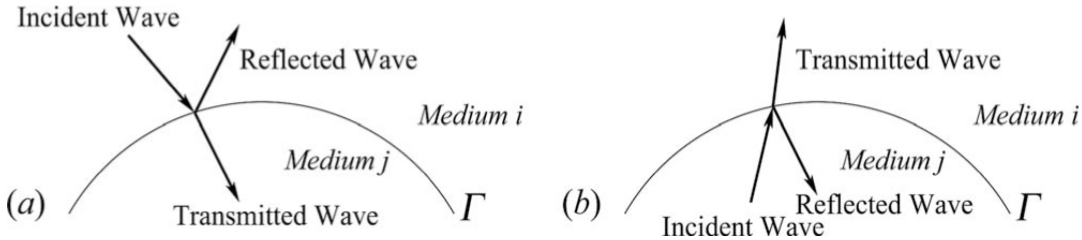

Figure 3.1: *Canonical problems defined by Cai (2004): (a) first canonical problem; (b) second canonical problem*

expressions are to be evaluated. The definitions are given as:

$$\mathfrak{X}^{\sigma}_{1q}(n,r) = [U^{(\sigma)}_{nq}(r)]' \tag{3.11}$$

$$\mathfrak{X}^{\sigma}_{2q}(n,r) = U^{(\sigma)}_{nq}(r) + inV^{(\sigma)}_{nq}(r) \tag{3.12}$$

$$\mathfrak{X}^{\sigma}_{3q}(n,r) = C_{13}[U^{(\sigma)}_{nq}(r)]' + C_{23}U^{(\sigma)}_{nq}(r)/r + inC_{23}V^{(\sigma)}_{nq}(r)/r \tag{3.13}$$

$$\mathfrak{X}^{\sigma}_{4q}(n,r) = C_{11}[U^{(\sigma)}_{nq}(r)]' + C_{12}U^{(\sigma)}_{nq}(r)/r + inC_{12}V^{(\sigma)}_{nq}(r)/r \tag{3.14}$$

$$\mathfrak{X}^{\sigma}_{5q}(n,r) = C_{12}[U^{(\sigma)}_{nq}(r)]' + C_{22}U^{(\sigma)}_{nq}(r)/r + inC_{22}V^{(\sigma)}_{nq}(r)/r \tag{3.15}$$

$$\mathfrak{X}^{\sigma}_{6q}(n,r) = inU^{(\sigma)}_{nq}(r) + r[V^{(\sigma)}_{nq}(r)]' - V^{(\sigma)}_{nq}(r) \tag{3.16}$$

$$\mathfrak{X}^{\sigma}_{7q}(n,r) = U^{(\sigma)}_{nq}(r) \tag{3.17}$$

$$\mathfrak{X}^{\sigma}_{8q}(n,r) = V^{(\sigma)}_{nq}(r) \tag{3.18}$$

3.3 Canonical Problems

The fundamental elements for solving acoustic scattering by multilayer scatterers having a mixture of isotropic fluid and orthotropic elastic layers are two sets of two canonical problems.

The first set of two canonical problems were defined by Cai (2004). They include two acoustic media i and j, which are separated by a closed interface Γ as shown in Fig. 3.1. In the first canonical problem, the incident wave encounters the interface Γ from medium i which generates the reflected wave in medium i and the transmitted wave in medium j. In

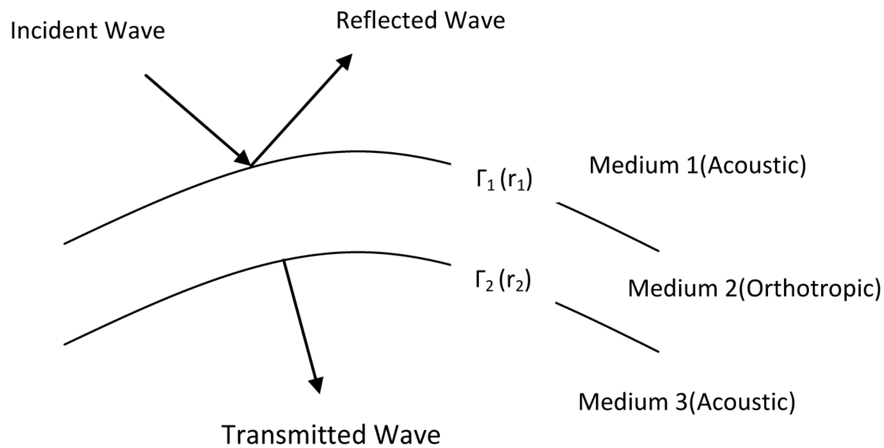

Figure 3.2: *First Canonical Problem*

the second canonical problem, the incident wave encounters the interface Γ from medium j, which generates the reflected wave in medium j and the transmitted wave in medium i.

The second set of two canonical problems were defined in this study. In this study, each canonical problem involves three media that are separated by two closed interfaces. The layer in the middle is orthotropic and it is denoted as medium 2. The outermost and innermost media are acoustic, which are denoted as media 1 and 3, respectively. The closed interface between media 1 and 2 is denoted as Γ_1 and the closed interface between media 2 and 3 is denoted as Γ_2. The first canonical problem is the inward problem in which the incident wave impinges onto Γ_1 from medium 1 as shown in Fig. 3.2. The second canonical problem is the outward problem, in which the incident wave impinges onto the interface Γ_2 from medium 3 as shown in Fig. 3.3. The details of the two canonical problems are discussed in the following sections.

3.3.1 First Canonical Problem

The first canonical problem is the inward problem. A refected wave in acoustic medium 1, a transmitted wave in acoustic medium 3, and waves in orthotropic medium 2 are generated.

In this problem, the incident wave in medium 1 and the transmitted wave in medium 3

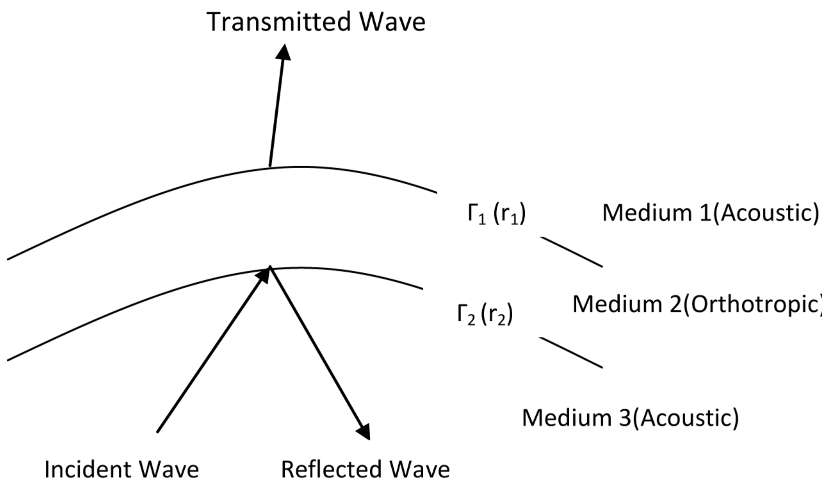

Figure 3.3: *Second Canonical Problem*

are incoming waves, and the scattered waves in medium 1 is an outgoing wave. Therefore, they are expressible as

$$p^{inc} = \sum_{n=-\infty}^{\infty} A_n J_n(k_1 r) e^{in\theta} = \{\boldsymbol{A}\}^T \{\boldsymbol{J}(k_1, \boldsymbol{r})\} \tag{3.19}$$

$$p^{scr} = \sum_{n=-\infty}^{\infty} B_n H_n^{(1)}(k_1 r) e^{in\theta} = \{\boldsymbol{B}\}^T \{\boldsymbol{H}(k_1, \boldsymbol{r})\} \tag{3.20}$$

$$p^{trm} = \sum_{n=-\infty}^{\infty} C_n J_n(k_3 r) e^{in\theta} = \{\boldsymbol{C}\}^T \{\boldsymbol{J}(k_3, \boldsymbol{r})\} \tag{3.21}$$

where p is the acoustic pressure, k_1 and k_3 are wave numbers in media 1 and 3, r is the radius, and $\{\boldsymbol{A}\}$, $\{\boldsymbol{B}\}$ and $\{\boldsymbol{C}\}$ are the wave expansion coefficient column matrices for the respective waves whose row index runs from $-\infty$ to ∞. Column matrices $\{\boldsymbol{J}(k_j, \boldsymbol{r})\}$ and $\{\boldsymbol{H}(k_j, \boldsymbol{r})\}$ are the regular and singular wave expansion bases in medium j, respectively.

According to Eqns. (3.8) and (3.9), the displacements u_r and u_θ in medium 2 are given as

$$u_r = \sum_{n=-\infty}^{\infty} \left[\mathsf{a}_{n2} \mathfrak{X}_{72}^1(n,r) + \mathsf{b}_{n2} \mathfrak{X}_{72}^2(n,r) + \mathsf{c}_{n2} \mathfrak{X}_{72}^3(n,r) + \mathsf{d}_{n2} \mathfrak{X}_{72}^4(n,r) \right] e^{in\theta} \quad (3.22)$$

$$= \{\boldsymbol{a}\}_2^T \{\boldsymbol{\mathfrak{X}}_{72}^1(\boldsymbol{r})\} + \{\boldsymbol{b}\}_2^T \{\boldsymbol{\mathfrak{X}}_{72}^2(\boldsymbol{r})\} + \{\boldsymbol{c}\}_2^T \{\boldsymbol{\mathfrak{X}}_{72}^3(\boldsymbol{r})\} + \{\boldsymbol{d}\}_2^T \{\boldsymbol{\mathfrak{X}}_{72}^4(\boldsymbol{r})\} \quad (3.23)$$

$$u_\theta = \sum_{n=-\infty}^{\infty} \left[\mathsf{a}_{n2} \mathfrak{X}_{82}^1(n,r) + \mathsf{b}_{n2} \mathfrak{X}_{82}^2(n,r) + \mathsf{c}_{n2} \mathfrak{X}_{82}^3(n,r) + \mathsf{d}_{n2} \mathfrak{X}_{82}^4(n,r) \right] e^{in\theta} \quad (3.24)$$

$$= \{\boldsymbol{a}\}_2^T \{\boldsymbol{\mathfrak{X}}_{82}^1(\boldsymbol{r})\} + \{\boldsymbol{b}\}_2^T \{\boldsymbol{\mathfrak{X}}_{82}^2(\boldsymbol{r})\} + \{\boldsymbol{c}\}_2^T \{\boldsymbol{\mathfrak{X}}_{82}^3(\boldsymbol{r})\} + \{\boldsymbol{d}\}_2^T \{\boldsymbol{\mathfrak{X}}_{82}^4(\boldsymbol{r})\} \quad (3.25)$$

where $\{\boldsymbol{a}\}$, $\{\boldsymbol{b}\}$, $\{\boldsymbol{c}\}$, and $\{\boldsymbol{d}\}$ are the constants column matrices whose row index runs from $-\infty$ to ∞.

In media 1 and 3, wave expansion coefficient matrices of the reflected and transmitted waves can be related to those of the incident wave as

$$\{\boldsymbol{B}\} = [\boldsymbol{R}_{123}]\{\boldsymbol{A}\} \qquad \{\boldsymbol{C}\} = [\boldsymbol{T}_{123}]\{\boldsymbol{A}\} \quad (3.26)$$

where the subscripts "123" denote the first canonical problem in which the incident wave is in medium 1 and travels toward media 2 and 3.

In medium 2, the constants column matrices can also be related to those of the incident wave as

$$\{\boldsymbol{a}\}_2 = [\boldsymbol{\mathfrak{A}}_{123}]\{\boldsymbol{A}\} \quad (3.27)$$

$$\{\boldsymbol{b}\}_2 = [\boldsymbol{\mathfrak{B}}_{123}]\{\boldsymbol{A}\} \quad (3.28)$$

$$\{\boldsymbol{c}\}_2 = [\boldsymbol{\mathfrak{C}}_{123}]\{\boldsymbol{A}\} \quad (3.29)$$

$$\{\boldsymbol{d}\}_2 = [\boldsymbol{\mathfrak{D}}_{123}]\{\boldsymbol{A}\} \quad (3.30)$$

where $[\boldsymbol{R}_{123}]$, $[\boldsymbol{T}_{123}]$, $[\boldsymbol{\mathfrak{A}}_{123}]$, $[\boldsymbol{\mathfrak{B}}_{123}]$, $[\boldsymbol{\mathfrak{C}}_{123}]$, and $[\boldsymbol{\mathfrak{D}}_{123}]$ are characteristic matrices.

The characteristic matrices can be obtained by considering the boundary conditions at the interfaces Γ_1 and Γ_2. These boundary conditions include: the continuity of normal fluid and solid velocities, the continuity of radial normal stress on the orthotropic side, which is the negative of the acoustic pressure on the acoustic side, and the vanishing of the tangential stress at $r = r_1$, and $r = r_2$ (since inviscid acoustic media can not support tangential stress). Mathematically, the boundary conditions are written as

$$(-i\omega)u_r|_{r=r_1} = v_r|_{r=r_1} \tag{3.31}$$

$$(-i\omega)u_r|_{r=r_2} = v_r|_{r=r_2} \tag{3.32}$$

$$\sigma_{rr}|_{r=r_1} = -p|_{r=r_1} \tag{3.33}$$

$$\sigma_{rr}|_{r=r_2} = -p|_{r=r_2} \tag{3.34}$$

$$\sigma_{r\theta}|_{r=r_1} = 0 \tag{3.35}$$

$$\sigma_{r\theta}|_{r=r_2} = 0 \tag{3.36}$$

The parameters on the left hand side are for the orthotropic solid case and the parameters on the right hand side are for the isotropic fluid case. According to Eqn. (3.1), the fluid particle velocity vector $\mathbf{v}$ can also be written as

$$\mathbf{v} = \frac{1}{i\omega\rho} \bigtriangledown p \tag{3.37}$$

where ω is circular frequency. According to Eqn. (3.37), the expression for the normal fluid velocity can be expressed as

$$v_r = -\frac{i}{\omega\rho}\frac{\partial p}{\partial r} \tag{3.38}$$

The total acoustic pressure at $r = r_1$ is written as

$$p = \left(p^{inc} + p^{scr}\right)\Big|_{r=r_1} = \sum_{n=-\infty}^{\infty} \left[A_n J_n(k_1 r_1) + B_n H_n(k_1 r_1)\right] e^{in\theta} \tag{3.39}$$

The boundary conditions (3.31) through (3.36) require,

$$\begin{aligned}
\mathsf{a}_{n2}\mathfrak{X}^1_{72}(n,r_1)+\mathsf{b}_{n2}\mathfrak{X}^2_{72}(n,r_1)+\mathsf{c}_{n2}\mathfrak{X}^3_{72}(n,r_1)+\mathsf{d}_{n2}\mathfrak{X}^4_{72}(n,r_1) &= \\
\frac{k_1}{\omega^2\rho_1}[A_nJ'_n(k_1r_1)+B_nH'_n(k_1r_1)] & \qquad (3.40)\\
\mathsf{a}_{n2}\mathfrak{X}^1_{72}(n,r_2)+\mathsf{b}_{n2}\mathfrak{X}^2_{72}(n,r_2)+\mathsf{c}_{n2}\mathfrak{X}^3_{72}(n,r_2)+\mathsf{d}_{n2}\mathfrak{X}^4_{72}(n,r_2) &= \\
\frac{k_3}{\omega^2\rho_3}C_nJ'_n(k_3r_2) & \qquad (3.41)\\
\mathsf{a}_{n2}\mathfrak{X}^1_{42}(n,r_1)+\mathsf{b}_{n2}\mathfrak{X}^2_{42}(n,r_1)+\mathsf{c}_{n2}\mathfrak{X}^3_{42}(n,r_1)+\mathsf{d}_{n2}\mathfrak{X}^4_{42}(n,r_1) &= \\
-[A_nJ_n(k_1r_1)+B_nH_n(k_1r_1)] & \qquad (3.42)\\
\mathsf{a}_{n2}\mathfrak{X}^1_{42}(n,r_2)+\mathsf{b}_{n2}\mathfrak{X}^2_{42}(n,r_2)+\mathsf{c}_{n2}\mathfrak{X}^3_{42}(n,r_2)+\mathsf{d}_{n2}\mathfrak{X}^4_{42}(n,r_2) &= -C_nJ_n(k_3r_2) \qquad (3.43)\\
\mathsf{a}_{n2}\mathfrak{X}^1_{62}(n,r_1)+\mathsf{b}_{n2}\mathfrak{X}^2_{62}(n,r_1)+\mathsf{c}_{n2}\mathfrak{X}^3_{62}(n,r_1)+\mathsf{d}_{n2}\mathfrak{X}^4_{62}(n,r_1) &= 0 \qquad (3.44)\\
\mathsf{a}_{n2}\mathfrak{X}^1_{62}(n,r_2)+\mathsf{b}_{n2}\mathfrak{X}^2_{62}(n,r_2)+\mathsf{d}_{n2}\mathfrak{X}^3_{62}(n,r_2)+\mathsf{d}_{n2}\mathfrak{X}^4_{62}(n,r_2) &= 0 \qquad (3.45)
\end{aligned}$$

Denote

$$[\mathfrak{m}_1]=\begin{bmatrix}
\mathfrak{X}^1_{72}(n,r_1) & \mathfrak{X}^2_{72}(n,r_1) & \mathfrak{X}^3_{72}(n,r_1) & \mathfrak{X}^4_{72}(n,r_1) & -\frac{k_1}{\omega^2\rho_1}H'_n(k_1r_1) & 0\\
\mathfrak{X}^1_{72}(n,r_2) & \mathfrak{X}^2_{72}(n,r_2) & \mathfrak{X}^3_{72}(n,r_2) & \mathfrak{X}^4_{72}(n,r_2) & 0 & -\frac{k_3}{\omega^2\rho_3}J'_n(k_3r_2)\\
\mathfrak{X}^1_{42}(n,r_1) & \mathfrak{X}^2_{42}(n,r_1) & \mathfrak{X}^3_{42}(n,r_1) & \mathfrak{X}^4_{42}(n,r_1) & H_n(k_1r_1) & 0\\
\mathfrak{X}^1_{42}(n,r_2) & \mathfrak{X}^2_{42}(n,r_2) & \mathfrak{X}^3_{42}(n,r_2) & \mathfrak{X}^4_{42}(n,r_2) & 0 & J_n(k_3r_2)\\
\mathfrak{X}^1_{62}(n,r_1) & \mathfrak{X}^2_{62}(n,r_1) & \mathfrak{X}^3_{62}(n,r_1) & \mathfrak{X}^4_{62}(n,r_1) & 0 & 0\\
\mathfrak{X}^1_{62}(n,r_2) & \mathfrak{X}^2_{62}(n,r_2) & \mathfrak{X}^3_{62}(n,r_2) & \mathfrak{X}^4_{62}(n,r_2) & 0 & 0
\end{bmatrix} \qquad (3.46)$$

Eqns. (3.40) through (3.45) can be solved as

$$\left\{\begin{matrix}[\boldsymbol{\mathfrak{A}}_{123}]_n\\ [\boldsymbol{\mathfrak{B}}_{123}]_n\\ [\boldsymbol{\mathfrak{C}}_{123}]_n\\ [\boldsymbol{\mathfrak{D}}_{123}]_n\\ [\boldsymbol{R}_{123}]_n\\ [\boldsymbol{T}_{123}]_n\end{matrix}\right\}=[\mathfrak{m}_1]^{-1}\left\{\begin{matrix}\frac{k_1}{\omega^2\rho_1}J'_n(k_1r_1)\\ 0\\ -J_n(k_1r_1)\\ 0\\ 0\\ 0\end{matrix}\right\} \qquad (3.47)$$

Through the above Eqn. (3.47), the characteristic matrices can be obtained. In addition, through the relations (3.26) to (3.30), the wave expansion coefficient column matrices for the respective waves in the acoustic medium and the constants column matrices for the orthotropic medium can be obtained.

3.3.2 Second Canonical Problem

The second canonical problem is the outward problem, in which the incident wave impinges onto the interface from medium 3.

The incident wave in medium 3 and transmitted wave in medium 1 are outgoing waves and the scattered waves in medium 3 is the incoming wave. Therefore they are expressible as

$$p^{inc} = \{\boldsymbol{A}\}^T\{\boldsymbol{H}(k_3,\boldsymbol{r})\} \tag{3.48}$$

$$p^{scr} = \{\boldsymbol{B}\}^T\{\boldsymbol{J}(k_3,\boldsymbol{r})\} \tag{3.49}$$

$$p^{scr} = \{\boldsymbol{C}\}^T\{\boldsymbol{H}(k_1,\boldsymbol{r})\} \tag{3.50}$$

In medium 2, the expressions for displacements are listed in Eqns. (3.22) through (3.25). The characteristic matrices are defined as

$$\{\boldsymbol{B}\} = [\boldsymbol{R}_{321}]\{\boldsymbol{A}\} \tag{3.51}$$

$$\{\boldsymbol{C}\} = [\boldsymbol{T}_{321}]\{\boldsymbol{A}\} \tag{3.52}$$

$$\{\boldsymbol{a}\}_2 = [\mathfrak{A}_{321}]\{\boldsymbol{A}\} \tag{3.53}$$

$$\{\boldsymbol{b}\}_2 = [\mathfrak{B}_{321}]\{\boldsymbol{A}\} \tag{3.54}$$

$$\{\boldsymbol{c}\}_2 = [\mathfrak{C}_{321}]\{\boldsymbol{A}\} \tag{3.55}$$

$$\{\boldsymbol{d}\}_2 = [\mathfrak{D}_{321}]\{\boldsymbol{A}\} \tag{3.56}$$

The boundary conditions at each interface include: the continuity of normal fluid and solid velocities, the continuity of the radial normal stress in the orthotropic side, which is the negative of the acoustic pressure in the acoustic side, and the vanishing of the tangential stress $r = r_1$, and $r = r_2$.

$$
\begin{aligned}
(-i\omega)u_r|_{r=r_2} &= v_r|_{r=r_2} && (3.57)\\
(-i\omega)u_r|_{r=r_1} &= v_r|_{r=r_1} && (3.58)\\
\sigma_{rr}|_{r=r_2} &= -p|_{r=r_2} && (3.59)\\
\sigma_{rr}|_{r=r_1} &= -p|_{r=r_1} && (3.60)\\
\sigma_{r\theta}|_{r=r_1} &= 0 && (3.61)\\
\sigma_{r\theta}|_{r=r_2} &= 0 && (3.62)
\end{aligned}
$$

Here the parameters on the left hand side are for the orthotropic solid case, and the parameters on the right hand side are for the isotropic fluid case. Eqns. (3.57) through (3.62) are expressible as

$$
\begin{aligned}
\mathsf{a}_{n2}\mathfrak{X}^1_{72}(n,r_2) + \mathsf{b}_{n2}\mathfrak{X}^2_{72}(n,r_2) + \mathsf{c}_{n2}\mathfrak{X}^3_{72}(n,r_2) + \mathsf{d}_{n2}\mathfrak{X}^4_{72}(n,r_2) &= \\
\frac{k_3}{\omega^2\rho_3}[A_n H_n'(k_3 r_2) + B_n J_n'(k_3 r_2)] & && (3.63)\\
\mathsf{a}_{n2}\mathfrak{X}^1_{72}(n,r_1) + \mathsf{b}_{n2}\mathfrak{X}^2_{72}(n,r_1) + \mathsf{c}_{n2}\mathfrak{X}^3_{72}(n,r_1) + \mathsf{d}_{n2}\mathfrak{X}^4_{72}(n,r_1) &= \\
\frac{k_1}{\omega^2\rho_1}C_n H_n'(k_1 r_1) & && (3.64)\\
\mathsf{a}_{n2}\mathfrak{X}^1_{42}(n,r_2) + \mathsf{b}_{n2}\mathfrak{X}^2_{42}(n,r_2) + \mathsf{c}_{n2}\mathfrak{X}^3_{42}(n,r_2) + \mathsf{d}_{n2}\mathfrak{X}^4_{42}(n,r_2) &= \\
-[A_n H_n(k_3 r_2) + B_n J_n(k_3 r_2)] & && (3.65)\\
\mathsf{a}_{n2}\mathfrak{X}^1_{42}(n,r_1) + \mathsf{b}_{n2}\mathfrak{X}^2_{42}(n,r_1) + \mathsf{c}_{n2}\mathfrak{X}^3_{42}(n,r_1) + \mathsf{d}_{n2}\mathfrak{X}^4_{42}(n,r_1) &= -C_n H_n(k_1 r_1) && (3.66)\\
\mathsf{a}_{n2}\mathfrak{X}^1_{62}(n,r_1) + \mathsf{b}_{n2}\mathfrak{X}^2_{62}(n,r_1) + \mathsf{c}_{n2}\mathfrak{X}^3_{62}(n,r_1) + \mathsf{d}_{n2}\mathfrak{X}^4_{62}(n,r_1) &= 0 && (3.67)\\
\mathsf{a}_{n2}\mathfrak{X}^1_{62}(n,r_2) + \mathsf{b}_{n2}\mathfrak{X}^2_{62}(n,r_2) + \mathsf{c}_{n2}\mathfrak{X}^3_{62}(n,r_2) + \mathsf{d}_{n2}\mathfrak{X}^4_{62}(n,r_2) &= 0 && (3.68)
\end{aligned}
$$

Denote

$$
[\mathfrak{m}_2] = \begin{bmatrix}
\mathfrak{X}^1_{72}(n,r_2) & \mathfrak{X}^2_{72}(n,r_2) & \mathfrak{X}^3_{72}(n,r_2) & \mathfrak{X}^4_{72}(n,r_2) & -\frac{k_3}{\omega^2\rho_3}J'_n(k_3r_2) & 0 \\
\mathfrak{X}^1_{72}(n,r_1) & \mathfrak{X}^2_{72}(n,r_1) & \mathfrak{X}^3_{72}(n,r_1) & \mathfrak{X}^4_{72}(n,r_1) & 0 & -\frac{k_1}{\omega^2\rho_1}H'_n(k_1r_1) \\
\mathfrak{X}^1_{42}(n,r_2) & \mathfrak{X}^2_{42}(n,r_2) & \mathfrak{X}^3_{42}(n,r_2) & \mathfrak{X}^4_{42}(n,r_2) & J_n(k_3r_2) & 0 \\
\mathfrak{X}^1_{42}(n,r_1) & \mathfrak{X}^2_{42}(n,r_1) & \mathfrak{X}^3_{42}(n,r_1) & \mathfrak{X}^4_{42}(n,r_1) & 0 & H_n(k_1r_1) \\
\mathfrak{X}^1_{62}(n,r_1) & \mathfrak{X}^2_{62}(n,r_1) & \mathfrak{X}^3_{62}(n,r_1) & \mathfrak{X}^4_{62}(n,r_1) & 0 & 0 \\
\mathfrak{X}^1_{62}(n,r_2) & \mathfrak{X}^2_{62}(n,r_2) & \mathfrak{X}^3_{62}(n,r_2) & \mathfrak{X}^4_{62}(n,r_2) & 0 & 0
\end{bmatrix} \tag{3.69}
$$

Eqns. (3.63) through (3.68) can be solved as

$$
\begin{Bmatrix}
[\mathfrak{A}_{321}]_n \\
[\mathfrak{B}_{321}]_n \\
[\mathfrak{C}_{321}]_n \\
[\mathfrak{D}_{321}]_n \\
[\boldsymbol{R}_{321}]_n \\
[\boldsymbol{T}_{321}]_n
\end{Bmatrix} = [\mathfrak{m}_2]^{-1} \begin{Bmatrix}
\frac{k_3}{\omega^2\rho_3}H'_n(k_3r_2) \\
0 \\
-H_n(k_3r_2) \\
0 \\
0 \\
0
\end{Bmatrix} \tag{3.70}
$$

3.4 Acoustic Scattering by Multilayer Scatterers

The set of two canonical problems defined above is used for solving acoustic scattering by multilayer scatterers in this section.

3.4.1 Special Multilayer Scatterers

Three special cases are solved first. Based on the solutions of the three special cases, the solution for a general multilayer scatterer can be obtained through a recursive solution procedure. The multilayer scattering problem is analyzed following the approach proposed by Cai (2004). The solving process of three special multilayer scatterers is introduced as follows.

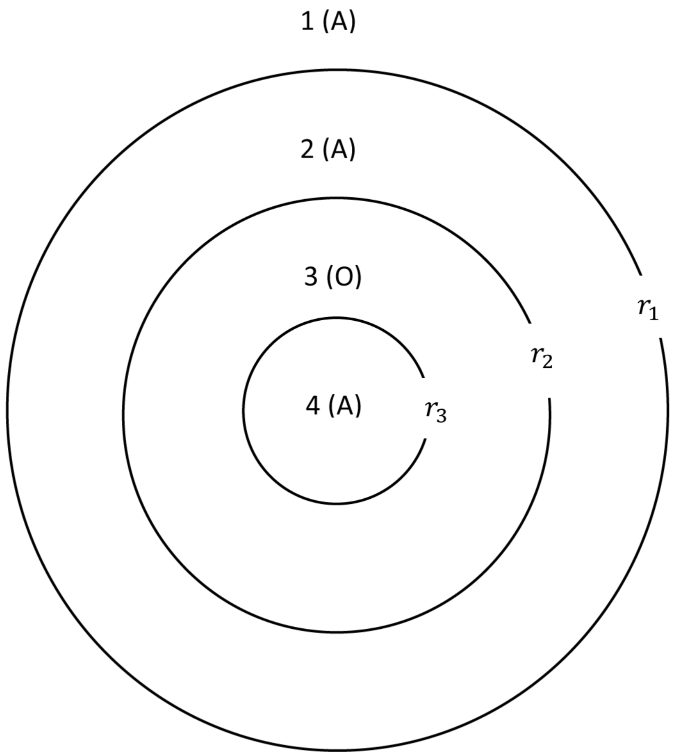

Figure 3.4: *Acoustic-Acoustic-Orthotropic-Acoustic*

Acoustic-Acoustic-Orthotropic-Acoustic

The scatterer solved in this section has three layers. Denote the host as medium 1, the intermediate layers as media 2 and 3, and the core of the scatterer as medium 4, as shown in Fig. 3.4. Media 1, 2, and 4 are acoustic materials, and medium 3 is an orthotropic material. Denote the radii of the interfaces between media 1 and 2, media 2 and 3,and media 3 and 4 as r_1, r_2, and r_3, respectively. The incident wave in medium 1 is expressible as

$$\phi^{inc} = \sum_{n=-\infty}^{\infty} A_n J_n(k_1 r) e^{in\theta} = \{\boldsymbol{A}\}^T \{\boldsymbol{J}(k_1, \boldsymbol{r})\} \tag{3.71}$$

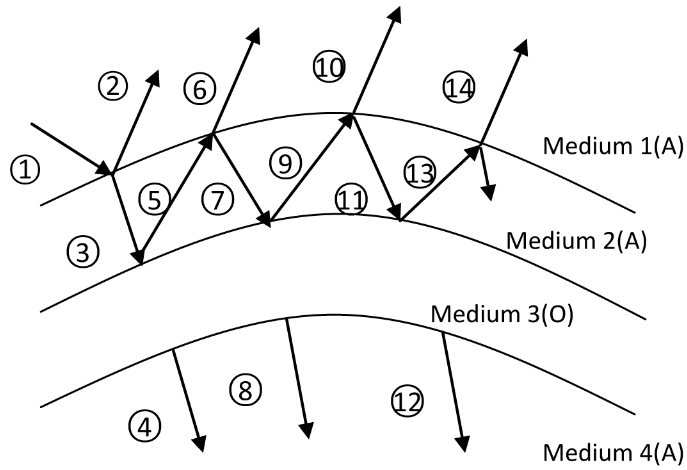

Figure 3.5: *Scattering process in scatterer with acoustic-orthotropic-acoustic layers*

The total waves in acoustic media 1, 2, and 4 are expressible as

$$\phi_1 = \phi^{inc} + \{\boldsymbol{B}\}^T\{\boldsymbol{H}(k_1, \boldsymbol{r})\} \tag{3.72}$$

$$\phi_2 = \{\boldsymbol{D}\}^T\{\boldsymbol{J}(k_2, \boldsymbol{r})\} + \{\boldsymbol{E}\}^T\{\boldsymbol{H}(k_2, \boldsymbol{r})\} \tag{3.73}$$

$$\phi_4 = \{\boldsymbol{C}\}^T\{\boldsymbol{J}(k_4, \boldsymbol{r})\} \tag{3.74}$$

where $\{\boldsymbol{B}\}$, $\{\boldsymbol{C}\}$, $\{\boldsymbol{D}\}$, and $\{\boldsymbol{E}\}$ are the wave expansion coefficient column matrices for the respective waves whose row index runs from $-\infty$ to ∞.

The different waves are numbered in the multiple scattering process to be easier to follow (Cai, 2004). The multiple scattering process is shown in Fig. 3.5. Wave ① is the incident wave, which is expressible as

$$\phi^{①} = \{\boldsymbol{A}\}^T\{\boldsymbol{J}_1(\boldsymbol{r}, \theta)\} \tag{3.75}$$

The incident wave impinges onto medium 2, producing reflected wave ② and transmitted wave ③. These are

$$\phi^{②} = ([\boldsymbol{R}_{12}]\{\boldsymbol{A}\})^T\{\boldsymbol{H}_1(\boldsymbol{r}, \theta)\} \tag{3.76}$$

$$\phi^{③} = ([\boldsymbol{T}_{12}]\{\boldsymbol{A}\})^T\{\boldsymbol{J}_2(\boldsymbol{r}, \theta)\} \tag{3.77}$$

When wave ③ impinges onto medium 3, producing the reflected wave ⑤ in medium 2 and transmitted wave ④ in medium 4, the process is described by the first canonical problem introduced above with wave ③ as the incident wave. According to Eqn. (3.26), the transmitted wave ④ in medium 4 and reflected wave ⑤ in medium 2 can be related to the incident wave ③ in medium 2, by linear transformations

$$\phi^{④} = ([\boldsymbol{T}_{234}][\boldsymbol{T}_{12}]\{\boldsymbol{A}\})^T\{\boldsymbol{J}_4(\boldsymbol{r},\theta)\} \qquad \phi^{⑤} = ([\boldsymbol{R}_{234}][\boldsymbol{T}_{12}]\{\boldsymbol{A}\})^T\{\boldsymbol{H}_2(\boldsymbol{r},\theta)\} \tag{3.78}$$

where subscript "234" signifies the first canonical problem in which the incident wave in medium 2 and travels toward media 3 and 4. The process continues with a similar procedure. The waves can be expressed as

$$\phi^{⑥} = ([\boldsymbol{T}_{21}][\boldsymbol{R}_{234}][\boldsymbol{T}_{12}]\{\boldsymbol{A}\})^T\{\boldsymbol{H}_1(\boldsymbol{r},\theta)\} \tag{3.79}$$

$$\phi^{⑦} = ([\boldsymbol{R}_{21}][\boldsymbol{R}_{234}][\boldsymbol{T}_{12}]\{\boldsymbol{A}\})^T\{\boldsymbol{J}_2(\boldsymbol{r},\theta)\} \tag{3.80}$$

$$\phi^{⑧} = ([\boldsymbol{T}_{234}][\boldsymbol{R}_{21}][\boldsymbol{R}_{234}][\boldsymbol{T}_{12}]\{\boldsymbol{A}\})^T\{\boldsymbol{J}_4(\boldsymbol{r},\theta)\} \tag{3.81}$$

$$\phi^{⑨} = ([\boldsymbol{R}_{234}][\boldsymbol{R}_{21}][\boldsymbol{R}_{234}][\boldsymbol{T}_{12}]\{\boldsymbol{A}\})^T\{\boldsymbol{H}_2(\boldsymbol{r},\theta)\} \tag{3.82}$$

$$\phi^{⑩} = ([\boldsymbol{T}_{21}][\boldsymbol{R}_{234}][\boldsymbol{R}_{21}][\boldsymbol{R}_{234}][\boldsymbol{T}_{12}]\{\boldsymbol{A}\})^T\{\boldsymbol{H}_1(\boldsymbol{r},\theta)\} \tag{3.83}$$

$$\phi^{⑪} = ([\boldsymbol{R}_{21}][\boldsymbol{R}_{234}][\boldsymbol{R}_{21}][\boldsymbol{R}_{234}][\boldsymbol{T}_{12}]\{\boldsymbol{A}\})^T\{\boldsymbol{J}_2(\boldsymbol{r},\theta)\} \tag{3.84}$$

$$\phi^{⑫} = ([\boldsymbol{T}_{234}][\boldsymbol{R}_{21}][\boldsymbol{R}_{234}][\boldsymbol{R}_{21}][\boldsymbol{R}_{234}][\boldsymbol{T}_{12}]\{\boldsymbol{A}\})^T\{\boldsymbol{J}_4(\boldsymbol{r},\theta)\} \tag{3.85}$$

$$\phi^{⑬} = ([\boldsymbol{R}_{234}][\boldsymbol{R}_{21}][\boldsymbol{R}_{234}][\boldsymbol{R}_{21}][\boldsymbol{R}_{234}][\boldsymbol{T}_{12}]\{\boldsymbol{A}\})^T\{\boldsymbol{H}_2(\boldsymbol{r},\theta)\} \tag{3.86}$$

$$\phi^{⑭} = ([\boldsymbol{T}_{21}][\boldsymbol{R}_{234}][\boldsymbol{R}_{21}][\boldsymbol{R}_{234}][\boldsymbol{R}_{21}][\boldsymbol{R}_{234}][\boldsymbol{T}_{12}]\{\boldsymbol{A}\})^T\{\boldsymbol{H}_1(\boldsymbol{r},\theta)\} \tag{3.87}$$

$$\phi^{⑮} = [\boldsymbol{R}_{21}][\boldsymbol{R}_{234}][\boldsymbol{R}_{21}][\boldsymbol{R}_{234}][\boldsymbol{R}_{21}][\boldsymbol{R}_{234}][\boldsymbol{T}_{12}]\{\boldsymbol{A}\}^T\{\boldsymbol{J}_2(\boldsymbol{r},\theta)\} \tag{3.88}$$

The total waves in each medium can be obtained by adding up all the waves that appear in the medium. For medium 1, the total wave consists of the incident wave ϕ^{inc}, the total scattered waves ②, ⑥, ⑩, ⑭ and subsequent waves. For medium 2, the total wave consists of waves ③, ⑤, ⑦, ⑨, ⑪, ⑬, ⑮, and subsequent waves. Similarly for medium 4, the total wave consists of waves ④, ⑧, ⑫, and subsequent waves. In medium 1, the total scattered wave can be written as

$$\begin{aligned}\phi_s = [(&[\boldsymbol{R}_{12}] + [\boldsymbol{T}_{21}][\boldsymbol{R}_{234}][\boldsymbol{T}_{12}] + [\boldsymbol{T}_{21}][\boldsymbol{R}_{234}][\boldsymbol{R}_{21}][\boldsymbol{R}_{234}][\boldsymbol{T}_{12}] \\ &[\boldsymbol{T}_{21}][\boldsymbol{R}_{234}][\boldsymbol{R}_{21}][\boldsymbol{R}_{234}][\boldsymbol{R}_{21}][\boldsymbol{R}_{234}][\boldsymbol{T}_{12}] + \cdots)\,\{\boldsymbol{A}\}]^T\,\{\boldsymbol{H}_1(\boldsymbol{r},\theta)\}\end{aligned} \tag{3.89}$$

Following the same manner introduced by Cai (2004), define

$$[\boldsymbol{E}] = [\boldsymbol{I}] + [\boldsymbol{R}_{21}][\boldsymbol{R}_{234}] + [\boldsymbol{R}_{21}][\boldsymbol{R}_{234}][\boldsymbol{R}_{21}][\boldsymbol{R}_{234}] + \cdots \tag{3.90}$$

Recalling the Taylor expansion

$$(1-x)^{-1} = 1 + x + x^2 + \cdots \tag{3.91}$$

Eqn. (3.90) can be written as

$$[\boldsymbol{E}] = ([\boldsymbol{I}] - [\boldsymbol{R}_{21}][\boldsymbol{R}_{234}])^{-1} \tag{3.92}$$

By defining

$$[\boldsymbol{S}] = [\boldsymbol{E}][\boldsymbol{T}_{12}] \tag{3.93}$$

Eqn. (3.89) can be written as

$$\phi_s = [([\boldsymbol{R}_{12}] + [\boldsymbol{T}_{21}][\boldsymbol{R}_{234}][\boldsymbol{S}])\,\{\boldsymbol{A}\}]^T\,\{\boldsymbol{H}_1(\boldsymbol{r},\theta)\} \tag{3.94}$$

The total wave in medium 1 can be written as

$$\phi_1 = \phi^{inc} + [([\boldsymbol{R}_{12}] + [\boldsymbol{T}_{21}][\boldsymbol{R}_{234}][\boldsymbol{S}])\,\{\boldsymbol{A}\}]^T\,\{\boldsymbol{H}_1(\boldsymbol{r},\theta)\} \tag{3.95}$$

Waves in medium 2 and 4 can be obtained following the same manner, which gives

$$\phi_2 = ([\boldsymbol{S}]\{\boldsymbol{A}\})^T\{\boldsymbol{J}_2(\boldsymbol{r},\theta) + ([\boldsymbol{R}_{234}][\boldsymbol{S}]\{\boldsymbol{A}\})^T\{\boldsymbol{H}_2(\boldsymbol{r},\theta)\} \tag{3.96}$$

$$\phi_4 = ([\boldsymbol{T}_{234}][\boldsymbol{S}]\{\boldsymbol{A}\})^T\{\boldsymbol{J}_4(\boldsymbol{r},\theta)\} \tag{3.97}$$

Define

$$[\boldsymbol{R}] = [\boldsymbol{R}_{12}] + [\boldsymbol{T}_{21}][\boldsymbol{R}_{234}][\boldsymbol{S}] \tag{3.98}$$

$$[\boldsymbol{F}] = [\boldsymbol{R}_{234}][\boldsymbol{S}] \tag{3.99}$$

$$[\boldsymbol{T}] = [\boldsymbol{T}_{234}][\boldsymbol{S}] \tag{3.100}$$

The total waves in medium 1, 2, and 4 can be written as

$$\phi_1 = \phi^{inc} + ([\boldsymbol{R}]\{\boldsymbol{A}\})^T\{\boldsymbol{H}_1(\boldsymbol{r},\theta)\} \tag{3.101}$$

$$\phi_2 = ([\boldsymbol{S}]\{\boldsymbol{A}\})^T\{\boldsymbol{J}_2(\boldsymbol{r},\theta) + ([\boldsymbol{F}]\{\boldsymbol{A}\})^T\{\boldsymbol{H}_2(\boldsymbol{r},\theta)\} \tag{3.102}$$

$$\phi_4 = ([\boldsymbol{T}]\{\boldsymbol{A}\})^T\{\boldsymbol{J}_4(\boldsymbol{r},\theta)\} \tag{3.103}$$

In Eqns. (3.101) though (3.103), matrices $[\boldsymbol{R}]$ and $[\boldsymbol{T}]$ are called reflection and transmission matrices, respectively. They represent the scattered wave in medium 1 and transmitted wave in medium 4, respectively (Cai, 2004). The characteristic matrices $[\boldsymbol{R}_{12}]$, $[\boldsymbol{R}_{21}]$, and $[\boldsymbol{T}_{21}]$ can be obtained by applying the two canonical problems defined by Cai (2004); while $[\boldsymbol{R}_{234}]$ and $[\boldsymbol{T}_{234}]$ can be solved by using the first canonical problem defined in this study.

To solve the waves in an orthotropic medium, the essential task is to obtain the constants column matrices which are related to those of the incident wave. When wave ③ impinges onto medium 3, it is an incident wave for medium 3 so the constants column matrices can be written as

$$
\begin{aligned}
\{\boldsymbol{a}\}_3^{\textcircled{1}} &= [\boldsymbol{\mathfrak{A}}_{234}][\boldsymbol{T}_{12}]\{\boldsymbol{A}\} && (3.104)\\
\{\boldsymbol{b}\}_3^{\textcircled{1}} &= [\boldsymbol{\mathfrak{B}}_{234}][\boldsymbol{T}_{12}]\{\boldsymbol{A}\} && (3.105)\\
\{\boldsymbol{c}\}_3^{\textcircled{1}} &= [\boldsymbol{\mathfrak{C}}_{234}][\boldsymbol{T}_{12}]\{\boldsymbol{A}\} && (3.106)\\
\{\boldsymbol{d}\}_3^{\textcircled{1}} &= [\boldsymbol{\mathfrak{D}}_{234}][\boldsymbol{T}_{12}]\{\boldsymbol{A}\} && (3.107)
\end{aligned}
$$

When wave $\textcircled{7}$ impinges onto medium 3, the constants column matrices can be given as

$$
\begin{aligned}
\{\boldsymbol{a}\}_3^{\textcircled{2}} &= [\boldsymbol{\mathfrak{A}}_{234}][\boldsymbol{R}_{21}][\boldsymbol{R}_{234}][\boldsymbol{T}_{12}]\{\boldsymbol{A}\} && (3.108)\\
\{\boldsymbol{b}\}_3^{\textcircled{2}} &= [\boldsymbol{\mathfrak{B}}_{234}][\boldsymbol{R}_{21}][\boldsymbol{R}_{234}][\boldsymbol{T}_{12}]\{\boldsymbol{A}\} && (3.109)\\
\{\boldsymbol{c}\}_3^{\textcircled{2}} &= [\boldsymbol{\mathfrak{C}}_{234}][\boldsymbol{R}_{21}][\boldsymbol{R}_{234}][\boldsymbol{T}_{12}]\{\boldsymbol{A}\} && (3.110)\\
\{\boldsymbol{d}\}_3^{\textcircled{2}} &= [\boldsymbol{\mathfrak{D}}_{234}][\boldsymbol{R}_{21}][\boldsymbol{R}_{234}][\boldsymbol{T}_{12}]\{\boldsymbol{A}\} && (3.111)
\end{aligned}
$$

When wave $\textcircled{11}$ impinges onto medium 3, the constants column matrices are expressible as

$$
\begin{aligned}
\{\boldsymbol{a}\}_3^{\textcircled{3}} &= [\boldsymbol{\mathfrak{A}}_{234}][\boldsymbol{R}_{21}][\boldsymbol{R}_{234}][\boldsymbol{R}_{21}][\boldsymbol{R}_{234}][\boldsymbol{T}_{12}]\{\boldsymbol{A}\} && (3.112)\\
\{\boldsymbol{b}\}_3^{\textcircled{3}} &= [\boldsymbol{\mathfrak{B}}_{234}][\boldsymbol{R}_{21}][\boldsymbol{R}_{234}][\boldsymbol{R}_{21}][\boldsymbol{R}_{234}][\boldsymbol{T}_{12}]\{\boldsymbol{A}\} && (3.113)\\
\{\boldsymbol{c}\}_3^{\textcircled{3}} &= [\boldsymbol{\mathfrak{C}}_{234}][\boldsymbol{R}_{21}][\boldsymbol{R}_{234}][\boldsymbol{R}_{21}][\boldsymbol{R}_{234}][\boldsymbol{T}_{12}]\{\boldsymbol{A}\} && (3.114)\\
\{\boldsymbol{d}\}_3^{\textcircled{3}} &= [\boldsymbol{\mathfrak{D}}_{234}][\boldsymbol{R}_{21}][\boldsymbol{R}_{234}][\boldsymbol{R}_{21}][\boldsymbol{R}_{234}][\boldsymbol{T}_{12}]\{\boldsymbol{A}\} && (3.115)
\end{aligned}
$$

When wave $\textcircled{15}$ impinges onto medium 3, the constants column matrices are expressible as

$$
\begin{aligned}
\{\boldsymbol{a}\}_3^{\textcircled{4}} &= [\boldsymbol{\mathfrak{A}}_{234}][\boldsymbol{R}_{21}][\boldsymbol{R}_{234}][\boldsymbol{R}_{21}][\boldsymbol{R}_{234}][\boldsymbol{R}_{21}]][\boldsymbol{R}_{234}][\boldsymbol{T}_{12}]\{\boldsymbol{A}\} && (3.116)\\
\{\boldsymbol{b}\}_3^{\textcircled{4}} &= [\boldsymbol{\mathfrak{B}}_{234}][\boldsymbol{R}_{21}][\boldsymbol{R}_{234}][\boldsymbol{R}_{21}][\boldsymbol{R}_{234}][R_{21}][\boldsymbol{R}_{234}][\boldsymbol{T}_{12}]\{\boldsymbol{A}\} && (3.117)\\
\{\boldsymbol{c}\}_3^{\textcircled{4}} &= [\boldsymbol{\mathfrak{C}}_{234}][\boldsymbol{R}_{21}][\boldsymbol{R}_{21}][\boldsymbol{R}_{234}][\boldsymbol{R}_{21}][\boldsymbol{R}_{234}][\boldsymbol{R}_{21}][\boldsymbol{R}_{234}][\boldsymbol{T}_{12}]\{\boldsymbol{A}\} && (3.118)\\
\{\boldsymbol{d}\}_3^{\textcircled{4}} &= [\boldsymbol{\mathfrak{D}}_{234}][\boldsymbol{R}_{21}][\boldsymbol{R}_{21}][\boldsymbol{R}_{234}][\boldsymbol{R}_{21}][\boldsymbol{R}_{234}][\boldsymbol{R}_{21}][\boldsymbol{R}_{234}][\boldsymbol{T}_{12}]\{\boldsymbol{A}\} && (3.119)
\end{aligned}
$$

So in medium 3, the total constants column matrix $\{\boldsymbol{a}\}_3$ can be summed to give,

$$\begin{aligned}\{\boldsymbol{a}\}_3 = \{\boldsymbol{a}\}_3^{①} + \{\boldsymbol{a}\}_3^{②} + \{\boldsymbol{a}\}_3^{③} + \{\boldsymbol{a}\}_3^{④} + \cdots \\ = [\boldsymbol{\mathfrak{A}}_{234}][\boldsymbol{T}_{12}]\{\boldsymbol{A}\} + [\boldsymbol{\mathfrak{A}}_{234}][\boldsymbol{R}_{21}][\boldsymbol{R}_{234}][\boldsymbol{T}_{12}]\{\boldsymbol{A}\} \\ + [\boldsymbol{\mathfrak{A}}_{234}][\boldsymbol{R}_{21}][\boldsymbol{R}_{234}][\boldsymbol{R}_{21}][\boldsymbol{R}_{234}][\boldsymbol{T}_{12}]\{\boldsymbol{A}\} \\ + [\boldsymbol{\mathfrak{A}}_{234}][\boldsymbol{R}_{21}][\boldsymbol{R}_{234}][\boldsymbol{R}_{21}][\boldsymbol{R}_{234}][\boldsymbol{R}_{21}][\boldsymbol{R}_{234}][\boldsymbol{T}_{12}]\{\boldsymbol{A}\} + \cdots \\ = [\boldsymbol{\mathfrak{A}}_{234}][\boldsymbol{T}_{12}]\{\boldsymbol{A}\}\left\{[\boldsymbol{I}] + [\boldsymbol{R}_{21}][\boldsymbol{R}_{234}] + ([\boldsymbol{R}_{21}][\boldsymbol{R}_{234}])^2 + ([\boldsymbol{R}_{21}][\boldsymbol{R}_{234}])^3 + \cdots\right\}\end{aligned} \tag{3.120}$$

Recalling the Taylor expansion

$$(1-x)^{-1} = 1 + x + x^2 + \cdots \tag{3.121}$$

Eqn. (3.120) can be written as

$$\begin{aligned}\{\boldsymbol{a}\}_3 &= [\boldsymbol{\mathfrak{A}}_{234}][\boldsymbol{T}_{12}]\{\boldsymbol{A}\}\left([\boldsymbol{I}] - [\boldsymbol{R}_{21}][\boldsymbol{R}_{234}]\right)^{-1} \\ &= [\boldsymbol{\mathfrak{A}}_{234}][\boldsymbol{E}][\boldsymbol{T}_{12}]\{\boldsymbol{A}\}\end{aligned} \tag{3.122}$$

Similarly,

$$\{\boldsymbol{b}\}_3 = [\boldsymbol{\mathfrak{B}}_{234}][\boldsymbol{E}][\boldsymbol{T}_{12}]\{\boldsymbol{A}\} \tag{3.123}$$

$$\{\boldsymbol{c}\}_3 = [\boldsymbol{\mathfrak{C}}_{234}][\boldsymbol{E}][\boldsymbol{T}_{12}]\{\boldsymbol{A}\} \tag{3.124}$$

$$\{\boldsymbol{d}\}_3 = [\boldsymbol{\mathfrak{D}}_{234}][\boldsymbol{E}][\boldsymbol{T}_{12}]\{\boldsymbol{A}\} \tag{3.125}$$

According to Eqn. (3.93), the above total constants column matrices can also be written as

$$\{\boldsymbol{a}\}_3 = [\mathfrak{A}_{234}][\boldsymbol{S}]\{\boldsymbol{A}\} \tag{3.126}$$

$$\{\boldsymbol{b}\}_3 = [\mathfrak{B}_{234}][\boldsymbol{S}]\{\boldsymbol{A}\} \tag{3.127}$$

$$\{\boldsymbol{c}\}_3 = [\mathfrak{C}_{234}][\boldsymbol{S}]\{\boldsymbol{A}\} \tag{3.128}$$

$$\{\boldsymbol{d}\}_3 = [\mathfrak{D}_{234}][\boldsymbol{S}]\{\boldsymbol{A}\} \tag{3.129}$$

So, the constants column matrices $\{\boldsymbol{a}\}_3$, $\{\boldsymbol{b}\}_3$, $\{\boldsymbol{c}\}_3$ and $\{\boldsymbol{d}\}_3$ can be solved using Eqns. (3.126) through (3.129). Then, the displacement and the stress in medium 3 can be obtained through Eqns. (3.8) and (3.9).

Acoustic-Orthotropic-Acoustic-Orthotropic-Acoustic

The scatterer solved in this section has four layers. Denote the host as medium 1, the intermediate layers as media 2, 3 and 4, and the core of the scatterer as medium 5, as shown in Fig. 3.6. Media 1, 3, and 5 are acoustic and media 2 and 4 are orthotropic. The radii of the interface between media 1 and 2, 2 and 3, 3 and 4, and 4 and 5 are denoted as r_1, r_2, r_3, and r_4, respectively.

Following the same procedure as in the last case, the total waves in acoustic media 1 (host), and 3 and 5 (innermost) can be expressed as

$$\phi_1 = \phi^{inc} + ([\boldsymbol{R}]\{\boldsymbol{A}\})^T\{\boldsymbol{H}_1(\boldsymbol{r},\theta)\} \tag{3.130}$$

$$\phi_3 = ([\boldsymbol{S}]\{\boldsymbol{A}\})^T\{\boldsymbol{J}_3(\boldsymbol{r},\theta) + ([\boldsymbol{F}]\{\boldsymbol{A}\})^T\{\boldsymbol{H}_3(\boldsymbol{r},\theta)\} \tag{3.131}$$

$$\phi_5 = ([\boldsymbol{T}]\{\boldsymbol{A}\})^T\{\boldsymbol{J}_5(\boldsymbol{r},\theta)\} \tag{3.132}$$

For the previous case, media 1 and 2 are acoustic. For this case, media 1, 2 and 3 are acoustic, orthotropic, and acoustic. So the first and second canonical problems for acoustic-acoustic interface in the previous case become the first and second canonical problems for

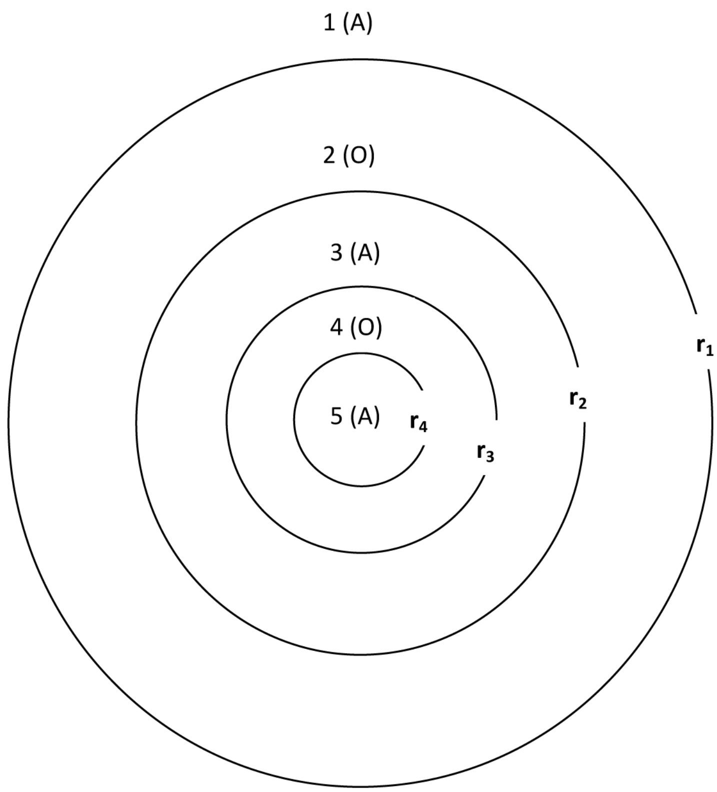

Figure 3.6: *Acoustic-Orthotropic-Acoustic-Orthotropic-Acoustic*

acoustic-orthotropic-acoustic interfaces in this case. Subscripts "12" and "21" become "123" and "321" in this case. For the previous case, media 2, 3, and 4 were acoustic, orthotropic, and acoustic. For the current case, media 3, 4, and 5 are acoustic, orthotropic, and acoustic. Therefore, the subscripts "234" become "345". According to Eqns. (3.92), (3.93), (3.133), (3.134), and (3.135), the following corresponding matrices are defined:

$$[\boldsymbol{R}] = [\boldsymbol{R}_{123}] + [\boldsymbol{T}_{321}][\boldsymbol{R}_{345}][\boldsymbol{S}] \tag{3.133}$$

$$[\boldsymbol{F}] = [\boldsymbol{R}_{345}][\boldsymbol{S}] \tag{3.134}$$

$$[\boldsymbol{T}] = [\boldsymbol{T}_{345}][\boldsymbol{S}] \tag{3.135}$$

$$[\boldsymbol{S}] = [\boldsymbol{E}][\boldsymbol{T}_{123}] \tag{3.136}$$

$$[\boldsymbol{E}] = ([\boldsymbol{I}] - [\boldsymbol{R}_{321}][\boldsymbol{R}_{345}])^{-1} \tag{3.137}$$

To obtain the constants column matrices for orthotropic medium 2, the wave expressions in Eqns. (3.78) to (3.88) for the previous case can be used for this case by updating the subscripts "12", "21", and "234" to "123", "321", and "345", respectively. When the incident wave ① impinges onto medium 2, the constants column matrices can be given as

$$\{\boldsymbol{a}\}_2^{①} = [\boldsymbol{\mathfrak{A}}_{123}]\{\boldsymbol{A}\} \tag{3.138}$$

$$\{\boldsymbol{b}\}_2^{①} = [\boldsymbol{\mathfrak{B}}_{123}]\{\boldsymbol{A}\} \tag{3.139}$$

$$\{\boldsymbol{c}\}_2^{①} = [\boldsymbol{\mathfrak{C}}_{123}]\{\boldsymbol{A}\} \tag{3.140}$$

$$\{\boldsymbol{d}\}_2^{①} = [\boldsymbol{\mathfrak{D}}_{123}]\{\boldsymbol{A}\} \tag{3.141}$$

When wave ⑤ impinges onto medium 2, the constants column matrices can be given as

$$\{\boldsymbol{a}\}_2^{②} = [\boldsymbol{\mathfrak{A}}_{321}][\boldsymbol{R}_{345}][\boldsymbol{T}_{123}]\{\boldsymbol{A}\} \tag{3.142}$$

$$\{\boldsymbol{b}\}_2^{②} = [\boldsymbol{\mathfrak{B}}_{321}][\boldsymbol{R}_{345}][\boldsymbol{T}_{123}]\{\boldsymbol{A}\} \tag{3.143}$$

$$\{\boldsymbol{c}\}_2^{②} = [\boldsymbol{\mathfrak{C}}_{321}][\boldsymbol{R}_{345}][\boldsymbol{T}_{123}]\{\boldsymbol{A}\} \tag{3.144}$$

$$\{\boldsymbol{d}\}_2^{②} = [\boldsymbol{\mathfrak{D}}_{321}][\boldsymbol{R}_{345}][\boldsymbol{T}_{123}]\{\boldsymbol{A}\} \tag{3.145}$$

When wave ⑨ impinges onto medium 2, the constants column matrices can be given as

$$\{\boldsymbol{a}\}_2^{③} = [\boldsymbol{\mathfrak{A}}_{321}][\boldsymbol{R}_{345}][\boldsymbol{R}_{321}][\boldsymbol{R}_{345}][\boldsymbol{T}_{123}]\{\boldsymbol{A}\} \tag{3.146}$$

$$\{\boldsymbol{b}\}_2^{③} = [\boldsymbol{\mathfrak{B}}_{321}][\boldsymbol{R}_{345}][\boldsymbol{R}_{321}][\boldsymbol{R}_{345}][\boldsymbol{T}_{123}]\{\boldsymbol{A}\} \tag{3.147}$$

$$\{\boldsymbol{c}\}_2^{③} = [\boldsymbol{\mathfrak{C}}_{321}][\boldsymbol{R}_{345}][\boldsymbol{R}_{321}][\boldsymbol{R}_{345}][\boldsymbol{T}_{123}]\{\boldsymbol{A}\} \tag{3.148}$$

$$\{\boldsymbol{d}\}_2^{③} = [\boldsymbol{\mathfrak{D}}_{321}][\boldsymbol{R}_{345}][\boldsymbol{R}_{321}][\boldsymbol{R}_{345}][\boldsymbol{T}_{123}]\{\boldsymbol{A}\} \tag{3.149}$$

When wave ⑬ impinges onto medium 2, the constants column matrices can be given as

$$\{\boldsymbol{a}\}_2^{④} = [\boldsymbol{\mathfrak{A}}_{321}][\boldsymbol{R}_{345}][\boldsymbol{R}_{321}][\boldsymbol{R}_{345}][\boldsymbol{R}_{321}][\boldsymbol{R}_{345}][\boldsymbol{T}_{123}]\{\boldsymbol{A}\} \tag{3.150}$$

$$\{\boldsymbol{b}\}_2^{④} = [\boldsymbol{\mathfrak{B}}_{321}][\boldsymbol{R}_{345}][\boldsymbol{R}_{321}][\boldsymbol{R}_{345}][\boldsymbol{R}_{321}][\boldsymbol{R}_{345}][\boldsymbol{T}_{123}]\{\boldsymbol{A}\} \tag{3.151}$$

$$\{\boldsymbol{c}\}_2^{④} = [\boldsymbol{\mathfrak{C}}_{321}][\boldsymbol{R}_{345}][\boldsymbol{R}_{321}][\boldsymbol{R}_{345}][\boldsymbol{R}_{321}][\boldsymbol{R}_{345}][\boldsymbol{T}_{123}]\{\boldsymbol{A}\} \tag{3.152}$$

$$\{\boldsymbol{d}\}_2^{④} = [\boldsymbol{\mathfrak{D}}_{321}][\boldsymbol{R}_{345}][\boldsymbol{R}_{321}][\boldsymbol{R}_{345}][\boldsymbol{R}_{321}][\boldsymbol{R}_{345}][\boldsymbol{T}_{123}]\{\boldsymbol{A}\} \tag{3.153}$$

So in medium 2, the total constants column matrix $\{\boldsymbol{a}\}_2$ can be summed to give,

$$
\begin{aligned}
\{\boldsymbol{a}\}_2 =& \{\boldsymbol{a}\}_2^{①} + \{\boldsymbol{a}\}_2^{②} + \{\boldsymbol{a}\}_2^{③} + \{\boldsymbol{a}\}_2^{④} + \cdots \\
=& [\mathfrak{A}_{123}]\{\boldsymbol{A}\} + [\mathfrak{A}_{321}][\boldsymbol{R}_{345}][\boldsymbol{T}_{123}]\{\boldsymbol{A}\} + [\mathfrak{A}_{321}][\boldsymbol{R}_{345}][\boldsymbol{R}_{321}][\boldsymbol{R}_{345}][\boldsymbol{T}_{123}]\{\boldsymbol{A}\} \\
& + [\mathfrak{A}_{321}][\boldsymbol{R}_{345}][\boldsymbol{R}_{321}][\boldsymbol{R}_{345}][\boldsymbol{R}_{321}][\boldsymbol{R}_{345}][\boldsymbol{T}_{123}]\{\boldsymbol{A}\} + \cdots \\
=& [\mathfrak{A}_{123}]\{\boldsymbol{A}\} + [\mathfrak{A}_{321}][\boldsymbol{R}_{345}]\left\{[\boldsymbol{I}] + [\boldsymbol{R}_{321}][\boldsymbol{R}_{345}] + ([\boldsymbol{R}_{321}][\boldsymbol{R}_{345}])^2\right. \\
& \left. + ([\boldsymbol{R}_{321}][\boldsymbol{R}_{345}])^3 + \cdots\right\}[\boldsymbol{T}_{123}]\{\boldsymbol{A}\} \\
=& [\mathfrak{A}_{123}]\{\boldsymbol{A}\} + [\mathfrak{A}_{321}][\boldsymbol{R}_{345}]\left([\boldsymbol{I}] - [\boldsymbol{R}_{321}][\boldsymbol{R}_{345}]\right)^{-1}[\boldsymbol{T}_{123}]\{\boldsymbol{A}\}
\end{aligned}
\tag{3.154}
$$

Recalling Eqn.(3.137), Eqn. (3.154) can be written as

$$
\{\boldsymbol{a}\}_2 = [\mathfrak{A}_{123}]\{\boldsymbol{A}\} + [\mathfrak{A}_{321}][\boldsymbol{R}_{345}][\boldsymbol{E}][\boldsymbol{T}_{123}]\{\boldsymbol{A}\} \tag{3.155}
$$

Similarly,

$$
\begin{aligned}
\{\boldsymbol{b}\}_2 &= [\mathfrak{B}_{123}]\{\boldsymbol{A}\} + [\mathfrak{B}_{321}][\boldsymbol{R}_{345}][\boldsymbol{E}][\boldsymbol{T}_{123}]\{\boldsymbol{A}\} && (3.156) \\
\{\boldsymbol{c}\}_2 &= [\mathfrak{C}_{123}]\{\boldsymbol{A}\} + [\mathfrak{C}_{321}][\boldsymbol{R}_{345}][\boldsymbol{E}][\boldsymbol{T}_{123}]\{\boldsymbol{A}\} && (3.157) \\
\{\boldsymbol{d}\}_2 &= [\mathfrak{D}_{123}]\{\boldsymbol{A}\} + [\mathfrak{D}_{321}][\boldsymbol{R}_{345}][\boldsymbol{E}][\boldsymbol{T}_{123}]\{\boldsymbol{A}\} && (3.158)
\end{aligned}
$$

Recalling Eqns. (3.136) and (3.134), the above total constants column matrices can be written as

$$
\begin{aligned}
\{\boldsymbol{a}\}_2 &= [\mathfrak{A}_{123}]\{\boldsymbol{A}\} + [\mathfrak{A}_{321}][\boldsymbol{F}]\{\boldsymbol{A}\} && (3.159) \\
\{\boldsymbol{b}\}_2 &= [\mathfrak{B}_{123}]\{\boldsymbol{A}\} + [\mathfrak{B}_{321}][\boldsymbol{F}]\{\boldsymbol{A}\} && (3.160) \\
\{\boldsymbol{c}\}_2 &= [\mathfrak{C}_{123}]\{\boldsymbol{A}\} + [\mathfrak{C}_{321}][\boldsymbol{F}]\{\boldsymbol{A}\} && (3.161) \\
\{\boldsymbol{d}\}_2 &= [\mathfrak{D}_{123}]\{\boldsymbol{A}\} + [\mathfrak{D}_{321}][\boldsymbol{F}]\{\boldsymbol{A}\} && (3.162)
\end{aligned}
$$

where $[\boldsymbol{E}]$ and $[\boldsymbol{F}]$ are defined in (3.137) and (3.134). According to Eqns. (3.120) to (3.129), by updating the subscripts "234" to "345", the total constants column matrices in orthotropic medium 4 can be obtained as

$$\{\boldsymbol{a}\}_4 = [\boldsymbol{\mathfrak{A}}_{345}][\boldsymbol{E}][\boldsymbol{T}_{123}]\{\boldsymbol{A}\} = [\boldsymbol{\mathfrak{A}}_{345}][\boldsymbol{S}]\{\boldsymbol{A}\} \tag{3.163}$$

$$\{\boldsymbol{b}\}_4 = [\boldsymbol{\mathfrak{B}}_{345}][\boldsymbol{E}][\boldsymbol{T}_{123}]\{\boldsymbol{A}\} = [\boldsymbol{\mathfrak{B}}_{345}][\boldsymbol{S}]\{\boldsymbol{A}\} \tag{3.164}$$

$$\{\boldsymbol{c}\}_4 = [\boldsymbol{\mathfrak{C}}_{345}][\boldsymbol{E}][\boldsymbol{T}_{123}]\{\boldsymbol{A}\} = [\boldsymbol{\mathfrak{C}}_{345}][\boldsymbol{S}]\{\boldsymbol{A}\} \tag{3.165}$$

$$\{\boldsymbol{d}\}_4 = [\boldsymbol{\mathfrak{D}}_{345}][\boldsymbol{E}][\boldsymbol{T}_{123}]\{\boldsymbol{A}\} = [\boldsymbol{\mathfrak{D}}_{345}][\boldsymbol{S}]\{\boldsymbol{A}\} \tag{3.166}$$

All the characteristic matrices can be solved by the first and second canonical problems. After obtaining the constants column matrices, the displacement and stress in orthotropic media 2 and 4 can be obtained through Eqns. (3.8) and (3.9); and the waves in acoustic media 1, 3 and 5 can be obtained through Eqns. (3.130) and (3.132).

Acoustic-Orthotropic-Acoustic-Acoustic

The scatterer solved in this section has three layers, as shown in Fig. 3.7. Denote the host as medium 1, the intermediate layers as media 2 and 3, and the core of the scatterer as medium 4. Media 1, 3, and 4 are acoustic and medium 2 is orthotropic. Denote the radius of the interface between media 1 and 2, 2 and 3, and 3 and 4 as r_1, r_2, r_3, and r_4, respectively.

Following the same procedure in the Acoustic-Acoustic-Orthotropic-Acoustic case, the total waves in acoustic media 1 (host), 3 and 4 (innermost) are expressible as

$$\phi_1 = \phi^{inc} + ([\boldsymbol{R}]\{\boldsymbol{A}\})^T\{\boldsymbol{H}_1(\boldsymbol{r},\theta)\} \tag{3.167}$$

$$\phi_3 = ([\boldsymbol{S}]\{\boldsymbol{A}\})^T\{\boldsymbol{J}_3(\boldsymbol{r},\theta) + ([\boldsymbol{F}]\{\boldsymbol{A}\})^T\{\boldsymbol{H}_3(\boldsymbol{r},\theta)\} \tag{3.168}$$

$$\phi_4 = ([\boldsymbol{T}]\{\boldsymbol{A}\})^T\{\boldsymbol{J}_4(\boldsymbol{r},\theta)\} \tag{3.169}$$

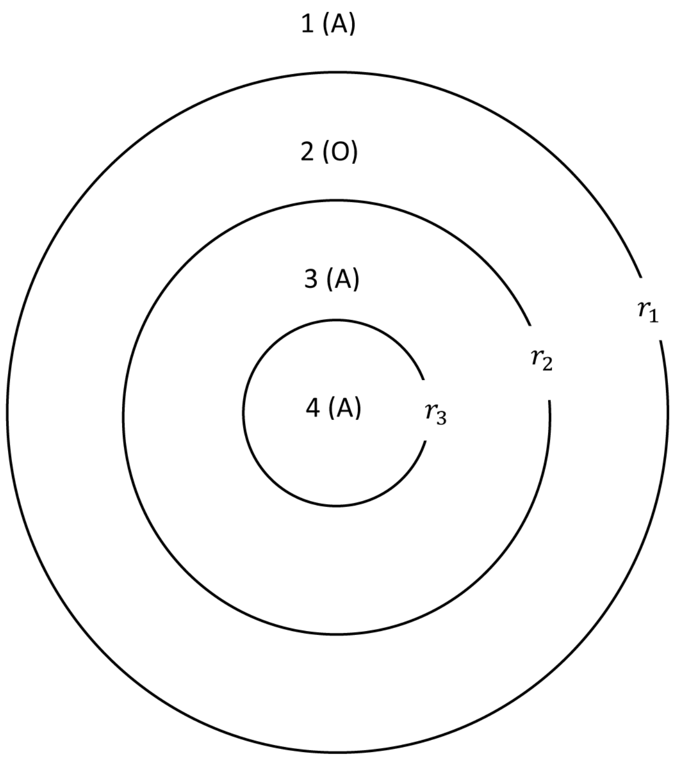

Figure 3.7: *Acoustic-Orthotropic-Acoustic-Acoustic*

The subscripts "12", "21", and "234" in the Acoustic-Acoustic-Orthotropic-Acoustic case are updated to "123", "321", and "34", respectively in this case, giving the following matrices

$$[\boldsymbol{R}] = [\boldsymbol{R}_{123}] + [\boldsymbol{T}_{321}][\boldsymbol{R}_{34}][\boldsymbol{S}] \tag{3.170}$$

$$[\boldsymbol{F}] = [\boldsymbol{R}_{34}][\boldsymbol{S}] \tag{3.171}$$

$$[\boldsymbol{T}] = [\boldsymbol{T}_{34}][\boldsymbol{S}] \tag{3.172}$$

$$[\boldsymbol{S}] = [\boldsymbol{E}][\boldsymbol{T}_{123}] \tag{3.173}$$

$$[\boldsymbol{E}] = ([\boldsymbol{I}] - [\boldsymbol{R}_{321}][\boldsymbol{R}_{34}])^{-1} \tag{3.174}$$

Following the same procedure in the Acoustic-Orthotropic-Acoustic-Orthotropic-Acoustic case, the total constants column matrices in medium 2 can be given as,

$$\{\boldsymbol{a}\}_2 = [\boldsymbol{\mathfrak{A}}_{123}]\{\boldsymbol{A}\} + [\boldsymbol{\mathfrak{A}}_{321}][\boldsymbol{F}]\{\boldsymbol{A}\} \tag{3.175}$$

$$\{\boldsymbol{b}\}_2 = [\boldsymbol{\mathfrak{B}}_{123}]\{\boldsymbol{A}\} + [\boldsymbol{\mathfrak{B}}_{321}][\boldsymbol{F}]\{\boldsymbol{A}\} \tag{3.176}$$

$$\{\boldsymbol{c}\}_2 = [\boldsymbol{\mathfrak{C}}_{123}]\{\boldsymbol{A}\} + [\boldsymbol{\mathfrak{C}}_{321}][\boldsymbol{F}]\{\boldsymbol{A}\} \tag{3.177}$$

$$\{\boldsymbol{d}\}_2 = [\boldsymbol{\mathfrak{D}}_{123}]\{\boldsymbol{A}\} + [\boldsymbol{\mathfrak{D}}_{321}][\boldsymbol{F}]\{\boldsymbol{A}\} \tag{3.178}$$

3.4.2 Solutions for a General Multilayer Scatterer

In this section, acoustic scattering by a general multilayer cylindrical scatterer is solved. A general multilayer scatterer means this scatterer can have an arbitrary number of layers and each layer can be arbitrarily chosen as isotropic fluid or orthotropic elastic. The structure for the multilayer scatterer is shown in Fig. 3.8 (Cai, 2008).

The scatterer consists of N layers, The radius of each layer is denoted as r_i ($i = 1, 2, \ldots N$), where i increases when the layer is nearer toward to the core. The radius of the innermost layer (core) is r_N. The host is called layer 0, the outermost layer is denoted

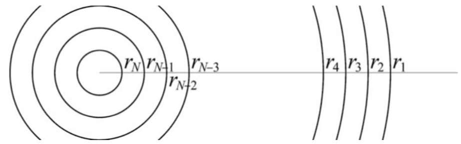

Figure 3.8: *Layer structure of the multilayer scatterer (Cai, 2008)*

as layer 1, the layer bounded by r_i and r_{i+1} is denoted as layer i, and the inner most layer is denoted as layer N.

General Solution for the Acoustic Layers of the General Scatterer

In acoustic medium 0 which is the host, the incident wave and the scattered wave are expressible as

$$\phi^{\text{inc}} = \{\boldsymbol{A}\}^T\{\boldsymbol{J}(k, \boldsymbol{r})\}, \qquad \phi^{\text{scr}} = \{\boldsymbol{B}\}^T\{\boldsymbol{H}(k, \boldsymbol{r})\} \tag{3.179}$$

The transmitted wave in the innermost layer is

$$\phi^{\text{trs}} = \{\boldsymbol{C}\}^T\{\boldsymbol{J_N}(k, \boldsymbol{r})\} \tag{3.180}$$

If layer i $(1 \leq i \leq N-1)$ is acoustic, the wave in layer i is expressible as

$$\phi^i = \{\boldsymbol{D_i}\}^T\{\boldsymbol{J_i}(k, \boldsymbol{r})\} + \{\boldsymbol{E_i}\}^T\{\boldsymbol{H_i}(k, \boldsymbol{r})\} \tag{3.181}$$

where

$$\{\boldsymbol{B}\} = [\boldsymbol{R}]\{\boldsymbol{A}\}, \quad \{\boldsymbol{C}\} = [\boldsymbol{T}]\{\boldsymbol{A}\}, \quad \{\boldsymbol{D_i}\} = [\boldsymbol{S_i}]\{\boldsymbol{A}\}, \quad \{\boldsymbol{E_i}\} = [\boldsymbol{F_i}]\{\boldsymbol{A}\} \tag{3.182}$$

The waves in acoustic media will be solved if these characteristic matrices are obtained. To solve these characteristic matrices, the strategy introduced by Cai, which is used for solving the general scatterer comprising all acoustic layers (Cai, 2008), is followed. In this study the materials of different layers need to be identified, because the layer can be orthotropic or acoustic.

Recursive Procedure

A brief introduction of the recursive procedure introduced by Cai (2008) for solving general acoustic scatterers will be given first. The same recursive procedure is adopted in this study.

For the all acoustic scatterer, the solving process starts from the innermost two layers, N and $N-1$, which are treated as media 3 and 2; layer $N-2$ is treated as medium 1. The solution of this step is directly given by the dual-layer case (Cai, 2008). Then, the innermost two layers are treated as a composite medium 3, layer $N-2$ and layer $N-3$ are treated as media 2 and 1, respectively. An intermediate series $[\boldsymbol{L}_i]$ is introduced to represent the incident wave into the composite medium 3 when layer i is treated as medium 2. The same procedure is adopted until the host is actually medium 1, layer 1 is medium 2, and layers 3 through N are treated as medium 3. The recursive equations are (Cai, 2008),

$$
\begin{aligned}
[\boldsymbol{L}_i] &= ([\boldsymbol{I}] - [\boldsymbol{\mathcal{R}}_{i(i-1)}][\boldsymbol{R}_{i+1}])^{-1}[\boldsymbol{\mathcal{T}}_{(i-1)i}] && (3.183)\\
[\boldsymbol{R}_i] &= [\boldsymbol{\mathcal{R}}_{(i-1)(i)}] + [\boldsymbol{\mathcal{T}}_{i(i-1)}][\boldsymbol{R}_{i+1}][\boldsymbol{L}_i] && (3.184)\\
[\boldsymbol{S}_i] &= \prod_{j=1}^{i}[\boldsymbol{L}_j] && (3.185)\\
[\boldsymbol{F}_i] &= [\boldsymbol{R}_{i+1}][\boldsymbol{S}_i] && (3.186)
\end{aligned}
$$

where i starts from $i = N-1$ to $i = 1$. The matrix $[\boldsymbol{R}_i]$ is defined to represent the total reflection into the host from the composite layer which includes layers i, $i+1$, ... until the innermost layer N. The total scattered wave in medium 1 and the transmitted wave in the core (layer N) are given as

$$[\boldsymbol{R}] = [\boldsymbol{R}_1], \quad [\boldsymbol{T}] = [\boldsymbol{\mathcal{T}}_{(N-1)N}][\boldsymbol{S}_{N-1}] \tag{3.187}$$

In this study, the waves in the acoustic layers of the mixed scatterer are also obtained through the recursive equations. But these recursive equations will need to be redefined according to the media of the layers which are adjacent to acoustic layer i. Four cases will be discussed.

Case 1. When layer $i+1$ and layer $i-1$ are both acoustic media, the recursive equations are the same with the all acoustic scatterer case (Cai, 2008), which are shown in Eqns. (3.183) through (3.186).

Case 2. When $i+1$ is orthotropic and layer $i-1$ is acoustic, the recursive equations can be given according to the solution for the Acoustic-Acoustic-Orthotropic-Acoustic case:

$$
\begin{aligned}
[\boldsymbol{L}_i] &= ([\boldsymbol{I}] - [\boldsymbol{\mathcal{R}}_{i(i-1)}][\boldsymbol{R}_{i+1}])^{-1}[\boldsymbol{\mathcal{T}}_{(i-1)i}] && (3.188)\\
[\boldsymbol{R}_i] &= [\boldsymbol{\mathcal{R}}_{(i-1)(i)}] + [\boldsymbol{\mathcal{T}}_{i(i-1)}][\boldsymbol{R}_{i+1}][\boldsymbol{L}_i] && (3.189)\\
[\boldsymbol{S}_i] &= \prod_{j=1}^{i}[\boldsymbol{L}_j] && (3.190)\\
[\boldsymbol{F}_i] &= [\boldsymbol{R}_{i+1}][\boldsymbol{S}_i] && (3.191)
\end{aligned}
$$

Case 3. When layer $i+1$ is acoustic and layer $i-1$ is orthotropic, the recursive equations can be given according to the solution for the Acoustic-Orthotropic-Acoustic-Acoustic case,

$$
\begin{aligned}
[\boldsymbol{L}_i] &= ([\boldsymbol{I}] - [\boldsymbol{\mathcal{R}}_{i(i-1)(i-2)}][\boldsymbol{R}_{i+1}])^{-1}[\boldsymbol{\mathcal{T}}_{(i-2)(i-1)i}] && (3.192)\\
[\boldsymbol{R}_i] &= [\boldsymbol{\mathcal{R}}_{(i-2)(i-1)(i)}] + [\boldsymbol{\mathcal{T}}_{i(i-1)(i-2)}][\boldsymbol{R}_{i+1}][\boldsymbol{L}_i] && (3.193)\\
[\boldsymbol{S}_i] &= \prod_{j=1}^{i}[\boldsymbol{L}_j] && (3.194)\\
[\boldsymbol{F}_i] &= [\boldsymbol{R}_{i+1}][\boldsymbol{S}_i] && (3.195)
\end{aligned}
$$

Since layer $i-1$ is orthotropic, for this step we set $[\boldsymbol{R}_{i-1}] = [\boldsymbol{R}_i]$

Case 4. When layer $i+1$ and layer $i-1$ are both orthotropic media, the recursive equations can be given according to the solution for the Acoustic-Orthotropic-Acoustic-

Orthotropic-Acoustic case,

$$\begin{aligned}
[\boldsymbol{L}_i] &= ([\boldsymbol{I}] - [\boldsymbol{\mathcal{R}}_{i(i-1)(i-2)}][\boldsymbol{R}_{i+1}])^{-1}[\boldsymbol{\mathcal{T}}_{(i-2)(i-1)i}] && (3.196)\\
[\boldsymbol{R}_i] &= [\boldsymbol{\mathcal{R}}_{(i-2)(i-1)(i)}] + [\boldsymbol{\mathcal{T}}_{i(i-1)(i-2)}][\boldsymbol{R}_{i+1}][\boldsymbol{L}_i] && (3.197)\\
[\boldsymbol{S}_i] &= \prod_{j=1}^{i}[\boldsymbol{L}_j] && (3.198)\\
[\boldsymbol{F}_i] &= [\boldsymbol{R}_{i+1}][\boldsymbol{S}_i] && (3.199)
\end{aligned}$$

Again, since layer $i-1$ is orthotropic, for this step we set $[\boldsymbol{R}_{i-1}] = [\boldsymbol{R}_i]$.

Since the recursive procedure starts from $i = N-1$ to $i = 1$, $[\boldsymbol{R}_N]$ needs to be solved first to enable the recursive procedure. The medium of layer $N-1$ needs to be identified to obtain $[\boldsymbol{R}_N]$. If layer $N-1$ is acoustic,

$$[\boldsymbol{R}_N] = [\boldsymbol{\mathcal{R}}_{(N-1)N}] \tag{3.200}$$

If layer $N-1$ is orthotropic,

$$[\boldsymbol{R}_N] = [\boldsymbol{\mathcal{R}}_{(N-2)(N-1)N}] \tag{3.201}$$

The characteristic matrices $[\boldsymbol{\mathcal{R}}_{(N-1)N}]$ and $[\boldsymbol{\mathcal{R}}_{(N-2)(N-1)N}]$ can be obtained by using the first canonical problem for acoustic-acoustic interface and the first canonical problem for the acoustic-orthotropic-acoustic interfaces, respectively. By substituting $[\boldsymbol{S}_i]$ and $[\boldsymbol{F}_i]$ into Eqn. (3.182), the waves in acoustic intermediate layer i are solved.

To solve the waves in the host and the innermost layer (core), the reflection matrix $[\boldsymbol{R}]$ and the transmission matrix $[\boldsymbol{T}]$ are defined as following,

$$[\boldsymbol{R}] = [\boldsymbol{R}_1] \tag{3.202}$$

if layer $N-1$ is acoustic,

$$[\boldsymbol{T}] = [\boldsymbol{\mathcal{T}}_{(N-1)N}][\boldsymbol{S}_{N-1}] \tag{3.203}$$

if layer $N-1$ is orthotropic,

$$[\boldsymbol{T}] = [\boldsymbol{\mathcal{T}}_{(N-2)(N-1)N}][\boldsymbol{S}_{N-1}] \tag{3.204}$$

General Solution for the Orthotropic Layers of the general scatterer

If layer i $(1 \leq i \leq N-1)$ is orthotropic, the constants column matrices are denoted as $\{\boldsymbol{a}\}_i$, $\{\boldsymbol{b}\}_i$, $\{\boldsymbol{c}\}_i$, $\{\boldsymbol{d}\}_i$. The expressions for these constants column matrices will need to be defined according to the materials of the layers which are adjacent to the orthotropic layer i.

Case 1. If layer $i+1$ is core, and layer $i-1$ is the host, the first canonical problem for the acoustic-orthotropic-acoustic case gives

$$\{\boldsymbol{a}\}_i = [\boldsymbol{\mathfrak{A}}_{(i-1)i(i+1)}]\{\boldsymbol{A}\} \tag{3.205}$$

$$\{\boldsymbol{b}\}_i = [\boldsymbol{\mathfrak{B}}_{(i-1)i(i+1)}]\{\boldsymbol{A}\} \tag{3.206}$$

$$\{\boldsymbol{c}\}_i = [\boldsymbol{\mathfrak{C}}_{(i-1)i(i+1)}]\{\boldsymbol{A}\} \tag{3.207}$$

$$\{\boldsymbol{d}\}_i = [\boldsymbol{\mathfrak{D}}_{(i-1)i(i+1)}]\{\boldsymbol{A}\} \tag{3.208}$$

Case 2. If layer $i+1$ is core and layer $i-1$ is not the host, then the solutions for the acoustic-acoustic-orthotropic-acoustic case and acoustic-orthotropic-acoustic-orthotropic-acoustic case are used to give

$$\{\boldsymbol{a}\}_i = [\boldsymbol{\mathfrak{A}}_{(i-1)i(i+1)}][\boldsymbol{S}_{i-1}]\{\boldsymbol{A}\} \tag{3.209}$$

$$\{\boldsymbol{b}\}_i = [\boldsymbol{\mathfrak{B}}_{(i-1)i(i+1)}][\boldsymbol{S}_{i-1}]\{\boldsymbol{A}\} \tag{3.210}$$

$$\{\boldsymbol{c}\}_i = [\boldsymbol{\mathfrak{C}}_{(i-1)i(i+1)}][\boldsymbol{S}_{i-1}]\{\boldsymbol{A}\} \tag{3.211}$$

$$\{\boldsymbol{d}\}_i = [\boldsymbol{\mathfrak{D}}_{(i-1)i(i+1)}][\boldsymbol{S}_{i-1}]\{\boldsymbol{A}\} \tag{3.212}$$

Case 3. If layer $i+1$ is not the core and layer $i-1$ is the host, the solutions for the acoustic-orthotropic-acoustic-orthotropic-acoustic case and acoustic-orthotropic-acoustic-acoustic case are used to give

$$\{\boldsymbol{a}\}_i = [\mathfrak{A}_{(i-1)i(i+1)}]\{\boldsymbol{A}\} + [\mathfrak{A}_{(i+1)i(i-1)}][\boldsymbol{F}_{i+1}]\{\boldsymbol{A}\} \tag{3.213}$$

$$\{\boldsymbol{b}\}_i = [\mathfrak{B}_{(i-1)i(i+1)}]\{\boldsymbol{A}\} + [\mathfrak{B}_{(i+1)i(i-1)}][\boldsymbol{F}_{i+1}]\{\boldsymbol{A}\} \tag{3.214}$$

$$\{\boldsymbol{c}\}_i = [\mathfrak{C}_{(i-1)i(i+1)}]\{\boldsymbol{A}\} + [\mathfrak{C}_{(i+1)i(i-1)}][\boldsymbol{F}_{i+1}]\{\boldsymbol{A}\} \tag{3.215}$$

$$\{\boldsymbol{d}\}_i = [\mathfrak{D}_{(i-1)i(i+1)}]\{\boldsymbol{A}\} + [\mathfrak{D}_{(i+1)i(i-1)}][\boldsymbol{F}_{i+1}]\{\boldsymbol{A}\} \tag{3.216}$$

Case 4. If layer $i+1$ is not the core and layer $i-1$ is not the host, solutions of case 2 and case 3 (obtained above), are used to give

$$\{\boldsymbol{a}\}_i = [\mathfrak{A}_{(i-1)i(i+1)}][\boldsymbol{S}_{i-1}]\{\boldsymbol{A}\} + [\mathfrak{A}_{(i+1)i(i-1)}][\boldsymbol{F}_{i+1}]\{\boldsymbol{A}\} \tag{3.217}$$

$$\{\boldsymbol{b}\}_i = [\mathfrak{B}_{(i-1)i(i+1)}][\boldsymbol{S}_{i-1}]\{\boldsymbol{A}\} + [\mathfrak{B}_{(i+1)i(i-1)}][\boldsymbol{F}_{i+1}]\{\boldsymbol{A}\} \tag{3.218}$$

$$\{\boldsymbol{c}\}_i = [\mathfrak{C}_{(i-1)i(i+1)}][\boldsymbol{S}_{i-1}]\{\boldsymbol{A}\} + [\mathfrak{C}_{(i+1)i(i-1)}][\boldsymbol{F}_{i+1}]\{\boldsymbol{A}\} \tag{3.219}$$

$$\{\boldsymbol{d}\}_i = [\mathfrak{D}_{(i-1)i(i+1)}][\boldsymbol{S}_{i-1}]\{\boldsymbol{A}\} + [\mathfrak{D}_{(i+1)i(i-1)}][\boldsymbol{F}_{i+1}]\{\boldsymbol{A}\} \tag{3.220}$$

After the total column matrices in orthotropic medium i are obtained, the displacement and stress can be solved through Eqns. (3.8) and (3.9).

Chapter 4

Solution Verification Through Two Approaches

In this Chapter, the solutions of acoustic scattering by multilayer scatterer which comprise a mixture of isotropic acoustic and orthotropic elastic layers are verified through two approaches. The first approach is to verify the solutions obtained in Chapter 3 via the exact analytical solutions that are obtained in this Chapter through considering the appropriate boundary conditions imposed at the surfaces of the multilayered shell. The second approach is to verify the solutions through comparison of the scattering by two pairs of scatterers. The first pair of scatterers are single layer scatterers. The second pair of scatterers are multilayer scatterers. For both pairs of scatterers, the first scatterers comprise isotropic acoustic and orthotropic elastic media, while the second scatterers are based on the first scatterers but the orthotropic elastic layers are replaced by isotropic elastic layers. The material properties of the orthotropic elastic media of the first scatterers are defined to be very close to the isotropic elastic media of the second scatterers.

4.1 Verification Via Exact Analytical Solution

4.1.1 Problem Statement

In this section, the exact analytical solutions for the acoustic-acoustic-orthotropic-acoustic case, which were solved using multiple scattering method in Chapter 3, are solved using single scattering method. For the acoutic-acoustic-orthotropic-acoustic case, media 2 and 4 are acoustic, and medium 3 is orthotropic, as shown in Fig. 3.4. Acoustic medium 1 is the host. Denote the radii of the interfaces between media 1 and 2, media 2 and 3, and media 3 and 4 as r_1, r_2, and r_3 respectively. The single scattering method is used to solve the scattering problem by considering the appropriate boundary conditions imposed at the interfaces which separate the acoustic-acoustic media, acoustic-orthotropic media, and orthotropic-acoustic media.

4.1.2 Obtaining the Exact Analytical Solution Using Single Scattering Method

The incident wave in medium 1 and the total waves in acoustic media 1, 2, and 4 are expressed in Eqns. (3.71) to (3.75). For easy reference, the expression of waves in acoustic media 1, 2, and 4 are repeated here

$$\phi_1 = \{\boldsymbol{A}\}^T\{\boldsymbol{J}(k_1,\boldsymbol{r})\} + \{\boldsymbol{B}\}^T\{\boldsymbol{H}(k_1,\boldsymbol{r})\} \tag{4.1}$$

$$\phi_2 = \{\boldsymbol{D}\}^T\{\boldsymbol{J}(k_2,\boldsymbol{r})\} + \{\boldsymbol{E}\}^T\{\boldsymbol{H}(k_2,\boldsymbol{r})\} \tag{4.2}$$

$$\phi_4 = \{\boldsymbol{C}\}^T\{\boldsymbol{J}(k_4,\boldsymbol{r})\} \tag{4.3}$$

Four characteristic matrices $[\boldsymbol{R}]$, $[\boldsymbol{T}]$, $[\boldsymbol{S}]$ and $[\boldsymbol{F}]$ are introduced to relate the wave expansion coefficient matrices of the generated waves $\{\boldsymbol{B}\}$, $\{\boldsymbol{C}\}$, $\{\boldsymbol{D}\}$ and $\{\boldsymbol{E}\}$ to the incident wave

$\{\boldsymbol{A}\}$, which are

$$\begin{aligned}
\{\boldsymbol{B}\} &= [\boldsymbol{R}]\{\boldsymbol{A}\} \\
\{\boldsymbol{C}\} &= [\boldsymbol{T}]\{\boldsymbol{A}\} \\
\{\boldsymbol{D}\} &= [\boldsymbol{S}]\{\boldsymbol{A}\} \\
\{\boldsymbol{E}\} &= [\boldsymbol{F}]\{\boldsymbol{A}\}
\end{aligned} \tag{4.4}$$

According to Eqns. (3.8) and (3.9), the displacements u_r and u_θ in orthotropic medium 3 are given as

$$u_r = \sum_{n=-\infty}^{\infty} \left[\mathsf{a}_{n3}\mathfrak{X}^1_{73}(n,r) + \mathsf{b}_{n3}\mathfrak{X}^2_{73}(n,r) + \mathsf{c}_{n3}\mathfrak{X}^3_{73}(n,r) + \mathsf{d}_{n3}\mathfrak{X}^4_{73}(n,r)\right] e^{in\theta} \tag{4.5}$$

$$= \{\boldsymbol{a}\}_3^T\{\boldsymbol{\mathfrak{X}}^1_{73}(\boldsymbol{r})\} + \{\boldsymbol{b}\}_3^T\{\boldsymbol{\mathfrak{X}}^2_{73}(\boldsymbol{r})\} + \{\boldsymbol{c}\}_3^T\{\boldsymbol{\mathfrak{X}}^3_{73}(\boldsymbol{r})\} + \{\boldsymbol{d}\}_3^T\{\boldsymbol{\mathfrak{X}}^4_{73}(\boldsymbol{r})\} \tag{4.6}$$

$$u_\theta = \sum_{n=-\infty}^{\infty} \left[\mathsf{a}_{n3}\mathfrak{X}^1_{83}(n,r) + \mathsf{b}_{n3}\mathfrak{X}^2_{83}(n,r) + \mathsf{c}_{n3}\mathfrak{X}^3_{83}(n,r) + \mathsf{d}_{n3}\mathfrak{X}^4_{83}(n,r)\right] e^{in\theta} \tag{4.7}$$

$$= \{\boldsymbol{a}\}_3^T\{\boldsymbol{\mathfrak{X}}^1_{83}(\boldsymbol{r})\} + \{\boldsymbol{b}\}_3^T\{\boldsymbol{\mathfrak{X}}^2_{83}(\boldsymbol{r})\} + \{\boldsymbol{c}\}_3^T\{\boldsymbol{\mathfrak{X}}^3_{83}(\boldsymbol{r})\} + \{\boldsymbol{d}\}_3^T\{\boldsymbol{\mathfrak{X}}^4_{83}(\boldsymbol{r})\} \tag{4.8}$$

The constants column matrices $\{\boldsymbol{a}\}_3$, $\{\boldsymbol{b}\}_3$, $\{\boldsymbol{c}\}_3$, $\{\boldsymbol{d}\}_3$ are related to those of the incident wave,

$$\begin{aligned}
\{\boldsymbol{a}\}_3 &= [\boldsymbol{\mathfrak{A}}_{234}]\{\boldsymbol{A}\} \\
\{\boldsymbol{b}\}_3 &= [\boldsymbol{\mathfrak{B}}_{234}]\{\boldsymbol{A}\} \\
\{\boldsymbol{c}\}_3 &= [\boldsymbol{\mathfrak{C}}_{234}]\{\boldsymbol{A}\} \\
\{\boldsymbol{d}\}_3 &= [\boldsymbol{\mathfrak{D}}_{234}]\{\boldsymbol{A}\}
\end{aligned} \tag{4.9}$$

The exact analytical solutions can be obtained by considering the boundary conditions at the three interfaces which separate media 1 and 2, media 2 and 3, and media 3 and 4. The boundary conditions at the acoustic-acoustic interface ($r = r_1$) which separates media 1 and 2 include: the continuity of acoustic pressure and radial component of the partial velocity, which are

$$
\begin{aligned}
A_n J_n(k_1, r_1) + B_n H_n(k_1, r_1) &= D_n J_n(k_2, r_1) + E_n H_n(k_2, r_1) && (4.10)\\
-\frac{ik_1}{\omega\rho_1}[A_n J_n'(k_1, r_1) + B_n H_n'(k_1, r_1)] &= -\frac{ik_2}{\omega\rho_2}[D_n J_n'(k_2, r_1) + E_n H_n'(k_2, r_1)] && (4.11)
\end{aligned}
$$

The boundary conditions at the acoustic-orthotropic interface ($r = r_2$) which separates media 2 and 3, and the orthotropic-acoustic interface ($r = r_3$) which separates media 3 and 4 include: continuity of normal fluid and solid velocities, continuity of acoustic pressure and the negative of the radial normal stress in the orthotropic side, and vanishing of tangential stress, which are

$$
\begin{aligned}
(-i\omega)u_r|_{r=r_2} &= v_r|_{r=r_2} && (4.12)\\
(-i\omega)u_r|_{r=r_3} &= v_r|_{r=r_3} && (4.13)\\
\sigma_{rr}|_{r=r_2} &= -p|_{r=r_2} && (4.14)\\
\sigma_{rr}|_{r=r_3} &= -p|_{r=r_3} && (4.15)\\
\sigma_{r\theta}|_{r=r_2} &= 0 && (4.16)\\
\sigma_{r\theta}|_{r=r_3} &= 0 && (4.17)
\end{aligned}
$$

The boundary conditions Eqns. (4.12) through (4.17) require,

$$\begin{aligned}
\mathsf{a}_{n3}\mathfrak{X}^1_{73}(n,r_2)+\mathsf{b}_{n3}\mathfrak{X}^2_{73}(n,r_2)+\mathsf{c}_{n3}\mathfrak{X}^3_{73}(n,r_2)+\mathsf{d}_{n3}\mathfrak{X}^4_{73}(n,r_2) &= \\
\frac{k_2}{\omega^2\rho_2}[D_nJ'_n(k_2r_2)+E_nH'_n(k_2r_2)] & \qquad (4.18)\\
\mathsf{a}_{n3}\mathfrak{X}^1_{73}(n,r_3)+\mathsf{b}_{n3}\mathfrak{X}^2_{73}(n,r_3)+\mathsf{c}_{n3}\mathfrak{X}^3_{73}(n,r_3)+\mathsf{d}_{n3}\mathfrak{X}^4_{73}(n,r_3) &= \\
\frac{k_4}{\omega^2\rho_4}C_nJ'_n(k_4r_3) & \qquad (4.19)\\
\mathsf{a}_{n3}\mathfrak{X}^1_{43}(n,r_2)+\mathsf{b}_{n3}\mathfrak{X}^2_{43}(n,r_2)+\mathsf{c}_{n3}\mathfrak{X}^3_{43}(n,r_2)+\mathsf{d}_{n3}\mathfrak{X}^4_{43}(n,r_2) &= \\
-[D_nJ_n(k_2r_2)+E_nH_n(k_2r_2)] & \qquad (4.20)\\
\mathsf{a}_{n3}\mathfrak{X}^1_{43}(n,r_3)+\mathsf{b}_{n3}\mathfrak{X}^2_{43}(n,r_3)+\mathsf{c}_{n3}\mathfrak{X}^3_{43}(n,r_3)+\mathsf{d}_{n3}\mathfrak{X}^4_{43}(n,r_3) &= -C_nJ_n(k_4r_3) \qquad (4.21)\\
\mathsf{a}_{n3}\mathfrak{X}^1_{63}(n,r_2)+\mathsf{b}_{n3}\mathfrak{X}^2_{63}(n,r_2)+\mathsf{c}_{n3}\mathfrak{X}^3_{63}(n,r_2)+\mathsf{d}_{n3}\mathfrak{X}^4_{63}(n,r_2) &= 0 \qquad (4.22)\\
\mathsf{a}_{n3}\mathfrak{X}^1_{63}(n,r_3)+\mathsf{b}_{n3}\mathfrak{X}^2_{63}(n,r_3)+\mathsf{c}_{n3}\mathfrak{X}^3_{63}(n,r_3)+\mathsf{d}_{n3}\mathfrak{X}^4_{63}(n,r_3) &= 0 \qquad (4.23)
\end{aligned}$$

Denote

$$[\mathfrak{M}_{c1}] = \begin{bmatrix}
\mathfrak{X}^1_{73}(n,r_2) & \mathfrak{X}^2_{73}(n,r_2) & \mathfrak{X}^3_{73}(n,r_2) & \mathfrak{X}^4_{73}(n,r_2)\\
\mathfrak{X}^1_{73}(n,r_3) & \mathfrak{X}^2_{73}(n,r_3) & \mathfrak{X}^3_{73}(n,r_3) & \mathfrak{X}^4_{73}(n,r_3)\\
\mathfrak{X}^1_{43}(n,r_2) & \mathfrak{X}^2_{43}(n,r_2) & \mathfrak{X}^3_{43}(n,r_2) & \mathfrak{X}^4_{43}(n,r_2)\\
\mathfrak{X}^1_{43}(n,r_3) & \mathfrak{X}^2_{43}(n,r_3) & \mathfrak{X}^3_{43}(n,r_3) & \mathfrak{X}^4_{43}(n,r_3)\\
\mathfrak{X}^1_{63}(n,r_2) & \mathfrak{X}^2_{63}(n,r_2) & \mathfrak{X}^3_{63}(n,r_2) & \mathfrak{X}^4_{63}(n,r_2)\\
\mathfrak{X}^1_{63}(n,r_3) & \mathfrak{X}^2_{63}(n,r_3) & \mathfrak{X}^3_{63}(n,r_3) & \mathfrak{X}^4_{63}(n,r_3)\\
0 & 0 & 0 & 0\\
0 & 0 & 0 & 0
\end{bmatrix} \qquad (4.24)$$

and

$$[\mathfrak{M}]_{c2} = \begin{bmatrix} 0 & 0 & -\frac{k_2}{\omega^2\rho_2}J_n'(k_2r_2) & -\frac{k_2}{\omega^2\rho_2}H_n'(k_2r_2) \\ 0 & -\frac{k_4}{\omega^2\rho_4}J_n'(k_4r_3) & 0 & 0 \\ 0 & 0 & J_n(k_2r_2) & H_n(k_2r_2) \\ 0 & J_n(k_4r_3) & 0 & 0 \\ 0 & 0 & 0 & 0 \\ 0 & 0 & 0 & 0 \\ H_n(k_1r_1) & 0 & -J_n(k_2r_1) & -H_n(k_2r_1) \\ \frac{k_1}{\rho_1}H_n'(k_1r_1) & 0 & -\frac{k_2}{\rho_2}J_n'(k_2r_1) & -\frac{k_2}{\rho_2}H_n'(k_2r_1) \end{bmatrix} \tag{4.25}$$

Next denote

$$[\mathfrak{M}]_c = \begin{bmatrix} [\mathfrak{M}]_{c1} & [\mathfrak{M}]_{c2} \end{bmatrix} \tag{4.26}$$

Then Eqns. (4.4), (4.9), (4.10), (4.11) and (4.18) through (4.23) can be solved as

$$\begin{Bmatrix} [\mathfrak{A}_{234}]_n \\ [\mathfrak{B}_{234}]_n \\ [\mathfrak{C}_{234}]_n \\ [\mathfrak{D}_{234}]_n \\ [\boldsymbol{R}]_n \\ [\boldsymbol{T}]_n \\ [\boldsymbol{S}]_n \\ [\boldsymbol{F}]_n \end{Bmatrix} = [\mathfrak{M}]_c^{-1} \begin{Bmatrix} 0 \\ 0 \\ 0 \\ 0 \\ 0 \\ 0 \\ -J_n(k_1r_1) \\ -\frac{k_1}{\rho_1}J_n'(k_1r_1) \end{Bmatrix} \tag{4.27}$$

4.1.3 Comparison of the Solutions Obtained with Two Methods

A comparison of the solutions obtained above through single scattering method and the solution obtained by using the method introduced in this study is presented in this section. One numerical example is used for solution verification. In this example, the material properties for acoustic media 1(host), 2, and 4 are listed in Table 4.1. The material

Table 4.1: *Material properties for acoustic media 1, 2, and 4*

Property	Medium 1	Medium 2	Medium 4
Density(kg/m^3)	1000	76.7201	76.7201
Sound speed(m/s)	1350	1475	1475

Table 4.2: *Material properties of the orthotropic medium 3*

Medium 3	Density(kg/m^3)	E_r(GPa)	E_θ(GPa)	$G_{r\theta}$(GPa)	$\nu_{r\theta}$
Property	1303.44	11.32	5.81	0.66	0.705128

properties of the orthotropic layer are listed in Table 4.2. Denote the radii of the interfaces between media 1 and 2, media 2 and 3, and media 3 and 4 as $r_1 = 1.2$(m), $r_2 = 1.06$(m), and $r_3 = 1$(m), respectively.

Two sets characteristic matrices are obtained through two methods. The computation is performed at frequency $ka = 1$, where k is a wavenumber, and a is the radius of innermost layer, $a = r_3 = 1$(m). The modulus of the characteristic matrices obtained through both methods are compared in Tables 4.3 and 4.4. Table 4.3 shows the results at $n = 0$. Table 4.4 shows the results at $n = 7$. The computation results have 14 significant figures.

Table 4.3: *The results and comparison for each pair of matrices at $n = 0$*

Characteristic Matrices	Single Scattering Method	Multiple Scattering Method
$\lvert[\mathfrak{A}_{234}]_n\rvert$	$1.4560747696338e-010$	$\cdots$
$\lvert[\mathfrak{B}_{234}]_n\rvert$	0	$\cdots$
$\lvert[\mathfrak{C}_{234}]_n\rvert$	$2.4406703777947e-010$	$\cdots$
$\lvert[\mathfrak{D}_{234}]_n\rvert$	0	$\cdots$
$\lvert[R]_n\rvert$	0.85157161769649	$\cdots$
$\lvert[T]_n\rvert$	0.13119554059894	$\cdots$
$\lvert[S]_n\rvert$	0.21350410606697	$\cdots$
$\lvert[F]_n\rvert$	0.045582669470002	0.045582669470003

In Tables 4.3 and 4.4, the dots $\cdots$ are used to identify the values which are identical to those of the analytical solutions for all 14 significant figures that are calculated using the stated boundary conditions. By comparing the other results shown in the two Tables, it can be found that the values obtained by the two methods only have small differences at the 13th or 14th significant figure. The small differences are considered as computation error. So the results shown in Tables 4.3 and 4.4 verify that the two solutions give identical

Table 4.4: *The results and comparison for each pair of matrices at $n = 7$*

Characteristic Matrices	Single Scattering Method	Multiple Scattering Method
$\lvert[\mathfrak{A}_{234}]_n\rvert$	$1.1253814162661e-015$	$\cdots$
$\lvert[\mathfrak{B}_{234}]_n\rvert$	$4.3288816995692e-014$	$4.3288816995693e-014$
$\lvert[\mathfrak{C}_{234}]_n\rvert$	$3.3751493747214e-015$	$3.3751493747215e-015$
$\lvert[\mathfrak{D}_{234}]_n\rvert$	$4.6661790072655e-014$	$4.6661790072656e-014$
$\lvert[R]_n\rvert$	$6.9068849846919e-010$	$6.906884984692e-010$
$\lvert[T]_n\rvert$	2.1739166880954	2.1739166880955
$\lvert[S]_n\rvert$	0.029524374236251	0.029524374236245
$\lvert[F]_n\rvert$	$4.8870447795789e-011$	$4.887044779579e-011$

results.

4.2 Verification Via Solutions for Scatterer which Comprises Both Isotropic Acoustic and Elastic Media

Acoustic scattering by scatterer which comprises both isotropic elastic and isotropic acoustic media were solved in the author's previous work and has been used for acoustic cloaking design (Bao and Cai, 2012). To verify the solutions of scattering by scatterers which comprise both isotropic acoustic and orthotropic elastic media which were obtained in this study, comparison between two pairs of scatterers are applied. The first pair of scatterers are single layer scatterers, and the second pair are multi-layer scatterers. For both pairs of scatterers, the first scatterers comprise isotropic acoustic and orthotropic elastic media. The second scatterers are based on the first ones but the orthotropic elastic layers are replaced by isotropic elastic layers. The material properties of the orthotropic elastic media of the first scatterers are defined to be very close to the isotropic elastic media of the second scatterers. Numerical simulations are implemented for the comparison. Details are provided in the following subsections.

Table 4.5: *Material properties for the media of the host and the core.*

Property	Host	Core
Density(kg/m^3)	1000	76.7201
Sound speed(m/s)	1350	1475

4.2.1 Single Layer Scatterer

In this example, numerical simulations of scattering by two single layer scatterers are performed. The first scatterer comprises an orthotropic elastic layer. The inner and outer radii of the scatterer are defined as $a = 0.6$(m), and $b = 1$(m), respectively. The core is denoted as acoustic material. The host is assumed as water. The material properties for the host and the core are listed in Table 4.5. The second scatterer is based on the first scatterer, but the orthotropic elastic layer is replaced by an isotropic elastic layer. The material properties of the orthotropic elastic medium of the first scatterer are defined to be very close to the isotropic elastic medium of the second scatterer.

For a plane-strain problem, the stress-strain relations of the orthotropic materials in stiffness form are

$$\begin{bmatrix} \sigma_{rr} \\ \sigma_{\theta\theta} \\ \sigma_{r\theta} \end{bmatrix} = \begin{bmatrix} C_{11} & C_{12} & 0 \\ C_{12} & C_{22} & 0 \\ 0 & 0 & C_{44} \end{bmatrix} \begin{bmatrix} \varepsilon_{rr} \\ \varepsilon_{\theta\theta} \\ 2\varepsilon_{r\theta} \end{bmatrix} \tag{4.28}$$

where C_{ij} are four independent elastic constants. The stress-strain relations of the isotropic materials in stiffness form are

$$\begin{bmatrix} \sigma_{rr} \\ \sigma_{\theta\theta} \\ \sigma_{r\theta} \end{bmatrix} = \begin{bmatrix} 2\mu+\lambda & \lambda & 0 \\ \lambda & 2\mu+\lambda & 0 \\ 0 & 0 & \mu \end{bmatrix} \begin{bmatrix} \varepsilon_{rr} \\ \varepsilon_{\theta\theta} \\ 2\varepsilon_{r\theta} \end{bmatrix} \tag{4.29}$$

where λ and μ are Lamé constants. According to the Eqns. (4.28) and (4.29), if $C_{11} = C_{22} = 2\mu + \lambda$, $C_{12} = \lambda$, and $C_{44} = \mu$, the orthotropic elastic material is actually an isotropic

Table 4.6: *Material properties of the orthotropic medium*

E_r(GPa)	E_θ(GPa)	$G_{r\theta}$(GPa)	$\nu_{r\theta}$	C_{11}(GPa)	C_{12}(GPa)	C_{22}(GPa)
13.2098684	13.2098684	4.85	0.361842	15.2	5.5	15.2

elastic material.

At first, the material properties of the orthotropic elastic layer of the first scatterer are defined to have the same properties with the isotropic elastic layer of the second scatterer. The mass densities of the orthotropic layer (ρ_o) and the elastic layer (ρ_e) are assumed to be the same, which are

$$\rho_{\mathrm{o}} = \rho_{\mathrm{e}} = 1303.44(\mathrm{kg/m^3}) \tag{4.30}$$

The Lamé constants of the isotropic elastic material are defined as

$$\lambda = 5.5(\mathrm{GPa}), \quad \mu = 4.85(\mathrm{GPa}) \tag{4.31}$$

The material properties of the orthotropic material are listed in Table 4.6. So we have $C_{11} = C_{22} = 2\mu+\lambda = 9.7+5.5 = 15.2(\mathrm{GPa})$, $C_{12} = \lambda = 5.5$ and $C_{44} = G_{r\theta} = \mu = 4.85(\mathrm{GPa})$, which means the orthotropic elastic medium is defined to be the same as the isotropic elastic medium. Then the numerical simulation of acoustic scattering by the two scatterers are implemented at frequency $ka = 0.6$. To verify the solutions, the value of 0-th mode of the characteristic matrices $[\boldsymbol{T}]$ from both methods are obtained. The modulus of $[\boldsymbol{T}]_0$ for the orthotropic case is

$$|[\boldsymbol{T}]_0| = 0.28960048500297 \tag{4.32}$$

The modulus of $[\boldsymbol{T}]_0$ for the elastic case is

$$|[\boldsymbol{T}]_0| = 0.28960048500296 \tag{4.33}$$

The two solutions only have a slight difference at the 14th significant figure, which is considered as computing error. Thus, the two solutions are identical.

Table 4.7: *Modulus of $[\boldsymbol{T}]_0$ for the orthotropic scatterer, when the value of Young's modulus along axis r is changing.*

E_r (GPa)	13.2098684	13.2198684	13.2398684	13.3098684	14.3098684	19.3098684
$\lvert[\boldsymbol{T}]_0\rvert$	0.2896	0.28958	0.289538	0.289395	0.287495	0.28093

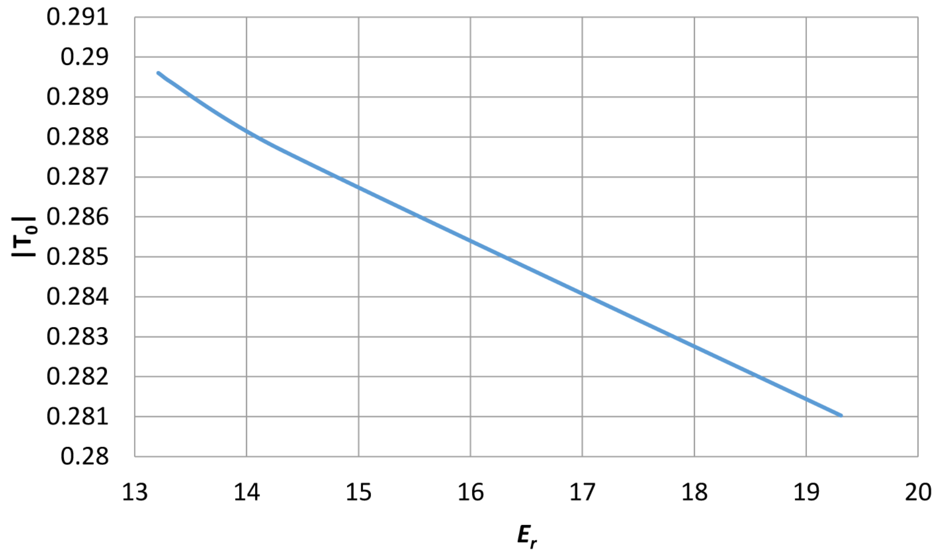

Figure 4.1: *Modulus of $[\boldsymbol{T}]_0$ for the orthotropic-acousitc case at different E_r*

Then, for the orthotropic elastic medium, the Young's modulus along the radial direction (E_r) is increased incrementally, while the other properties are held constant. Table 4.7 shows the different values of E_r that are taken and the simulation results of $\lvert[\boldsymbol{T}]_0\rvert$ under different E_r. From 4.7 it can be found that when $E_r = 13.2098684$, which is the situation when the orthotropic elastic medium is the same as the isotropic elastic medium, the simulation results of $\lvert[\boldsymbol{T}]_0\rvert$ for both cases are identical. When E_r is chosen larger and larger, $\lvert[\boldsymbol{T}]_0\rvert$ gets smaller and smaller. Fig. 4.1 also shows the modulus of $[\boldsymbol{T}]_0$ when E_r is chosen differently. Fig. 4.1 is plotted based on the data listed in Table 4.7. It is easy to see from Fig. 4.1 that when the value of E_r gets further from the original value of 13.2098684 (GPa), the modulus of $[\boldsymbol{T}]_0$ also deviates further from its original value of 0.2896. The curve is smooth without a rapid fluctuation, which can be a verification of the solutions obtained in this study.

Fig. 4.2 shows the total acoustic pressure distribution due to impinging of the pla-

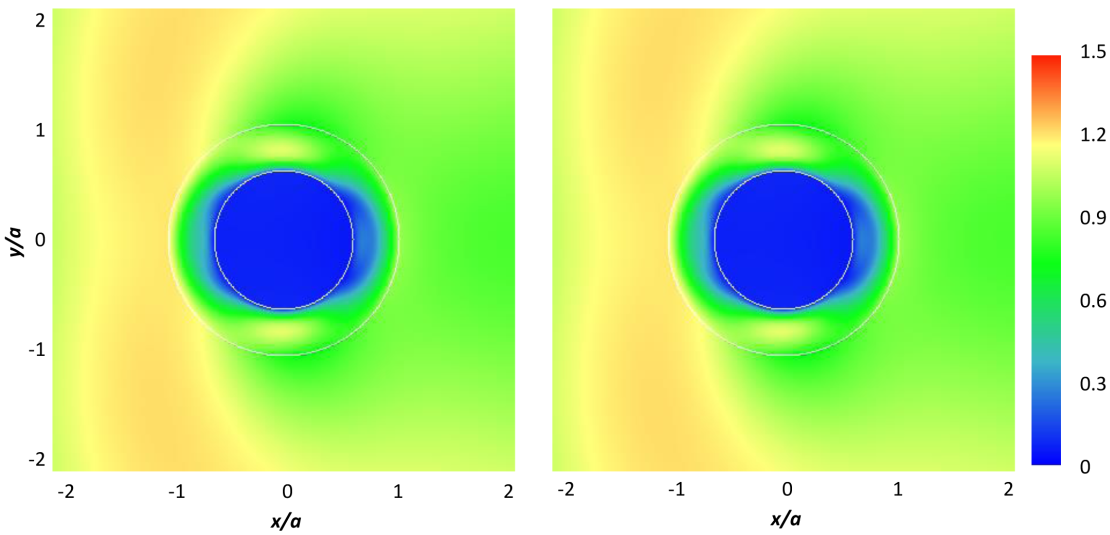

Figure 4.2: *Total acoustic pressure field. Left: orthotropic scatterer; Right: elastic scatterer.*

nar incident wave onto the scatterers comprising orthotropic (left) and elastic (right) layers. The Young's Modulus of the orthotropic layer along r direction is taken as $E_r =$ 13.30986842(GPa) which is slightly different with the original value 13.209868(GPa). Other properties of the orthotropic elastic medium are kept the same with those listed in Table 4.6. So in this case, the orthotropic elastic medium of the first scatterer is defined to be very close to the isotropic elastic medium of the second scatterer. Fig. 4.2 shows that the total acoustic pressure field of both cases are almost identical. So the solutions are further verified.

Another way to verify the solutions obtained in this study is the continuity of the pressure amplitude distributions. The boundary conditions at each interface define the canonical problems. One of the conditions is the continuity of radial normal stress in the orthotropic side and the negative of the acoustic pressure in the acoustic side. The continuity should be satisfied at all the interfaces. Fig. 4.2 shows the continuity of the pressure amplitude distributions and the radial normal stress distributions in acoustic layer and orthotropic layer of the scatterer. The white circles are used to show the exterior boundary of the scatterer and the boundary of the core. Thus, the continuity of the pressure field shown in

Fig. 4.2 is also a verification of the solutions.

4.2.2 Multiple Layer Scatterer

In this example, scattering by two multilayer scatterers are solved through numerical simulation. Both scatterers have ten layers of the same thickness. For the first scatterer, the even numbered layers are orthotropic elastic media and the odd numbered layers are isotropic acoustic media. For the second scatterer, the even numbered layers are isotropic elastic media and the odd numbered layers are isotropic acoustic media. The inner-most and outer-most radii of both scatterers are $a = 1$(m) and $b = 1.2a$, respectively.

The material properties of the host, core, acoustic layers, orthotropic elastic layers, and isotropic elastic layers of both scatterers are the same as those in the example shown in Fig. 4.2.

The simulations are run at frequency $ka = 1$ and 3. Both scattering simulations use the same planar incident wave. Fig. 4.3 shows the simulation results of the total acoustic field. Fig. 4.3 (a1)-(a2) show the results of the scattering by the first scatterer which comprises orthotropic elastic layers at frequency $ka = 1$ and 3, respectively. Fig. 4.3 (b1)-(b2) show the results of the scattering by the second scatterer which comprises isotropic elastic layers at frequency $ka = 1$ and 3, respectively.

It is apparent from Fig. 4.3 that the simulation results of both cases obtained with different methods are almost identical. This further verifies the solutions for multi-layer scatterers obtained in this study. Another verification is the continuity of acoustic pressure inside the 10 layer scatterer. It is easy to find from Fig. 4.3 that the pressure field is continuous at both the inside and outside of the scatterer.

For a more in-depth view, the modulus of acoustic pressure p along radial direction ($\theta = 0$) for both cases at frequency $ka = 1$ and $ka = 3$ are shown in Fig. 4.4 and Fig. 4.5, respectively. The calculation pitch of the point along radial direction is $r = 0.005$. The values of modulus of acoustic pressure for both cases are different. But the values are too

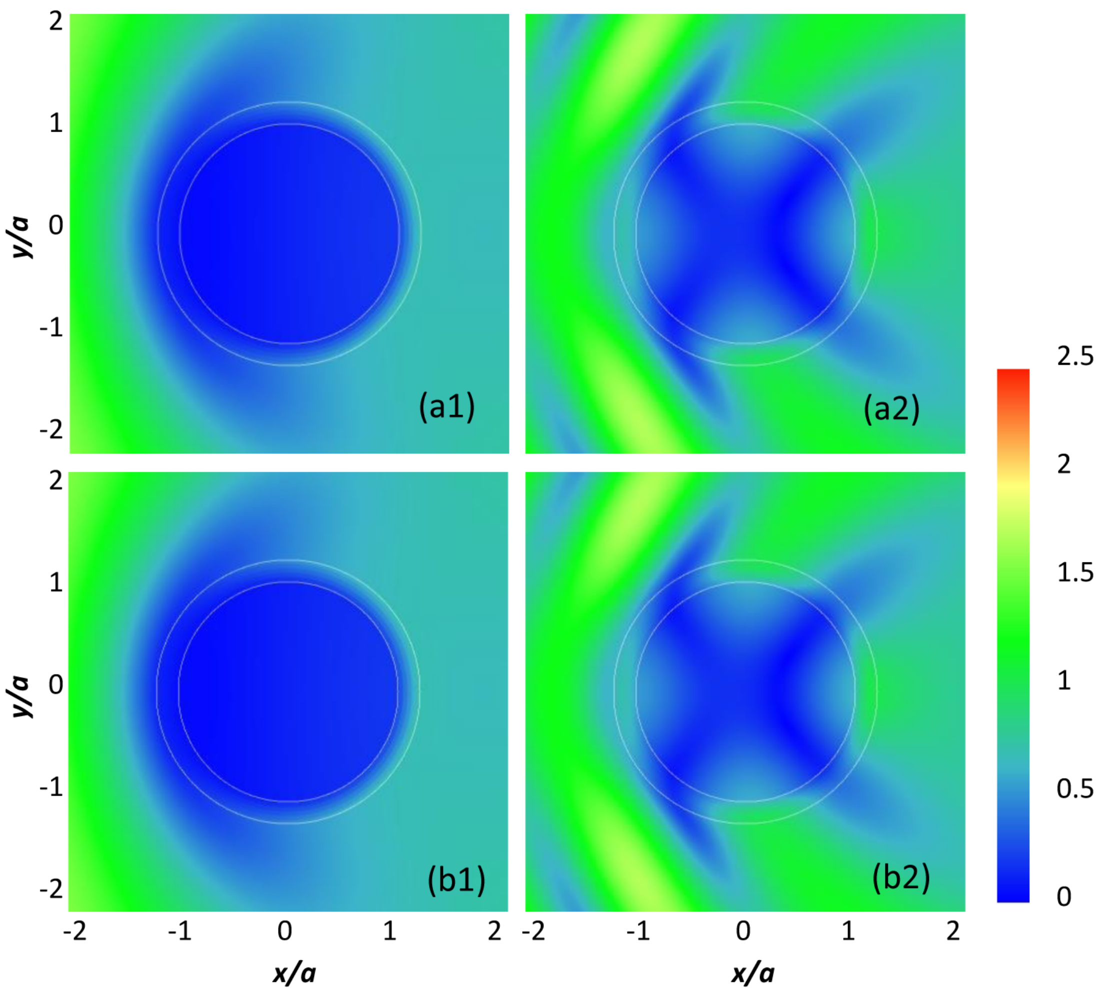

Figure 4.3: *Total acoustic pressure field. (a1)-(a2): scattering by the scatterer having orthotropic elastic layers at frequency $ka = 1, 3$, respectively; (b1)-(b2): scattering by the scatterer having isotropic elastic layers at frequency $ka = 1, 3$, respectively.*

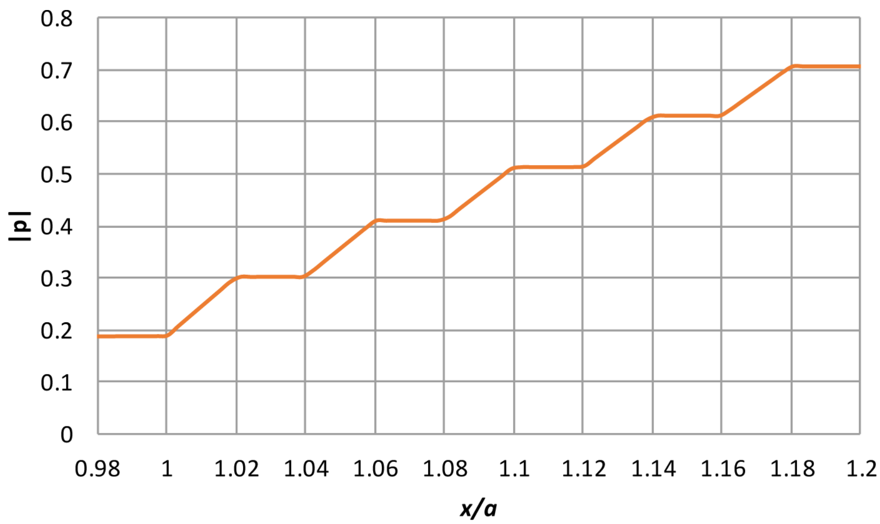

Figure 4.4: *Modulus of acoustic pressure along radial direction (*$0.98 < x/a < 1.2$*,* $y/a = 0$*) for both cases at frequency* $ka = 1$*.*

close to show different curves in Fig. 4.4 and Fig. 4.5. Both figures show the continuity of acoustic pressure along radial direction from $x/a = 0.98$ to $x/a = 1.2$ $(y/a = 0)$.

Table 4.8 provides the values of modulus of acoustic pressure along radial direction ($0.98 < x/a < 1.2$, $y/a = 0$) of both cases. The first column shows the values of r around interfaces of all the layers, the second and third columns show the modulus of pressure of both cases at frequency $ka = 1$, and the fourth and fifth columns show the modulus of pressure of both cases at frequency $ka = 3$. In Table 4.8, O and E stand for the scatterer having orthotropic elastic layers and isotropic elastic layers, respectively. The values in Table 4.8 show that the results for both cases are very close to each other. The difference of the results of both cases start from around the fifth significant figure.

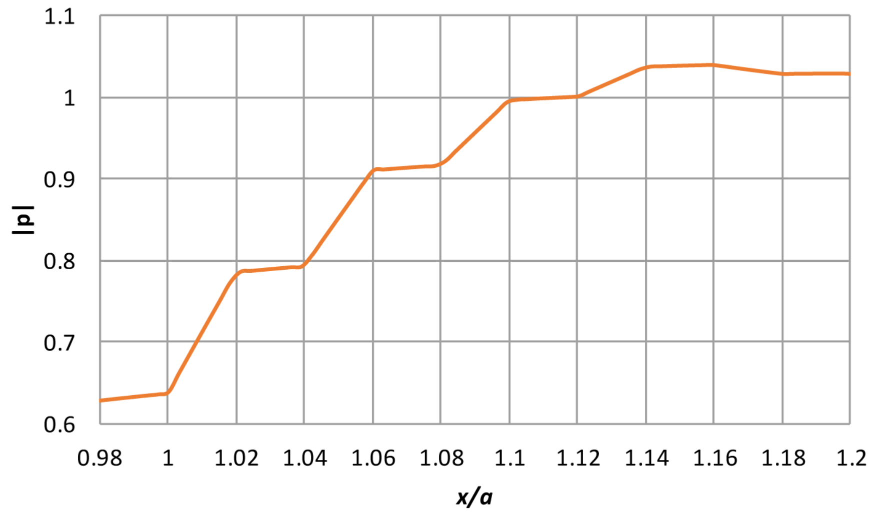

Figure 4.5: *Modulus of acoustic pressure along radial direction ($0.98 < x/a < 1.2$, $y/a = 0$) for both cases at frequency $ka = 3$.*

Table 4.8: *Modulus of acoustic pressure along radial direction ($0.98 < x/a < 1.2$, $y/a = 0$) for both cases*

x/a	$\|p\|$			
	O($ka = 1$)	E($ka = 1$)	O($ka = 3$)	E($ka = 3$)
0.97922403	0.187349661	0.187353236	0.627828691	0.627941587
1.000250313	0.189293152	0.189296586	0.638898554	0.639014488
1.021276596	0.301762207	0.301771641	0.785981826	0.786104438
1.039299124	0.302147948	0.30215724	0.792808124	0.792932953
1.060325407	0.409861799	0.409876662	0.910574367	0.910694279
1.08135169	0.417181161	0.417196218	0.921981232	0.922101718
1.099374218	0.509801476	0.509821416	0.993940522	0.994043885
1.120400501	0.5152033799	0.515223526	1.00145534	1.001558855
1.141426783	0.611911319	0.611936767	1.03757957	1.037649289
1.159449312	0.611966543	0.611991943	1.03966472	1.039735142
1.180475594	0.7069115441	0.706942465	1.02870718	1.028727155
1.201501877	0.706569391	0.706600245	1.02831336	1.028333493

Chapter 5

Scattering Numerical Simulations

Theoretical solutions of scattering by multilayer scatterers which include orthotropic materials were solved in Chapter 3, and solutions were verified in Chapter 4. A computational system is built in this study based on the theoretical solutions obtained in Chapter 2 and Chapter 3. In this Chapter, numerical simulations of acoustic scattering by different scatterers are applied through the computational system.

5.1 Simulations of Acoustic Scattering by an Orthotropic Pipe

In this section, acoustic scattering by an orthotropic pipe are calculated. The incident wave is a planar incident wave, which is specified in the following form:

$$p^{inc} = \sum_{n=-\infty}^{\infty} A_n J_n(kr) e^{in\theta} = \{\boldsymbol{A}\}^T \{\boldsymbol{J}(r,\theta)\} \tag{5.1}$$

The idea of the simulations in this section is to maintain the material properties of the orthotropic pipe while varying the material properties of the host and core of the scatterer for different examples. Then scattering phenomena of different examples will be observed through the simulation results.

The material properties of the orthotropic pipe include (Young's and shear moduli being in GPa): $E_r = 3.132$, $E_\theta = 2.081$, $G_{r\theta} = 0.66$, $\nu_{r\theta} = 0.205128$, and $\rho_o = 1303.44(\mathrm{kg/m^3})$. The inner and outer radii of the pipe are $a = 1(\mathrm{m})$ and $b = 1.2a$, respectively.

The following two examples are analyzed in this section: 1) the host and core (innermost layer) are both defined as water and 2) the host and core are both defined as air. Material properties of air at 10 °C include: mass density $\rho_a = 1.24664(\mathrm{kg/m^3})$ and sound speed $c_a = 337.31(\mathrm{m/s})$. The material properties of water at 10 °C include: $\rho_w = 999.7281(\mathrm{kg/m^3})$ and $c_w = 1447.29(\mathrm{m/s})$.

In the computations, the infinite series of summations ($\sum_{n=-\infty}^{n=\infty}$) is not realizable. So the number of n needs to be truncated at the N_tth term, which we call the truncation number. The results get smaller when term n is increased. When $n > N_t$, the results are too small to be added to the summation. In this case, the summation will not change when $n > N_t$. For both examples, the truncation numbers are chosen as 14, 24, and 36 at frequency $ka = 2$, 4, and 6, respectively.

Fig. 5.1 shows the total acoustic pressure distribution when a planar incident wave encounters the orthotropic pipe. Fig. 5.1, (a1)-(a3) show the case when the host and core are both water at $ka = 2$, 4, and 6, respectively; (b1)-(b3) show the case when the host and core are both air at $ka = 2$, 4, and 6, respectively.

Fig. 5.1 shows that when the planar incident wave impinges onto the orthotropic pipe, some pressure beams form. Both cases reveal that when frequency is increased, the beams get narrower and the number of beams increases. It also can be found that the beams in Fig. 5.1 (a1)-(a3) are not as clear as those in Fig. 5.1 (b1)-(b3), especially at lower frequency ($ka = 2$, and 4). Clearly, if the host, scatterer, and core are made of the same material, the pressure should be the same everywhere which means no pressure beams will be found in the pressure field. For the first case, the mass densities of the host and the orthotropic pipe are fairly close. The sound speeds of the pipe along radial and tangential directions can be

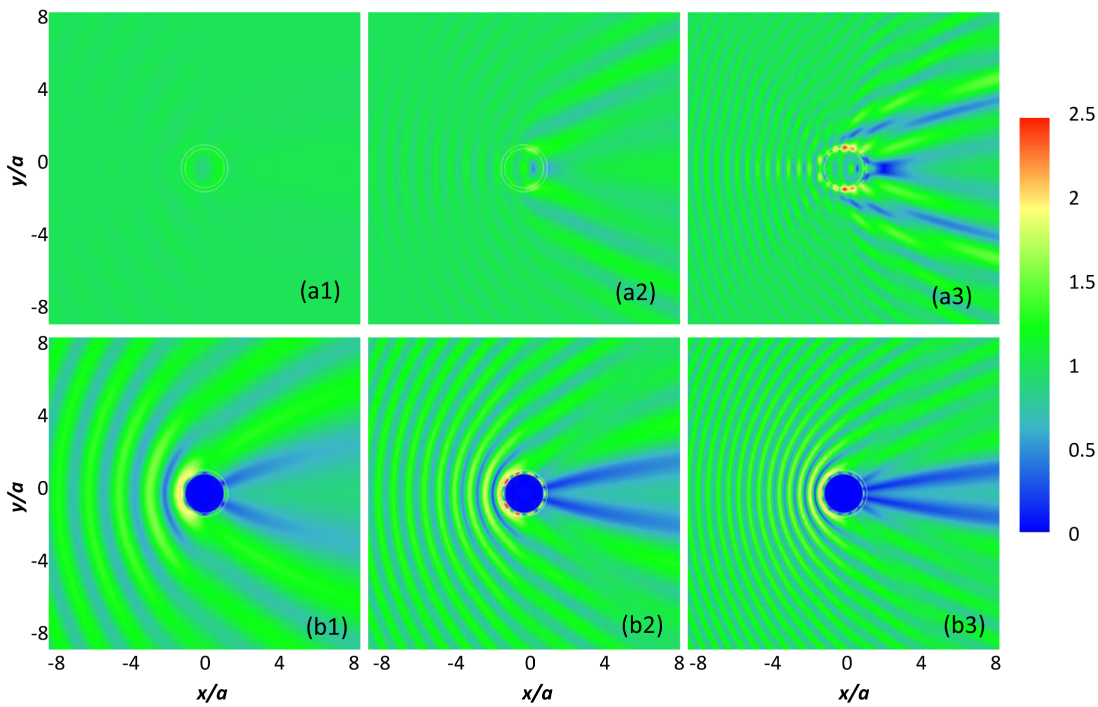

Figure 5.1: *Total acoustic pressure field due to impinging of a planar incident wave onto a orthotropic pipe. [(a1)-(a3)]: the case which has the host defined as water and the pipe is filled with water at frequency $ka = 2, 4, 6$, respectively. [(b1)-(b3)]: the case which has the host defined as air and the pipe is filled with air at frequency $ka = 2, 4, 6$, respectively.*

given as the following (Aauld, 1973; Dahmen et al., 2010)

$$c_r = \sqrt{\frac{C_{11}}{\rho_o}} = 1572.52(\text{m/s}), \quad c_\theta = \sqrt{\frac{C_{22}}{\rho_o}} = 1281.8(\text{m/s}) \tag{5.2}$$

where C_{11} and C_{22} are the independent elastic constants along r and θ directions. Eqn. (5.2) shows that the sound speeds of the orthotropic pipe along two directions are both fairly close to the sound speed of water. For the second case, the host and core are both air; which has significantly different material properties compared to the orthotropic pipe.

5.2 Scattering Simulation Study Through Parametric Changing of Orthotropic Medium

As discussed in the earlier chapters, having different sound speeds along axes r and θ is important for designing acoustic cloaks. For orthotropic medium, we have (Aauld, 1973; Dahmen et al., 2010)

$$c_r/c_\theta = \sqrt{E_r/E_\theta} \tag{5.3}$$

Therefore, different Young's moduli of the orthotropic layer along radial (E_r) and tangential (E_θ) directions would be helpful for the future design of acoustic cloaks. In this section, some numerical simulations of scattering by scatterers which have single orthotropic layer are studied. For each scatterer, the Young's moduli of the orthotropic layer are defined differently. The simulations are started from the case when E_r and E_θ of the orthotropic medium are about the same. Then more simulations are implemented with $E_r > E_\theta$ and $E_r < E_\theta$. The incident wave is the same as for the simulations of the previous section.

The core of the scatterer is assumed as acoustic medium, whose material properties include: mass density $\rho_a = 76.7201(\text{kg/m}^3)$ and sound speed $c_a = 1475(\text{m/s})$. The host is assumed to be water, whose material properties include: $\rho_w = 1000(\text{kg/m}^3)$ and sound speed $c_w = 1350$(m/s). The material properties of the core and the host are kept the same through all the simulations in this section.

5.2.1 Young's Modulus Along Radial Direction (E_r) Greater Than That Along Tangential Direction (E_θ)

Simulation 1: $E_r/E_\theta \approx 1$

For this example, the material properties of the orthotropic layer are defined as (Young's and shear moduli being in GPa): $E_r = 13.309868$, $E_\theta = 12.2$, $G_{r\theta} = 6.3$, $\nu_{r\theta} = 0.01$, and $\rho_o = 1303.44(\text{kg/m}^3)$. The independent elastic constants of the orthotropic medium are given as (in GPa): $C_{11} = 13.31$, $C_{22} = 12.2$, $C_{12} = 0.122$, $C_{44} = G_{r\theta} = 6.3$. For this case, the Young's moduli E_r and E_θ are about the same, which has the ratio $E_r/E_\theta = 1.091$. The simulation is run at frequency $ka = 2$, 4, and 6. The radius of the core is $a = 1$(m), and the outer radius of the scatterer is $b = 1.2a$.

The sound speeds along r and θ directions are given as

$$c_r = \sqrt{\frac{C_{11}}{\rho_o}} = 3196.2(\text{m/s}), \quad c_\theta = \sqrt{\frac{C_{22}}{\rho_o}} = 3059.44(\text{m/s}) \tag{5.4}$$

The above Eqn. (5.4) shows that the sound speeds c_r and c_θ are very close. The truncation numbers N_t are chosen as 14, 24, and 33 at frequency $ka = 2$, 4, and 6, respectively.

Table 5.1 provides the the entries of coefficient matrix $\{\boldsymbol{R}\}$ which represents the scattered waves. In Table 5.1 the N_t denotes the truncation numbers 14, 24, and 33 for three frequencies $ka = 2$, 4, and 6, respectively. Table 5.1 shows that the value of $|R|$ decreases when the terms n gets higher. At lower frequency the decreasing of $|R|$ is faster, while at higher frequency the decreasing of $|R|$ is slower. So the value of the truncation number N_t needs to be chosen larger at higher frequency. Table 5.1 also shows that at frequency $ka = 2$, 4 and 6, the values of $|R|$ are very small at the terms of 14, 24, and 33, respectively.

Table 5.1: *The entries of coefficient matrix $\{\boldsymbol{R}\}$ at different terms (shown in modulus) for the $E_r/E_\theta \approx 1$ case*

n	$\lvert[R]_{nn}\rvert$		
	$ka = 2$	$ka = 4$	$ka = 6$
0	0.06641936962334	0.99930784471137	0.71115871340874
1	0.4322323720724	0.41621241690061	0.45648199404495
2	0.3831892812302	0.99977358576407	0.90210915516909
3	0.092604051921764	0.84953554395498	0.52125198567453
4	0.018601256055423	0.4560484737499	0.74058077954076
5	0.0062296600947761	0.17491766960125	0.88061247947373
6	0.00064479295075777	0.07145010379986	0.5403408940378
7	$1.1006744387488 \times 10^{-5}$	0.038068031945226	0.28900243200937
8	$2.4310709871511 \times 10^{-7}$	0.1057271903407	0.17568692076832
9	$4.6543374844228 \times 10^{-9}$	0.00087603019751202	0.12659138840631
10	$7.378263871253 \times 10^{-11}$	$4.4411847857065 \times 10^{-5}$	0.4710494769391
N_t	$7.9398155089316 \times 10^{-19}$	$2.2030190312324 \times 10^{-28}$	$3.3366305542292 \times 10^{-36}$

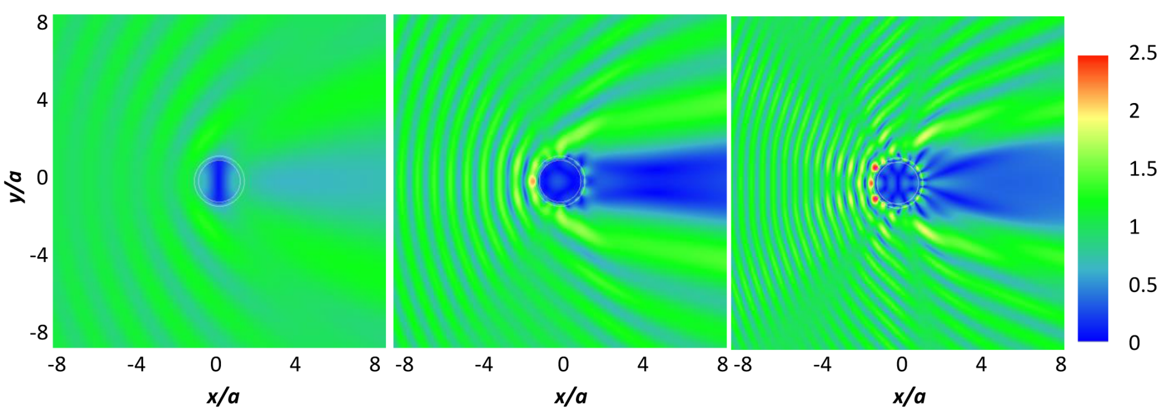

Figure 5.2: *Total acoustic pressure field for the $E_r/E_\theta \approx 1$ case, at frequency $ka = 2$ (left), 4 (middle), and 6 (right).*

When $n > N_t$, the value of $|R|$ become small enough that it can be truncated. The error is assumed in the order of the term N_t.

Fig. 5.2 shows the total acoustic pressure field at frequency $ka = 2$, 4, and 6, respectively. In Fig. 5.2, the scatterer is too small to observe the acoustic pressure inside of it. Fig. 5.3 provides the enlarged view of the pressure field near the scatterer. It can be found from Fig. 5.3 that the pressure is continuous everywhere in the pressure field, which includes the inside and outside of the scatterer. The continuity of the pressure field is a validation of the

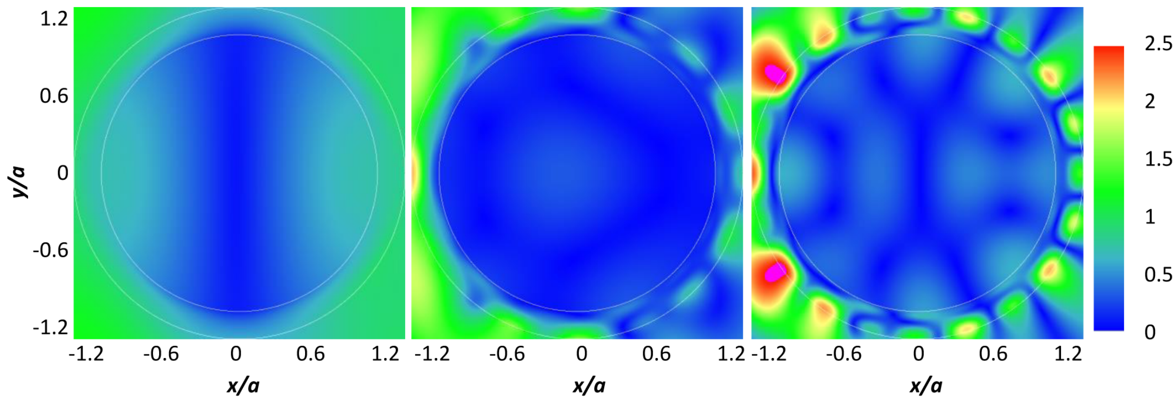

Figure 5.3: *Enlarged view of pressure field around scatterer for the $E_r/E_\theta \approx 1$ case, at frequency $ka = 2$ (left), 4 (middle), and 6 (right).*

solution and simulation.

Simulation 2: $E_r/E_\theta \approx 10$

For this example, the Young's modulus of the orthotropic layer along radial direction is taken as $E_r = 133.09868$ (GPa). Since E_r is changed, the corresponding independent elastic constant C_{11} is also changed. Here $C_{11} = 133.1$ (GPa). Other properties of the orthotropic layer are kept the same as those in the last example. The inner and outer radii of the scatterer are also the same; these are $a = 1$(m) and $b = 1.2a$, respectively. The ratio of Young's Moduli along radio an tangential directions is: $E_r/E_\theta = 133.09868/12.2 = 10.91$. The simulation is run at frequency $ka = 2$, 4, and 6.

The sound speeds along r and θ directions are given as

$$c_r = \sqrt{\frac{C_{11}}{\rho_o}} = 10105.16(\text{m/s}), \quad c_\theta = \sqrt{\frac{C_{22}}{\rho_o}} = 3059.44(\text{m/s}) \tag{5.5}$$

The truncation number N_t of this case at $ka = 2$, 4, and 6 are the same as for the previous simulation, which are 14, 24, and 33, respectively.

Table 5.2 provides the the entries of coefficient matrix $\{\boldsymbol{R}\}$ which represents the scattered waves. By comparing the entries of the coefficient matrix $\{\boldsymbol{R}\}$ shown in Table 5.1 and Table

Table 5.2: *The entries of coefficient matrix* $\{\boldsymbol{R}\}$ *at different terms (shown in modulus) for the* $E_r/E_\theta \approx 10$ *case*

n	$\lvert[R]_{nn}\rvert$		
	$ka = 2$	$ka = 4$	$ka = 6$
0	0.066475033414755	0.99796507280763	0.73178282337258
1	0.45895672330272	0.42398529407813	0.44376491934169
2	0.38706167972956	0.99997888420932	0.91474948225914
3	0.09400193999563	0.86287657469474	0.4828172453602
4	0.018810439728244	0.46964722085198	0.7264414168943
5	0.006247349601539	0.18186725301678	0.90081713559685
6	0.00063676615892458	0.072896128100458	0.56603142495105
7	$1.0896410560018 \times 10^{-5}$	0.038199331559288	0.30278376546104
8	$2.4081475231618 \times 10^{-7}$	0.080680810543282	0.17826928558071
9	$4.6133147519763 \times 10^{-9}$	0.0008360679809522	0.12781828619718
10	$7.3177890391773 \times 10^{-11}$	$4.2743881619159 \times 10^{-5}$	0.92970220593882
N_t	$7.89118388 \times 10^{-19}$	$2.1740482713822 \times 10^{-28}$	$3.2759768093569 \times 10^{-36}$

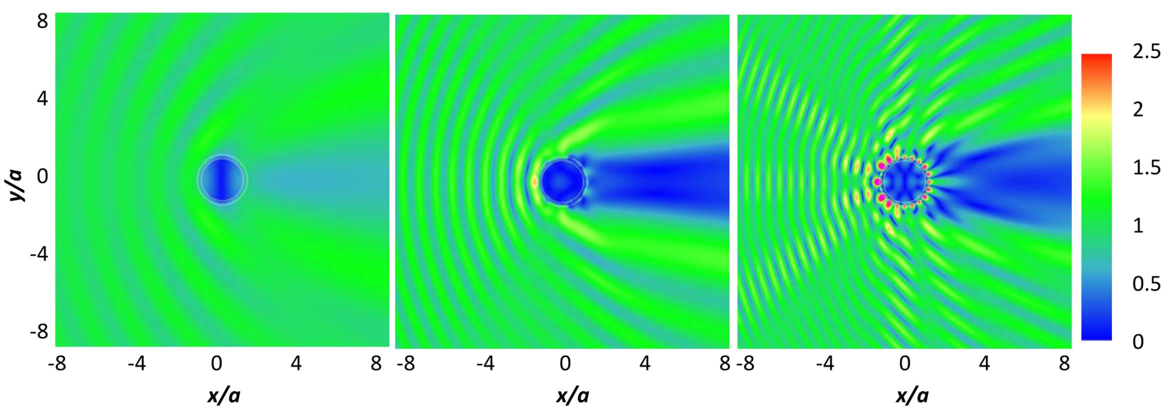

Figure 5.4: *Total acoustic pressure field for the* $E_r/E_\theta \approx 10$ *case, at frequency* $ka = 2$ *(left), 4 (middle), and 6 (right).*

5.2, it can be found that the entries of the coefficient matrix $\{\boldsymbol{R}\}$ are not very different at lower frequency $ka = 2$ and 4. The biggest difference is 0.02. At frequency $ka = 6$, the entries of the coefficient matrix $\{\boldsymbol{R}\}$ for the case $E_r/E_\theta \approx 10$ are bigger.

Fig. 5.4 shows the total acoustic pressure field at frequency $ka = 2$, 4, and 6, respectively. Fig. 5.5 provides a enlarged view of the pressure field near the scatterer. It can be observed from Figs. 5.4 and 5.5 that at lower frequency $ka = 2$ and 4, the pressure fields are similar with those shown in Figs. 5.2 and 5.3. At frequency $ka = 6$, the acoustic pressure around

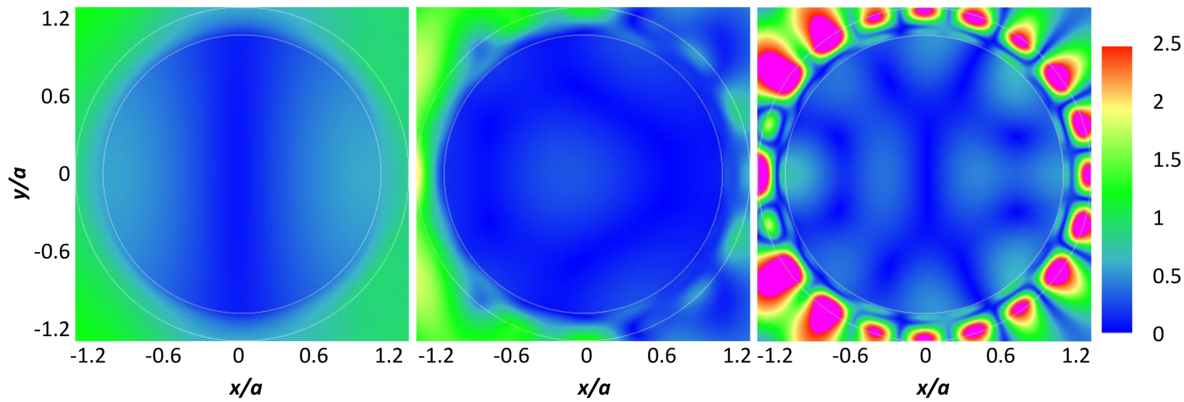

Figure 5.5: *Enlarged view of pressure field around scatterer for the $E_r/E_\theta \approx 10$ case, at frequency $ka = 2$ (left), 4 (middle), and 6 (right).*

the interface between the host and the scatterer is obviously higher than the one for the previous case when $E_r/E_\theta \approx 1$. In Fig. 5.5 (right), there are some places that are bright pink which is because the acoustic pressure there is higher than the maximum value (2.5) for the color bar. The same pressure field is shown in Fig. 5.6 but with the maximum value of the pressure for the color bar increased to 3.5. The continuity of the acoustic pressure field shown in Figs. 5.5 and 5.6 can validate the simulation results.

Simulation 3: $E_r/E_\theta \approx 100$

For this example, the material properties of the orthotropic layer are the same with those of the previous example, except that $E_r = 1330.9868$ (GPa). The corresponding independent elastic constant C_{11} is also changed; $C_{11} = 1331$ (GPa). The inner and outer radii of the scatterer are still the same; $a = 1$(m) and $b = 1.2a$, respectively. The ratio of Young's Moduli along radial and tangential directions is: $E_r/E_\theta = 1330.9868/12.2 = 109.1$. The simulation is run at frequency $ka = 2$, 4, and 6. The truncation numbers at the three frequencies are the same as for those of the last two cases. The sound speeds along r and θ

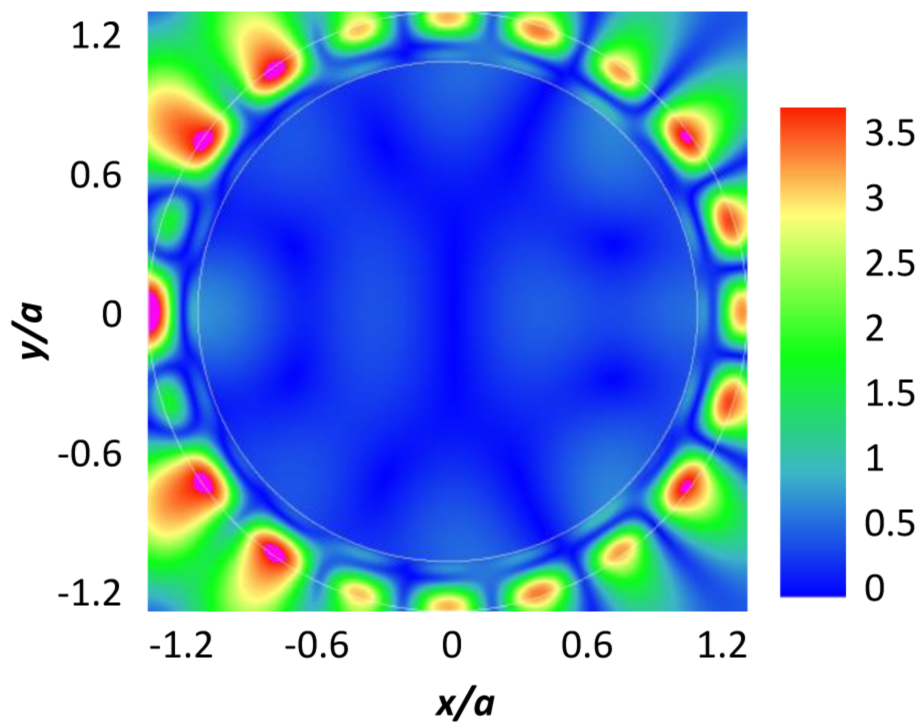

Figure 5.6: *Same pressure with shown in Fig. 5.5 (right), while increasing maximum value of the pressure for the color bar increased to 3.5.*

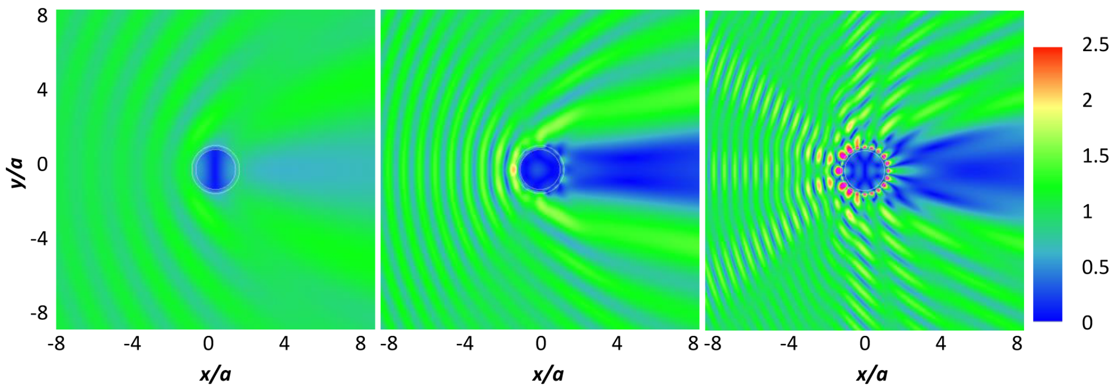

Figure 5.7: *Total acoustic pressure field for the $E_r/E_\theta \approx 100$ case, at frequency $ka = 2$ (left), 4 (middle), and 6 (right).*

directions are given as

$$c_r = \sqrt{\frac{C_{11}}{\rho_o}} = 31955.2(\mathrm{m/s}), \quad c_\theta = \sqrt{\frac{C_{22}}{\rho_o}} = 3059.44(\mathrm{m/s}) \tag{5.6}$$

Fig. 5.7 shows the total acoustic pressure field at frequency $ka = 2$, 4, and 6, respectively. It can be found that the pressure fields in Fig. 5.7 are quite similar with those in Figs. 5.4 and 5.2. The acoustic pressure is higher when E_r increases while the other properties are held constant, which is easier to observe at higher frequency $ka = 6$.

Simulation 4: $E_r/E_\theta \approx 10^7$

For this example, the ratio of the Young's moduli of the orthotropic material along r and θ direction is $E_r/E_\theta \approx 10^7$. This example shows that the ratio of the Young's moduli can be higher by increasing the value of shear modulus, while the other properties are kept the same.

The material properties of the orthotropic layer are the same as those in the previous example, except that $E_r = 13.309868 \times 10^7$ (GPa) and $G_{r\theta} = 6300$ (GPa). The ratio of Young's Moduli along radial and tangential directions is: $E_r/E_\theta = 1.091 \times 10^7$. The independent elastic constants of the orthotropic medium are give as (in GPa): $C_{11} = 1.331\times$

Table 5.3: *The entries of coefficient matrix $\{\boldsymbol{R}\}$ at different terms (shown in modulus) for the $E_r/E_\theta \approx 10^7$ case*

n	$\lvert[R]_{nn}\rvert$		
	$ka = 2$	$ka = 4$	$ka = 6$
0	0.066481232420553	0.99778018629739	0.73394137033288
1	0.46168091058588	0.42493971739573	0.44220183630868
2	0.38757939857614	0.99994665451973	0.91619727424358
3	0.095027044886687	0.86445538067188	0.47702852052348
4	0.020448785838989	0.47387363174547	0.72341282281814
5	0.0095281737657016	0.1930137439373	0.9049690454997
6	0.00045020601543243	0.09165979210499	0.58602031625161
7	$9.7539390672951 \times 10^{-6}$	0.078783970227281	0.35653704761994
8	$2.2686388256284 \times 10^{-7}$	0.012454036708584	0.28019965297289
9	$4.4418664380569 \times 10^{-9}$	0.00060443710169708	0.50278319062474
10	$7.1287595972197 \times 10^{-11}$	$3.6221652039026 \times 10^{-5}$	0.051344555445278
N_t	$7.8202409614933 \times 10^{-19}$	$2.1564236987475 \times 10^{-28}$	$3.2491688052501 \times 10^{-36}$

10^8, $C_{22} = 12.2$, $C_{12} = 0.122$, $C_{44} = G_{r\theta} = 6300$. The sound speeds along r and θ directions are given as

$$c_r = \sqrt{\frac{C_{11}}{\rho_o}} = 10105117.29(\text{m/s}), \quad c_\theta = \sqrt{\frac{C_{22}}{\rho_o}} = 3059.44(\text{m/s}) \tag{5.7}$$

Therefore, for this example, the ratio of the sound speeds along radial and tangential directions is 3302.9. The simulation is run at frequency $ka = 2$, 4, and 6. The truncation numbers are chosen as 14, 24, and 33 at three frequencies, respectively.

Table 5.3 provides the the entries of coefficient matrix $\{\boldsymbol{R}\}$. In Table 5.3, $N_t = 14$, 24, and 33 at frequency $ka = 2$, 4, and 6, respectively. The values provided in Table 5.3 show that the truncation numbers chosen are large enough. When $n > N_t$, the results are small enough to be truncated.

Fig. 5.8 shows the total acoustic pressure field at frequency $ka = 2$, 4, and 6, respectively. Fig. 5.9 shows the enlarged view of the pressure field around the scatterer in Fig. 5.8. Fig. 5.9 clearly shows the continuity of the pressure field, which includes both inside and outside of the scatterer.

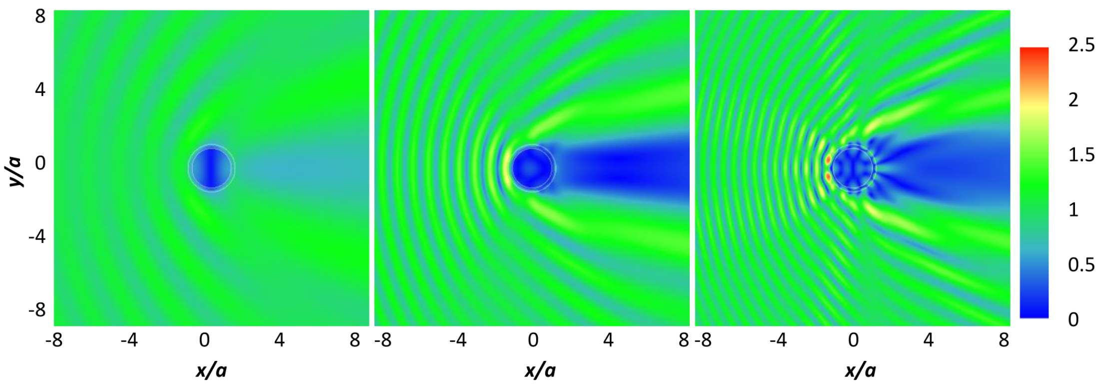

Figure 5.8: *Total acoustic pressure field for the $E_r/E_\theta \approx 1 \times 10^7$ case, at frequency $ka =$ 2 (left), 4 (middle), and 6 (right).*

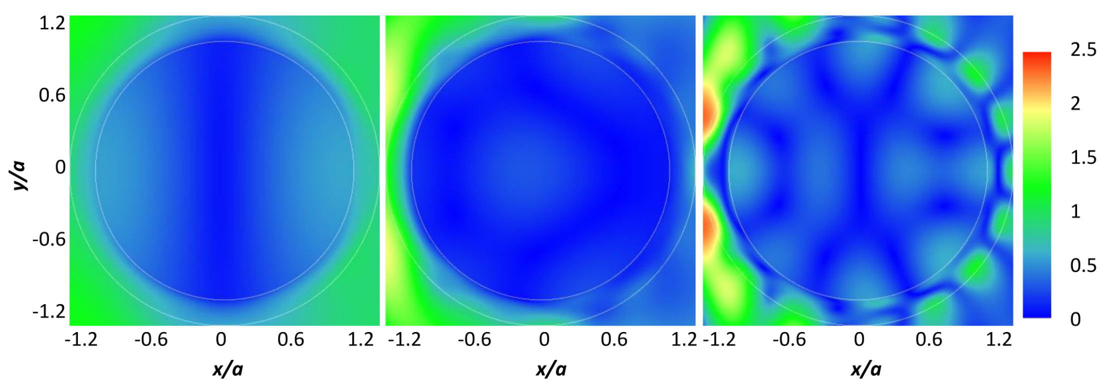

Figure 5.9: *Total acoustic pressure field for the $E_r/E_\theta \approx 1 \times 10^7$ case, at frequency $ka =$ 2 (left), 4 (middle), and 6 (right).*

Table 5.4: *The values of b_0, U_n, and V_n for the orthotropic medium when index $\alpha = \alpha_1$ at term $n = 30$ (shown in modulus).*

E_r/E_θ	$\lvert b_0\rvert$	$\lvert U_n(r)\rvert$	$\lvert V_n(r)\rvert$
1 ($G_{r\theta} = 6.3$ GPa)	1.2784659055059	18.398666658824	23.513525222316
10 ($G_{r\theta} = 6.3$ GPa)	29.844441147778	50.295716786913	1500.3859317444
100 ($G_{r\theta} = 6.3$ GPa)	308.75216896391	52.714472850934	16268.350415454
10^7 ($G_{r\theta} = 6.3$ GPa)	30987487.730903	48.819137091501	1506600504.1521
10^7 ($G_{r\theta} = 6300$ GPa)	2913.9041811694	1.1685740439733	3404.1920818544

In this simulation, the shear modulus of the orthotropic layer is increased so that E_r can be chosen about 10^7 times greater than E_θ. In this way, the accuracy of the solutions for the orthotropic medium can be ensured. Table 5.4 provides the values of coefficient b_0, and displacements $U_n(r)$, and $V_n(r)$ when $\alpha = \alpha_1$ for the orthotropic medium of the cases computed above. The term n is randomly chosen as $n = 30$. The radius r is assumed as $r = 1.1$. In this study, the coefficient a_0 is assumed as $a_0 = 1$ for every example. Table 5.4 shows that when E_r becomes much larger than E_θ, the value of b_0 increases. The difference between displacements $|U_n(r)|$ and $|V_n(r)|$ increases rapidly when E_r/E_θ increases. For the example when $E_r/E_\theta = 10^7$ while the shear modulus is kept the same with the previous cases ($G_{r\theta} = 6.3$ GPa), $|V_n(r)|$ is so much larger than $|U_n(r)|$ that errors are expected to occur for the mathematical operations, This is called loss of significance. Table 5.4 also shows that for the case $E_r/E_\theta \approx 10^7$ by increasing the value of shear modulus $G_{r\theta}$, $|b_0|$ is reduced, as well as the difference of $|U_n(r)|$ and $|V_n(r)|$. Using this approach, the accuracy of the solution for the orthotropic medium during the numerical simulation can be ensured.

5.2.2 Young's Modulus Along Radial Direction (E_r) Smaller Than That Along Tangential Direction (E_θ)

Simulation 5: $E_r/E_\theta \approx 10^{-1}$

In this example, the material properties of the orthotropic material include (Young's and shear moduli being in GPa): $E_r = 1.3309868$, $E_\theta = 12.2$, $G_{r\theta} = 1.3$, $\nu_{r\theta} = 0.01$, and

Table 5.5: *The entries of coefficient matrix $\{\boldsymbol{R}\}$ at different terms (shown in modulus) for the $E_r/E_\theta \approx 10^{-1}$ case*

	$\|[R]_{nn}\|$		
n	$ka = 1$	$ka = 3$	$ka = 5$
0	0.3188202795966	0.71419548774304	0.44528726628225
1	0.2779062720334	0.22197397517724	0.84988636578111
2	0.047077690437927	0.6124722306012	0.16834919270872
3	0.0042561875942602	0.31344336926491	0.97296285294819
4	0.00080850859956977	0.074763218951917	0.40599622021585
5	$1.3213369469612 \times 10^{-5}$	0.017807077091543	0.04236837357114
6	$9.7544982253749 \times 10^{-8}$	0.0055682511547072	0.075875988224313
N_t	$7.3078949909829 \times 10^{-10}$	$1.724872802234 \times 10^{-21}$	$3.6059534710933 \times 10^{-35}$

$\rho_o = 1303.44(\text{kg/m}^3)$. The ratio of Young's Moduli along radial and tangential directions is: $E_r/E_\theta \approx 10^{-1}$. The independent elastic constants of the orthotropic medium are given as (in GPa): $C_{11} = 1.331$, $C_{22} = 12.2$, $C_{12} = 0.122$, $C_{44} = G_{r\theta} = 1.3$. The inner and outer radii of the scatterer are $a = 1$ and $b = 1.2a$, respectively. The simulation is run at frequency $ka = 1$, 3, and 5. The truncation number N_t at three frequencies are taken as 7, 18, and 30, respectively.

Table 5.5 provides the the entries of coefficient matrix $\{\boldsymbol{R}\}$, which represents the scattered waves. Table 5.5 shows that the truncation numbers at three frequencies are large enough to ensure the accuracy of the results. Fig. 5.10 shows the total acoustic pressure field at frequency $ka = 1$, 3, and 5, respectively. Fig. 5.11 shows the enlarged view of the total acoustic pressure field at frequency $ka = 1$, 3, and 5, respectively. The continuity of the pressure field can be observed from Fig. 5.11.

Simulation 6: $E_r/E_\theta \approx 10^{-2}$

For this example, the ratio of the Young's Moduli of the orthotropic material along r and θ directions is: $E_r/E_\theta \approx 10^{-2}$, where $E_r = 1.3309868$ (GPa) and $E_\theta = 122$ (GPa). Compared with the previous example, the shear modulus $G_{r\theta}$ is increased to 5.8 to be able to reduce the ratio of the Young's Moduli E_r/E_θ from 10^{-1} to 10^{-2}. Mass density and

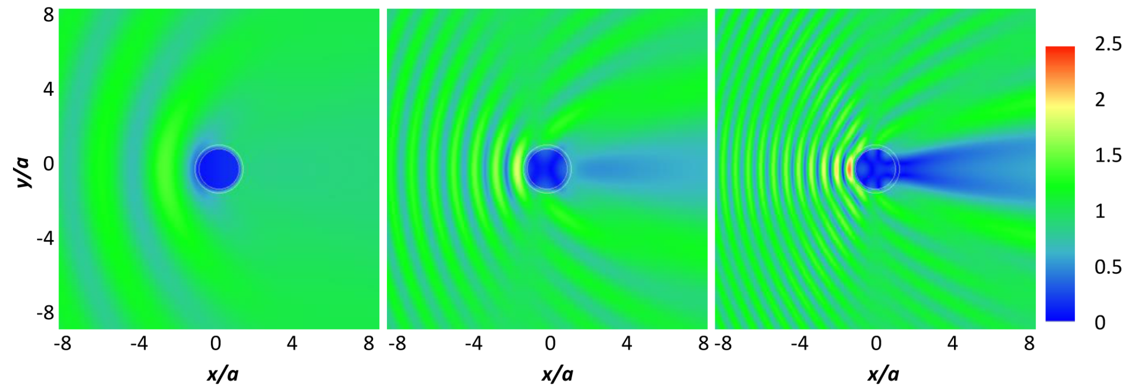

Figure 5.10: *Total acoustic pressure field for the $E_r/E_\theta \approx 10^{-1}$ case, at frequency $ka =$ 1 (left), 3 (middle), and 5 (right).*

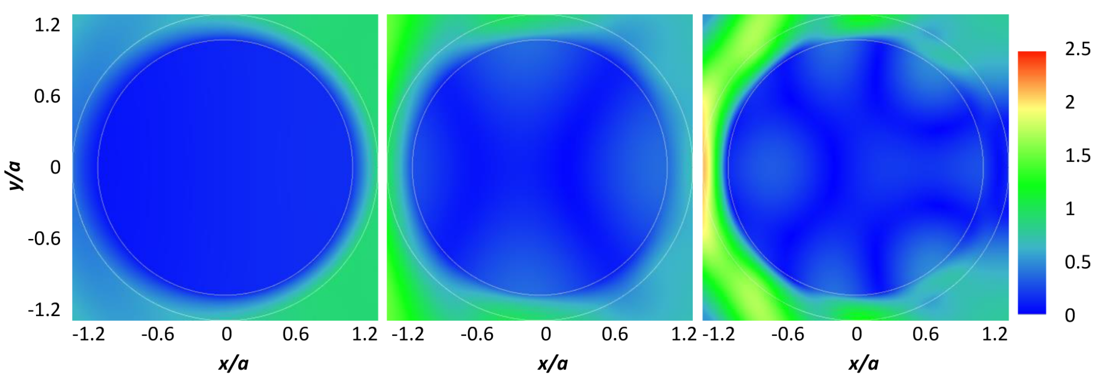

Figure 5.11: *Enlarged view of total acoustic pressure field for the $E_r/E_\theta \approx 10^{-1}$ case, at frequency $ka =$ 1 (left), 3 (middle), and 5 (right).*

Table 5.6: *The entries of coefficient matrix $\{\boldsymbol{R}\}$ at different terms (shown in modulus) for the $E_r/E_\theta \approx 10^{-2}$ case*

	$\lvert[R]_{nn}\rvert$		
n	$ka = 1$	$ka = 3$	$ka = 5$
0	0.5048135930979	0.69912061206557	0.90003047407033
1	0.30969480701464	0.94801784089994	0.48026829316544
2	0.072749000644758	0.66932369855269	0.43435982449345
3	0.045225383464889	0.40244032429088	0.89857212756527
4	0.00040407528193242	0.33943060762603	0.49362328761546
5	$6.4444523272227 \times 10^{-6}$	0.60651607869972	0.61909918703873
6	$7.5405312157044 \times 10^{-8}$	0.040226107118862	0.69050262403842
N_t	$6.4310865461953 \times 10^{-10}$	$1.5959588636729 \times 10^{-21}$	$3.1776196053986 \times 10^{-33}$

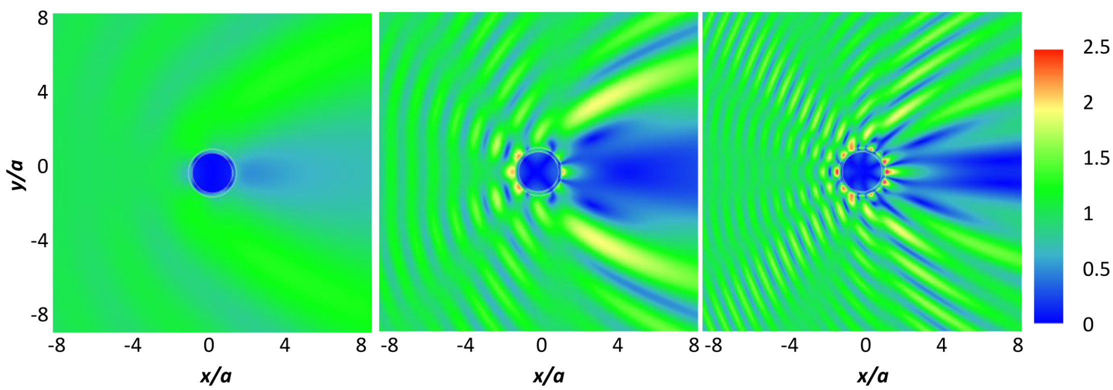

Figure 5.12: *Total acoustic pressure field for the $E_r/E_\theta \approx 10^{-2}$ case, at frequency ka = 1 (left), 3 (middle), and 5 (right).*

Poisson's ratio are kept the same as those in the previous example. The truncation numbers N_t at frequencies $ka = 1$, 3, and 5 are taken as 7, 18, and 29, respectively.

Table 5.6 provides the the entries of coefficient matrix $\{\boldsymbol{R}\}$. Table 5.6 shows that the truncation numbers at three frequencies are large enough to ensure the accuracy of the results. Fig. 5.12 shows simulation results of the total acoustic pressure field at frequency $ka = 1$, 3, and 5, respectively. Through comparison between Tables 5.5 and 5.6, Figs. 5.10 and 5.12, it can be found that when $E_r < E_\theta$, modifying E_r/E_θ can cause larger changes for pressure fields compared with the case when $E_r > E_\theta$. The acoustic pressure in the host for this case (with a larger E_θ) is higher than that of the previous case (with a smaller E_θ). Fig. 5.13 provides a enlarged view of the pressure field around the scatterer in Fig. 5.12.

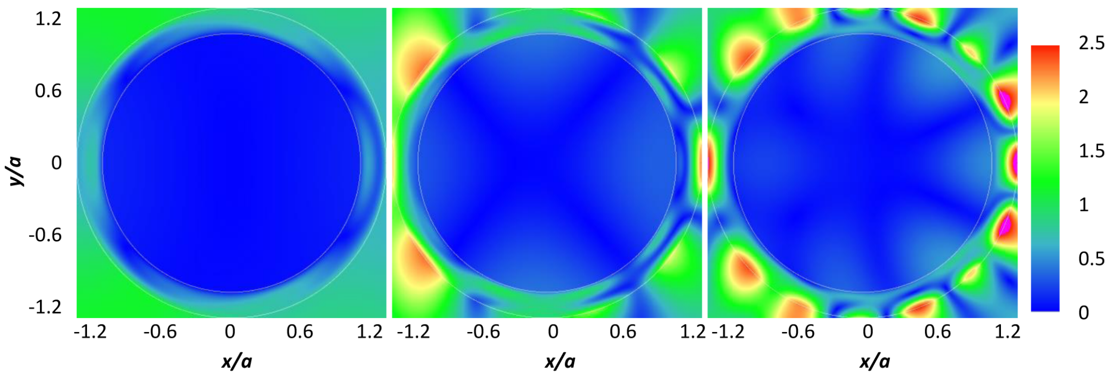

Figure 5.13: *Enlarged view of pressure field around the scatterer in Fig. 5.12.*

The continuity of pressure field can be observed in Fig. 5.13.

For the situation when $E_r < E_\theta$, the index α_σ, where $\sigma = 1$, 2, 3, and 4 are very large. For this simulation, when $E_r/E_\theta \approx 10^{-2}$, the values of the index are $\alpha_{1,2} = \pm 113.55$ and $\alpha_{3,4} = \pm 70.82$. Recall the expressions of the $U_n(r)$ and $V_n(r)$ in Frobenius series form:

$$U_n(r) = \sum_{m=0}^{\infty} a_m r^{m+\alpha}, \quad V_n(r) = \sum_{m=0}^{\infty} b_m r^{m+\alpha} \tag{5.8}$$

In Eqn. (5.8), the coefficients a_m and b_m will decrease when m increases, while $r^{m+\alpha}$ will increase when m increases. If α is too big such that the increase of $r^{m+\alpha}$ is faster than the reduction of a_m and b_m, then $U_n(r)$ and $V_n(r)$ will increase and finally will go to infinity. In this case, the Frobenius method fails. Two methods can be used to solve this problem: 1) try to reduce α and 2) reduce the value of r. Both methods can work for reducing the increasing speed of $r^{m+\alpha}$. In this simulation, the shear modulus is increased to reduce the value of α.

Simulation 7: $E_r/E_\theta \approx 10^{-4}$

In this section, by increasing the shear modulus and reducing the thickness of the orthotropic layer, the ratio of the Young's moduli along r and θ directions can be reduced to $E_r/E_\theta \approx 10^{-4}$. The Young's Moduli along r and θ directions in this example are defined as:

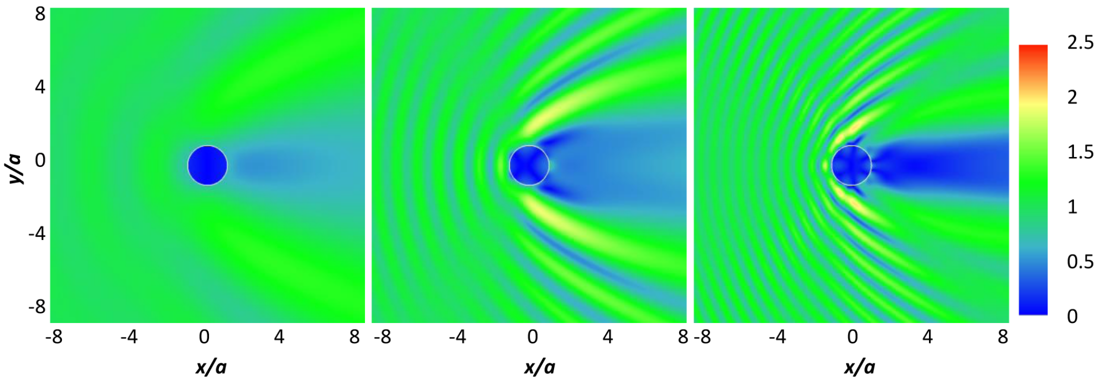

Figure 5.14: *Total acoustic pressure field for the $E_r/E_\theta \approx 10^{-5}$ case, at frequency ka = 1 (left), 3 (middle), and 5 (right).*

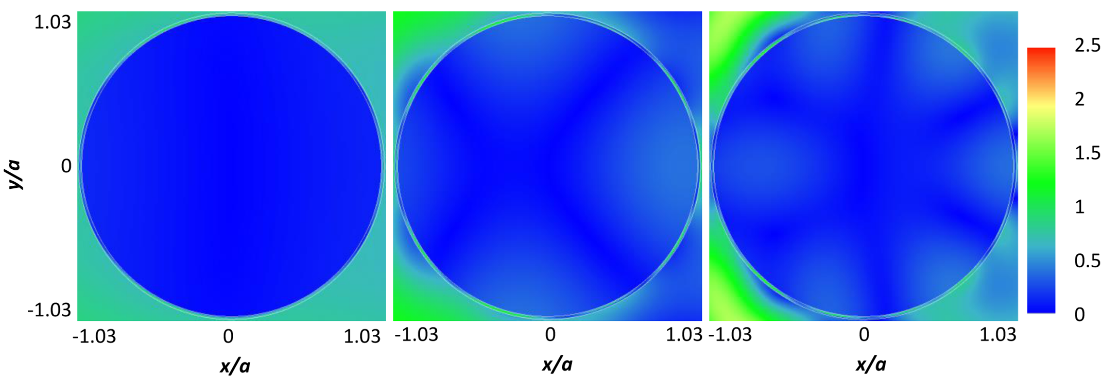

Figure 5.15: *Enlarged view of the pressure distribution of Fig. 5.14 .*

$E_r = 1.3309868$ and $E_\theta = 1.22003459 \times 10^4$. The other properties of the orthotropic layer are kept the same with those in the last example. The shear modulus $G_{r\theta}$ is increased to 18.5 (GPa). The inner radius of the scatterer is kept the same with that in the last example ($a = 1$), while the outer radius of the scatterer is reduced to $b = 1.02a$.

Fig. 5.14 shows simulation results of the total acoustic pressure field at frequency ka = 1, 3, and 5, respectively. To observe the pressure field inside the scatterer, an enlarged view is provided in Fig. 5.15. Since for this case the thickness of the orthotropic layer is very small, it is hard to observe the pressure inside the entire scatterer. Fig. 5.16 shows a very small part of the pressure field which is $-1.03 < x/a < -0.99$ and $0 < y/a < 0.06$. It is apparent from Fig. 5.16 that the pressure is continuous in the host, orthotropic layer,

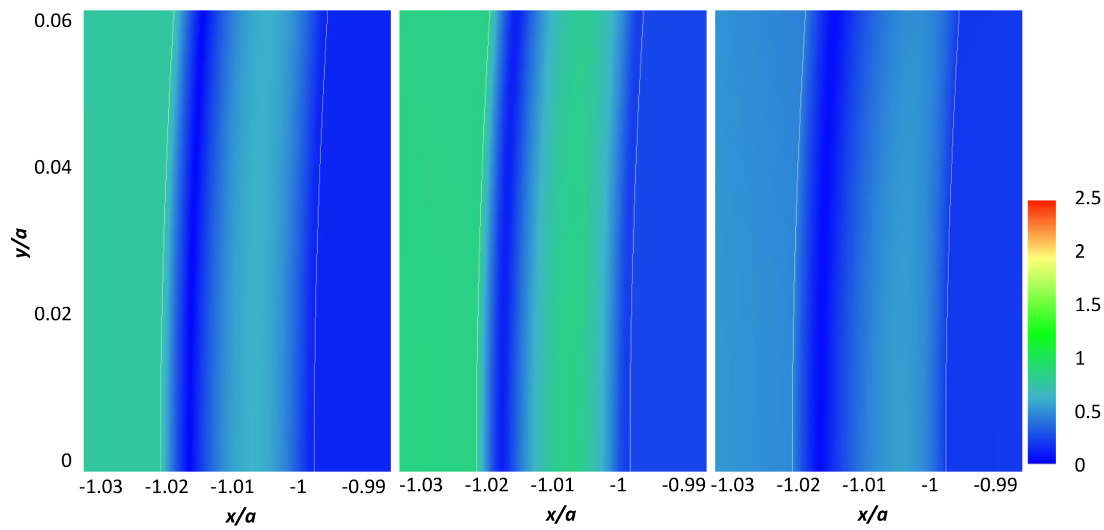

Figure 5.16: *Enlarged view of the pressure distribution of Fig. 5.14 and Fig. 5.15.*

core, as well as at the interfaces between the host and orthotropic layer, and the core and orthotropic layer.

5.2.3 Remarks

The simulations carried out above successfully show that the difference of the Young's moduli along r and θ directions can reach a large range from $E_r/E_\theta \approx 10^7$ to $E_r/E_\theta \approx 10^{-5}$. These simulations also show that the difference of E_r and E_θ can be increased by increasing the value of shear modulus of the orthotropic layer or reducing the thickness of the orthotropic layer, while the other properties are kept the same. This factor would be helpful for future study.

5.3 Simulation of Acoustic Scattering by a Specially Designed Multilayered Scatterer

In this section, the numerical example of the acoustic scattering by a multilayered scatterer which comprises a mixture of isotropic acoustic and orthotropic solid layers is implemented. The scatterer has ten layers ($N = 10$) of equal thickness, which include five isotropic acoustic layers and five orthotropic solid layers. The innermost radius of the scatterer, which is the radius of the core, is $a = 1$(m). The outermost radius of the scatterer is $b = 1.2a$. The host is water with a sound speed of 1350 m/s and a mass density of 1000 kg/m^3. The core is an acoustic medium with a mass density of 76.7201 kg/m^3 and a sound speed of 1475 m/s.

A Cummer-Schurig cloak requires the mass density and bulk modulus to satisfy the following relations

$$\frac{\rho_r}{\rho_0} = \frac{r}{r-a}, \quad \frac{\rho_\theta}{\rho_0} = \frac{r-a}{r}, \quad \frac{K}{K_0} = \left(\frac{b-a}{b}\right)^2 \frac{r}{r-a} \tag{5.9}$$

In an acoustic medium, the sound speed is given by

$$c = \frac{K}{\rho} \tag{5.10}$$

By combining Eqns. (5.9) and (5.10), the sound speeds required by the Cummer-Schurig cloaking design are given as

$$c_r = \frac{K}{\rho_r} = \frac{b-a}{b}\sqrt{\frac{K_0}{\rho_0}}, \quad c_\theta = \frac{K}{\rho_\theta} = \frac{b-a}{b}\frac{r}{r-a}\sqrt{\frac{K_0}{\rho_0}} \tag{5.11}$$

where c_r and c_θ are the sound speeds in radial and tangential directions, respectively. According to the above Eqn. (5.11), the ratio of the sound speeds along r and θ directions can be given as

$$\frac{c_r}{c_\theta} = \frac{r-a}{r} \tag{5.12}$$

For the five orthotropic layers of the scatterer, the ratios of their sound speeds along r and θ directions are determained based on the Cummer-Schurig cloaking design which has five anisotropic layers. The radii of five anisotropic layers of the Cummer-Schurig cloaking

Table 5.7: *Material properties of the orthotropic medium*

	r_i	E_r(GPa)	E_θ(GPa)	$G_{r\theta}$(GPa)	$\nu_{r\theta}$
layer 1	1.02	1.330986842	3461.905	18.5	0.01
layer 3	1.06	1.330986842	415.4159389	6.85	0.01
layer 5	1.10	1.330986842	161.0494079	5.85	0.01
layer 7	1.14	1.330986842	91.35428384	4.85	0.01
layer 9	1.18	1.330986842	57.20034592	3.85	0.01

design are given as $r_i = 1.02$, 1.06, 1.10, 1.14, and 1.18, where $i = 1$, 2, 3, 4, and 5. The inner-most and outer-most radii of the Cummer-Schurig cloaking shell are $a = 1$ and $b = 1.2a$, respectively. According to Eqn. (5.12), for each anisotropic layer, the ratio between c_r and c_θ can be given as: $c_{r_1}/c_\theta = (r_1 - a)/r_1 = 0.0196$, $c_{r_2}/c_\theta = (r_2 - a)/r_2 = 0.0566$, $c_{r_3}/c_\theta = (r_3 - a)/r_3 = 0.09091$, $c_{r_4}/c_\theta = (r_4 - a)/r_4 = 0.1228$, and $c_{r_5}/c_\theta = (r_5 - a)/r_5 = 0.15254$, respectively.

To satisfy the relations between c_r and c_θ required by Cummer-Schurig cloaking design, the Young's moduli E_r and E_θ of the orthotropic solid layers need to satisfy the following relation (Aauld, 1973; Dahmen et al., 2010)

$$\frac{c_r}{c_\theta} = \sqrt{\frac{E_r}{E_\theta}} \tag{5.13}$$

The material properties of the five orthotropic solid layers of the scatterer are provided in Table 5.7. The table shows that the radii of the orthotropic solid layers of the scatterer are the same with those of the anisotropic layers of the Cummer-Schurig cloaking design. The Young's moduli along the radial direction (E_r) are defined to be the same, while those along the tangential direction (E_θ) are defined differently at each layer. The relations between c_r and c_θ required by Cummer-Schurig cloaking design are satified in these five orthotropic solid layers. The even numbered layers of the scatterer are all acoustic layers which have the same material properties as the core. Fig. 5.17 shows the simulation results of the total acoustic pressure field at frequency $ka = 2$, 4, and 6, respectively.

To watch the continuity of the pressure inside and outside the scatterer, the case when

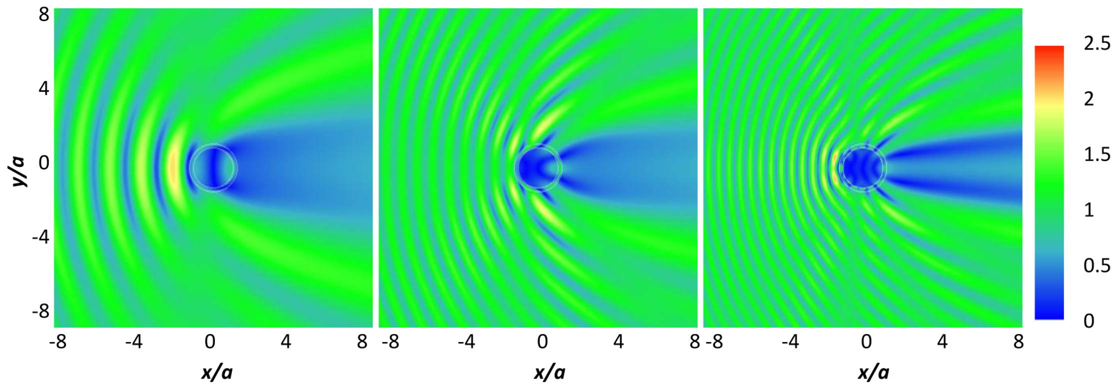

Figure 5.17: *Total acoustic pressure field distribution due to impinging of a planar incident wave onto the multi-layer scatterer at frequency $ka = 2$ (left), 4 (middle), and 6 (right).*

frequency $ka = 4$ is used as an example. Fig. 5.18 shows the enlarged view of the acoustic pressure field around the scatterer at frequency $ka = 4$. Two white circles in Fig. 5.18 show the inner-most and outer-most radii of the scatterer. Fig. 5.18 provides useful information about the continuity of the pressure. However, in some points of the pressure field, the continuity of the pressure is not clearly observable. To get a better view, Fig. 5.19 (left) shows the right upper corner of Fig. 5.18. Fig. 5.19 (right) shows the enlarged view of the field inside of the red square shown in Fig. 5.19 (left). So through these figures, the continuity of the pressure can be easily observed.

Figs. 5.20 and 5.21 provide the modulus of acoustic pressure inside the scatterer along the radial direction ($y/a = 0$): $-1.2 < x/a < -0.98$ and $0.98 < x/a < 1.2$, respectively. The calculation pitch of the point along radial direction is $x/a = 0.003$. It is easy to tell from Figs. 5.20 and 5.21 that the pressure is continuous at all the surfaces of the ten layers.

Fig. 5.20 shows the acoustic pressure inside the core ($-1 < x/a < -0.98$) is low, around 0.2. Then starting from the first layer of the scatterer, the pressure eventually increases. In the orthotropic layers, the pressure increases more than in the acoustic layers. There is a slight drop of the pressure in layers 7 and 8. Then a large increase happens in layer 9, which is an orthotropic layer. The same phenomenon can also be observed from Figs. 5.17 and 5.18.

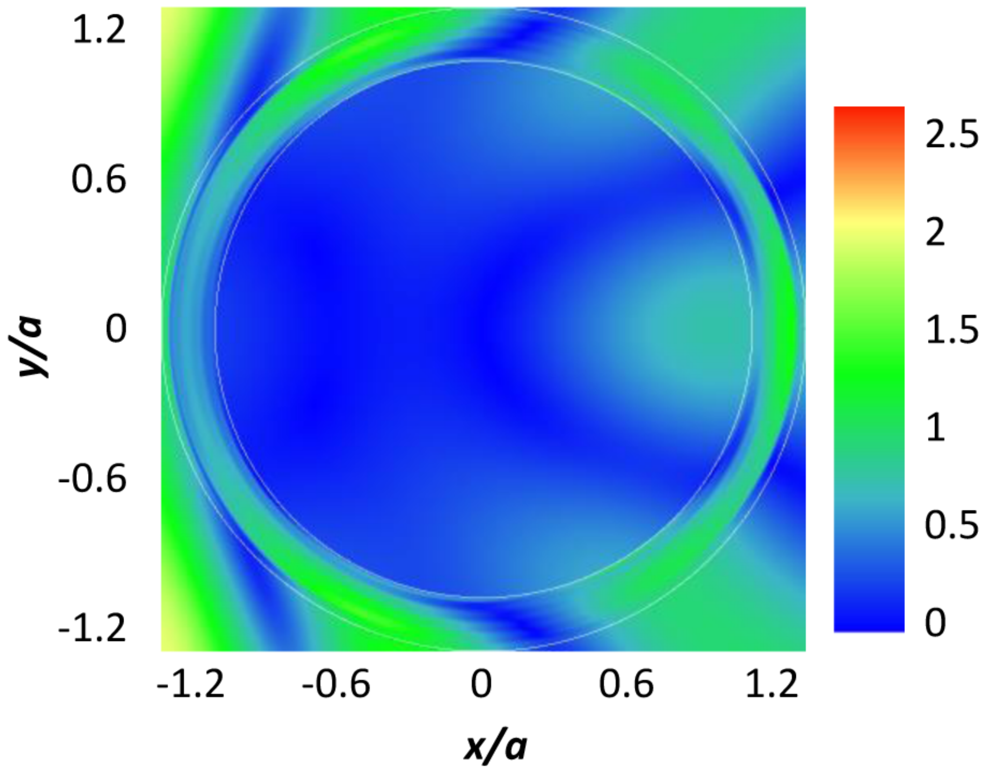

Figure 5.18: *Enlarged view of total acoustic pressure field distribution around the scatterer of Fig. 5.17 at frequency* $ka = 4$.

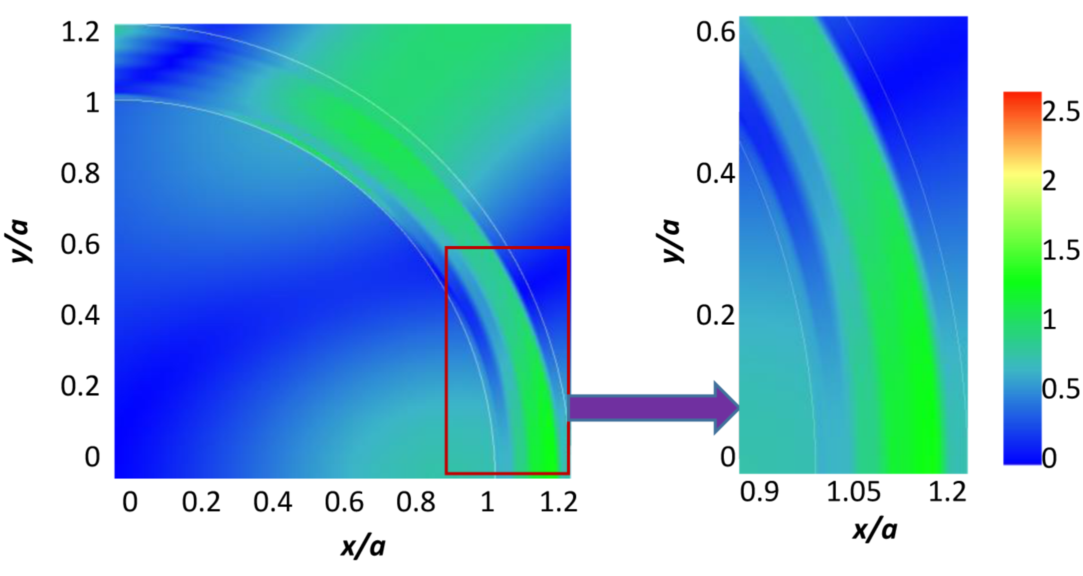

Figure 5.19: *Enlarged view of total acoustic pressure field distribution around the scatterer of Fig. 5.18 at frequency* $ka = 4$.

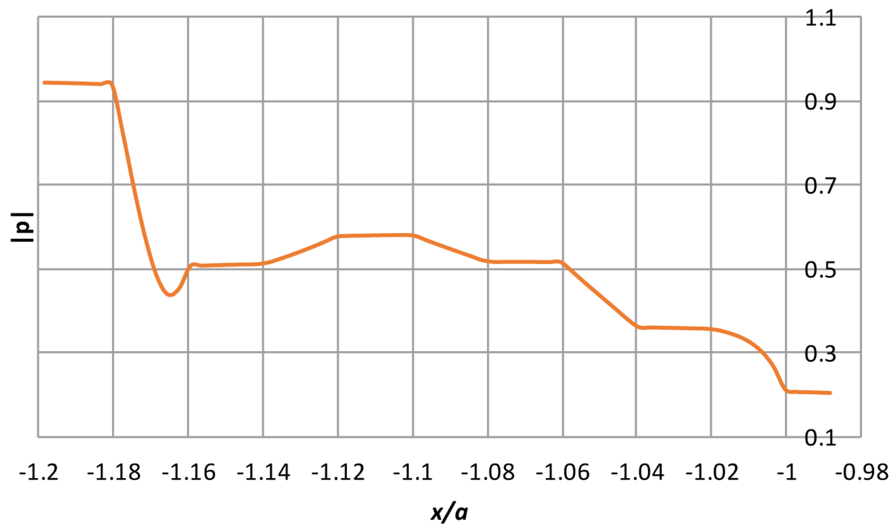

Figure 5.20: *Modulus of acoustic pressure* $|p|$ *along radial direction* $(-1.2 < x/a < -0.98, y/a = 0)$ *at frequency* $ka = 4$.

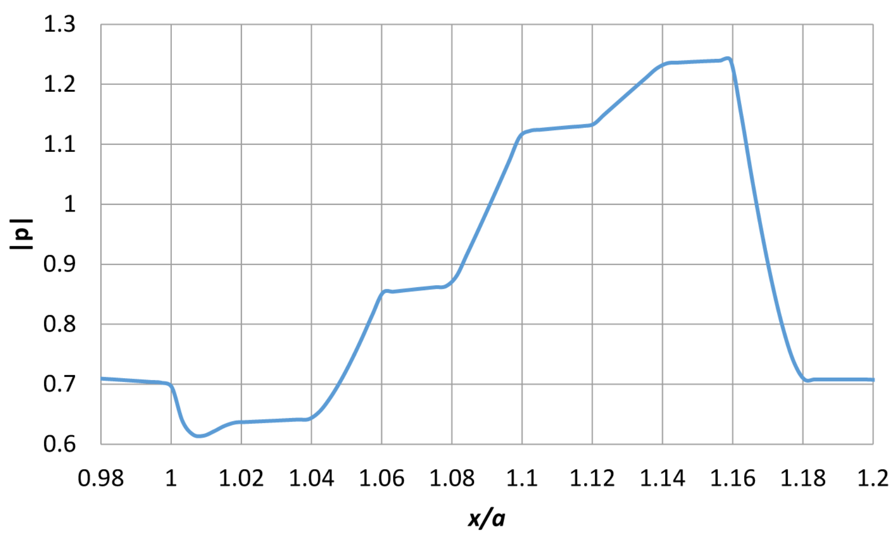

Figure 5.21: *Modulus of acoustic pressure* $|p|$ *along radial direction* $(0.98 < x/a < 1.2, y/a = 0)$ *at frequency* $ka = 4$.

In Fig. 5.21, the modulus of the pressure inside the core where $0.98 < x/a < 1$ is around 0.7. In the first layer, the pressure has a slight drop and then increases. In the orthotropic layer 9, the pressure has a significant decrease. The pressure has a larger change in the orthotropic solid layers and a smaller change in the isotropic acoustic layers. The same phenomenon can be observed in Fig. 5.19.

From Figs. 5.18 to 5.21, the continuity of the pressure both inside and outside the scatterer can be seen. The continuity of the pressure is a validation of the simulation results. This numerical example verified the analytically exact solutions for scattering by the multilayered scatterer which comprises a mixture of both isotropic acoustic and orthotropic solid layers. It also demonstrates that the computational system built in this study has the capability to simulate the scatterer solutions obtained in this study. In addition, the numerical example also shows that the difference of the sound speeds along radial and tangential directions required by Cummer-Schurig design can be realized at the orthotropic layers of the multilayered scatterer. This work is ready to support future study of acoustic cloaking design.

Chapter 6

Conclusion

6.1 Summary

In this thesis, analytically exact solutions for waves in cylindrically orthotropic elastic media, and acoustic scattering by multilayered scatterer which has a mixture of isotropic acoustic and orthotropic elastic layers are derived. A computational system is built and proven capable of conducting numerical simulations of the acoustic scattering problems presented in this study. The major achievements of this thesis are summarized in the following paragraphs.

1. The analytically exact solutions for waves in cylindrically orthotropic elastic media are derived. The equation of motion in terms of displacement are solved using Frobenius method. Three special cases are discussed in detail in the solving process to give complete solutions, which include: 1) two α's differ by an integer, 2) when α is repeated root, and 3) when n=0.

2. A new set of two canonical problems are defined. Each canonical problem involves one incident wave and three media which are separated by two interfaces. The media are acoustic-orthotropic-acoustic. They are solved by considering appropriate boundary conditions at each interface.

3. Analytically exact solutions for acoustic scattering by a "general" multilayered scatterer are derived, implemented and verified. The solutions are capable of handling scatterers which have an arbitrary number of layers and each layer can be either acoustic fluid or orthotropic elastic.

4. A computational system is built and demonstrated to be capable of conducting the numerical simulations of the scattering by general multilayered scatterers.

6.2 Future Work

In our previous work, optimization approaches were adopted for designing acoustic cloaks (Bao and Cai, 2012). This work showed that perfect cloaking design can be obtained by using a mixture of isotropic fluid and isotropic elastic layers. In the current study, acoustic scattering by scatterers which have a mixture of isotropic fluid and orthotropic elastic layers are solved and implemented. Future work is to apply optimization approaches for the design of acoustic cloaks which comprise isotropic fluid and orthotropic elastic layers.

Bibliography

Aauld, B. A. (1973). *Acoustic Fields and waves in solids, vol. 1.* Wiley Interscience, New York.

Bao, C. and Cai, L. W. (2012). Use multi-objective optimization for designing cloaks with acoustic and elastic materials. *ASME 2012 International Mechanical Engineering Congress and Exposition*, 12:389–396.

Cai, L. W. (2004). Multiple scattering in single scatterers. *The Journal of the Acoustical Society of America*, 115:986–995.

Cai, L. W. (2008). Acoustical scattering by radially stratified scatterers. *The Journal of the Acoustical Society of America*, 124:2715–2726.

Cai, L. W. (2012). Optimizing imperfect cloaks to perfection. *The Journal of the Acoustical Society of America*, 132:2923–2931.

Cai, L. W. and Sanchez-Dehesa, J. (2007). Analysis of cummer-schurig acoustic cloaking. *New journal of physics*, 9:450.

Cai, L. W. and Sánchez-Dehesa, J. (2012). Analysis of equivalent anisotropy arising from dual isotropic layers of acoustic media. *The Journal of the Acoustical Society of America*, 132:2915.

Campbell, S. L. and Haberman, R. (1996). *Introduction to differential equations: with boundary value problems.* Houghton Mifflin.

Chen, H. and Chan, C. T. (2007). Acoustic cloaking in three dimensions using acoustic metamaterials. *Applied Physics Letters*, 91:183518.

Chen, H. and Chan, C. T. (2008). Electromagnetic wave manipulation by layered systems using the transformation media concept. *Physical Review B*, 78:054204.

Chen, H., Wu, B.-I., Zhang, B., and Kong, J. A. (2007). Electromagnetic wave interactions with a metamaterial cloak. *Physical Review Letters*, 99:063903.

Chen, H. Y., Yang, T., Luo, X. D., and Ma, H. R. (2008). The impedance-matched reduced acoustic cloaking with realizable mass and its layered design. *Chinese Physics Letters*, 25:3696–3699.

Chen, Y., Liu, X., and Hu, G. (2015). Latticed pentamode acoustic cloak. *Science Reports*, 110:124301.

Cheng, Y. and Liu, X. J. (2008a). Resonance effects in broadband acoustic cloak with multilayered homogeneous isotropic materials. *Applied Physicas Letters*, 93:071903.

Cheng, Y. and Liu, X. J. (2008b). Specific multiple-scattering process in acoustic cloak with multilayered homogeneous isotropic materials. *Journal of Applied Physics*, 104:104911.

Cheng, Y., Xu, J. Y., and Liu, X. J. (2009). Broadband acoustic cloak with multilayered homogeneous isotropic materials. *Piers Online*, 5:177–180.

Cheng, Y., Yang, F., Xu, J. Y., and Liu, X. J. (2008). A multilayer structured acoustic cloak with homogeneous isotropic materials. *Applied Physics Letters*, 92:151913.

Cummer, S. A., Popa, B., Schurig, D., Smith, D. R., Pendry, J., Rahm, M., and Starr, A. (2008). Scattering theory derivation of a 3D acoustic cloaking shell. *Physical Review Letters*, 100:024301.

Cummer, S. A., Popa, B.-I., Schurig, D., Smith, D. R., and Pendry, J. B. (2006). Full-wave simulations of electromagnetic cloaking structures. *Physical Review E*, 74:036621.

Cummer, S. A. and Schurig, D. (2007). One path to acoustic cloaking. *New journal of physics*, 9:45.

Dahmen, S., Ketata, H., Ghozlen, M. H. B. G., and Hosten, B. (2010). Elastic constants measurement of anisotropic olivier wood plates using air-coupled transducers generated lamb wave and ultrasonic bulk wave. *Ultrasonics*, 50:502–507.

Edwards, C. H. and Penney, D. E. (1996). *Differential equations and boundary value problems: computing and modeling (4th Edition)*. Pearson.

Farhat, M., Enoch, S., Guenneau, S., and Movchan, A. B. (2008a). Broadband cylindrical acoustic cloak for linear surface waves in a fluid. *Physical Review Letters*, 101:134501.

Farhat, M., Guenneau, S., Enoch, S., Movchan, A. B., Zolla, F., and Nicolet, A. (2008b). A homogenization route towards square cylindrical acoustic cloaks. *New Journal of Physics*, 10:115030.

Farlow, S. J. (2006). *An introduction to differential equations and their applications (Dover Books on Mathematics)*. Dover Publications.

García-Chocano, V. M., Sanchis, L., Díaz-Rubio, A., Martínez-Pastor, J., Cervera, F., Llopis-Pontiveros, R., and Sánchez-Dehesa, J. (2011). Acoustic cloak for airborne sound by inverse design. *Applied Physics Letters*, 99:074102.

Hu, J., Zhou, X., and Hu, G. (2009). Nonsingular two dimentional cloak of arbitrary shape. *Applied Physics Letters*, 95:011107.

Jiang, W. X., Cui, T. J., Yang, X. M., Cheng, Q., Liu, R., and Smith, D. R. (2008). Invisibility cloak without singularity. *Applied Physics Letters*, 93:194102.

Kadic, M. B., Bückmann, T., Stenger, N., Thiel, M., and Wegener, M. (2012). On the practicability of pentamode mechanical metamaterials. *Applied Physics Letters*, 100:191901.

Kwon, D. H. and Werner, D. H. (2008). Two-dimensional eccentric elliptic electromagnetic cloaks. *Applied Physics Letters*, 92:013505.

Leonhardt, U. (2006). Optical conformal mapping. *Science*, 312:1777–1780.

Li, J. and Pendry, J. B. (2008). Hiding under the carpet: a new strategy for cloaking. *Physical Review Letters*, 101:203901.

Liu, R., Ji, C., Mock, J. J., Chin, J. Y., Cui, T. J., and Smith, D. R. (2008). Broadband ground-plane cloak. *Science*, 323:366–369.

Markus, S. and Mead, D. J. (1995). Axisymmetric and asymmetric wave motion in orthotropic cylinders. *Journal of Sound and Vibration*, 181:127–147.

Martin, P. A. and Berger, J. R. (2001). Waves in wood: free vibrations of a wooden pole. *Journal of the Mechanics and Physics of Solids*, 49:1155–1178.

McQuarrie, D. A. (2003). *Mathematical Methods for Scientists and Engineers*. University Science Books.

Miller, D. A. B. (2006). On perfect cloaking. *Optics Express*, 14:12457.

Milton, G. W. and Cherkaev, A. V. (1995). Which elasticity tensors are realizable. *Journal of Engineering Materials and Technology*, 117:483–493.

Misky, I. (1965). Wave propagation in transversely isotropic circular cylinderspart ii: numerical results. *The Journal of the Acoustical Society of America*, 37:1022–1026.

Norris, A. N. (2008a). Acoustic cloaking in 2D and 3D using finite mass. http://arxiv.org/abs/0802.0701v1.

Norris, A. N. (2008b). Acoustic cloaking theory. *Proceedings of the Royal Society A*, 464:2411–2434.

Norris, A. N. (2009). Acoustic metafluids. *The Journal of the Acoustical Society of America*, 125:839–849.

Pao, Y.-H. and Mow, C.-C. (1971). *The diffraction of elastic waves and dynamic stress concentrations*. Crane Russak, New York.

Patnaik, P. K. (2009). *Introduction to differential equations*. PHI Learning Pvt. Ltd.

Pendry, J. B., Schurig, D., and Smith, D. R. (2006). Controlling electromagnetic fields. *Science*, 312:1780–1782.

Pierce, A. D. (1991). *Acoustics: An Introduction to its Physical Principles and Applications*. American Institute of Physics, New York.

Popa, B. I. and Cummer, S. A. (2011). Homogeneous and compact acoustic ground cloaks. *Physical Review B*, 83:224304.

Popa, B. I., Zigoneanu, L., and Cummer, S. A. (2011). Experimental acoustic ground cloak in air. *Physical Review Letters*, 106:253901.

Rahm, M., Schurig, D., Roberts, D. A., Cummer, S. A., Pendry, J. B., and Smith, D. R. (2008). Design of electromagnetic cloaks and concentrators using form-invariant coordinate transformations of Maxwell's equations. *Photonnics and Nanostructures - Fundamentals and Applications*, 6:87.

Ren, C. Y., Xiang, Z. H., and Cen, Z. Z. (2011). Acoustic carpet invisibility cloak with two open windows using multilayered homogeneous isotropic material. *Chinese Physic B*, 20:114301.

Riley, K. F., Hobson, M. P., and Bence, S. J. (2006). *Mathematical methods for physics and engineering, third edition*. Cambridge University Press.

Ruan, Z., Yan, M., Neff, C. W., and Qiu, M. (2007). Ideal cylindrical cloak: perfect but sensitive to tiny perturbations. *Physical Review Letters*, 99:113903.

Sanchis, L., García-Chocano, V. M., Llopis-Pontiveros, R., Climente, A., Martínez-Pastor, J., Cervera, F., and Sánchez-Dehesa, J. (2015). Three-dimensional axisymmetric cloak based on the cancellation of acoustic scattering from a sphere. *Physical Review Letters*, 5:15745.

Scandrett, C. L., Boisvert, J. E., and Howarth, T. R. (2010). Acoustic cloaking using layered pentamode materials. *The Journal of the Acoustical Society of America*, 127:2856–2865.

Scandrett, C. L., Boisvert, J. E., and Howarth, T. R. (2011). Broadband optimization of a pentamode-layered spherical acoustic waveguide. *Wave Motion*, 48:505–514.

Schurig, D., Mork, J. J., Justice, B. J., Cummer, S. A., Pendry, J. B., Starr, A. F., and Smith, D. R. (2006a). Metamaterial electromagnetic cloak at microwave frequencies. *Science*, 314:977–980.

Schurig, D., Pendry, J. B., and Smith, D. R. (2006b). Calculation of material properties and ray tracing in transformation media. *Optics Express*, 14:97949804.

Shuvalov, A. L. (2002). The frobenius power series solution for cylindrically anisotropic radially inhomogeneous elastic materials. *Quarterly Jnl. of Mechanics and App. Maths.*, 56:327–345.

Smith, J. D. and Verrier, P. E. (2011). The effect of shear on acoustic cloaking. *Proceedings of The Royal Society A*, 467:2291–2309.

Torrent, D. and Sánchez-Dehesa, J. (2008). Acoustic cloaking in two dimensions: a feasible approach. *New Journal of Physics*, 10:063015.

Urzhumov, Y., Landy, N., and Smith, D. R. (2012). Isotropic-medium three-dimensional cloaks for acoustic and electromagnetic waves. *Journal of Applied Physics*, 111:053105.

Zhang, S., Xia, C., and Fang, N. (2011). Broadband acoustic cloak for ultrasound waves. *Physical Review Letters*, 106:024301.

Zigoneanu, L., Popa, B. I., and Cummer, S. A. (2014). Three-dimensional broadband omidirectional acoustic ground cloak. *Nature Materials*, 13:352–355.